CFT Column-to-Cap Beam Connections for Accelerated Bridge Construction in Seismic Regions

Lisa Marie Berg

A thesis submitted in partial fulfillment of the
requirements for the degree of

Master of Science in Civil Engineering

University of Washington

2014

Program Authorized to Offer Degree:
Civil and Environmental Engineering

©Copyright 2014

Lisa M. Berg

University of Washington

Abstract

CFT Column-to-Cap Beam Connections for
Accelerated Bridge Construction in Seismic Regions

Lisa M. Berg

Chair of the Supervisory Committee:
Associate Professor Dawn E. Lehman
Dept. of Civil & Environmental Engineering

Due to their increased mechanical properties and ease of construction, Concrete filled steel tubes (CFTs) offer an efficient and economical alternative compared to traditional reinforced concrete columns. Despite their inherent advantages, the implementation of CFT construction within the US is limited due to unverified design expressions and lack of standard connection details. As an effort to facilitate the use of CFTs, a research program has been undertaken by the University of Washington to develop practical connection details for the use of CFTs in bridge construction in seismic regions. The focus of this research is the development of CFT column-to-cap beam connections. Three categories of the CFT column to cap beam connection have been experimentally evaluated; an embedded connection in which the steel tube is embedded in the cap beam concrete, a welded reinforced concrete connection in which headed reinforcing bars are welded to the inside of the steel tube and extended into the cap beam, and a reinforced concrete connection in which a traditional reinforced concrete cage is placed within the CFT column and extended into the cap beam. Experimental results show that these connections can achieve strength and ductility objectives with limited damage to superstructure components.

TABLE OF CONTENTS

Chapter 1 Introduction……...…15

1.1 Concrete filled tubes 14

1.2 Research objective 15

1.3 Report overview 15

Chapter 2 Review of Design Provisions……...…18

2.1 AISC Design Provisions 17

2.1.1 Material and Geometric Limitations 17

2.1.2 Effective Stiffness 18

2.1.3 Compressive Strength 18

2.1.4 Flexural Strength 19

2.1.5 Combined Flexure and Axial Compression 19

2.2 AASHTO Design Provisions 21

2.2.1 Stability Limitations 21

2.2.2 Effective Stiffness 21

2.2.3 Compressive Strength 22

2.2.4 Flexural Strength 22

2.2.5 Combined Flexure and Axial Compression 23

2.3 ACI Design Provisions 23

2.3.1 Stability Limitations 23

2.3.2 Effective Stiffness 24

2.3.3 Combined Strength 24

2.4 Comparison of Design Provisions 25

2.4.1 Comparison of Stability Limits 26

2.4.2 Comparison of Effective Stiffness 26

Chapter 3 Literature Review 29

3.1 Exposed Base Plate Connection 28

3.2 Embedded Fixed-Base Connection 30

3.3 Reinforced Concrete-Filled Steel Tube Connection Tests 32

3.4 Embedded CFT Connections 33

3.4.1 Kingsley (2005) Footing Connection Tests 37

3.4.2 Williams (2006) Footing Connection Tests 38

3.4.3 Lee (2011) Footing Connection Tests 40

3.4.4 O'Neill (2011) Footing Connection Test 41

3.5 Design Expressions from University of Washington Tests 42

3.5.1 Required Embedment Depth 42

3.5.2 Minimum Footing Depth 43

3.5.3 Shear Reinforcing Requirements 43

Chapter 4 Experimental Test Program 45

4.1 Specimen Test Matrix 44

4.1.1 Embedded CFT Connections 45

4.1.2 Welded Reinforced Concrete Connections 46

4.1.3 Reinforced Concrete Connection 47

4.2 Specimen Layout 47

4.3 Specimen Design and Construction 49

4.3.1 Caltrans Seismic Design Criteria 49

4.3.2 Embedded CFT Connections 51

4.3.3 Welded RC Connections 57

4.3.4 RC Connection 62

4.4 Specimen Materials 65

4.5 Experimental Test Setup 67

4.6 Load Protocol 71

4.7 Specimen Instrumentation 73

4.7.1 Global Instrumentation 74

4.7.2 Column Instrumentation 75

4.7.3 Connection Instrumentation 77

Chapter 5 Experimental Observations 85

5.1 Introduction 84

5.2 Overview of Damage States 86

5.3 Specimen EMB80 90

5.3.1 EMB 80 Damage State Summary 91

5.3.2 Low Drift Cycles (0.0% - 2.0% Drift) 93

5.3.3 Moderate to High Drift Cycles (2.0% - 7.0% Drift) 94

5.3.4 Specimen Failure (7.0%+ Drift) 96

5.4 Specimen WRC 100

5.4.1 WRC Damage State Summary 101

5.4.2 Low Drift Cycles (0.0% - 2.0% Drift) 103

5.4.3 Moderate to High Drift Cycles (2.0% - 8.0% Drift) 104

5.4.4 Specimen Failure (8.0% + Drift) 111

5.5 Specimen WRCUB 116
5.5.1 WRCUB Performance State Summary 117
5.5.2 Low Drift Cycles (0.0% - 2.0% Drift) 119
5.5.3 Moderate to High Drift Cycles (2.0% - 11.0% Drift) 119
5.5.4 Specimen Failure (11.0%+ Drift) 124
5.6 Specimen RC 127
5.6.1 RC Performance State Summary 128
5.6.2 Low Drift Cycles (0.0% - 2.0% Drift) 130
5.6.3 Moderate to High Drift Cycles (2.0% - 9.0% Drift) 131
5.6.4 Specimen Failure (9.0%+ Drift) 135
5.7 Specimen EMB96 137
5.7.1 EMB96 Performance State Summary 138
5.7.2 Low Drift Cycles (0.0% - 2.0% Drift) 140
5.7.3 Moderate to High Drift Cycles (2.0% - 7.0% Drift) 141
5.7.4 Specimen Failure (7.0%+ Drift) 144
Chapter 6 Data Interpretation and Analysis……..149
6.1 Force-drift response 148
6.2 Moment-drift response 150
6.3 Longitudinal Strain Profiles 153
6.3.1 Longitudinal Tube Strains 154
6.3.2 Longitudinal Reinforcing Bar Strains 156
6.4 Curvature Profiles 159
6.5 Column Rotation Profiles 165

6.5.1 Embedded CFT Specimen Rotation Profiles 166

6.5.2 RC Connection Rotation Profiles..... 168

6.6 Moment-Rotation..... 171

6.7 Column Displacement Profiles 172

6.8 Connection Rotation and Column Rotation..... 175

6.8.1 Embedded Specimen Rotation Contributions..... 175

6.8.2 WRC Specimen Rotation Contributions..... 177

6.8.3 RC Specimen Rotation Contributions..... 178

6.9 Column Buckled Shape Profile..... 178

6.9.1 Buckled Profile of Specimen EMB80..... 179

6.9.2 Buckled Profile of Specimen EMB96..... 181

6.10 Fragility Curves 186

6.11 Assessment of Performance..... 188

6.11.1 Comparison of EMB80 with Previous Work..... 190

6.11.2 Comparison of Specimens EMB80 and EMB96 193

6.11.3 Comparison of Specimens WRC AND WRCUB..... 193

6.11.4 Comparison of Specimens RC and WRC 193

6.12 Design Recommendations 194

Chapter 7 Conclusions……..……197

7.1 Summary of Research 196

7.2 Research Results and Conclusions..... 197

7.3 Recommendations for Future Research 198

LIST OF FIGURES

Figure 2.1: Plastic Stress Distribution Method 20

Figure 2.2: Strain Compatibility Method 21

Figure 2.3: ACI Model for Strength Prediction 25

Figure 2.4: CFT Column redesigned from Laguna de Santa Rosa RC Column 26

Figure 3.1: CFT-Footing Connection Configuration by Kawaguchi and Morino. 28

Figure 4.1: Proposed CFT column-to-cap beam connections 45

Figure 4.2: Embedded CFT force transfer mechanism 45

Figure 4.3: Basic Specimen Layout 48

Figure 4.4: Specimen EMB80 Reinforcing Details 53

Figure 4.5: Specimen EMB96 Reinforcing Details 54

Figure 4.6: Embedded CFT connection construction sequence 55

Figure 4.7: Cap Beam Reinforcing and Formwork 55

Figure 4.8: EMB80 tube and annular ring 56

Figure 4.9: Specimens WRC, WRCUB, and RC Reinforcing Details 59

Figure 4.10: Welded RC Connections Construction Sequence 60

Figure 4.11: Specimen WRC annular ring and reinforcing bars 61

Figure 4.12: RC Connection Construction Sequence 63

Figure 4.13: Reinforcing cage of Specimen RC 64

Figure 4.14: Experimental Test Rig 67

Figure 4.15: Williams Rods Layout 68

Figure 4.16: Axial Load Apparatus 69

Figure 4.17: Experimental test rig with Specimen EMB80 70

Figure 4.18: Target load protocol 72

Figure 4.19: Global Instrumentation Schematic 74

Figure 4.20: Column Instrumentation Schematic 76

Figure 4.21: EMB80 Strain Gauge Schematic 78

Figure 4.22: Strain gauge schematic for (a) Specimens WRC, WRCUB, and (b) RC 80

Figure 4.23: EMB80 Optotrak Target Layout 83

Figure 5.1: Specimen drift 85

Figure 5.2: Idealized Drift History 86

Figure 5.3: EMB80 Connection Detail 90

Figure 5.4: EMB80 Moment-Drift Response 91

Figure 5.5: EMB80 Cracking on South side of Column at 0.41% drift 93

Figure 5.6: EMB80 Radial cracking at 1.45% drif 94

Figure 5.7: EMB80 hairline cracking on the west side of the cap beam at 2.25% drift ... 94

Figure 5.8: EMB80 South tube buckling at (a) 3.19% drift, and (b) 4.43% drift 95

Figure 5.9: EMB80 South tube buckling at 7.0% drift 96

Figure 5.10: EMB80 tear initiation on North side of column at 7.0% drift 97

Figure 5.11: EMB80 tear initiation on South side of column at 7.0% drift 97

Figure 5.12: EMB80 tear propagation on North side of column at 8.54% drift 98

Figure 5.13: EMB80 tear propagation on South side of column at 8.30% drift 98

Figure 5.14: WRC Connection Detail 100

Figure 5.15: WRC Moment-Drift Response 101

Figure 5.16: WRC soffit cracking at 0.3% drift 103

Figure 5.17: WRC soffit openings on (a) North side of column at 1.48% drift, and (b) south side of column at 1.62% drift 104

Figure 5.18: WRC radial cracking on (a) North side of column at 1.48% drift, and (b) south side of column at 1.62% drift 104

Figure 5.19: WRC North grout pad cracking at 2.08% drift 105

Figure 5.20: WRC South grout pad cracking at 3.43% drift North 106

Figure 5.21: WRC Residual soffit openings after 10th load set (a) North side of column, and (b) south side of column 106

Figure 5.22: WRC residual grout extrusion after 10th load set 107

Figure 5.23: WRC cap beam cracking during the 11th cycle level (a) North side of specimen, (b) South side of specimen 107

Figure 5.24: WRC cracking on South face of cap beam at 7.04% drift 108

Figure 5.25: WRC cap beam cracking on (a) South side of specimen, and (b) North side of specimen 108

Figure 5.26: WRC North soffit cracking at 7.08% drift South 109

Figure 5.27: WRC exposed reinforcing bar at 8.43% drift South 110

Figure 5.28: WRC South soffit openings at 8.33% drift North 110

Figure 5.29: WRC South cap beam concrete uplift at 8.33% drift North 111

Figure 5.30: WRC North cap beam damage at 9.71% drift South (Cycle 1) 112

Figure 5.31: WRC South cap beam damage at 9.46% drift North 112

Figure 5.32: WRC North cap beam uplift at 9.71% drift South (Cycle 2) 113

Figure 5.33: WRC North cap beam damage at 11.47% drift South 114

Figure 5.34: WRC South soffit damage at 11.47% drift South 114

Figure 5.35: WRC South cap beam (a) uplift and (b) cracking at 11.01% drift North... 115

Figure 5.36: WRC (a) North, and (b) South cap beam damage after test termination ... 115

Figure 5.37: WRCUB Connection Detail 116

Figure 5.38: WRCUB Moment-drift response..... 117

Figure 5.39: WRCUB North cap beam damage at 1.58% drift South..... 119

Figure 5.40: WRCUB North (a) soffit-flange opening, and (b) cap beam crack widths at 2.24% drift South 120

Figure 5.41: WRCUB North soffit-flange opening at 3.51% drift South..... 121

Figure 5.42: WRCUB (a) soffit-flange opening, and (b) grout crushing at 4.72% drift South 121

Figure 5.43: WRC North soffit opening at 7.17% drift South..... 122

Figure 5.44: WRCUB (a) grout extrusion, and (b) residual soffit-flange opening after 13th cycle level 123

Figure 5.45: WRCUB South (a) cap beam cracking, and (b) exposed reinforcing bar at 8.19% drift North 123

Figure 5.46: WRCUB North exposed reinforcing bars at 9.76% drift South 124

Figure 5.47: WRCUB (a) Soffit-flange opening at first bar fracture, and (b) South concrete uplift at 10.53% drift North 125

Figure 5.48: WRCUB (a) North bar fracture, and (b) North cap beam damage at 12.27% drift South 126

Figure 5.49: WRCUB South cap beam damage at 11.58% drift North..... 126

Figure 6.1: EMB80 Force-Drift Response ……149

Figure 6.2: EMB96 Force-Drift Response ……149

Figure 6.3: WRC Force-Drift Response ……149

Figure 6.4: WRCUB Force-Drift Response... ……149

Figure 6.5: RC Force-Drift Response 149

Figure 6.6: EMB80 Moment-Drift Response 151

Figure 6.7: EMB96 Moment-Drift Response 151

Figure 6.8: WRC Moment-Drift Response 151

Figure 6.9: WRCUB Moment-Drift Response 151

Figure 6.10: RC Moment-Drift Response..... 151

Figure 6.11: Normalized moment-drift envelope comparison of all specimens..... 152

Figure 6.12: EMB80 Longitudinal strain profiles of steel tube 154

Figure 6.13: Longitudinal strain profiles of steel tube..... 155

Figure 6.14: WRC Longitudinal strain profiles of North & South reinforcing bars 156

Figure 6.15: WRCUB Longitudinal Strain Profiles of North & South reinforcing bars 157

Figure 6.16: RC Longitudinal strain profiles of North & South reinforcing bars 158

Figure 6.17: Curvature calculation from strain gauges..... 159

Figure 6.18: EMB80 Curvature profiles 160

Figure 6.19: EMB90 Curvature Profiles..... 161

Figure 6.20: WRC Curvature profiles..... 162

Figure 6.21: WRCUB Curvature profiles 163

Figure 6.22: RC Curvature profiles 164

Figure 6.23: EMB80 Rotation profiles 166

Figure 6.24: EMB96 Rotation profiles 167

Figure 6.25: WRC Rotation profiles..... 168

Figure 6.26: WRCUB Rotation profiles 169

Figure 6.27: RC Rotation profiles..... 170

Figure 6.28: EMB80 Moment-rotation response 171

Figure 6.29: EMB96 Moment-rotation response 171

Figure 6.30: WRC Moment-rotation response..... 171

Figure 6.31: WRCUB Moment-rotation response 171

Figure 6.32: RC Moment-rotation response 172

Figure 6.33: EMB80 Column displacement profile..... 172

Figure 6.34: EMB96 Column displacement profile..... 173

Figure 6.35: WRC Column displacement profile 173

Figure 6.36: WRCUB Column displacement profile..... 174

Figure 6.37: RC Column displacement profile 174

Figure 6.42: RC Rotation Contributions from column & connection 178

Figure 6.43: EMB80 Buckled Profile – Drift Set 5 179

Figure 6.44: EMB80 Buckled Profile – Drift Set 7 180

Figure 6.46: EMB96 Buckled Profile – Drift Set 10 182

Figure 6.47: EMB96 Buckled Profile – Drift Set 11 183

Figure 6.48: EMB96 Buckled Profile – Drift Set 13 184

Figure 6.49: EMB96 Buckled Profile – Drift Set 14 185

CHAPTER 1
INTRODUCTION

1.1 CONCRETE FILLED TUBES

Concrete filled steel tubes (CFTs) are composite structural elements consisting of circular or rectangular steel tubes with concrete infill. CFTs efficiently combine the tensile strength and ductility of steel with the compressive strength of concrete to create a competitive alternative to traditional reinforced concrete columns.

The location of the steel and concrete components in the CFT cross section optimizes the strength and stiffness of the section. By placing the steel component at the outermost fiber of the cross section, the steel is at its optimal location to effectively resist bending moment. In addition, the concrete core delays, and often prevents, local buckling of the steel tube, while the steel tube confines the concrete infill and prevents spalling.

In addition to their increased strength and stiffness, CFTs provide economic benefits as the steel tube eliminates the need for temporary shoring and formwork during construction. In addition, the hollow tube has the strength to support dead weight prior to casting concrete, facilitating rapid construction by eliminating concrete curing delays.

Despite their inherent advantages, CFTs are not currently used extensively in bridge construction in the United States due to unverified design methods and limited knowledge regarding their behavior.

1.2 RESEARCH OBJECTIVE

This is the continuation of an ongoing research program undertaken by the University of Washington to investigate the behavior of CFT column connections. Extensive research has been conducted to develop expressions for the design of CFT column-to-foundation connections capable of transferring the full moment capacity of the CFT column to its adjacent footing element. Full realization of the system, however, requires the development of CFT column-to-cap beam connection details, which present additional challenges due to geometric and reinforcement constraints.

In an effort to address these constraints, this research program investigates the response of five CFT column-to-cap beam specimens with varying connection parameters. Three primary connection types are investigated in this research program: 1) Embedded, in which the CFT column is embedded into a precast reinforced concrete cap element through a recessed fiber-reinforced grouted connection, 2) Welded Reinforced Concrete, in which headed reinforcing bars are welded to the inside of the steel tube and are developed into the cap beam, and 3) Reinforced Concrete Connection, in which longitudinal and transverse reinforcing extend from the CFT column into the cap beam.

1.3 REPORT OVERVIEW

This report includes 8 chapters.

Chapter 2 outlines the current design provisions available for CFT members in the AISC Steel Design Manual, the AASHTO LRFD Bridge Design Specification, and the

ACI Building Code. A brief comparison of the three design provisions using a prototype column is provided at the end of the chapter.

Chapter 3 summarizes previous research that has been conducted on CFT column-to-footing connections.

Chapter 4 provides an overview of the five specimens in the test program, introducing their force transfer mechanisms and strength and ductility limitations. It also provides a detailed description of the design rationale and construction procedure for each specimen, as well as the testing apparatus, loading protocol, and instrumentation used to test each specimen.

Chapter 5 discusses the experimental results of the five tests, including photographs and a description of damage states used to evaluate the performance of each specimen.

Chapter 6 discusses the data interpretation and analysis of the five tests based on measured responses from specimen instrumentation. This chapter includes force-displacement plots, as well as strain, curvature, and rotation profiles.

Chapter 7 summarizes the conclusions drawn based on the results of the five experimental tests in this program.

CHAPTER 2

REVIEW OF DESIGN PROVISIONS

This chapter outlines the current design provisions for CFT members available in the 14th Edition of the American Institute for Steel Construction (AISC) Steel Design Manual (AISC, 2011), the AASHTO LRFD Bridge Design Specifications (AASHTO, 2011), and the American Concrete Institute (ACI) Building Code Requirements for Structural Concrete (ACI, 2011).

2.1 AISC DESIGN PROVISIONS

AISC provides recommendations for the design of CFT members in Chapter I of the 2010 Steel Construction Manual (AISC, 2011). These recommendations include material property and geometric limitations, as well as expressions to determine the strength and stiffness of composite CFT sections.

2.1.1 Material and Geometric Limitations

For the purpose of strength determination, material limitations provided in AISC Section I1.3 require the concrete to have a compressive strength between 3 and 10-ksi, and the steel to have a yield stress not exceeding 75-ksi. Although these limitations may not be exceeded in strength calculations, AISC permits the use of higher strength concrete material properties when calculating the stiffness of the CFT section. For the CFT to be considered a composite member, AISC Section I2.2 requires the cross-sectional area of the steel component to comprise at least 1% of the total composite cross section area.

Limitations in Section I1.4 also require the member to be classified for local buckling based on its diameter-to-thickness $\left(\frac{D}{t}\right)$ ratio. This limitation is defined by the expression:

$$\frac{D}{t} \leq 0.15\frac{E}{F_y} \tag{2.1}$$

where E and F_y are the respective elastic modulus and nominal yield stress of steel tube.

2.1.2 Effective Stiffness

The effective stiffness, EI_{eff}, of the composite CFT section is defined in AISC Eq. I2-12 as:

$$EI_{eff} = E_s I_s + C_3 E_c I_c \tag{2.2a}$$

$$C_3 = 0.6 + 2\left[\frac{A_s}{A_c + A_s}\right] \leq 0.9 \tag{2.2b}$$

In Equations 2.2a and 2.2b, $E, I,$ and A represent the section's modulus of elasticity, moment of inertia, and area, respectively. The properties of steel and concrete are denoted by their respective subscripts, s and c.

2.1.3 Compressive Strength

The compressive strength, P_o, of an axially loaded filled composite member is defined in AISC Eq. I2-9b as:

$$P_o = F_y A_s + C_2 f_c' A_c \tag{2.3}$$

where f_c' is the design compressive strength of concrete, and C_2 is taken as 0.95 for circular sections. The compressive strength of the CFT member is limited by the flexural buckling limit states:

$$P_{cr} = P_o\left[0.658^{\frac{P_o}{P_e}}\right] \qquad for\ \frac{P_o}{P_e} \leq 2.25 \qquad (2.4a)$$

$$P_{cr} = 0.877P_e \qquad for\ \frac{P_o}{P_e} > 2.25 \qquad (2.4b)$$

in which P_e is the elastic critical buckling load defined in AISC Eq. I2-5 as:

$$P_e = \frac{\pi^2\left(EI_{eff}\right)}{(KL)^2} \qquad (2.5)$$

where K is the AISC effective length factor, and L is the length of the member.

2.1.4 Flexural Strength

The nominal flexural strength of a CFT is defined in AISC Eqs. I3-3a and I3-3b as:

$$M_n = M_p \qquad for\ \frac{D}{t} \leq 0.15\frac{E}{F_y} \qquad (2.6a)$$

$$M_n = M_p - \left(M_p - M_y\right)\left(\frac{\lambda - \lambda_p}{\lambda_r - \lambda_p}\right) \qquad for\ \frac{D}{t} > 0.15\frac{E}{F_y} \qquad (2.6b)$$

where M_p is the plastic moment capacity of the composite cross section, M_y is the yield moment, and λ, λ_p, and λ_r are slenderness ratios determined from AISC Table I1.1b.

2.1.5 Combined Flexure and Axial Compression

Section I1.2 of AISC permits use of two different methods to calculate the combined axial-flexure capacity of the CFT: the plastic stress distribution method, and the strain-compatibility method. In the plastic stress distribution method, the strength of the CFT is computed assuming the entire steel tube has reached its yield stress in either tension or compression. The component of concrete subject to compression is assumed to have reached a uniform stress of $0.95f_c'$, while the tension component of concrete is assumed

to have a negligible contribution. The 0.95 coefficient on the concrete stress is only permitted for use in circular CFTs, as this increased strength accounts for the effects of concrete confinement attributed to circular components. The moment capacity of the section is determined by satisfying equilibrium, with the applied axial load acting at the centroid of the cross section, as shown in Figure 2.1.

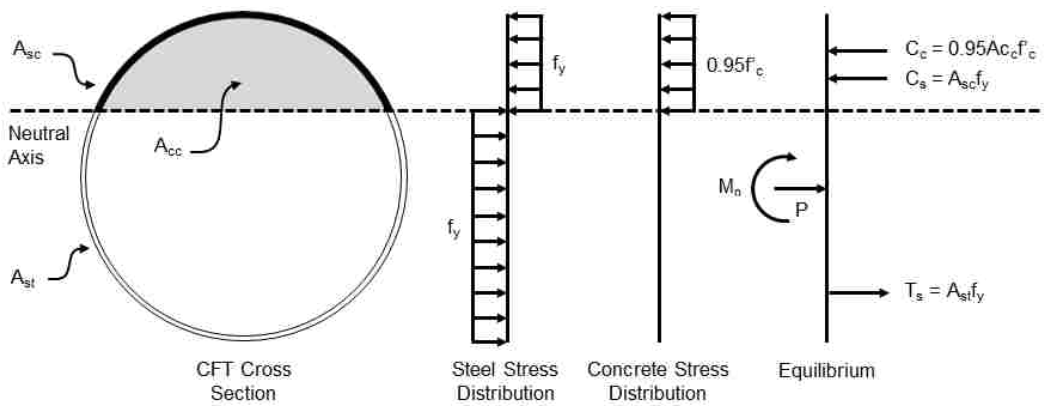

Figure 2.1: Plastic Stress Distribution Method

In the strain compatibility method, the strength of the CFT is computed assuming a linear distribution of strains across the section, with a maximum concrete compressive strain of 0.003. Figure 2.2 shows the distribution of stresses used in the strain compatibility method.

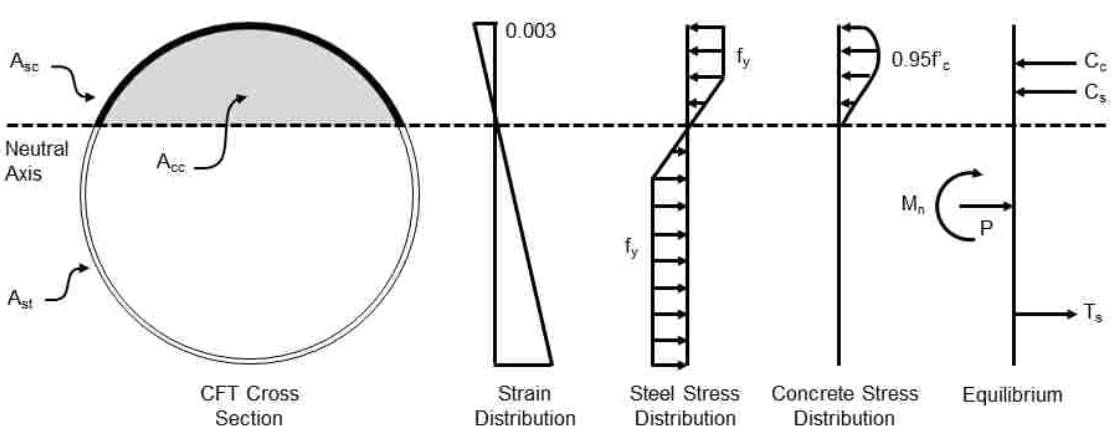

Figure 2.2: Strain Compatibility Method

2.2 AASHTO DESIGN PROVISIONS

Articles 6.9.5 and 6.12.2 of the AASHTO LRFD Bridge Design Specifications (2011) provide recommendations for the design of CFT members. The following section will discuss the stability limitations specified in the AASHTO LRFD, as well as the expressions to determine the strength and stiffness of CFT sections.

2.2.1 Stability Limitations

The AASHTO LRFD Specifications employ a $\frac{D}{t}$ ratio to limit local buckling of the steel tube. This limit is defined in Eq. 6.12.2.3.2-1 as:

$$\frac{D}{t} < 2.0\sqrt{\frac{E}{F_y}} \tag{2.7}$$

where E and F_y are the elastic modulus and nominal yield stress of the steel, respectively.

2.2.2 Effective Stiffness

AASHTO defines the effective stiffness of the composite section, EI_{eff}, in Eq. 6.9.5.1-5 as:

$$EI_{eff} = E_s I_s \left[1 + \left(\frac{C_3}{n}\right)\left(\frac{A_c}{A_s}\right)\right] \tag{2.8}$$

where I and A represent the section's moment of inertia and area, respectively, and subscripts s and c refer to the properties of the steel and concrete sections. The composite column coefficient, $C_{3,}$ is specified in Table 6.9.5.1-1 as 0.40 for a CFT, and n represents

the modular ratio of the concrete, defined in Eq. 6.10.1.1.1b-1 as: $n = \frac{E}{E_c}$, where E_c is the elastic modulus of the concrete.

2.2.3 Compressive Strength

The nominal compressive resistance, P_o, of a CFT is defined in AASHTO Eq. 6.9.5.1-4 as:

$$P_o = 0.85 f_c' A_c + F_y A_s \tag{2.9}$$

where the variables have been defined previously. This provision is similar to that as defined by AISC, except the resistance provided by the concrete is multiplied by a coefficient of 0.85, as opposed to 0.95. The column buckling is addressed in AASHTO Eqs. 6.9.5.1-1 and 6.9.5.1-2, which have been provided previously in Eqs. 2.4a and 2.4b above.

2.2.4 Flexural Strength

The nominal flexural resistance of the CFT is dependent on its $\frac{D}{t}$ ratio, as well its material properties E and F_y. AASHTO Eqs. 6.12.2.3.2-1 and 6.12.2.3.2-2 define the flexural resistance as:

$$M_n = M_{ps} \qquad for\ \frac{D}{t} \leq 2.0\sqrt{\frac{E}{F_y}} \tag{2.10a}$$

$$M_n = M_{yc} \qquad for\ \frac{D}{t} > 2.0\sqrt{\frac{E}{F_y}} \tag{2.10b}$$

where M_{ps} is the plastic moment of the steel section, and M_{yc} is the yield moment of the composite section determined by Article 6.19.3.1.2.

2.2.5 Combined Flexure and Axial Compression

Article 6.9.2.2 requires the axial compressive load, P_u, and concurrent moments, $M_{ux}$and M_{uy}, to satisfy the relationships defined in Eqns. 6.9.2.2-1 and 6.9.2.2-2 as:

$$\frac{P_u}{2P_r} + \left(\frac{M_{ux}}{M_{rx}} + \frac{M_{uy}}{M_{ry}}\right) \leq 1.0 \qquad for\ \frac{P_u}{P_r} < 0.2 \qquad (2.11a)$$

$$\frac{P_u}{P_r} + \frac{8}{9}\left(\frac{M_{ux}}{M_{rx}} + \frac{M_{uy}}{M_{ry}}\right) \leq 1.0 \qquad for\ \frac{P_u}{P_r} \geq 0.2 \qquad (2.11b)$$

where subscripts x and y correspond to loading about the x and y axes, M_u and M_r represent the flexural moment demand and resistance, and P_u and P_r represent the axial load demand and resistance, respectively.

2.3 ACI DESIGN PROVISIONS

The American Concrete Institute (ACI) provides recommendations for the design of CFT members in Section 10.13 of the Building Code Requirements for Structural Concrete (ACI, 2011).

2.3.1 Stability Limitations

Section 10.13.6.1 of the ACI Building Code specifies a minimum $\frac{D}{t}$ ratio to prevent local buckling of the section. This limit is defined as:

$$\frac{D}{t} \leq \sqrt{\frac{8E}{F_y}} \tag{2.12}$$

2.3.2 Effective Stiffness

ACI defines the effective stiffness of composite compression members in Eq. 10-23 as:

$$\mathrm{EI}_{eff} = \frac{0.2E_c I_g}{1 + \beta_{dns}} + E_s I_{sx} \tag{2.13}$$

where E_c and E_s represents the elastic modulus of the concrete and steel sections, I_g and I_{sx} represent the moment of inertia of the gross concrete section and the structural steel tube about the centroid of the composite member, and β_{dns} is a ratio used to account for the reduction of column stiffness due to sustained axial loading.

2.3.3 Combined Strength

The ACI procedure to calculate the strength of a composite member is similar to the AISC strain compatibility method, except the ACI method permits the use of an equivalent rectangular compressive stress block to replace the more exact concrete stress distribution. The equivalent stress block is assumed to have a uniformly distributed stress of $0.85f_c'$ that acts over a depth of $\beta_1 c$, where β_1 is dependent on the specified compressive strength of the concrete, and c is the distance from the extreme compression fiber to the neutral axis. Figure 2.3 shows the ACI stress distribution models.

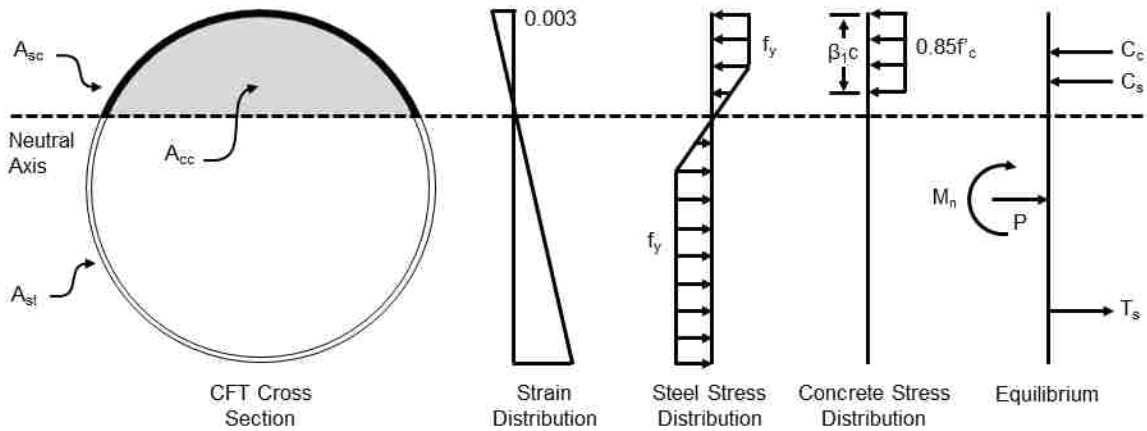

Figure 2.3: ACI Model for Strength Prediction

2.4 COMPARISON OF DESIGN PROVISIONS

For the purpose of comparison between the AISC, AASHTO and ACI design provisions, a prototype column will be used to evaluate the stability limits and effective stiffness from the three different design methods. Figure 2.4 shows the cross section of the prototype column, which is based off of a reinforced concrete column in the Laguna de Santa Rosa Bridge. The RC column has been redesigned using a comparable CFT that is 42-in. in diameter and has a 0.5-in. steel tube thickness. It will be assumed that the steel has an elastic modulus and yield stress of 29,000-ksi and 50-ksi, respectively, and the concrete has a design compressive strength of 6-ksi.

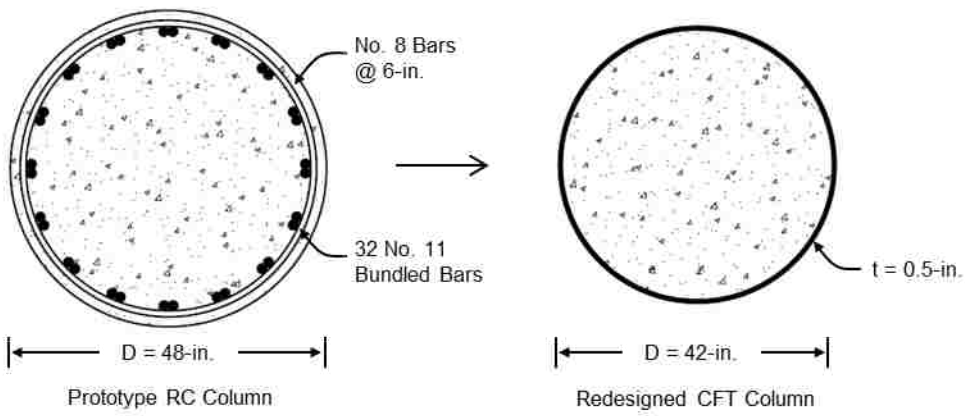

Figure 2.4: CFT Column redesigned from Laguna de Santa Rosa RC Column

2.4.1 Comparison of Stability Limits

Using the steel properties provided above, the AISC, AASHTO, and ACI stability limitations provided in Eqs. 2.1, 2.7, and 2.12 yield the following D/t limits:

AISC: $D/t \leq 87$

AASHTO: $D/t \leq 48$

ACI: $D/t \leq 68$

From the above D/t limits, it can be seen that there is a wide variation in the local slenderness limits between the different codes.

2.4.2 Comparison of Effective Stiffness

The effective stiffness was computed using the AISC, AASHTO, and ACI design provisions provided in Eqs. 2.2a, 2.8 and 2.13, respectively. In the ACI design provision, it is assumed that stiffness reduction ratio, β_{dns}, is taken as 1.0. Because of this assumption, the AISC and AASHTO provisions predict a significantly larger effective stiffness, as can be seen through the predicted values below:

AISC: $\mathrm{EI}_{eff} = 8.3\ x10^8\ k - in^2$

AASHTO: $\mathrm{EI}_{eff} = 9.1\ x10^8\ k - in^2$

ACI: $\mathrm{EI}_{eff} = 4.7\ x10^8\ k - in^2$

CHAPTER 3

LITERATURE REVIEW

Due to their unverified design expressions and lack of standard connection details, CFTs are not currently used extensively in bridge construction in the United States. As an effort to promote the use of this bridge system, research has been conducted on a variety of

different CFT column-to-footing connections to develop a detail capable of transferring the strength of a CFT column to its adjacent footing element. The following section summarizes some of the research that has been conducted on various CFT column-to-footing connections.

3.1 EXPOSED BASE PLATE CONNECTION

Kawaguchi and Morino (2006) developed a CFT-foundation connection consisting of an exposed base plate with anchor bolts and central reinforcing bars. The central reinforcing bars are embedded into the concrete foundation, and they extend into the CFT column through a hole in the base plate. The reinforcing bars are intended to increase the strength and stiffness of the connection when compared to those without the reinforcing bars. Figure 3.1 shows an overview of the proposed connection detail, as well as the construction procedure.

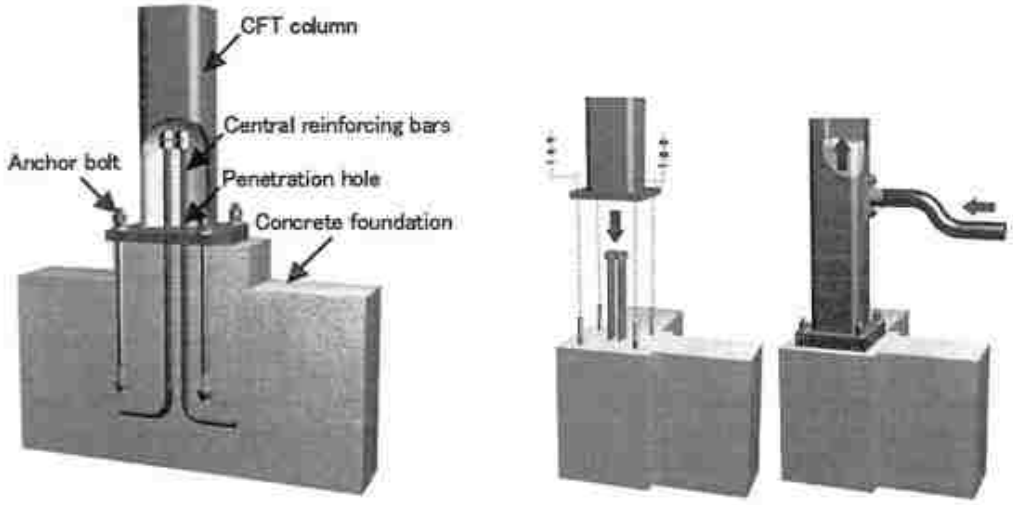

Figure 3.1: CFT-Footing Connection Configuration by Kawaguchi and Morino (Kawaguchi and Morino, 2006).

A series of 10 specimens were tested to investigate the behavior of this proposed connection. Six of the specimens consisted of 12-in. square steel tube columns with ¾-in. thickness, and the remaining four consisted of 16-in. diameter circular steel tubes with ½-in. thickness. Each specimen was constructed using a 20-in. square, 0.5-in. thick base plate with identical anchor bolts. Varying test parameters included: 1) axial force: zero, constant tension, varying tension and compression, 2) presence of central reinforcing bars, and 3) varying strength of the central reinforcing bars.

The observed failure modes of the tests consisted of a combination of conical failure of the foundation concrete due to pulling out of the anchor bolts, shear failure of concrete along the side surface of the cone, and compressive failure of the filler mortar below the base plate. None of the specimens experienced failure of the base plate or the anchor bolts. Figure 3.2 shows an example of the moment-rotation hysteretic behavior experienced by a 12-in. square CFT subjected to a constant tensile axial load of 1200-kN.

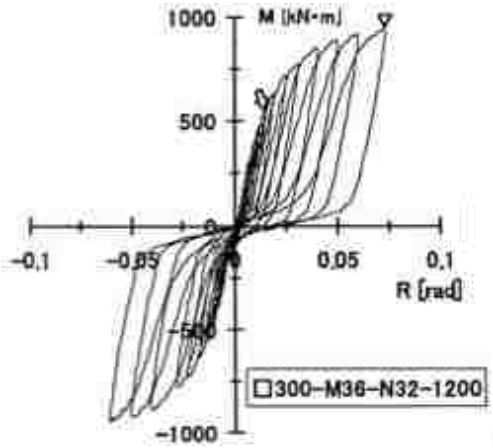

Figure 3.2: Moment-Rotation Behavior of 12-in. CFT with +1200 kN Axial Load (Kawaguchi and Morino, 2006)

Results from the experimental tests showed that the column bases with central reinforcing bars exhibited a larger stiffness and strength compared to those without the central bars. Specifically, the connections with central reinforcing bars produced an increased stiffness of 1.2, and an increased maximum strength of 1.4 – 1.8 times those of the column bases without central reinforcing.

3.2 EMBEDDED FIXED-BASE CONNECTION

Marson and Bruneau (2004) developed a foundation detail capable of transferring the full composite moment capacity of a circular concrete-filled steel tube column. In this connection detail, the strength of the column is resisted entirely by structural steel components that are welded to the steel tube and encased inside the concrete foundation. Because these steel members are designed to transfer all of the forces, no reinforcing bars are required in the concrete foundation. Figure 3.3 shows the schematic of the fixed-base connection.

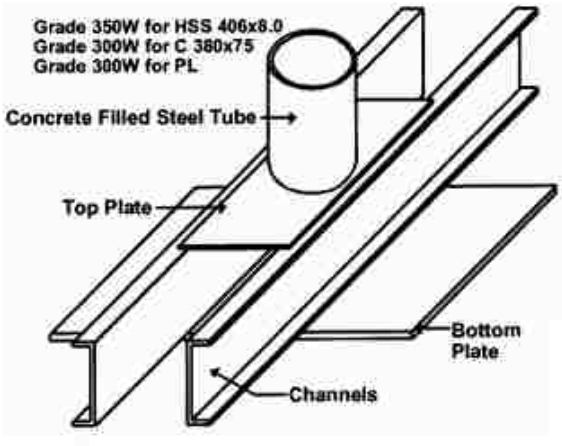

Figure 3.3: Fixed-Base Connection Schematic from Marson and Bruneau (Marson and Bruneau, 2004)

As shown in Figure 3.3, the base of the CFT column is welded to the top of a steel bottom plate. Two C channels run along the sides of the steel tube, oriented such that their flanges point away from one another. The bottom flanges of the two channels are welded longitudinally to the bottom plate. A top plate with a hole cut out of its center is then slid over the column, and is welded to the steel tube and the top flanges of the channels.

Four specimens were tested using this connection detail, with diameters of 12.75-in. and 16-in., and D/t ratios ranging between 34 and 64. The specimens were subjected to a constant axial load, as well as a cyclic lateral load following ATC-24 protocol. Figure 3.4 shows the resulting moment-drift hysteretic behavior of Specimen CFST 51, which consisted of a 12.75-in. diameter CFT with a thickness of 1/4-in., resulting in a D/t ratio of 51.

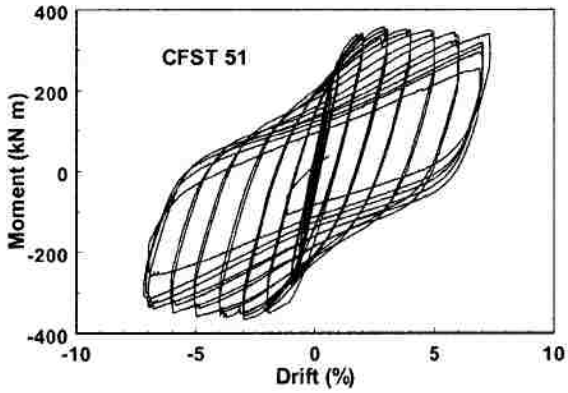

Figure 3.4: Moment-Drift Behavior from Marson and Bruneau (Marson and Bruneau, 2004)

The embedded fixed-base connection successfully developed the full plastic moment capacity of each CFT during testing. The failure mode of the specimens consisted of local buckling, followed by subsequent ductile tearing in the buckled regions. The columns exceeded 7% drift before significant strength loss, and exhibited large energy dissipation.

3.3 REINFORCED CONCRETE-FILLED STEEL TUBE CONNECTION TESTS

Montejo (2012) tested a series of reinforced concrete-filled steel tube (RCFST) column-cap beam connection specimens. In a RCFST column, a conventional steel cage inside of the tube provides the primary flexural strength of the specimen. A gap is left between the base of the steel tube and its adjacent cap element such that the need for a special joint connection is avoided, and the contribution of the steel tube on shear strength and concrete confinement is maximized. In this test program, the specimens were designed to replicate a half-scale bridge column. The columns were 18-in. in diameter and 3/8-in. thick, such that the resulting D/t ratio replicated that used in actual practice. Varying amounts of longitudinal reinforcing was used between specimens. Figure 3.5 shows an overview of the specimen geometry and test setup.

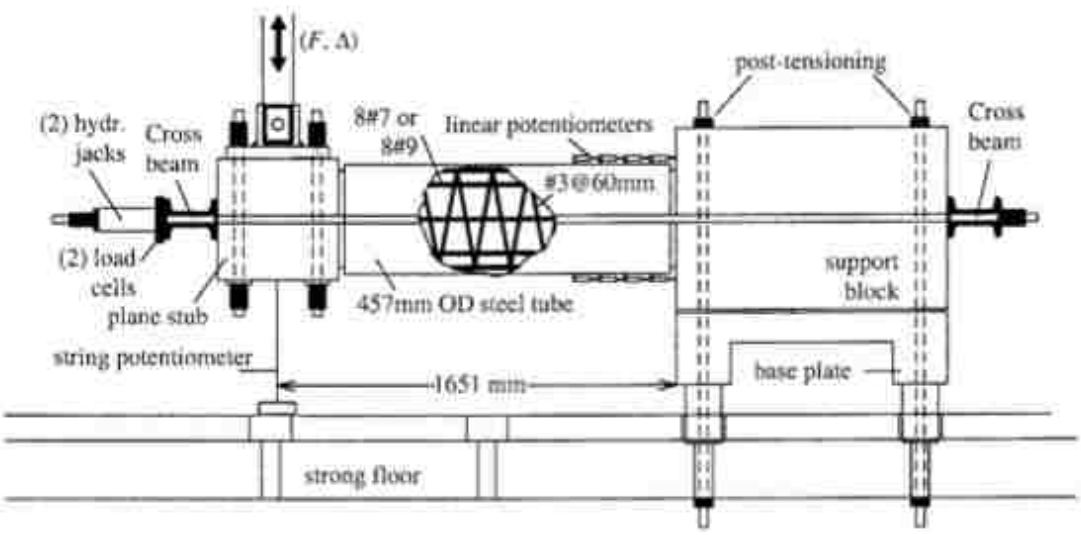

Figure 3.5: RCFST Geometry and Test Setup by Montejo (2012)

Specimen failure consisted of longitudinal reinforcement buckling with damage to the support block near the column. The reduced D/t ratio typical of RCFST columns causes

the specimens to deflect as a rigid body with a reduced plastic hinge length, compared to jacketed RC column.

3.4 EMBEDDED CFT CONNECTIONS

An extensive experimental research program was conducted at the University of Washington to develop a connection capable of transferring the full plastic moment capacity of a CFT column to a reinforced concrete footing. In the CFT-footing connection design, an annular steel ring is welded to the embedded end of the CFT column. The ring is intended to provide anchorage of the column, and to transfer shear and moment to the footing concrete and reinforcement via compression struts. The footing is reinforced with standard shear and flexural reinforcement.

Two variations of the CFT-footing connection were investigated in the test program; a monolithic and an isolated method. In the monolithic method, the steel tube is temporarily supported such that the footing and the column are cast simultaneously. In the isolated method, the footing is cast around a void created by a lightweight corrugated steel pipe. The end of the steel tube with the annular ring is lowered into the void, which is then filled with high-strength, fiber-reinforced grout. Finally, the steel tube is filed with low-shrinkage, self-consolidating concrete. The latter method achieves the strength and ductility of the embedded connection, while providing a more constructible alternative to the monolithic method. The two construction methods are illustrated in Figure 3.6.

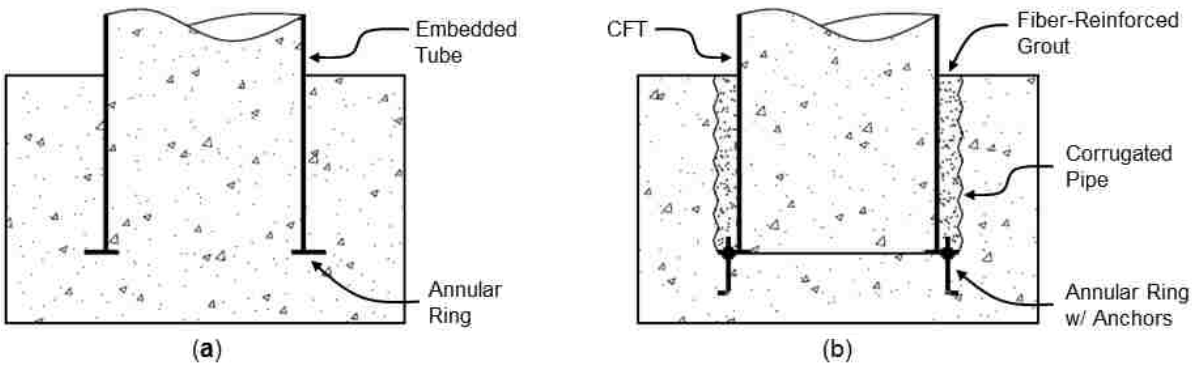

Figure 3.6: (a) Monolithic Connection, and (b) Isolated Connection

The experimental test program to investigate the embedded CFT connection consisted of a series of 19 CFT column-footing specimens. The specimens simulated an approximate half-scale bridge pier column, with the majority of them having a 20-in. diameter column. In all cases, the thickness of the steel tube was ¼-in., resulting in a D/t ratio of 80. The annular rings were all ¼-in. thick, and they extended 4-in. (16t) and 2-in. (8t) from the respective outer and inner diameters of the steel tube. Figure 3.7 shows the typical specimen geometry and reinforcement layout.

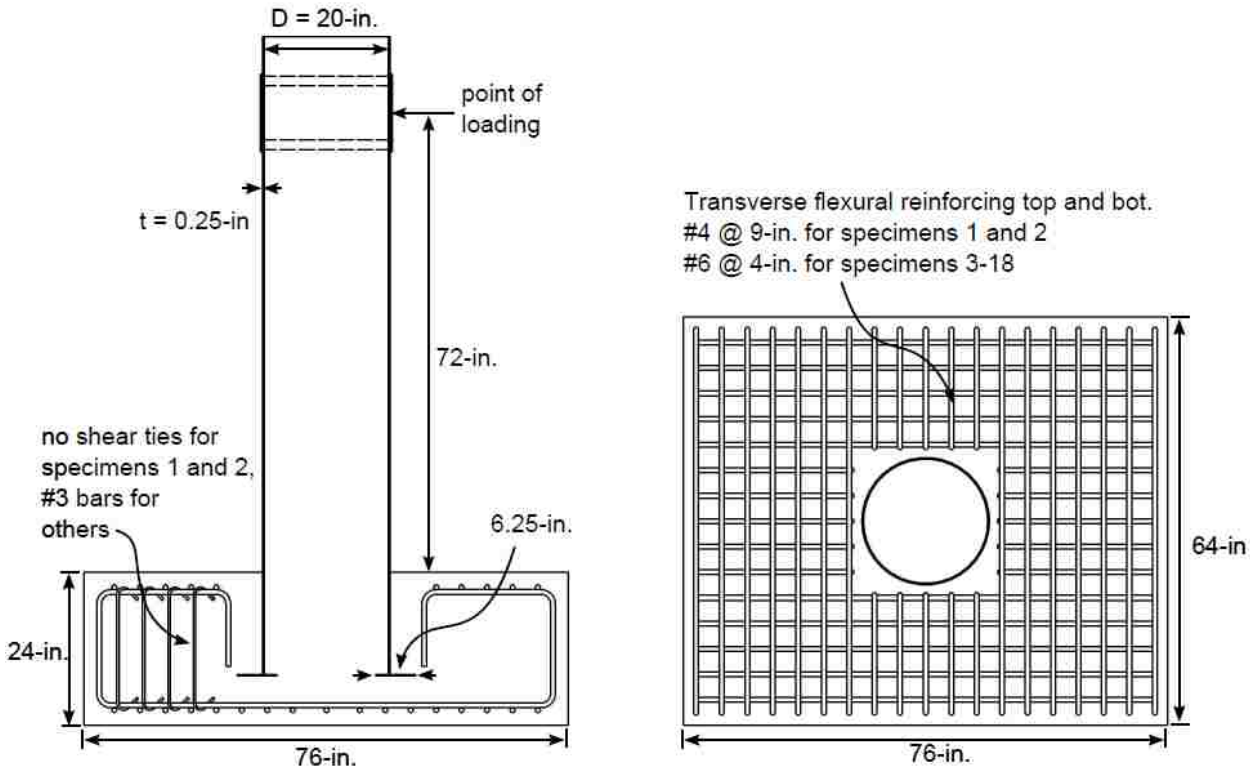

Figure 3.7: Typical specimen geometry and reinforcing (Stephens, 2014)

The series of tests investigated the effects of several different parameters, including variations on column embedment depth, connection type, and tube fabrication techniques. A summary of the study parameters for each CFT column-footing specimen is provided in table 3.1.

Table 3.1: University of Washington Experimental Test Parameters

Specimen Designation	Researcher	$\frac{l_e}{D}$	Connection Type	Study Parameter
I	Kingsley	0.6	Monolithic	No shear reinforcing
II	Kingsley	0.6	Monolithic	Shear reinforcing
III	Kingsley	0.9	Monolithic	Embedment depth
IV	Kingsley	0.6	Isolated	Connection type
5	Williams	0.9	Monolithic	Flexible underlay
6	Williams	0.75	Isolated	Flexible underlay
7	Williams	0.75	Isolated	Monotonic axial loading
8	Williams	0.75	Isolated	Cyclic axial loading
9	Chronister	0.9	Isolated	Galvanized tube
10	Chronister	0.9	Isolated	Galvanized tube, Load history
11	Chronister	0.9	Isolated	$0.15P_o$ Axial load
12	Chronister	0.9	Isolated	$0.20P_o$ Axial load
1-50	Lee	0.8	Monolithic	Straight seam tube
2-50	Lee	0.775	Isolated	Straight seam tube
3-50	Lee	0.775	Isolated	Spiral weld tube
4-50	Lee	0.8	Monolithic	Spiral weld tube
5-50	Lee	0.7	Isolated	Spiral wed tube
6-50	Lee	0.6	Isolated	Spiral weld tube
19	O'Neill	0.62	Isolated	30-in. tube, $0.05P_o$ Axial load

3.4.1 Kingsley (2005) Footing Connection Tests

Kingsley's experimental test program consisted of a series of four CFT-footing connection specimens. The first three specimens were selected to evaluate the effect of shear reinforcement and embedment depth on the strength and behavior of the connection. The fourth specimen was tested to evaluate the efficiency and potential structural benefits of using an isolated connection procedure as opposed to the monolithic option.

Each specimen was constructed using a 20-in. diameter, high-strength vanadium alloy steel tube. The tubes were ¼-in. thick, resulting in a D/t ratio of 80. The footings were designed with sufficient flexural reinforcement to resist the strength of the CFT column, and the dimensions of the footing were selected such that the footing size did not influence the connection behavior or the failure mode.

The specimens were subjected to a constant axial load equivalent to 10% of their crushing load, as well as a cyclic horizontal drift history based on ATC-24 protocol. Results from the four tests suggested the following conclusions:

- The presence of vertical shear reinforcement in specimen II had little effect on the load capacity of the connection, but appeared to reduce the severity of footing damage compared to that of Specimen I.
- Increasing the embedment depth from 0.6D to 0.9D increased the load capacity of the specimen by approximately 25%. The increased embedment depth also improved the drift capacity, as well as the energy dissipation capacity.

- The increased embedment depth of 0.9D resulted in tube tearing and subsequent ductile tearing with minimal damage to the footing.
- The isolated connection method provided comparable strength, while reducing and delaying damage to the concrete footing.

The force-drift hysteretic behavior of Specimens I and III is presented in Figure 3.8. By comparing the two hystereses, it can be seen that the overall strength and ductility of the connection is greatly influenced by the embedment depth of the column.

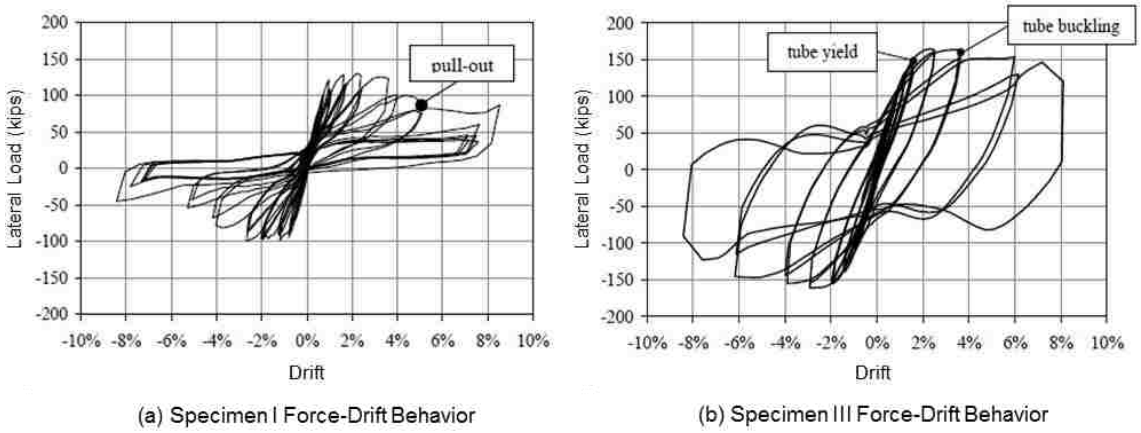

Figure 3.8: Force-Drift Response from adequately and inadequately embedded specimens (Kinsley, 2005)

3.4.2 Williams (2006) Footing Connection Tests

Williams tested four CFT-footing specimens to evaluate the effects of embedment depth, flexible underlay, connection design, and axial loading. Similar to Kinglsey, each column consisted of a 20-in. diameter spiral welded high-strength vanadium alloy steel tube, with a ¼-in. thickness. The first two specimens (Specimens 5 and 6) were constructed to evaluate the effect of varying column embedment depths under the presence of a flexible underlay to simulate flexible soil. The flexible underlay was constructed by placing deformable plywood underneath the specimens, to allow damage to occur on the

underside of the footing. Specimen 5 was cast monolithically, while Specimen 6 was cast using the isolated construction method. The two specimens were subjected to a constant axial load of 10% of their ultimate axial capacity, as well as a cyclic lateral load based on ATC-24 protocol.

Specimens 7 and 8 were constructed with half-height columns to evaluate the punching shear strength of the footing. To replicate the soil resistance expected in practice, the base of each specimen was supported by a stiff Hydrostone perimeter filled with loose sand. Both specimens were cast using the isolated construction method, and were subjected to axial loading only. Specimen 7 was loaded monotonically, while Specimen 8 was loaded cyclically for ten cycles, and then loaded monotonically until failure. Results from the four tests suggested the following conclusions:

- The monolithically constructed specimen with 0.9D embedment experienced limited cracking in the footing, with no observed damage on the underside of the specimen.
- The smaller embedment depth of Specimen 6 resulted in damage on the underside of the specimen, suggesting a punching-shear effect on the footing.
- The decreased embedment of 0.75D was sufficient to develop the full flexural capacity of the CFT. Considerable cracking in the footing suggested high demands, but below the ultimate capacity.
- Local buckling of the steel tube causes degradation in stiffness, but not in strength. Repeated buckling leads to tearing of the tube.

3.4.3 Lee (2011) Footing Connection Tests

Lee tested a series of six CFT-footing specimens to evaluate the effects of using different construction methods, different tube fabrication methods, and varying embedment depths. Unlike the previous specimens tested by Kingsley, Williams and Chronister in which high-strength vanadium alloy steel tubes were used, this test program investigated the response using steel tubes with a 50 ksi yield strength.

Specimens 1-50 and 2-50 were both constructed using straight seam welded tubes, while the remaining four specimens were constructed using spiral weld tubes. Specimens 1-50 and 4-50 were cast monolithically, whereas the remaining four specimens were cast using the isolated construction method. Specimens 4-50, 5-50, and 6-50 were constructed with varying embedment depths of 0.8D, 0.7D, and 0.6D, respectively. All specimens were subjected to a constant axial load of 10% of their ultimate axial capacity, as well as a cyclic lateral load following ATC-24 protocol. Results from the six tests suggested the following conclusions:

- Both isolated and monolithic connections exhibited comparable strength, ductility, and stiffness.
- Specimens with shallower embedment depths experienced increased footing damage.
- The 50 ksi steel tubes resulted in a lower stiffness compared to the previously tested 75 ksi vanadium alloy steel tubes. The lower strength tubes also experienced an increased ductility.
- Both straight seam and spiral welded steel tubes provided similar strengths and stiffness. Although specimens using straight seam tubes experienced a

25% increase in drift ductility, toughness testing suggested this increase was attributed to the base metal as opposed to tube fabrication methods.

3.4.4 O'Neill (2011) Footing Connection Test

This experimental test program investigated the performance of a CFT-footing specimen using a steel tube of 50% larger diameter than pervious tests. The thickness of the tube was ¼-in., resulting in a D/t ratio of 120, as opposed to the previously tested specimens with D/t ratios of 80. The specimen was cast using the isolated construction method, with an 18-in. (0.62D) embedment depth. The specimen was subjected to a constant axial load equal to 5% of the gross axial capacity, as well as a cyclic lateral load adapted from ATC-24 protocol. Results from the four tests suggested the following conclusions:

- The 30-in. diameter specimen possessed similar normalized stiffness compared to the previously tested 20-in. diameter specimens with similar study parameters.
- Tube tearing occurred at a lower drift value than in previously studied specimens.
- The decrease in moment capacity following tube tearing occurred more rapidly in the 30-in. diameter specimen than in the 20-in. diameter specimens.

3.5 DESIGN EXPRESSIONS FROM UNIVERSITY OF WASHINGTON TESTS

Lehman and Roeder (2012) used results from the University of Washington experimental test program to develop a series of expressions for the design of CFT column-to-footing connections that are capable of transferring the full plastic moment capacity of the CFT to its adjacent footing element. These expressions include: the required column embedment depth, the minimum total footing depth, and a minimum shear reinforcing requirement.

3.5.1 Required Embedment Depth

The cone pullout model shown in Figure 3.9 was used to develop an expression for the required column embedment depth, l_e, to assure ductile behavior of the connection. The expression is defined as:

$$l_e \geq \sqrt{\frac{D_o^2}{4} + \frac{DtF_u}{6\sqrt{f'_{cf}}}} - \frac{D_o}{2} \tag{3.1}$$

In Eq. 3.1, D_o represents the outside diameter of the annular ring in a monolithic connection, or the diameter of the corrugated pipe in an isolated connection. D and t represent the diameter and thickness of the steel tube, respectively, F_u is the tensile strength of the tube, and f'_{cf} is the compressive strength of the footing concrete.

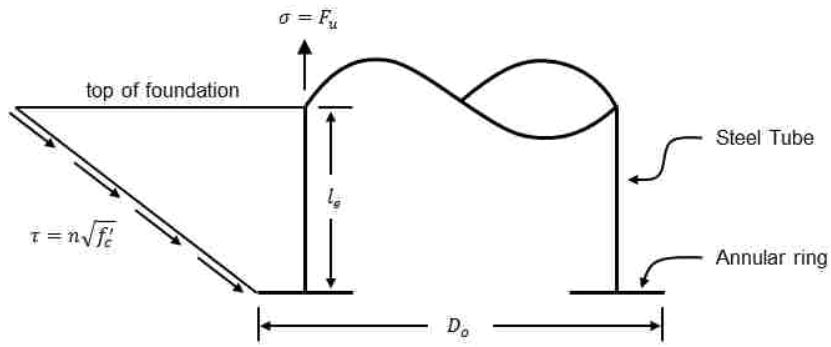

Figure 3.9: Cone pullout model for required CFT embedment depth

3.5.2 Minimum Footing Depth

In order to prevent punching shear failure in the foundation, adequate concrete depth must be provided below the concrete filled tube. Using ACI requirements as a basis for punching shear evaluation (ACI, 2011), Lehman and Roeder developed an expression for the required total footing depth, d_f, to prevent punching shear failure:

$$d_f = \sqrt{\frac{D^2}{4} + \frac{250C_{max}}{\sqrt{f_{cf}'}}} - \frac{D}{2} \tag{3.2a}$$

$$C_{max} = C_s + C_c \tag{3.2b}$$

where C_s and C_c are the compression forces in the concrete and steel due to combined bending and axial load as computed by the PSDM.

3.5.3 Shear Reinforcing Requirements

The required embedment depth defined in Eq. 3.1 results in a shear stress of $6\sqrt{f_c'}$ in the critical area surrounding the tube. Assuming the concrete resists a shear demand of $2\sqrt{f_c'}$, the vertical shear reinforcement in this area must be designed to resist $4\sqrt{f_c'}$.

CHAPTER 4
EXPERIMENTAL TEST PROGRAM

As discussed in the previous chapter, the University of Washington has conducted an extensive research program to develop expressions for the design of CFT column-to-foundation connections. Full realization of the system, however, requires the development of CFT column-to-cap beam connection details, which present additional challenges due to geometric and reinforcement constraints. In an effort to address these constraints, a continuation of the University of Washington experimental test program has been implemented to investigate the response of five different CFT column-to-cap beam connections. Section 4.1 provides an overview of the five specimens in the test program, introducing their force transfer mechanisms and strength and ductility limitations. The basic geometric layouts are presented in Section 4.2, followed by the design and construction processes in Section 4.3. The specimen material properties are presented in Section 4.4, followed by the experimental test set up, loading protocol, and instrumentation set up in Sections 4.5, 4.6, and 4.7, respectively.

4.1 SPECIMEN TEST MATRIX

This section describes the force transfer mechanisms and strength and ductility limitations of the five proposed specimens in this test program. The specimens are divided into three categories depending on their connection type: 1) embedded CFT connections, 2) welded reinforced concrete connections, and 3) reinforced concrete connections. The three proposed connection types are presented in Figure 4.1.

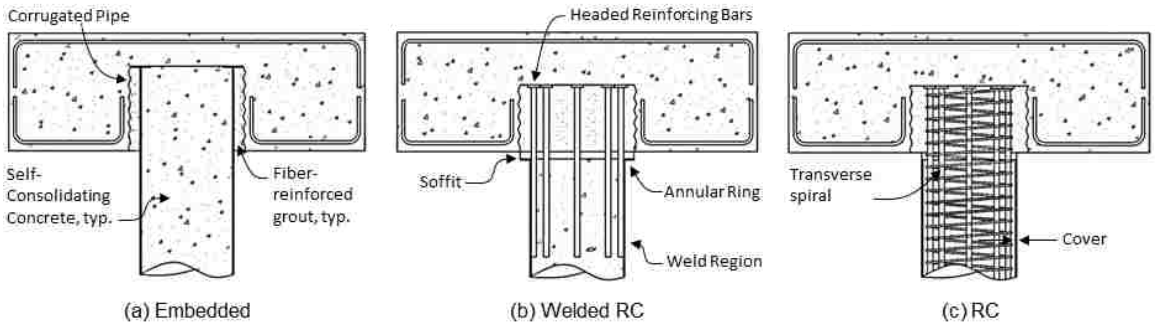

Figure 4.1: Proposed CFT column-to-cap beam connections

4.1.1 Embedded CFT Connections

Figure 4.1a shows the embedded CFT connection, in which the CFT column is embedded into a precast RC cap element through a recessed fiber-reinforced grouted connection. An annular steel ring is welded to the embedded end of the steel tube to provide anchorage of the column, and to transfer shear and moment to the surrounding concrete and reinforcing bars via diagonal compression struts, as shown in Figure 4.2. The strength and ductility of this connection is controlled by the steel tube component, as long as adequate embedment of the CFT is provided (Lehman and Roeder, 2012).

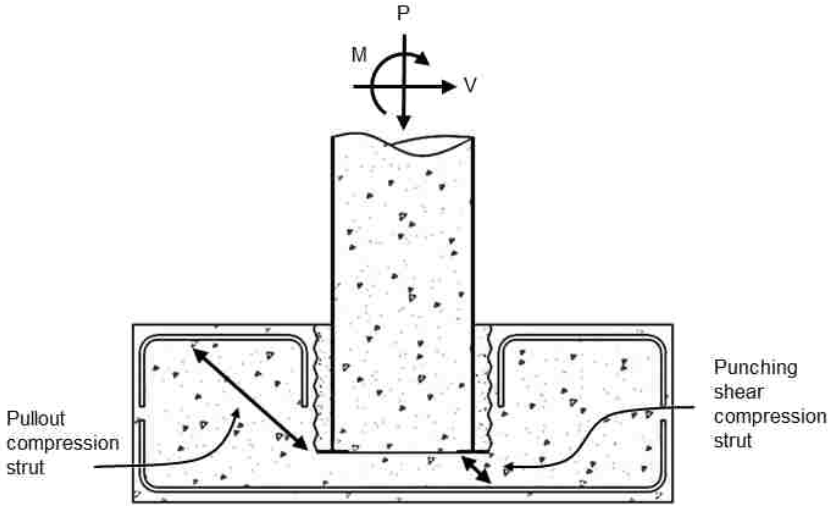

Figure 4.2: Embedded CFT force transfer mechanism

Two specimens with the embedded CFT connection type are investigated in this test program. The first specimen, EMB80, is constructed using a 20-in. diameter spiral-weld steel tube. The second specimen, EMB96, is constructed using a 24-in. diameter straight-seam tube. Because the straight-seam weld does not impose strain concentrations in the buckled region of the steel tube, it is intended that Specimen EMB96 will experience an increased ductility response compared EMB80 with the spiral-welded tube.

4.1.2 Welded Reinforced Concrete Connections

Figure 4.1b shows the welded reinforced concrete connection, in which headed reinforcing bars are welded to the inside of the steel tube and are developed into the cap beam. The axial, moment, and shear transfer is provided by the longitudinal reinforcing bars, which also control the strength and ductility of the specimen. The force transfer mechanism of this connection is similar to that in Figure 4.2, except the compression struts initiate from the heads of the embedded reinforcing bars, as opposed to the annular ring in the embedded CFT connection. Because the reinforcing ratio of the welded RC connection is lower than that of the embedded connection, the specimens with this connection type do not achieve the plastic moment capacity of the CFT.

Two specimens with the welded RC connection detail are investigated in the test program. The first welded RC connection specimen, WRC, contains longitudinal reinforcing bars that are fully bonded to the surrounding concrete. In the second welded RC connection specimen, WRCUB, the reinforcing bars are partially debonded in the column-to-cap beam interface region. This intentional debonding is intended to increase the ductility of the connection, by allowing deformations to distribute along a greater

length of the reinforcing bar, consequently decreasing the strains in the steel (Stringer, 2010).

4.1.3 Reinforced Concrete Connection

Figure 4.1c shows the traditional reinforced concrete (RC) connection, in which longitudinal and transverse reinforcing extend from the CFT column into the cap beam. Cover is provided between the longitudinal reinforcing bars and the inside of the steel tube, and there is a grouted soffit between the base of the steel tube and the surface of the cap beam. The test program investigates one specimen with this connection detail, as this is standard practice in the state of Alaska.

4.2 SPECIMEN LAYOUT

The geometric and reinforcement layouts of the specimens in this test program are based off the Laguna De Santa Rosa Bridge located outside of Santa Rosa, California. The prototype bridge is constructed with conventional reinforced concrete columns that are 48-in. in diameter, and are reinforced longitudinally with 32 bundled No. 11 bars, and transversely with No. 8 bars spaced at 6-in. on-center. For the purpose of this study, the prototype RC column was redesigned using a comparable CFT, shown previously in Figure 2.4. The redesigned CFT column uses a 42-in. diameter, 0.5-in. thick steel tube with a resulting D/t ratio of 84.

Based on material availability and test apparatus limitations, four 20-in. diameter columns and one 24-in. diameter column with steel tube thicknesses of .25-in. were selected to represent 45% and 55% scaled specimens with respective D/t ratios of 80 and

96. The widths of the cap beams varied from the prototype bridge, as they were selected from results of a parametric study performed by Stephens (Stephens, 2014) that evaluated the connection performance for differing cap beam widths. Results from the study suggested that the width of the cap beam could be minimized to 2D while still achieving strength and ductility performance objectives.

Figure 4.3a presents the resulting geometry for the four specimens containing 20-in. diameter columns. The cap beams for these specimens are 25-in. high, 40-in. (2D) wide, and 76-in. in length. Figure 4.3b presents the geometry for Specimen EMB96, which has a 24-in. diameter column. The cap beam for this specimen stands 29.75-in. high, 48-in (2D) wide, and 76-in. in length.

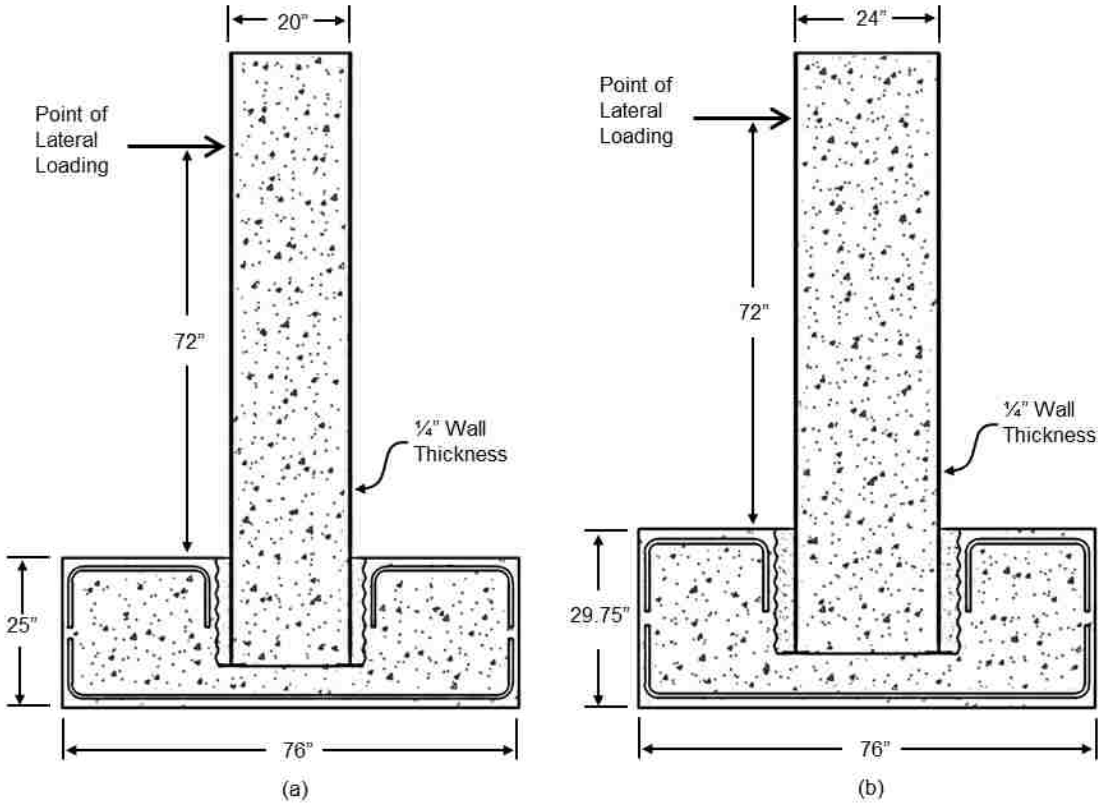

Figure 4.3: Basic Layout of (a) Specimens EMB80, WRC, WRCUB and RC, and (b) EMB96

4.3 SPECIMEN DESIGN AND CONSTRUCTION

The objective of the design process was to design each specimen such that a plastic hinge would form in the column, and the cap beam would remain essentially elastic when subject to axial and lateral loading. In order to assure these performance objectives were met, the specimens were designed using a combination of standard design provisions, the 2010 Caltrans Seismic Design Criteria, and design expressions developed from previous CFT column-to-footing experimental research. An overview of the relevant design expressions specified in the Caltrans Seismic Design Criteria is provided in Section 4.3.1. Sections 4.3.2 through 4.3.4 outline the specific design processes and construction procedures used for the embedded CFT specimens, welded RC specimens, and RC specimen, respectively.

4.3.1 Caltrans Seismic Design Criteria

The 2010 Caltrans Seismic Design Criteria (SDC) specifies seismic design requirements for concrete bridge construction. Section 7.4 of the SDC provides the minimum detailing requirements of joint regions in RC bridges such that the superstructure remains elastic, while plastic hinges form in adjacent substructure elements. The proceeding section summarizes the design expressions from the SDC that are relevant to this research.

Joint Performance

Section 7.4.1 of the Caltrans SDC requires moment resisting connections between the superstructure and column to be designed to transmit the maximum forces produced when the column reaches its overstrength capacity, M_o^{col}. The overstrength capacity is defined in Caltrans SDC Eq. 4.4 as:

$$M_o^{col} = 1.2M_p^{col} \tag{4.1}$$

where M_p^{col} is the plastic moment capacity of the CFT. The 20% overstrength magnifier is applied to the moment capacity of the column to account for material strength variations between the column and the cap beam.

Joint Shear Reinforcement Requirements

If the principal tension stress in the joint region exceeds $3.5\sqrt{f_c'}$, additional joint shear reinforcement is required in the form of horizontal and vertical stirrups, as well as horizontal side reinforcing. Section 7.4.4.3 of the Caltrans SDC defines the required horizontal and vertical joint shear reinforcement area, A_s^{jh} and A_s^{jv}, as:

$$A_s^{jh} = 01A_{st} \tag{4.2a}$$

$$A_s^{jv} = 0.2A_{st} \tag{4.2b}$$

where A_s^{jv} is the total area of column reinforcement anchored in the joint. Caltrans requires the horizontal and vertical stirrups to be placed transversely within a distance D_c extending from either side of the column centerline, where D_c is the diameter of the column. The horizontal stirrups are to be placed around the vertical stirrups in two or more intermediate layers, with vertical spacing not to exceed 18-in.

The required area of longitudinal side reinforcing, A_s^{sf}, is defined by Caltrans Eq. 7.21 as:

$$A_s^{sf} \geq \begin{cases} 0.1A_{cap}^{top} \\ 0.1A_{cap}^{bot} \end{cases} \tag{4.3}$$

where A_{cap}^{top} and A_{cap}^{bot} refer to the area of flexural steel at the top and bottom of the cap beam, respectively. The side reinforcement is to be placed near the sides of the cap beam, with a maximum spacing of 12-in.

4.3.2 Embedded CFT Connections

Specimen Design

Two CFT column-to-cap beam specimens were proposed using the embedded CFT connection: EMB80 and EMB96. Specimen EMB80 contains a 20-in. diameter spiral-weld steel tube, and EMB96 contains a 24-in. diameter straight-seam tube. Both tubes are ¼-in. thick, resulting in respective D/t ratios of 80 and 96.

For both specimens, the required embedment depth was calculated using Eq. 3.1, which was derived from previous CFT-footing research at UW. The sizes of the annular rings were selected based on results of a parametric study performed by Stephens (Stephens, 2014), which suggested that the outside diameter of the annular ring could be minimized to D+16t without influencing the behavior of the connection. Using this design limitation with a 1/4-in. steel thickness, the resulting annular ring diameters were 24-in and 28-in. for Specimens EMB80 and EMB96, respectively. The annular rings were welded to the base of the steel tubes using ¼-in. fillet welds on both the inside and outside of the tube, such that the full strength of the tube could be developed.

In order to minimize inelastic deformations in the cap beam, the primary flexure reinforcing was designed to resist the plastic moment capacity of the CFT with an additional 20% overstrength factor. The shear reinforcing was selected to meet Caltrans Seismic Design Criteria (SDC) requirements, as well as design recommendations from the embedded foundation connection in which the concrete was assumed to take $2\sqrt{f_c'}$ of the shear demand (Lehman and Roeder, 2012). Horizontal stirrups were included on either side of the column per Caltrans SDC requirements, as well as on the extreme ends of the specimen to provide additional confinement around the hold-down regions. The complete reinforcing and connection details for Specimens EMB80 and EMB96 are shown in Figures 4.4 and 4.5, respectively.

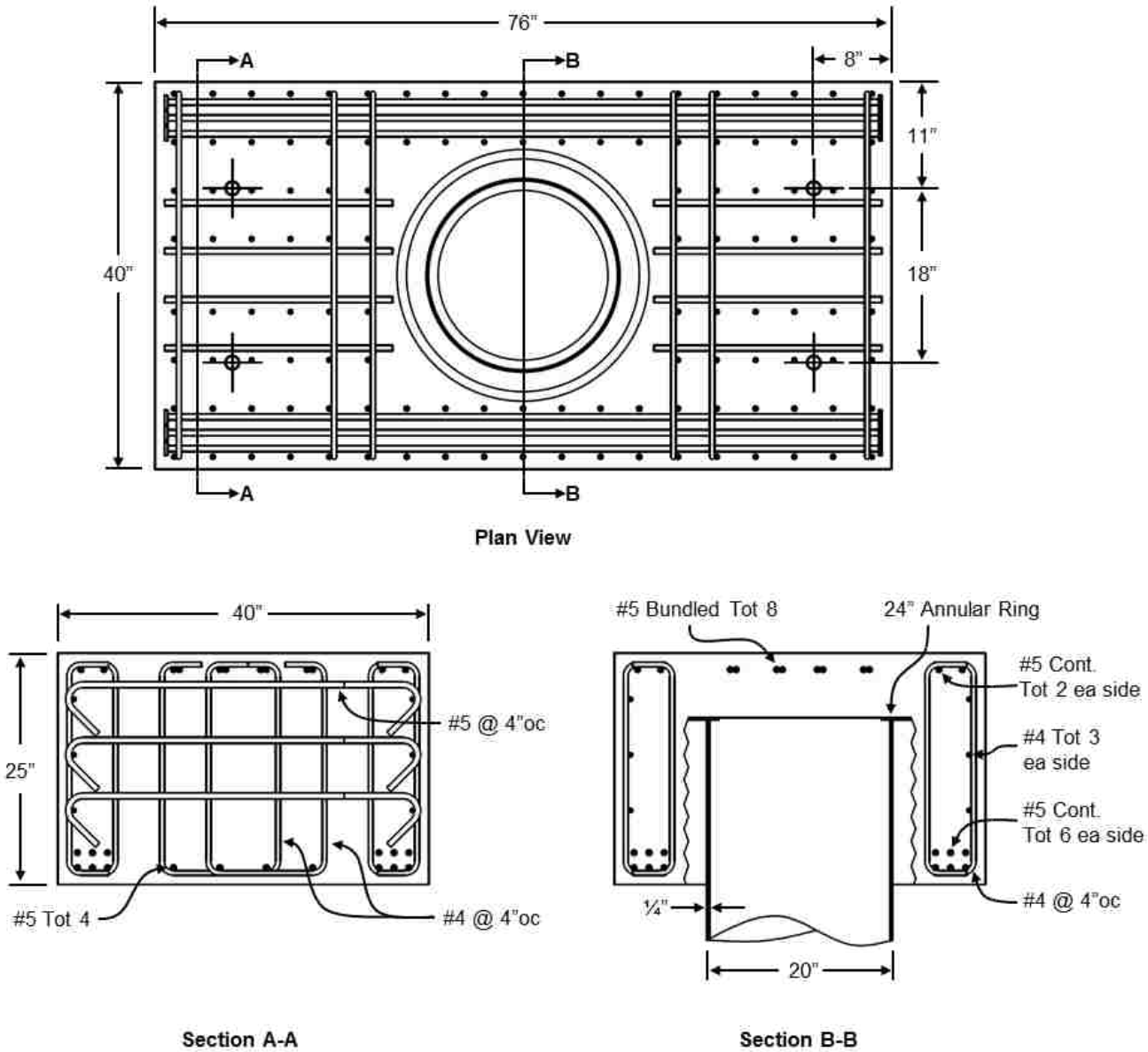

Figure 4.4: Specimen EMB80 Reinforcing Details

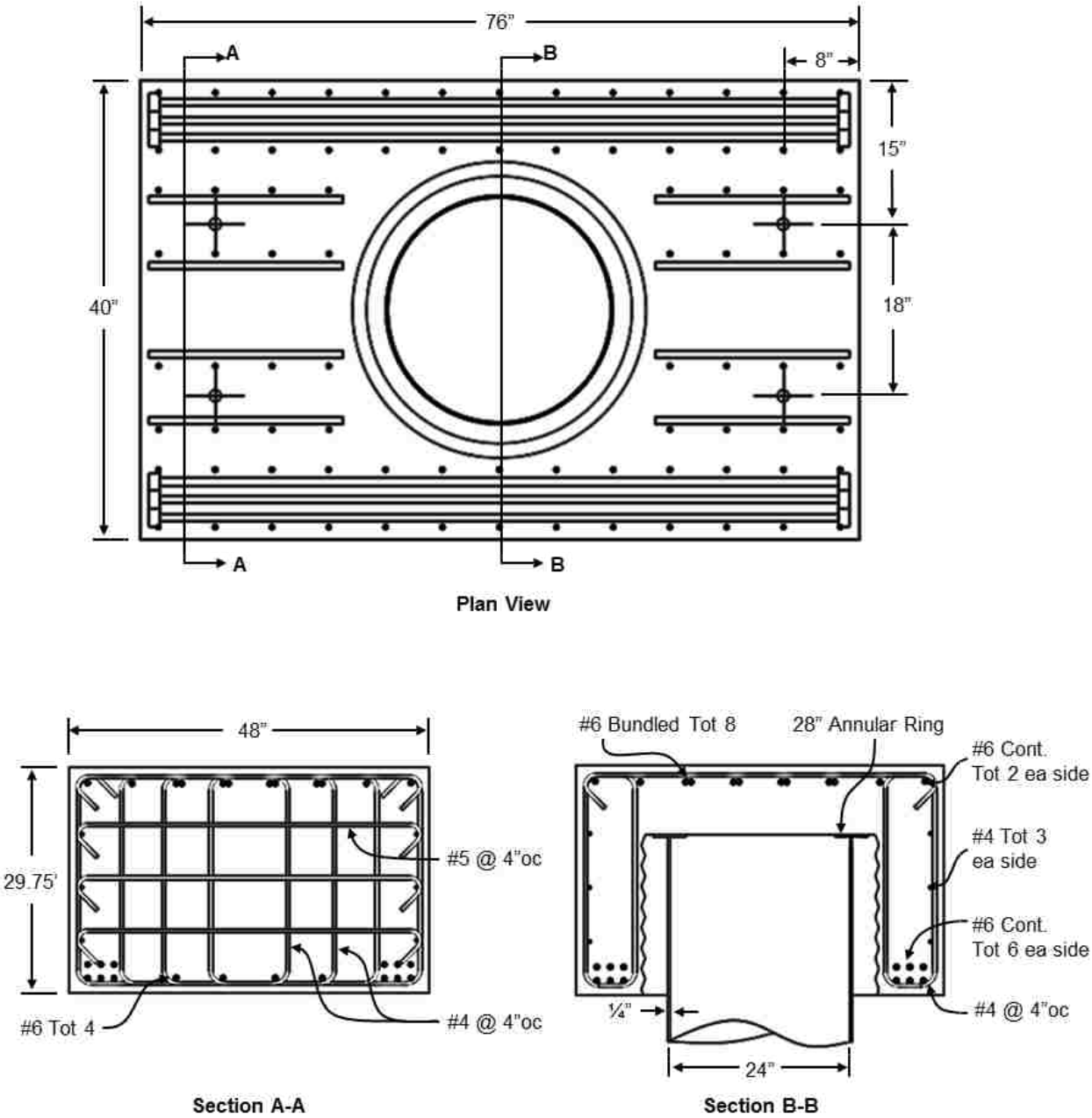

Figure 4.5: Specimen EMB96 Reinforcing Details

Specimen Construction

Figure 4.6 provides an overview of the construction process used to construct the two embedded CFT connection specimens.

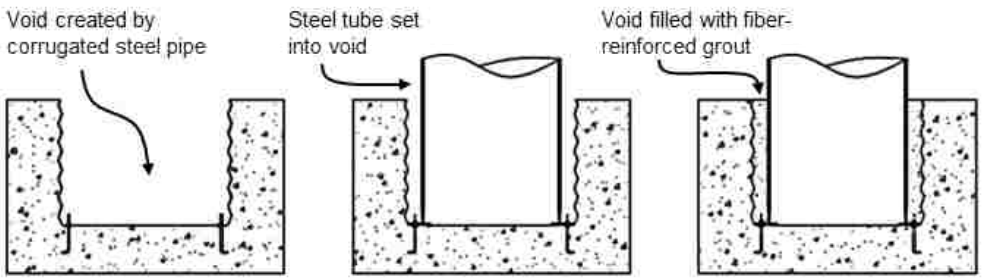

Figure 4.6: Embedded CFT connection construction sequence

As shown in Figure 4.6, the first step of the construction process was to cast the cap beam around a lightweight corrugated steel pipe, such that a void was created in the center of the cap beam with a diameter greater than that of the annular ring. Figure 4.7 shows the formwork and corrugated pipe used to create the void for the column.

Figure 4.7: Cap Beam Reinforcing and Formwork

As the concrete cured, the annular ring was welded to the base of the steel tube, using fillet welds on both the inside and outside perimeters of the tube. Four holes were drilled through the annular ring, which would later be used to help stabilize the column. Figure 4.8 shows the steel tube with the annular ring clamped to the base, in preparation for welding.

Figure 4.8:EMB80 tube and annular ring

Once the concrete had cured sufficiently, the column (with annular ring welded to the base) was then lowered into the void such that the holes in the annular ring slid over four threaded anchor rods that had been embedded into the concrete during casting. Steel washers were placed around the anchors underneath the annular ring as necessary until the column was plumb. Once the column was leveled, the remaining void between the cap beam and steel tube was then filled with 6-ksi fiber-reinforced grout. The first lift of the grout pour was left to set for several hours, such that subsequent grout pours wouldn't

seep underneath the annular ring and fill up the embedded portion of the steel tube. Once the grout was cured, the column was finally filled with low-shrinkage, 6-ksi self-consolidating concrete.

4.3.3 Welded RC Connections

Two specimens were designed with welded RC connections: one with fully bonded reinforcing bars, and one with partially debonded reinforcing bars intended to increase the ductility of the connection. For both specimens, the target reinforcement ratio of the connection was 3%, per discussion with Caltrans. However, based on construction limitations, the final design was limited to 8 No. 9 longitudinal reinforcing bars, with a resulting reinforcement ratio of 2.5%. The bars were embedded 14-in. ($12d_b$) into the cap beam, as calculated from standard ACI requirements for headed reinforcing bars using respective steel and concrete design strengths of 60 ksi and 6 ksi. Per discussion with Caltrans, the reinforcing bars were developed 27-in. ($24d_b$) into the CFT column. The ends of the reinforcing bars were welded to the inside of the steel tube using ¼-in. flare bevel groove welds. The weld lengths were designed such that the strength of each pair exceeded the ultimate strength of the reinforcing bar.

For Specimen III, the required debonded bar length was calculated using Equation 4.4 (Stringer 2010).

$$l_{db} = \frac{\theta_{fail}}{\phi_{s,0.05}} \tag{4.4}$$

Where:

θ_{fail} = Target rotation of connection at failure (in radians)

$\phi_{s,0.05}$ = Curvature of connection at a steel strain limit of 0.05 in/in, as obtained from a moment curvature analysis.

Assuming a target connection rotation of 8% at failure, the resulting debonded bar length was 22-in., centered at the column-cap beam interface.

The flexure reinforcing for the welded RC connections was again designed to exceed the plastic moment capacity of the CFT, while the shear reinforcing was designed according to Caltrans SDC requirements. The complete reinforcing details for both welded connection specimens are presented in Figure 4.9.

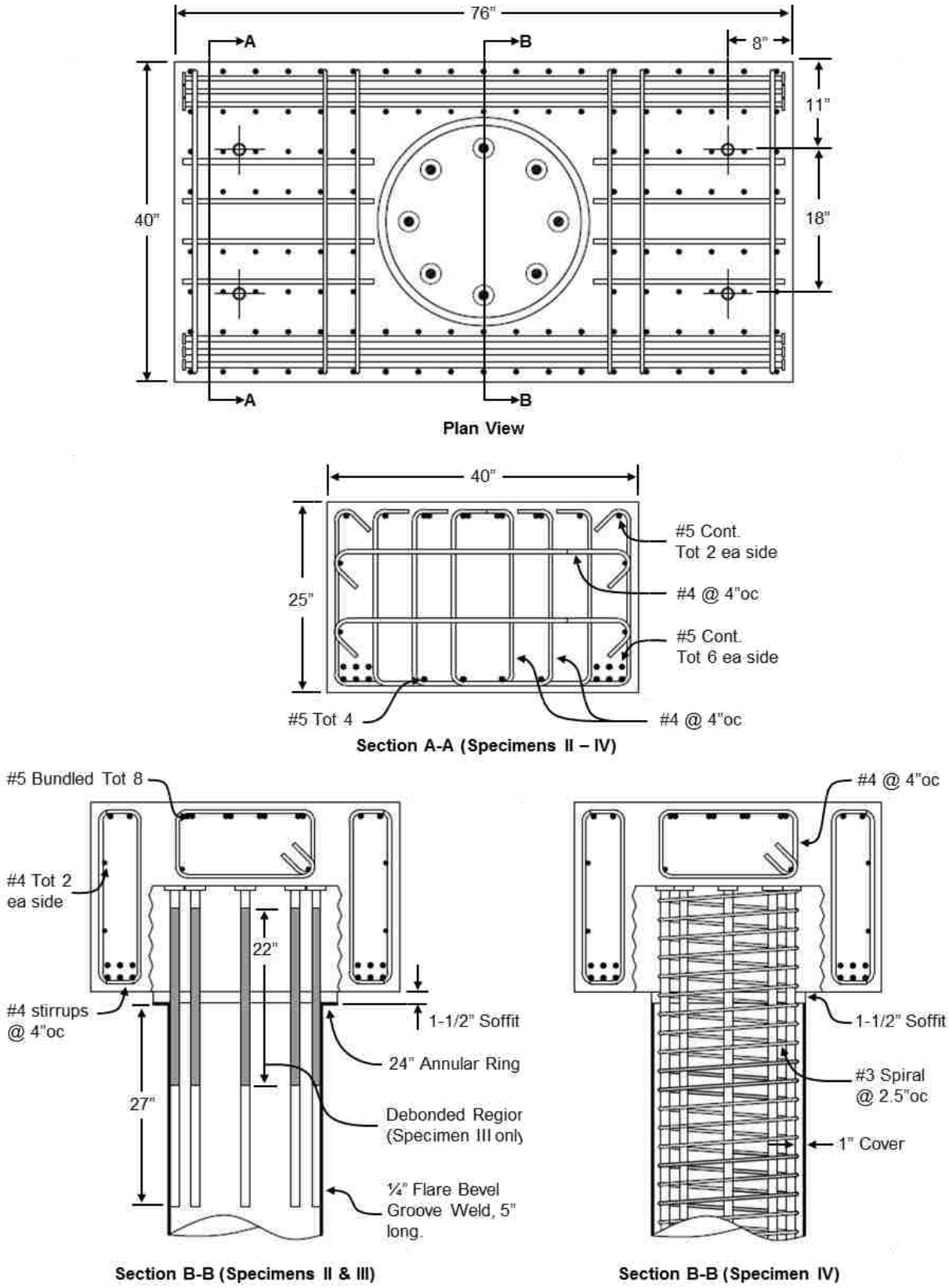

Figure 4.9: Specimens WRC, WRCUB, and RC Reinforcing Details

Specimen Construction

Figure 4.10 shows the sequence used to construct the two welded RC specimens. Similar to the previous sequence, the cap beams were first cast around a void created by corrugated steel pipe.

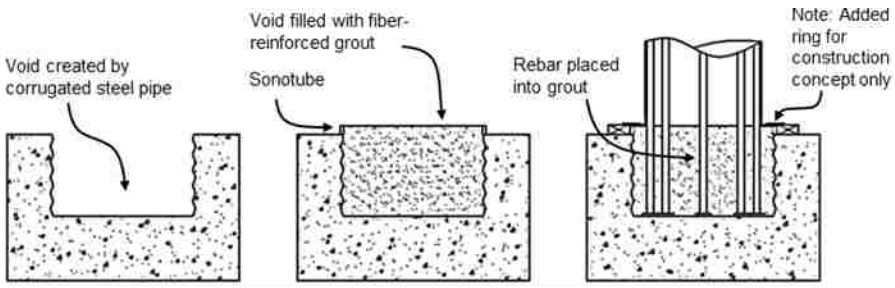

Figure 4.10: Welded RC Connections Construction Sequence

As the concrete cured, the annular ring was welded to the base of the steel tube using a ¼-in. fillet weld, and the longitudinal reinforcing bars were welded to the inside of the steel tube such that the heads of the bars projected 15.5-in. from the end of the column. This projection accounts for the 14-in. embedment into the cap beam, as well as the 1.5-in. grouted soffit. Figure 4.11 shows Specimen WRC after the annular ring and reinforcing bars had been welded to the steel tube.

Figure 4.11: Specimen WRC annular ring and reinforcing bars

Due to the relatively small diameter of the steel tube in conjunction with the depth of the weld region inside the tube, only four of the eight total bars (every-other bar) could be welded from the base of the tube, and the remaining four had to be welded from the other free end. After the bars were welded, 1¼-in. lightweight PVC was placed over the bars in Specimen WRCUB to debond them from surrounding concrete. Hydrostone was applied to the ends of the PVC to ensure a watertight seal.

To serve as formwork for the grouted soffit, a 24-in. diameter Sonotube was placed on top of the cap beam around the existing void. Both the void and the Sonotube were then quickly filled with 6-ksi, fiber-reinforced grout. The steel tube and reinforcing bars were then promptly lowered until the heads reached the bottom of the grout-filled void.

Ratchet straps were used to level and support the column while the grout set. Lastly, the steel tube was filled with low-shrinkage, self-consolidating concrete.

Because the CFT-to-cap beam specimens would be constructed right side up in the field, there is concern for the weight of the cap beam bearing solely on top of the headed reinforcing bars. Because of this, the construction process was altered slightly for the second welded RC connection, to provide proof of concept for construction in the field. For this alternative method, a second steel ring of larger diameter was tack welded to the top of the existing annular ring. Shims were then placed between the surface of the cap beam and the second steel ring, such that the weight of the cap beam would bear on this added ring as opposed to the reinforcing bars. The void was then filled with fiber-reinforced grout, and the ring was removed by grinding through the welds after the grout had cured.

4.3.4 RC Connection

Specimen Design

The design of the RC connection was similar to that of the welded RC connections, except the reinforcing bars were not welded to the inside of the steel tube. Instead, a 1-in. cover was provided between the longitudinal reinforcing bars and the inside of the steel tube, and the bars were fully developed into the CFT. The development length of the bars was calculated from standard ACI requirements, assuming a design steel strength of 60 ksi, and a specified concrete compressive strength of 6 ksi. The transverse reinforcement was selected based on the required Caltrans SDC minimum reinforcement ratio, resulting

with a No. 3 spiral spaced at 2.5-in. on center. The remaining flexure and shear reinforcing was the same as that of the welded connections, as shown in Figure 4.9.

Specimen Construction

The construction sequence for the RC connection specimen is shown in Figure 4.12. Again, it should be noted that this sequence differs from that in the field, due to constructing the specimen upside-down in the structures laboratory.

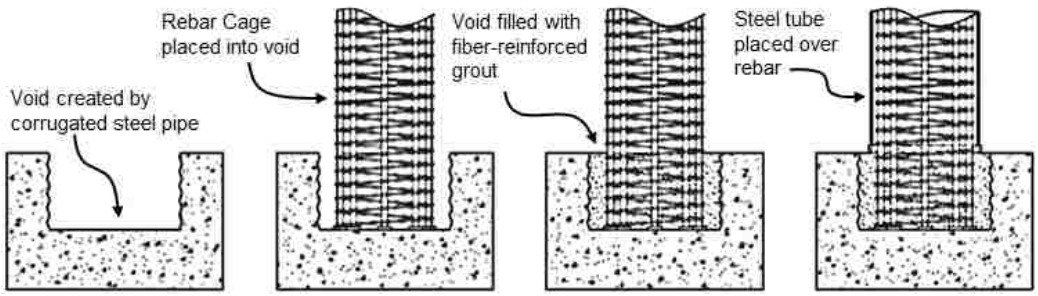

Figure 4.12: RC Connection Construction Sequence

Similar to the previous construction processes, the cap beam was first cast around a void created by a corrugated steel pipe. The longitudinal rebar cage, shown in Figure 4.13, was then lowered into the void, which was subsequently filled with fiber-reinforced grout. Once set, a 20-in. diameter Sonotube was placed above the grouted surface, and filled with an additional 1.5-inches of grout to create the soffit beneath the column. Lastly, the steel tube was lowered around the rebar cage onto the soffit, and filled with self-consolidating, low-shrinkage concrete.

Figure 4.13: Reinforcing cage of Specimen RC

4.4 SPECIMEN MATERIALS

A variety of materials were used in the construction of the CFT column-to-cap beam specimens. These materials are summarized in Table 4.1, along with their respective specifications and supplying vendors.

Table 4.1: Material List (Adapted from Lee, 2011)

Item	Designation	Vendor
Spiral Weld Steel Tube	AWWA C200, ASTM A1018-07 SS	Northwest Pipe
Straight Seam Steel Tube		
Annular Ring	ASTM A572	Bloch Steel
Reinforcing Steel	ASTM A615-09 Grade 60	Addison Supply
Corrugated Pipe	AASHTO M36, ASTM A760	Washington Culvert Company
Concrete	Self-consolidating, low-shrinkage, 6-ksi	Stoneway Concrete
Grout	ASTM C-1107 Grades A, B and C	Mason Supply
Fiber Reinforcement	Polypropylene, Strux 85/50	Grace Construction Products

The concrete used for the construction of the columns and cap beams was mixed and delivered by Stoneway Concrete, with a specified compressive strength of 6-ksi. The cap beams were constructed using conventional concrete, whereas the steel tubes were filled with self-consolidating, low-shrinkage concrete. The two embedded specimens were cast independently, and the cap beams and columns of the three RC specimens were cast simultaneously. Table 4.2 provides the measured strengths of the concrete and grout components for each specimen on its respective day of testing.

Table 4.2: Day-of-Test Concrete and Grout Compressive Strengths

Specimen Designation		Test Date	Cap Beam Stress (ksi)	Column Stress (ksi)	Grout Stress (ksi)
I	EMB80	10-31-13	9905	10732	6767
II	WRC	1-20-14	9767	8766	7916
III	WRCUB	2-14-14	9452	7516	8078
IV	RC	3-14-14	10016	9742	N/A
V	EMB96	7-8-14	10057	8256	N/A

Four specimens were constructed using 20-in. diameter spiral weld steel tubes, and one specimen was constructed using a 24-in. diameter straight seam steel tube. Table 4.3 summarizes the tensile test results of the five steel tubes.

Table 4.3: Steel Tube Material Properties

Specimen Designation		Tube Type	Yield Stress (ksi)	Ultimate Stress (ksi)
I	EMB80	Spiral Weld		
II	WRC	Spiral Weld		
III	WRCUB	Spiral Weld		
IV	RC	Spiral Weld		
V	EMB96	Straight Seam		

Table 4.4 presents the average material properties of the reinforcing bars used in the three RC connection specimens.

Table 4.4: Longitudinal Reinforcing Bar Material Properties

Specimen Designation		Yield Stress (ksi)	Ultimate Stress (ksi)
I-III	WRC, WRCUB, RC		

4.5 EXPERIMENTAL TEST SETUP

The CFT column-to-cap beam specimens were tested using a self-reacting rig developed by Angela Kingsley, as shown in Figure 4.14. The rig is centered underneath a 2400-kip Baldwin Universal Testing Machine, which applies a constant axial load to the top of the column. A 220-kip actuator is used to apply a cyclic, displacement-controlled lateral load to the specimen at a height of 72-in. above the surface of the cap beam.

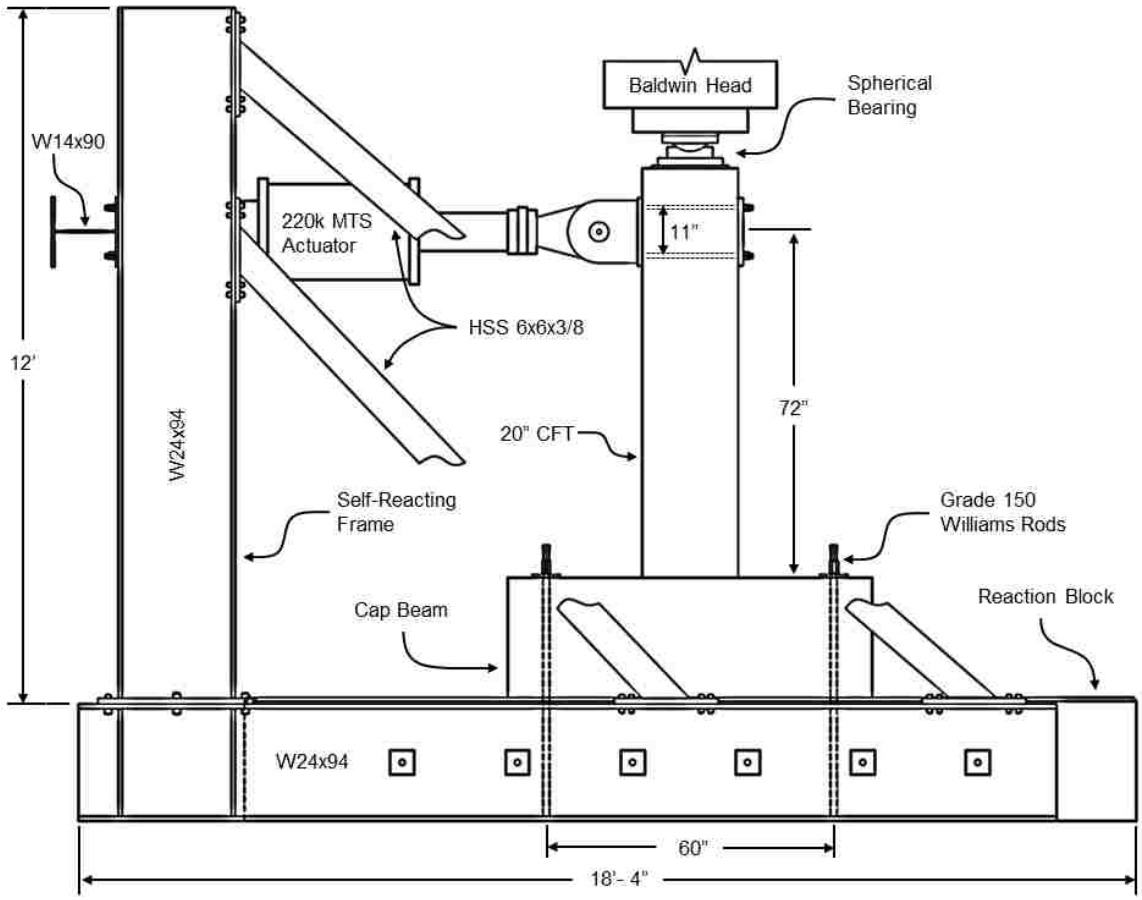

Figure 4.14: Experimental Test Rig

The cap beam was fixed to the reaction block using high-strength Williams all-thread bars. As shown in Figure 4.15, the bars are spaced at 60-in. on-center in the direction of loading, and 18-in. on-center in the direction perpendicular to loading. Each rod was

post-tensioned to 120-kips to prevent any uplift or slip from occurring during testing. A layer of hydrostone was placed between the surface of the reaction block and the underside of the cap beam to ensure a level bearing surface.

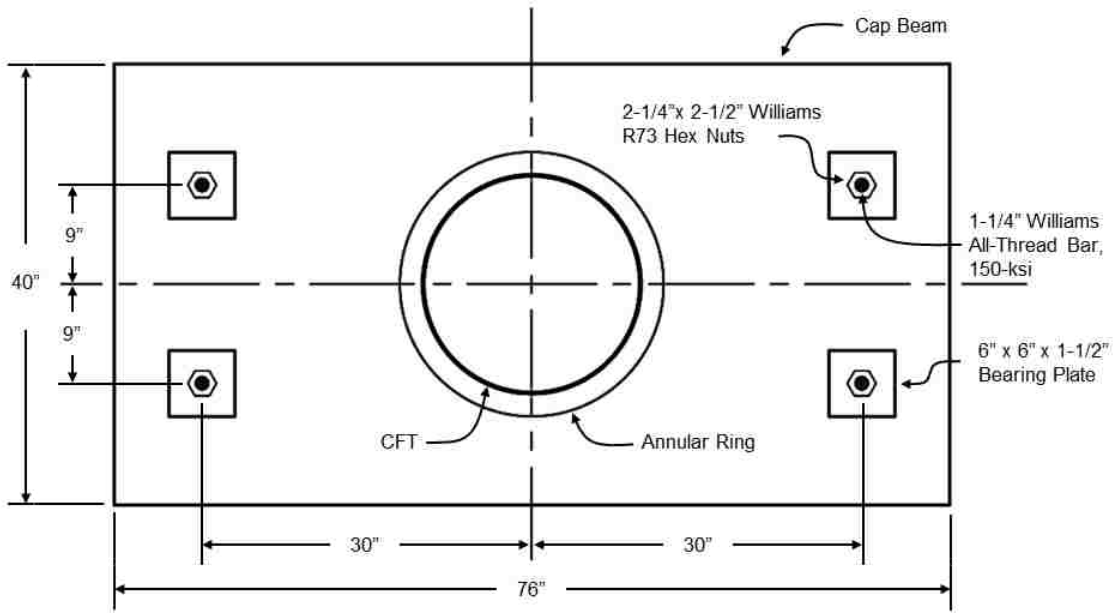

Figure 4.15: Williams Rods Layout

A spherical, swivel-head bearing was fixed to the top of the CFT column to allow for lateral displacements while still maintaining a constant axial load. The bearing sat within a recessed steel plate, which was lined with a polytetrafluoroethylene (PTFE) sliding surface, as shown in Figure 4.16. Under lateral loading, the PTFE slid within a stainless steel-lined channel, which was fixed to the bottom of the Baldwin head to prevent out-of-plane drifts. A silicone lubricant was applied between the PTFE and stainless steel to create a low-friction sliding surface.

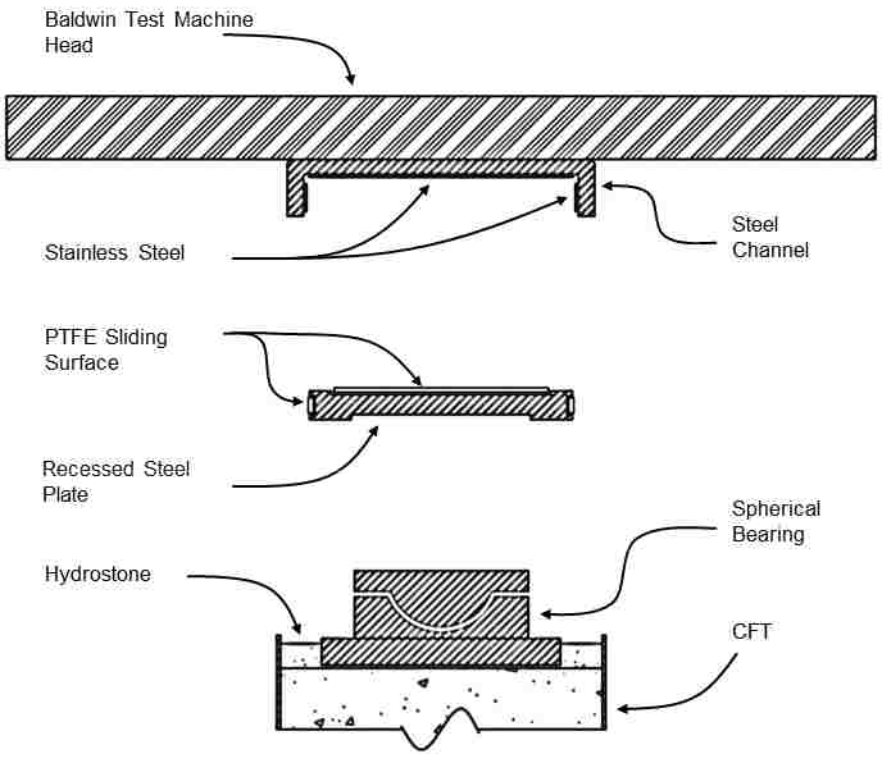

Figure 4.16: Axial Load Apparatus

Figure 4.17 shows the actual test rig with Specimen EMB80 anchored to the reaction block.

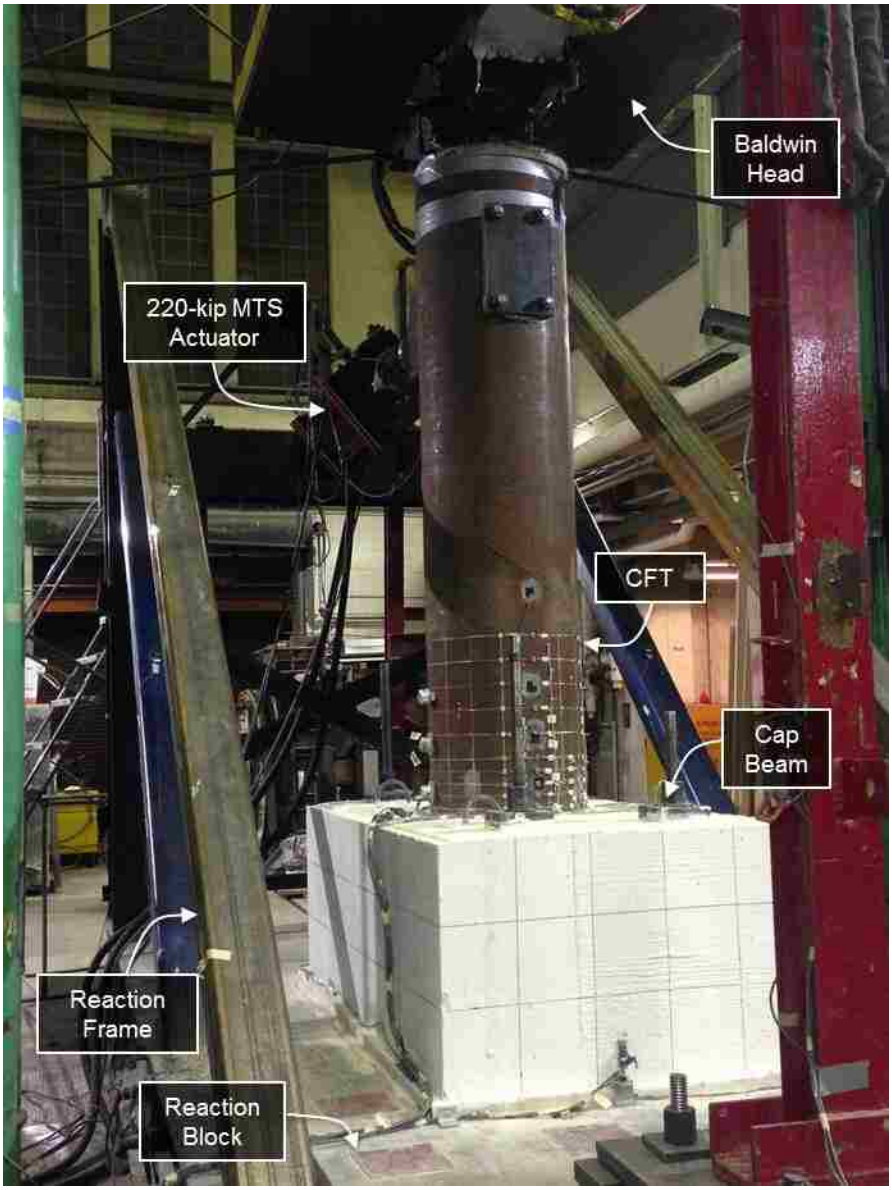

Figure 4.17: Experimental test rig with Specimen EMB80

4.6 LOAD PROTOCOL

Each specimen was subjected to a constant axial load, as well as a cyclic, displacement-controlled lateral load. The lateral load protocol was adapted from that of previous University of Washington tests, and ATC-24 (Guidelines for Cyclic Seismic Testing of Components of Steel Structures), in which the imposed displacements are based on incremental multiples of the member's yield displacement. The target lateral load protocol for each specimen is tabulated in Table 4.5 and displayed in Figure 4.18.

Table 4.5: Target Load Protocol

Cycle Range	No. of Cycles	Increment ($\%\Delta_y$)	Specimens 1-IV		Specimen V	
			Displacement (in)	Drift Ratio (%)	Displacement (in)	Drift Ratio (%)
1-2	2	0.125	0.075	0.10%	0.088	0.12%
3-4	2	0.25	0.15	0.21%	0.175	0.24%
5-6	2	0.50	0.30	0.42%	0.350	0.49%
7-8	2	0.75	0.45	0.63%	0.525	0.73%
9-11	3	1	0.60	0.83%	0.700	0.97%
13-15	3	1.5	1.35	1.88%	1.050	1.46%
16-18	3	2	1.80	2.50%	1.400	1.94%
20-21	2	3	2.70	3.75%	2.100	2.92%
22-23	2	4	3.60	5.00%	2.800	3.89%
25-26	2	6	5.40	7.50%	4.200	5.83%
27-28	2	7	6.30	8.75%	5.600	7.78%
30-31	2	8	7.20	10.0%	6.300	8.75%
33-34	2	9	8.10	11.25%	7.000	9.72%
36-37	2	10	9.00	12.50%	8.000	11.18%

Specimens I-IV were subjected to an axial load equal to 10% of their compressive load capacity, while Specimen V was only subjected to an axial load equal to 5% of its compressive load capacity. The axial load was reduced for Specimen V to ensure the actuator had sufficient capacity to apply the necessary load to reach the plastic moment capacity of the larger specimen.

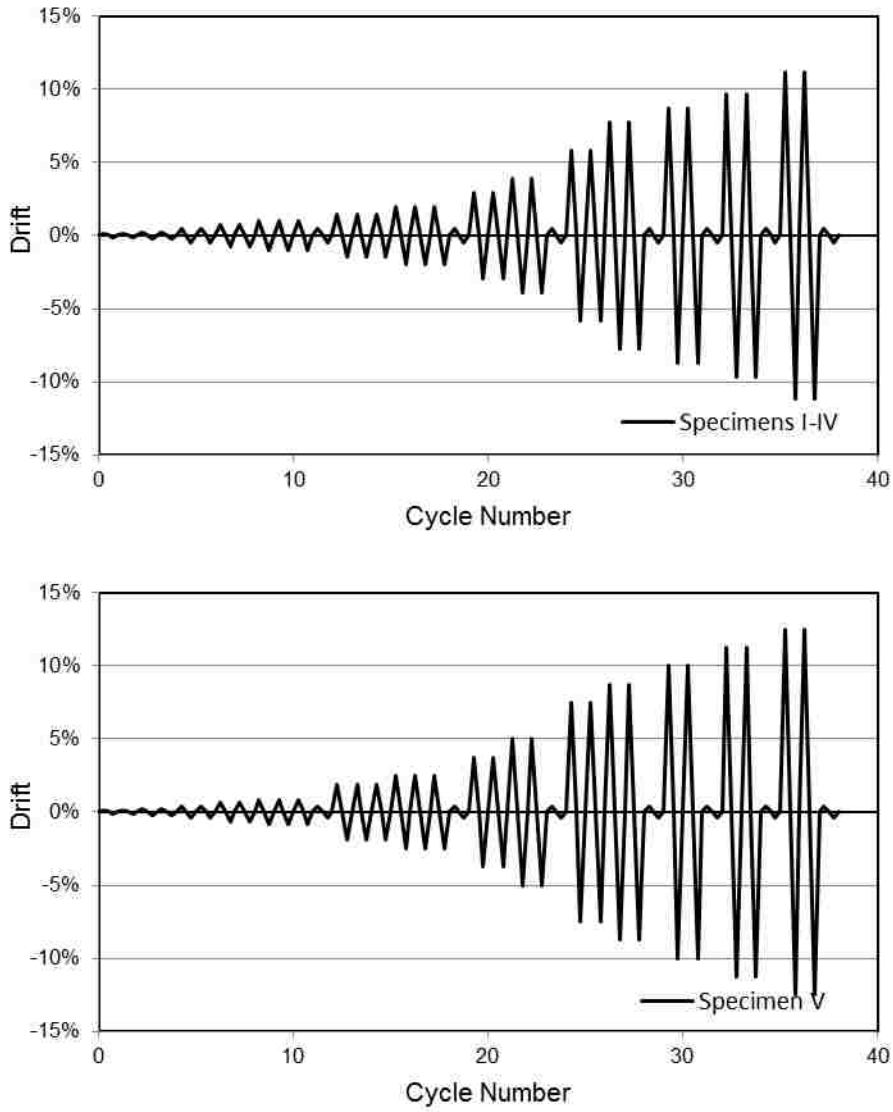

Figure 4.18: Target load protocol

4.7 SPECIMEN INSTRUMENTATION

This section describes the instrumentation used to capture the behavior of the specimens during testing. An overview of the five instrument types is presented in Table 4.6. The global instrumentation plan is described in Section 4.7.1, followed by the column and connection instrumentation plans respectively in Sections 4.7.2 and 4.7.3.

Table 4.6: Instrument Overview

Instrument Type	Purpose	Picture
Spectrotilt Inclinometer	Column rotation	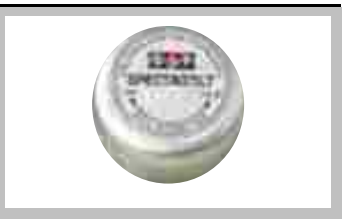
String Potentiometer	Column displacement	
Duncan Potentiometer	Actuator beam deflection, cap beam slip, test rig slip	
Tokyo Sokki KenKyujo Strain Gauge	Steel tube strains, reinforcing bar strains	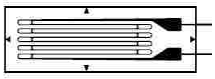
NDI Optotrak Certus Motion Capture system	Connection displacement & rotation	

4.7.1 Global Instrumentation

Duncan potentiometers were used to capture any global displacements that occurred during testing. As shown in Figure 4.19, three Duncan potentiometers were fixed to the base of the cap beam, intended to measure any horizontal slip or vertical uplift of the cap beam relative to the reaction block. Similarly, three additional Duncan potentiometers were fixed to the base of the reaction block to measure any slip or uplift relative to the laboratory floor. A final Duncan potentiometer was mounted to a reference column South of the test rig, such that lateral deflections of the actuator beam could be measured during loading. A summary of the Duncan potentiometer locations is provided in Table 4.7.

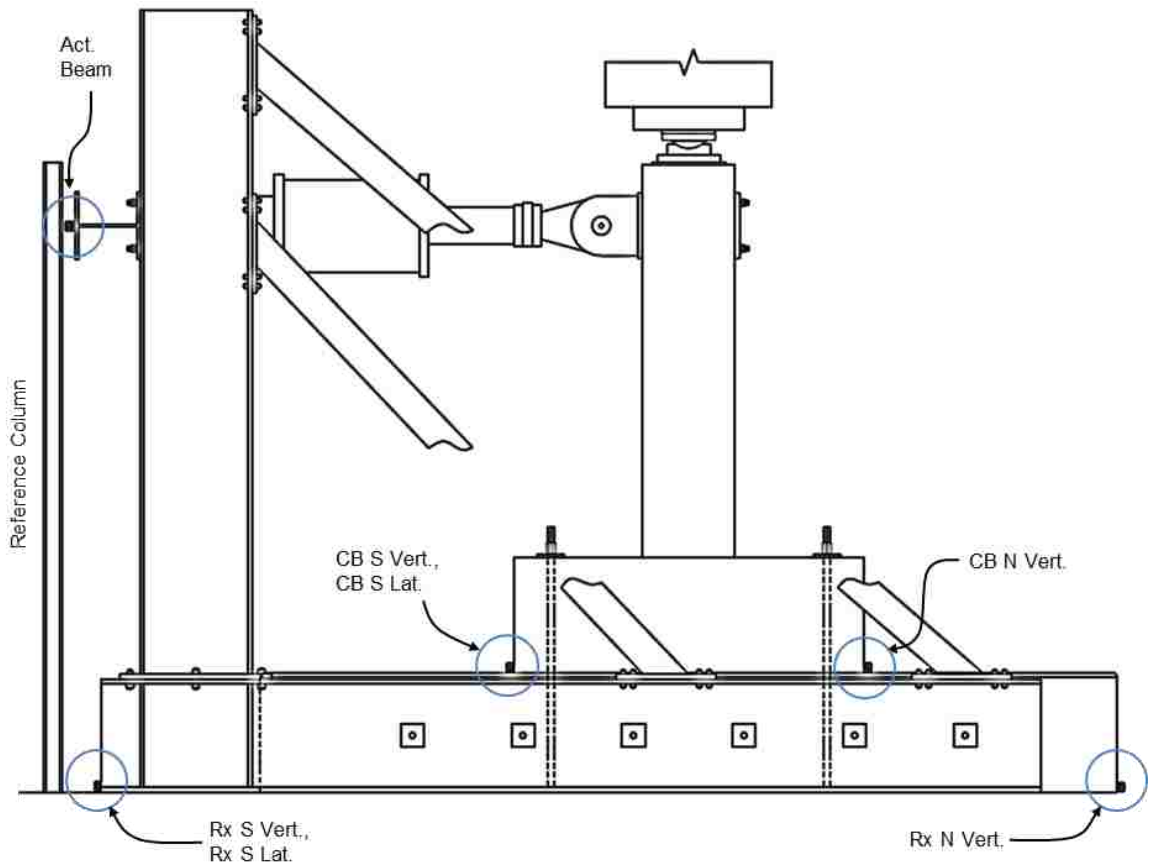

Figure 4.19: Global Instrumentation Schematic

Table 4.7: Global Instrumentation Summary

Instrument Name	Instrument Type	Instrument Location	Description of Measurement
Act. Beam	Duncan Potentiometer	Behind actuator beam	Horizontal beam deflections
CB N Vert	Duncan Potentiometer	North side of cap beam	Cap beam uplift
CB S Vert	Duncan Potentiometer	South side of cap beam	Cap beam uplift
CB S Lat	Duncan Potentiometer	South side of cap beam	Horizontal cap beam slip
Rx N Vert	Duncan Potentiometer	North side of reaction block	Reaction block uplift
Rx S Vert	Duncan Potentiometer	South side of reaction block	Reaction block uplift
Rx S Lat	Duncan Potentiometer	South side of reaction block	Horizontal reaction block slip

4.7.2 Column Instrumentation

A combination of string potentiometers and inclinometers was used to capture the behavior of the column during testing. Descriptions of two instrumentation types are provided in the following sections with their locations shown in Figure 4.20 and summarized in Table 4.8.

String Potentiometers

A series of four string potentiometers was used to measure horizontal displacements along the North side of the column. As shown in Figure 4.20, three string potentiometers were placed in the plastic region of the column, at 6-in. intervals above the surface of the cap beam. Additionally, a fourth string potentiometer was attached to the point of lateral loading (72 inches above the cap beam surface) such that the measured displacements from the string potentiometer could be compared to those from the LVDT. The string

potentiometers were attached to the CFT column using a magnetic connection, and were secured with hot glue to ensure they did not slip. The housings of the potentiometers were secured to a reference column that was fixed to the North side of the reaction block.

Inclinometers

A series of three inclinometers was used to measure rotations along the height of the column. The inclinometers were spaced at 6-in. intervals, starting 3-in. above the surface of the cap beam. The inclinometers were fixed to the East side of the column, closest to the data acquisition system.

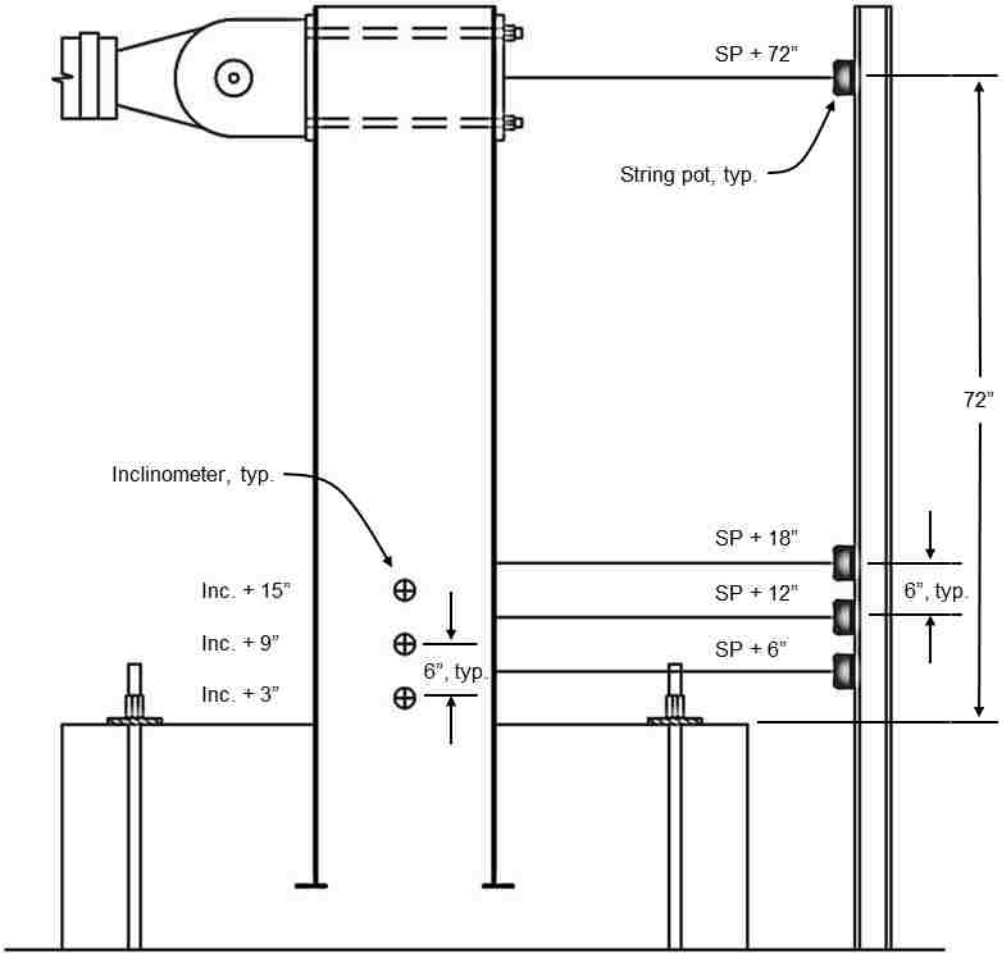

Figure 4.20: Column Instrumentation Schematic

Table 4.8: Column Instrumentation Summary

Instrument Name	Instrument Type	Instrument Location	Description of Measurement
SP +6	String Potentiometer	North side of column, 6” above cap beam surface	Column displacement
SP +12	String Potentiometer	North side of column, 12” above cap beam surface	Column displacement
SP +18	String Potentiometer	North side of column, 18” above cap beam surface	Column displacement
SP +72	String Potentiometer	North side of column, 72” above cap beam surface	Column displacement
Inc. +3	Inclinometer	East side of column, 3” above cap beam surface	Column rotation
Inc. +9	Inclinometer	East side of column, 9” above cap beam surface	Column rotation
Inc. +15	Inclinometer	East side of column, 15” above cap beam surface	Column rotation

4.7.3 Connection Instrumentation

The Optotrak Certus Motion System was used in conjunction with a series of uniaxial and biaxial strain gauges to capture the behavior of the column-to-cap beam connection region during testing. Section 4.7.3.1 details the strain gauge setup, and Section 4.7.3.2 describes the Optotrak Certus Motion System.

4.7.3.1 Strain Gauge Setup

High-elongation, 5-mm strain gauges were used to measure strains in the steel tube and longitudinal reinforcing bars during testing. The strain gauges were placed within the plastic hinge region of the column, primarily on the Northern & Southern-most sides of the specimens. Uniaxial strain gauges were used to measure longitudinal strains, whereas

biaxial strain gauges were used in areas where both longitudinal and hoop strains were of interest. The strain gauge schematic for Specimen EMB80 is presented in Figure 4.21, and the schematic for the RC specimens is presented in Figure 4.22.

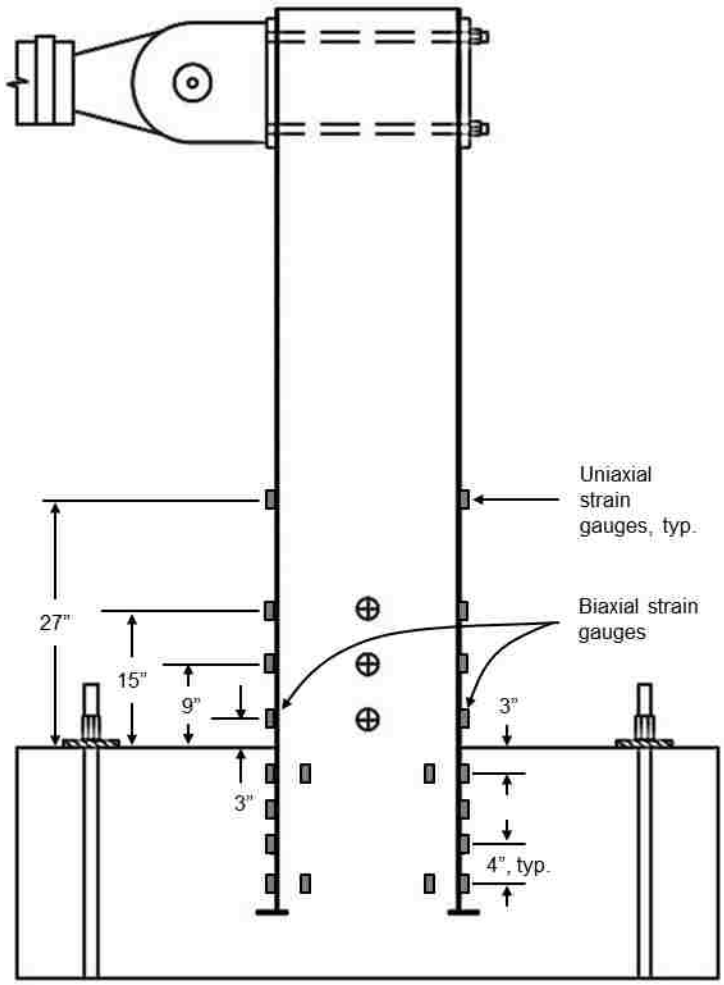

Figure 4.21: EMB80 Strain Gauge Schematic

As shown in Figure 4.21, Specimen EMB80 had uniaxial strain gauges running along the north and south sides of the column, with two additional gauges in the NE, NW, SE and SW directions. Biaxial strain gauges were placed 3-in. above the surface of the cap beam, at the anticipated apex of local buckling. Table 4.9 summarizes the strain gauge locations for Specimen EMB80.

Table 4.9: EMB80 Strain Gauge Locations

Instrument Name		Strain Gauge Type		Instrument Location
SG	N -15	2-wire	Uniaxial	North reinforcing bar, 15 inches below cap beam surface
SG	N -11	2-wire	Uniaxial	North reinforcing bar, 11 inches below cap beam surface
SG	N -7	2-wire	Uniaxial	North reinforcing bar, 7 inches below cap beam surface
SG	N -3	2-wire	Uniaxial	North reinforcing bar, 3 inches below cap beam surface
SG	N +3	2-wire	Biaxial	North side of tube, 3 inches above cap beam surface
SG	N +5	2-wire	Uniaxial	North reinforcing bar, 9 inches above cap beam surface
SG	N +13	2-wire	Uniaxial	North reinforcing bar, 15 inches above cap beam surface
SG	N +27	2-wire	Uniaxial	North side of tube, 27 inches above cap beam surface
SG	NE -15	2-wire	Uniaxial	Northeast reinforcing bar, 15 inches blow cap beam surface
SG	NE -3	2-wire	Uniaxial	Northeast reinforcing bar, 3 inches blow cap beam surface
SG	NW -15	2-wire	Uniaxial	Northwest reinforcing bar, 15 inches blow cap beam surface
SG	NW -3	2-wire	Uniaxial	Northwest reinforcing bar, 3 inches blow cap beam surface
SG	S -15	2-wire	Uniaxial	South reinforcing bar, 15 inches below cap beam surface
SG	S -11	2-wire	Uniaxial	South reinforcing bar, 11 inches below cap beam surface
SG	S -7	2-wire	Uniaxial	South reinforcing bar, 7 inches below cap beam surface
SG	S -3	2-wire	Uniaxial	South reinforcing bar, 3 inches below cap beam surface
SG	S +3	2-wire	Biaxial	South side of tube, 3 inches above cap beam surface
SG	S +5	2-wire	Uniaxial	South reinforcing bar, 5 inches above cap beam surface
SG	S +13	2-wire	Uniaxial	South reinforcing bar, 13 inches above cap beam surface
SG	S +27	2-wire	Uniaxial	South side of tube, 27 inches above cap beam surface
SG	SE -15	2-wire	Uniaxial	Southeast reinforcing bar, 15 inches blow cap beam surface
SG	SE -3	2-wire	Uniaxial	Southeast reinforcing bar, 3 inches blow cap beam surface
SG	SW -15	2-wire	Uniaxial	Southwest reinforcing bar, 15 inches blow cap beam surface
SG	SW -3	2-wire	Uniaxial	Southwest reinforcing bar, 3 inches blow cap beam surface

Figure 4.22a shows the strain gauge locations for both Specimens WRC and WRCUB. Four uniaxial strain gauges were placed on the north and south reinforcing bars, and two were placed on the NE, NW, SE and SW bars. Two additional gauges were placed on the North and South sides of the steel tube to measure strains in the region where the reinforcing bars are welded to the steel tube and at the base of the column in case any unexpected local buckling occurred.

As shown in Figure 4.22b, Specimen RC had three strain gauges on the north and south reinforcing bars, and one gauge in the grouted soffit region on the NE, NW, SE and SW bars. Three additional strain gauges were placed on the transverse spiral to measure confining strains at heights of -7, +0.75 and +7.75, relative to the top surface of the cap beam.

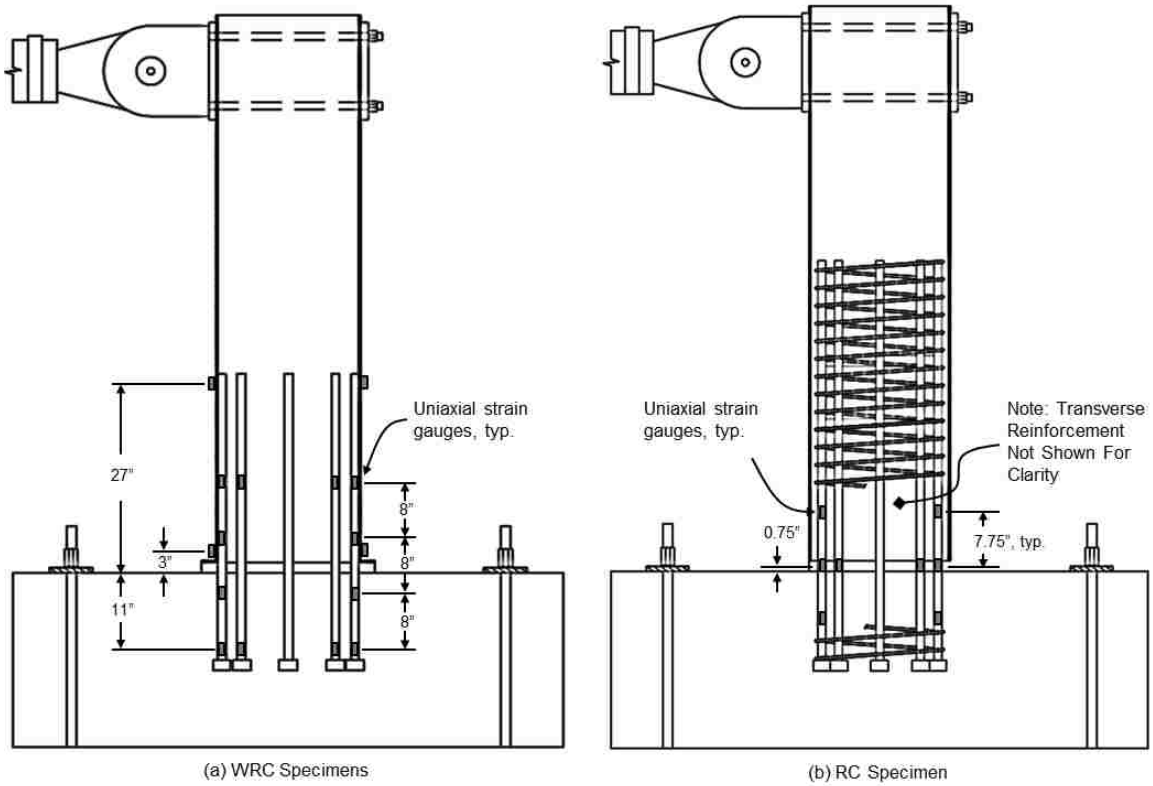

Figure 4.22: Strain gauge schematic for (a) Specimens WRC, WRCUB, and (b) RC

Tables 4.10 and 4.11 summarize the strain gauge locations for the WRC and RC specimens, respectively.

Table 4.4.10: Specimen WRC and WRCUB Strain Gauge Locations

Instrument Name	Strain Gauge Type		Instrument Location
SG N -11	2-wire	Uniaxial	North side, 11 inches below cap beam surface
SG N -3	2-wire	Uniaxial	North side, 3 inches below cap beam surface
SG N +3	2-wire	Uniaxial	North side, 7 inches below cap beam surface
SG N +5	2-wire	Uniaxial	North side, 3 inches below cap beam surface
SG N +13	2-wire	Uniaxial	North side, 3 inches above cap beam surface
SG N +27	2-wire	Uniaxial	North side, 9 inches above cap beam surface
SG S -11	2-wire	Uniaxial	North side, 15 inches above cap beam surface
SG S -3	2-wire	Uniaxial	North side, 27 inches above cap beam surface
SG S +3	2-wire	Uniaxial	Northeast side, 15 inches below cap beam surface
SG S +5	2-wire	Uniaxial	Northeast side, 3 inches below cap beam surface
SG S +13	2-wire	Uniaxial	Northwest side, 15 inches below cap beam surface
SG S +27	2-wire	Uniaxial	Northwest side, 3 inches below cap beam surface
SG NE -3	2-wire	Uniaxial	South side, 15 inches below cap beam surface
SG NE +5	2-wire	Uniaxial	South side, 11 inches below cap beam surface
SG NW -3	2-wire	Uniaxial	South side, 7 inches below cap beam surface
SG NW +5	2-wire	Uniaxial	South side, 3 inches below cap beam surface
SG SE -3	2-wire	Uniaxial	South side, 3 inches above cap beam surface
SG SE +5	2-wire	Uniaxial	South side, 9 inches above cap beam surface
SG SW -3	2-wire	Uniaxial	South side, 15 inches above cap beam surface
SG SW +5	2-wire	Uniaxial	South side, 27 inches above cap beam surface

Table 4.11: Specimen RC Strain Gauge Locations

Instrument Name	Strain Gauge Type		Instrument Location
SG N -7	2-wire	Uniaxial	North reinforcing bar, 7 inches below cap beam surface
SG N +.75	2-wire	Uniaxial	North reinforcing bar, .75 inches above cap beam surface
SG N +8.5	2-wire	Uniaxial	North reinforcing bar, 8.5 inches above cap beam surface
SG S -7	2-wire	Uniaxial	South reinforcing bar, 7 inches below cap beam surface
SG S +.75	2-wire	Uniaxial	South reinforcing bar, .75 inches above cap beam surface
SG S +8.5	2-wire	Uniaxial	South reinforcing bar, 8.5 inches above cap beam surface
SG V -7	2-wire	Uniaxial	Transverse spiral, 7 inches below cap beam surface
SG V +.75	2-wire	Uniaxial	Transverse spiral, .75 inches above cap beam surface
SG V +8.5	2-wire	Uniaxial	Transverse spiral, 8.5 inches above cap beam surface
SG NE +.75	2-wire	Uniaxial	Northeast reinforcing bar, .75 inches above cap beam surface
SG NW +.75	2-wire	Uniaxial	Northwest reinforcing bar, .75 inches above cap beam surface
SG SE +.75	2-wire	Uniaxial	Southeast reinforcing bar, .75 inches above cap beam surface
SG SW +.75	2-wire	Uniaxial	Southwest reinforcing bar, .75 inches above cap beam surface

4.7.3.2. Optotrak Certus Motion Capture System

The Optotrak Certus motion capture system was used to capture the deformed shape of the column in the plastic region. This system used precision cameras to track 3D displacements of small LED targets that were attached to the steel tube in the arrangements presented in Figures 4.22 and 4.23. For each specimen, targets were placed around the tube with a circumferential spacing of 4 inches, and a vertical spacing of 1.5”

in the anticipated buckled region, and 3” in the remainder of the plastic hinge region. As shown in Figure 4.24, additional targets were placed above the plastic hinge region of the column to capture deformations in the regions where the longitudinal reinforcing bars were welded to the inside of the steel tube.

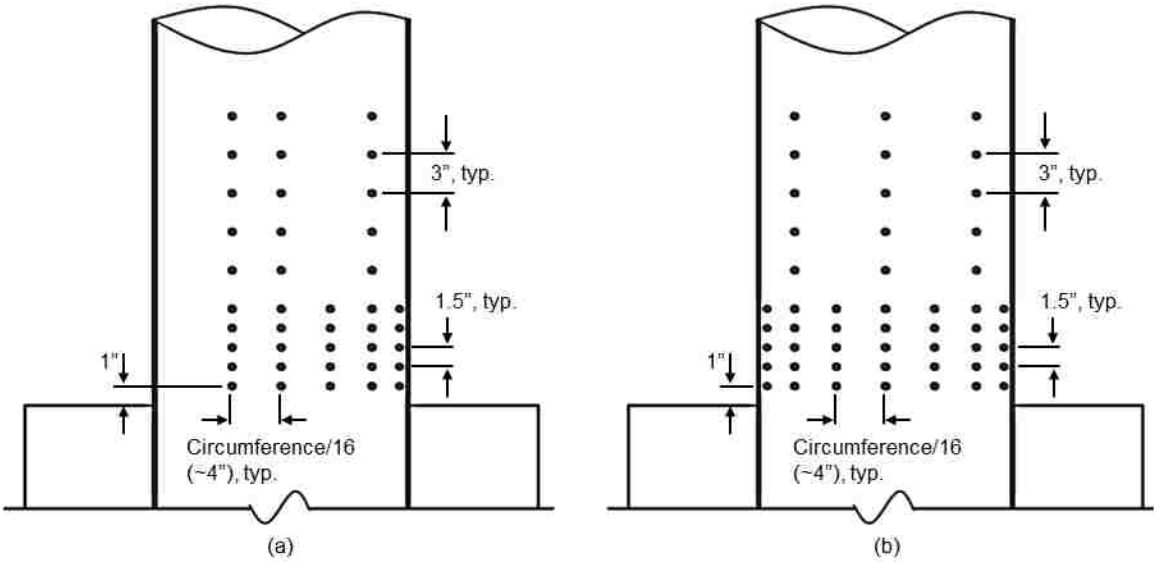

Figure 4.23: EMB80 Optotrak Target Layout (a) North & South Face, (b) West Face

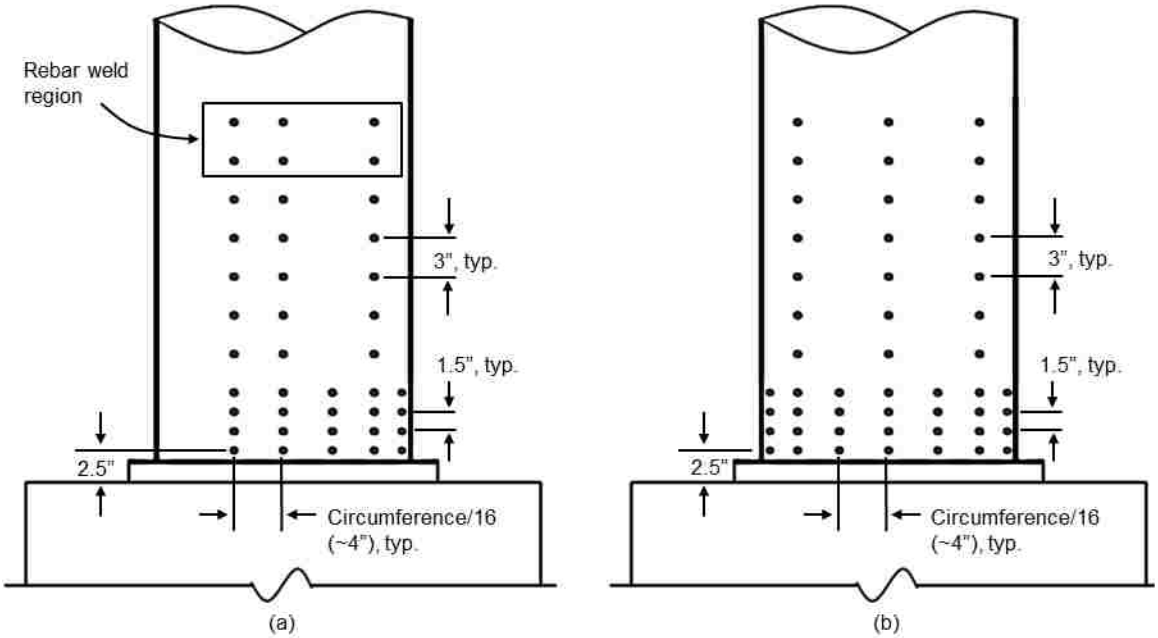

Figure 4.24: WRC, WRCUB, and RC Optotrak Target Layout (a) North & South Face, (b) West Face

CHAPTER 5
EXPERIMENTAL OBSERVATIONS

5.1 INTRODUCTION

The objective of this chapter is to provide a detailed discussion of the observations made during testing. A series of physical damage states, outlined in Section 5.2, will be used to evaluate the performance of each specimen. For reference, Table 5.1 provides a summary of the connection properties specific to each specimen.

Table 5.1: Transverse Specimen Text Matrix

Specimen Designation	Test Date	Column Diameter	Steel Tube Thickness	Steel Tube Designation	Annular Ring Outer Diameter	Connection Reinforcing	Reinforcing Embedment Depth	Steel Tube Embedment Depth
EMB80	10-31-13	20-in.	¼-in.	AWWA C200 Spiral Seam	24-in.	N/A	N/A	18-in.
WRC	1-20-14	20-in.	¼-in.	AWWA C200 Spiral Seam	24-in.	8 No. 9 headed bars	14-in.	N/A
WRCUB	2-14-14	20-in.	¼-in.	AWWA C200 Spiral Seam	24-in.	8 No. 9 headed bars	14-in.	N/A
RC	3-14-14	20-in.	¼-in.	AWWA C200 Spiral Seam	N/A	8 No. 9 headed bars	14-in.	N/A
EMB96	7-8-14	24-in.	¼-in.	API 5L Straight Seam	28-in.	N/A	N/A	20.75-in.

The observed damage progression for each specimen, described in Sections 5.3 through 5.7, is separated into three drift ranges: low drift cycles (0% -2% drift), moderate to high drift cycles (> 2% drift), and specimen failure. The drift ratio is defined in Equation 5.1 as:

$$Drift = \frac{\Delta}{L_{col}} \tag{5.1}$$

in which Δ represents the lateral displacement at the point of loading, and L_{col} is the length of the column, shown in Figure 5.1.

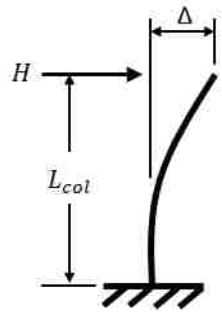

Figure 5.1: Specimen drift

For reference, the idealized drift history is summarized in Table 5.2, and displayed in Figure 5.2.

Table 5.2: Idealized Drift History

Cycle Range	No. of Cycles	Increment ($\%\Delta_y$)	Specimens EMB80, WRC, WRCUB, RC		Specimen EMB96	
			Displacement (in)	Drift Ratio (%)	Displacement (in)	Drift Ratio (%)
1-2	2	0.125	0.075	0.10%	0.088	0.12%
3-4	2	0.25	0.15	0.21%	0.175	0.24%
5-6	2	0.50	0.30	0.42%	0.350	0.49%
7-8	2	0.75	0.45	0.63%	0.525	0.73%
9-11	3	1	0.60	0.83%	0.70	0.97%
13-15	3	1.5	1.35	1.88%	1.05	1.46%
16-18	3	2	1.80	2.50%	1.40	1.94%
20-21	2	3	2.70	3.75%	2.10	2.92%
22-23	2	4	3.60	5.00%	2.80	3.89%
25-26	2	6	5.40	7.50%	4.20	5.83%
27-28	2	7	6.30	8.75%	5.60	7.78%
30-31	2	8	7.20	10.0%	6.30	8.75%
33-34	2	9	8.10	11.25%	7.00	9.72%
36-37	2	10	9.00	12.50%	8.00	11.18%

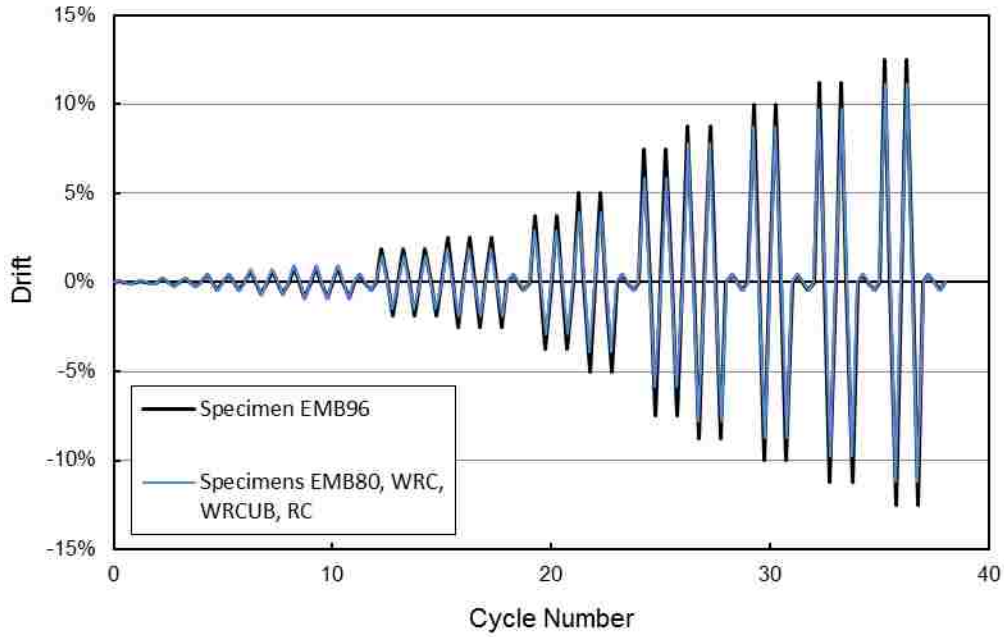

Figure 5.2: Idealized Drift History

Sections 5.3 through 5.7 also provide a hysteretic moment-drift response of each specimen, where the moment is defined in Equation 5.2 as:

$$Moment = H * L_{col} + P * \Delta \tag{5.2}$$

in which variables H and P represent the applied lateral load and axial load, respectively.

5.2 OVERVIEW OF DAMAGE STATES

This section describes the damage states used to evaluate the performance of each specimen. The damage states are separated into three categories: CFT connection damage states, RC connection damage states, and cap beam damage states.

As shown in Table 5.3, the damage states for the embedded CFT specimens progress from initial yielding of the steel tube to local buckling at the base of the column. The failure mode consists of subsequent tearing at the apex of the buckled region. The steel

tube yielding is measured from actual strain gauge data, while the rest of the damage states are observed visually.

Table 5.3: CFT Damage State Descriptions

Symbol	Description	Detailed Description	Photo
Y1	Initial Yielding	Initial yielding of steel tube.	No observable damage.
B1	Initial Buckling	Residual out-of-plane displacement at the apex of the buckled region exceeds 0.	
B2	Buckling > 2t	Residual out-of-plane displacement at the apex of the buckled region exceeds 2t.	
B3	Buckling > 4t	Residual out-of-plane displacement at the apex of the buckled region exceeds 4t.	
T1	Tube Tearing	Visual tearing initiation in the buckled region of the steel tube.	

As shown in Table 5.4, the damage states for the RC connection specimens progress from initial yielding of the reinforcing bars, to cracking and crushing of the grout pad, and ultimate fracture of the reinforcing bars. Initial yielding is measured from strain gauge data, while the remaining damage states are observed visually.

Table 5.4: RC Damage State Descriptions

Symbol	Description	Detailed Description	Photo
Y1	Initial Yielding	Initial yielding of reinforcing bars.	No observable damage.
G1	Grout Cracking	Hairline radial cracks visible in grout pad	
G2	Grout Crushing	Crushing of grout pad	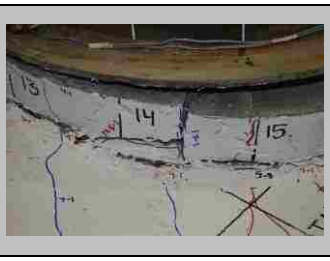
BV	Bars Visible	Reinforcing bars visible	
BF	Bar Fracture	Fracture of reinforcing bars.	

Table 5.4 defines the damage states for the cap beam, in which damage progresses from hairline radial cracks to uplift in the concrete.

Table 5.5: Cap Beam Damage State Descriptions

Symbol	Description	Detailed Description	Photo
C1	Initial Cracking	Hairline radial cracks visible in cap beam	
C2	Cracking > 2mm	Radial crack width exceeds 2mm.	
U1	Initial Uplift	Visual uplift of concrete	
U2	Uplift > 5mm	Concrete uplift exceeds 5mm.	
U3	Uplift > 10mm	Concrete uplift exceeds 10mm	

5.3 SPECIMEN EMB80

Specimen EMB80 consisted of a 20-in. diameter spiral-welded CFT embedded 18-in. (.9D) into a precast reinforced concrete cap beam, as shown in Figure 5.3. The thickness of the steel tube was ¼-in, resulting in a diameter-to-thickness (D/t) ratio of 80.

The purpose of testing Specimen EMB80 was to evaluate its overall performance given its reduced annular ring diameter of 24-in. (D + 16t), and reduced cap beam width of 40-in. (2D). The behavior of this specimen will later be compared to Specimen 3-50 tested by Jason Lee (2011), which has an annular ring diameter of 28-in., and cap beam width of 68-in.

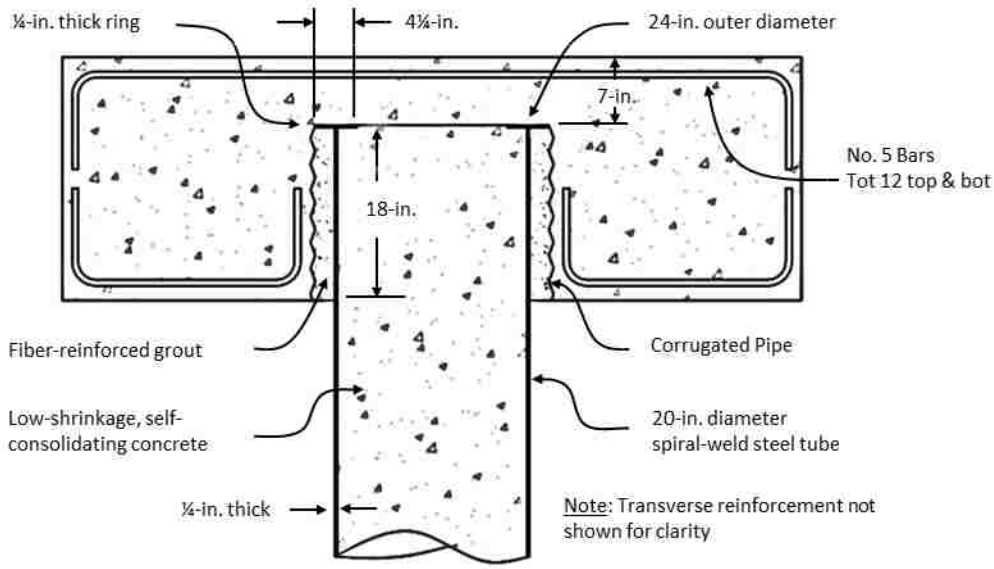

Figure 5.3: EMB80 Connection Detail

Specimen EMB80 was subjected to a constant axial load of 350-kips, as well as a cyclic, displacement-controlled lateral load following the load protocol outlined in Table 5.2. The actual drift history achieved during testing is summarized in Table 5.6.

The general behavior of the specimen consisted of yielding of the steel tube, followed by local buckling at the base of the column. Failure consisted of subsequent ductile tearing at the apex of the buckled region on both the North and South sides of the column. The moment-drift response of the specimen, with noted damage states, is shown in Figure 5.4. The dashed line represents the plastic moment capacity of the CFT, calculated using the PSDM method with specified design strengths.

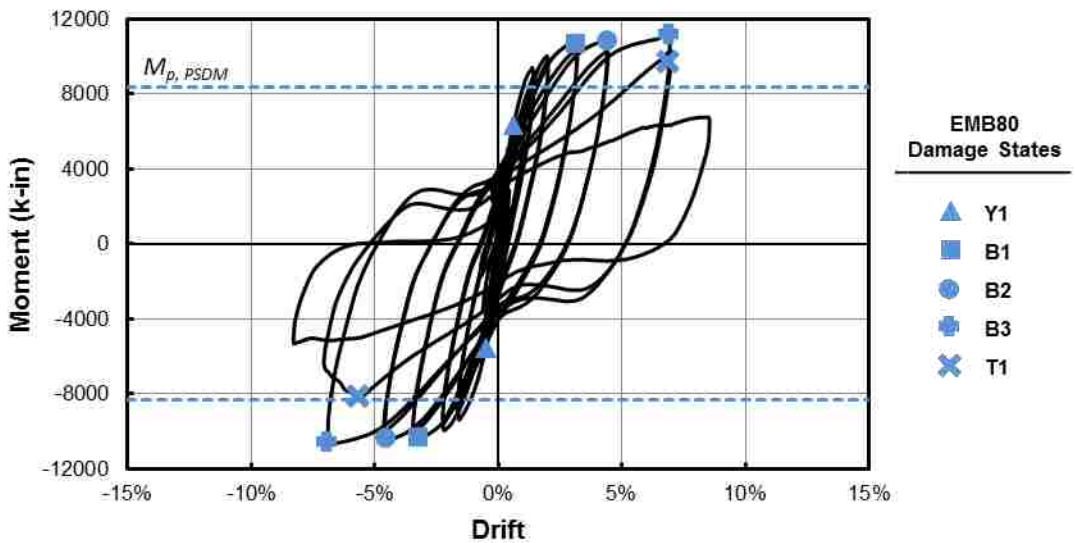

Figure 5.4: EMB80 Moment-Drift Response

5.3.1 EMB 80 Damage State Summary

Table 5.6 summarizes the progression of damage that was observed to the column and cap beam during testing, as well as the magnitude of repair that would be required at each damage state. As shown in Table 5.6, the CFT column reached its final damage state of tube tearing at 7.0% drift, while the cap beam experienced only limited cracking throughout the duration of the test. The following section provides a detailed description of the damage progression, and will refer to this damage state progression table.

Table 5.6: EMB80 Damage State Progression Table

Set No.	Target Drift (%)	Actual Drift (%)	Column Damage	Cap Beam Damage		Lateral Load[1] (kips)
				North	South	
1	0.10	0.04				21.1
	-0.10	-0.10				-23.8
2	0.21	0.10				36.3
	-0.21	-0.18				-38.1
3	0.42	0.24				52.6
	-0.42	-0.34				-54.1
4	0.63	0.41				69.3
	-0.63	-0.52				-71.1
5	0.83	0.57	**Y1**			82.9
	-0.83	-0.69				-84.1
7	1.88	1.45		**C1**		124.7
	-1.88	-1.67			**C1**	-124.0
8	2.50	2.00				130.9
	-2.50	-2.25				-129.3
10	3.75	3.19	**B1**			136.7
	-3.75	-3.45				-131.6
11	5.00	4.43	**B2**			132.8
	-5.00	-4.64				-127.6
13	7.50	7.00	**B3 / T1**			128.9
	-7.50	-7.07				-120.9
14	8.75	8.54				61.9
	-8.75	-8.30				-46.5

[1] Lateral Load represents the peak load of the first cycle in each drift set

Repair States

	No Repair Required
	Repair
	Full Replacement

5.3.2 Low Drift Cycles (0.0% - 2.0% Drift)

There was no visual damage observed to the column or cap beam during the first three sets of loading. At an imposed drift of 0.41%, circumferential hairline cracks initiated on the South side of the specimen along the grout-cap beam interface and the column-grout interface, as shown in Figure 5.5. During the next load set at 0.57% drift, yielding of the steel tube was measured by strain gauges located 3-in. above the surface of the cap beam on both the North and South sides of the column.

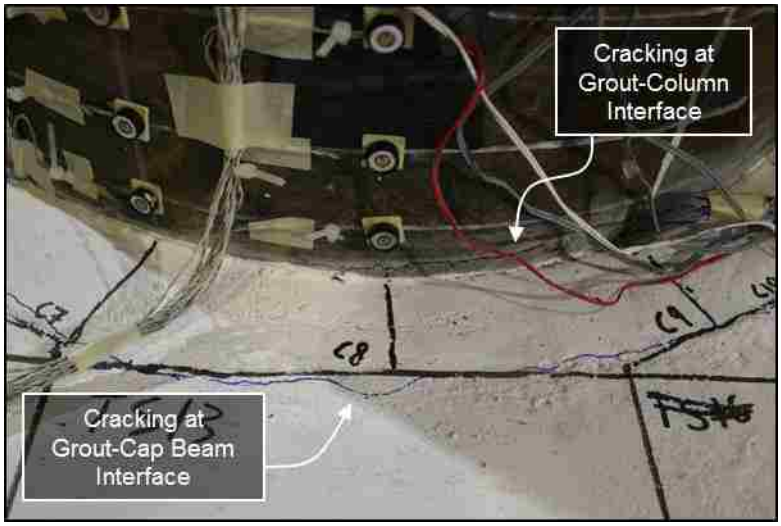

Figure 5.5: EMB80 Cracking on South side of Column at 0.41% drift (Column displaced to the North)

At 1.45% drift, circumferential hairline cracks initiated along the grout interface on the North side of the specimen, similar to those shown in Figure 5.5. At this same drift, cracks were observed propagating radially in the grout pad and the cap beam, as shown in Figures 5.6a and 5.6b. These cracks were hairline in width, and they continued propagating down the East and West sides of the cap beam.

During the third cycle of this load set, slight flaking of the grouted region was observed near the grout-cap beam interface, as shown in Figure 5.6a. The portions of

grout that flaked off ranged between ½-in. and 1-in. in diameter, and were less than ¼-in. in thickness.

(a) (b)

Figure 5.6: EMB80 Radial cracking at 1.45% drift in (a) grout region, and (b) cap beam

5.3.3 Moderate to High Drift Cycles (2.0% - 7.0% Drift)

During the 8th load set, additional hairline cracks continued to develop radially from the column and diagonally down the East and West sides of the cap beam. Figure 5.7 shows cracking on the west side of the cap beam after the column was subjected to 2.25% drift in the North direction.

Figure 5.7: EMB80 hairline cracking on the west side of the cap beam at 2.25% drift

Initial buckling of the North and South sides of the steel tube was observed visually during the 10th load set, at 3.19% and -3.45% drift, respectively. At this point, the specimen had reached its maximum lateral load resistance of 136.7-kips in the South direction, followed by 131.6-kips in the North direction. The apex of the buckled region was approximately 1.75-in. above the surface of the cap beam, as shown in Figure 5.8a. Additional hairline cracks formed radially in the top surface of the cap beam, as well as vertically and diagonally down the East and West faces of the cap beam. No cracks were observed on the North and South faces of the cap beam.

The magnitude of the residual out-of-plane displacement (measured at zero drift) of the buckled region increased with subsequent cycles. Figure 5.8b shows the buckled region on the South side of the column as it was subjected to 4.43% drift. Again, the apex of the buckled region was approximately 1.75-in. above the surface of the cap beam, and the total height of the buckled region was approximately 3.5-in.

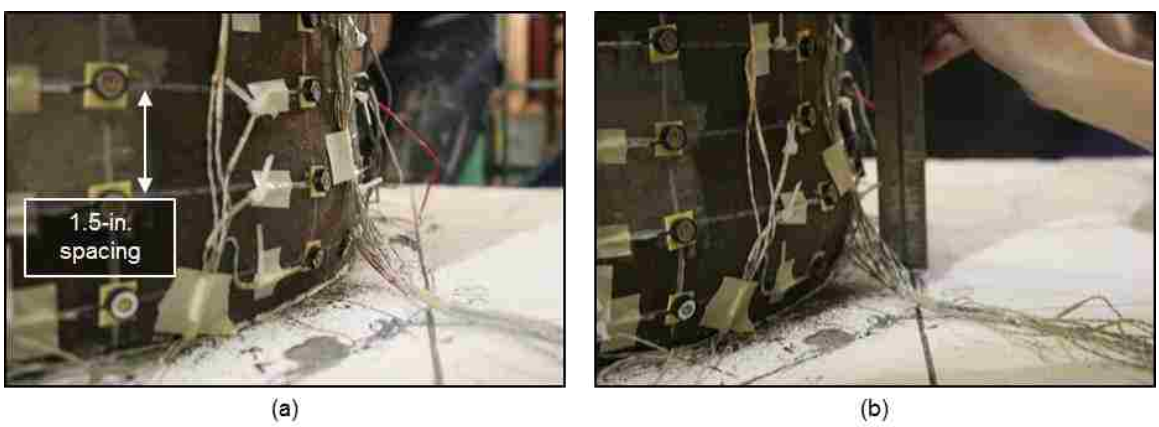

Figure 5.8: EMB80 South tube buckling at (a) 3.19% drift, and (b) 4.43% drift

5.3.4 Specimen Failure (7.0%+ Drift)

During the first complete cycle of the 13th load set, the magnitude of the out-of-plane displacement of the buckled region on both the North and South sides of the column increased without any tearing observed. Figure 5.9 shows the buckled region on the South side of the tube after the column was subjected to 7.0% drift to the North. The lateral load resistance remained stable through the first cycle of this drift set.

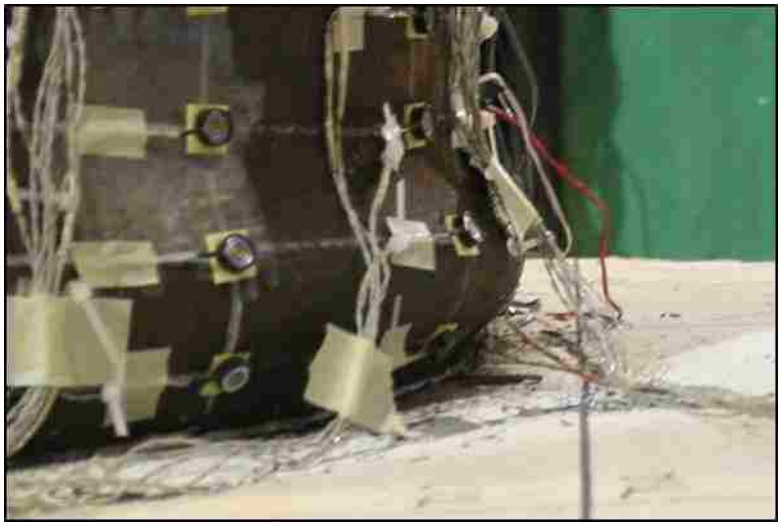

Figure 5.9: EMB80 South tube buckling at 7.0% drift

During the second cycle of the same drift set, tearing was observed in the buckled regions on both the North and South sides of the column, as shown in Figures 5.10 and 5.11, respectively. During this cycle, the lateral load resistance had decreased to 114.1-kips in the South direction, and 91.6-kips in the North direction.

The tear on the North side of the column formed approximately 2-in. above the surface of the cap beam, and was approximately 1 in. in length. As shown in Figure 5.11, tearing initiated at two locations on the South side of the column: circumferentially along

the apex of the buckled region, and diagonally in the heat affected zone along the weld seam at the base of the column. All tearing initiated at the apexes of the buckled regions.

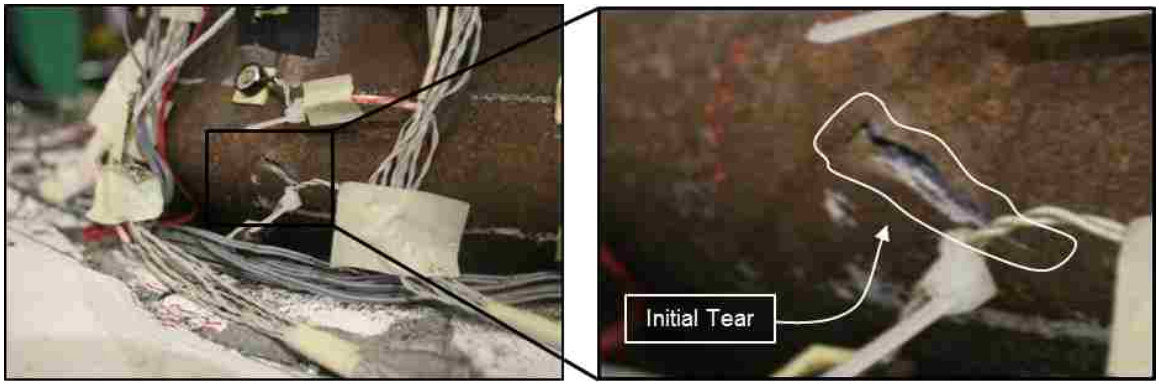

Figure 5.10: EMB80 tear initiation on North side of column at 7.0% drift

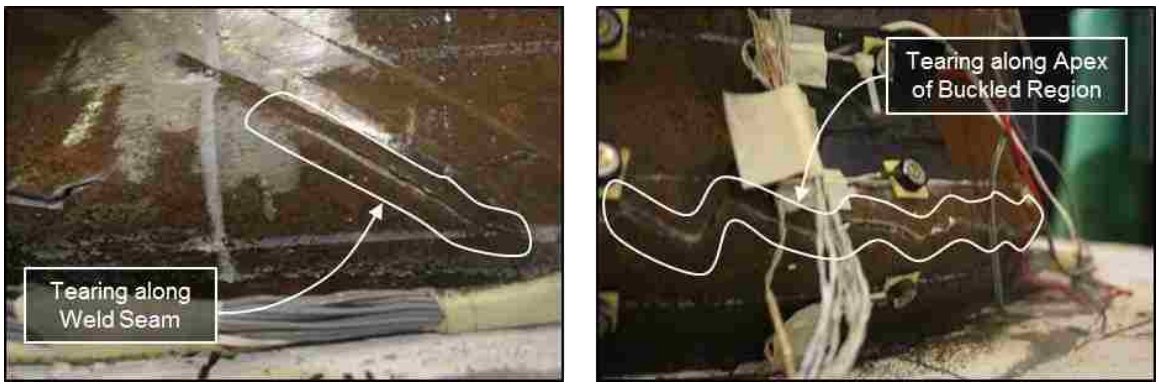

Figure 5.11: EMB80 tear initiation on South side of column at 7.0% drift

After tearing initiated, the specimen was subjected to one more complete load cycle. As the column reached 8.54% drift in the South direction, the initial tear on the North side of the column propagated circumferentially, as shown in Figure 5.12.

Figure 5.12: EMB80 tear propagation on North side of column at 8.54% drift

The tear propagated along the apex of the buckled region, and the width of the tear at the Northern-most point was approximately 1-in. as it was subject to tension. As the column cycled to 8.30% drift in the North direction, the two existing tears on the South side of the column propagated together as shown in Figure 5.13.

Figure 5.13: EMB80 tear propagation on South side of column at 8.30% drift

During this cycle, the lateral load resistance in the North direction had decreased to 46.5-kips; a 65% decrease from its maximum load of 131.6-kips. Due to this significant reduction in lateral load resistance, the test was terminated after this cycle was completed. After the test was terminated, examination of the cap beam revealed no additional concrete cracking, nor any widening of the existing hairline cracks.

5.4 SPECIMEN WRC

Specimen WRC consisted of a 20-in. diameter CFT column connected to a precast RC cap beam via 8 No. 9 headed reinforcing bars that were fully bonded to the surrounding concrete. The reinforcing bars were welded to the inside of the column, and extended 14-in. ($12d_b$) into the cap beam, as shown in Figure 5.14.

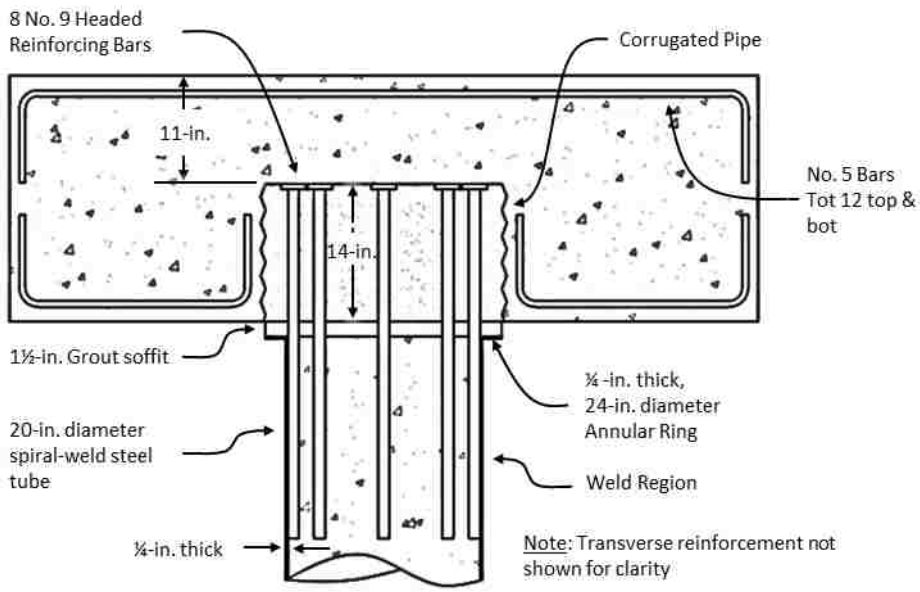

Figure 5.14: WRC Connection Detail

The purpose of testing this specimen was to: 1) compare its response to the previously tested EMB80 specimen, and 2) compare its response to Specimen WRCUB, which has a similar layout with the exception of partially debonded reinforcing bars. The specimen was subjected to a constant axial load of 350-kips, as well as a cyclic, displacement-controlled lateral load following the load protocol outlined in Table 5.2. The actual drift history achieved during testing is summarized in Table 5.7.

The behavior of the specimen consisted of yielding of the reinforcing bars, followed by crushing of the grouted soffit region. Failure of the specimen consisted of concrete cracking and uplift in the cap beam, with no reinforcing bar fracture. The moment-drift response of the specimen, with noted damage states, is shown in Figure 5.15. The dashed line represents the plastic moment capacity of the RC section, as calculated by the PSDM method using specified design strengths.

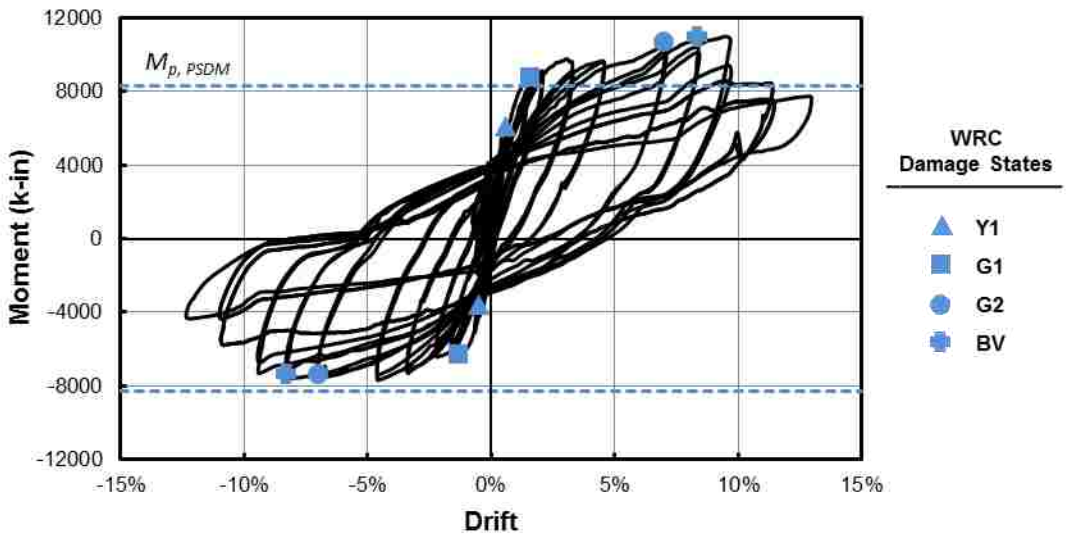

Figure 5.15: WRC Moment-Drift Response

5.4.1 WRC Damage State Summary

Table 5.7 summarizes the progression of damage that was observed to the column and cap beam during testing, as well as the magnitude of repair that would be required at each damage state. As shown in the table, there was no reinforcing bar fracture, and failure of the specimen consisted of cracking and uplift in the cap beam. The proceeding section provides a detailed description of the damage progression, and will refer to the damage state progression table.

Table 5.7: WRC Damage State Progression Table

Set No.	Target Drift (%)	Actual Drift (%)	Column Damage	Cap Beam Damage		Lateral Load (kips)
				North	South	
1	0.10	0.07				5.86
	-0.10	-0.06				-25.24
2	0.21	0.14				19.74
	-0.21	-0.15				-35.15
3	0.42	0.27	**Y1**			45.33
	-0.42	-0.32				-47.37
4	0.63	0.43				73.92
	-0.63	-0.5				-56.76
5	0.83	0.59				75.51
	-0.83	-0.67				-65.19
7	1.88	1.48	**G1**	**C1**		112.20
	-1.88	-1.62			**C1**	-82.60
8	2.50	2.08				116.30
	-2.50	-2.24				-80.31
10	3.75	3.3				123.00
	-3.75	-3.43				-84.62
11	5.00	4.58				115.50
	-5.00	-4.63				-87.71
13	7.50	7.08	**G2**	**C2**		117.40
	-7.50	-7.04			**C2**	-75.46
14	8.75	8.43	**BV**			115.60
	-8.75	-8.33			**U2**	-74.12
16	10.00	9.71		**U2**		113.40
	-10.00	-9.46			**U3**	-63.06
18	11.25	11.47		**U3**		80.11
	-11.25	-11.01				-47.42
20	12.50	12.96				58.08
	-12.50	-12.35				-22.00

Repair States

	No Repair Required
	Repair
	Full Replacement

5.4.2 Low Drift Cycles (0.0% - 2.0% Drift)

There was no observed damage to the specimen during the first two cycle levels. During the third cycle level, a hairline crack initiated circumferentially along the grout soffit-steel flange interface on both the North and South sides of the specimen. On the South side of the specimen, a circumferential hairline crack also initiated along the base of the soffit, at the grout-cap beam interface. Figures 5.16a and 5.16b show the initiation of cracking on the North and South sides of the specimen, respectively.

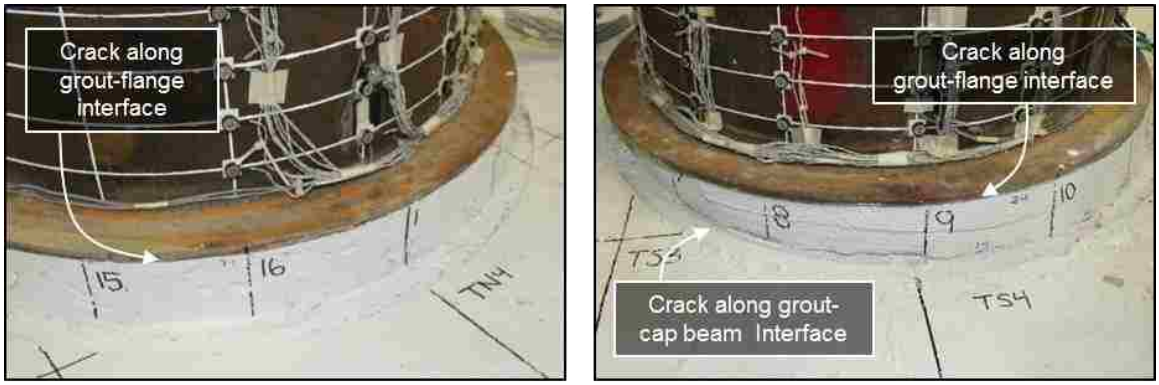

(a) (b)

Figure 5.16: WRC soffit cracking at 0.3% drift on the (a) North side of specimen, and (b) South side of specimen

The existing circumferential cracks along the grout soffit gradually widened with increasing drift levels. During the 7th drift set, the openings between the soffit and the flange on both the North and South sides of the column measured approximately 4-mm while they were each subjected to tensile loading. The cracks between the soffit and cap beam on the South side of the specimen increased to approximately 3-mm, while circumferential hairline cracks initiated at the base of the soffit on the North side of the specimen. Figures 5.17a and 5.17b show the increased soffit openings on the North and South sides of the specimen at 1.48% and 1.62% drift, respectively.

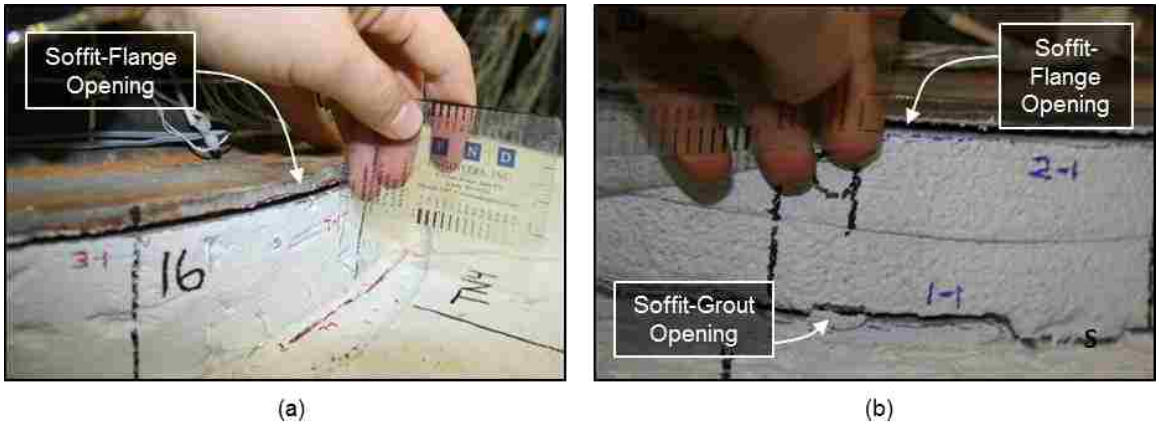

(a) (b)

Figure 5.17: WRC soffit openings on (a) North side of column at 1.48% drift, and (b) south side of column at 1.62% drift

During the same drift set, hairline cracks initiated radially in the grouted soffit, as well as in the cap beam. The cap beam cracks formed at approximate angles of 30-45° of one another, and continued vertically down the East and West faces of the cap beam. Figures 5.18a and 5.18b show the radial cap beam cracking on the North and South sides of the specimen, respectively.

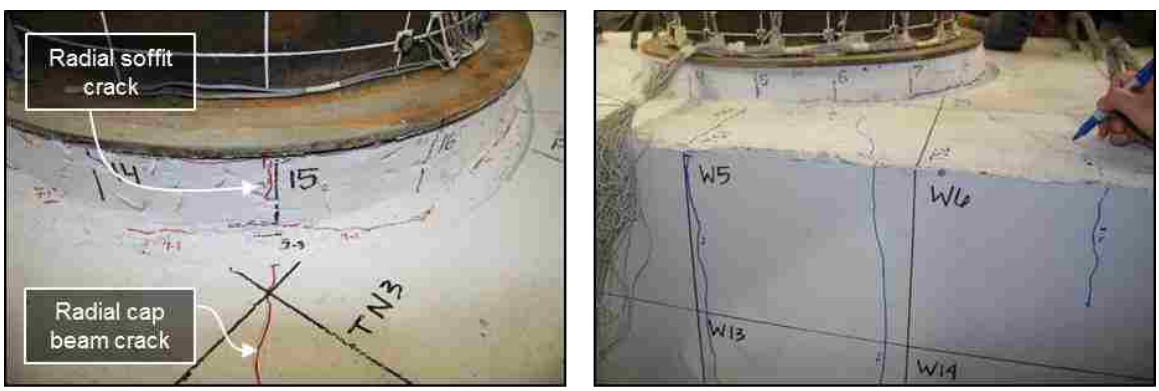

(a) (b)

Figure 5.18: WRC radial cracking on (a) North side of column at 1.48% drift, and (b) south side of column at 1.62% drift

5.4.3 Moderate to High Drift Cycles (2.0% - 8.0% Drift)

Additional cracks continued to initiate radially from the column as target drift levels increased. During the 8th cycle level, some of the existing radial cracks in both the cap

beam and grout pad were observed to have widened slightly, such that they were no longer hairline in width. In addition, the opening between the grout pad and the column flange increased to approximately 6 mm when the side of the specimen was in tension. Figure 5.19 shows this soffit-flange opening and increased grout pad crack width on the North side of the specimen as it was subject to 2.08% drift in the South direction.

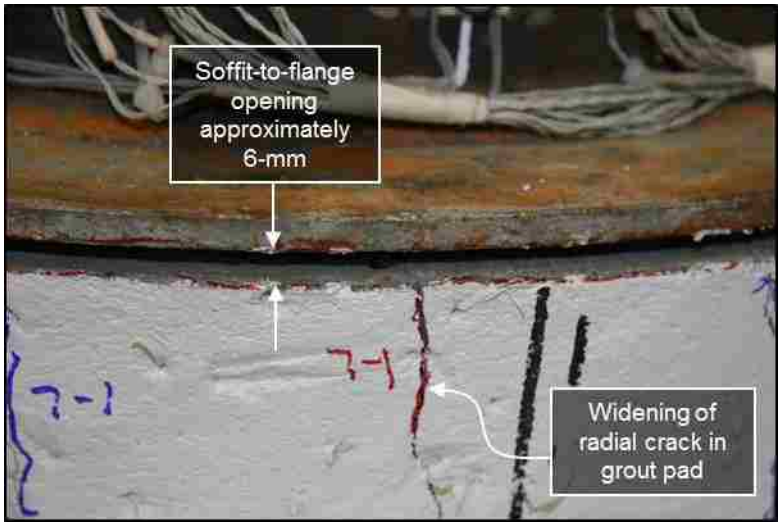

Figure 5.19: WRC North grout pad cracking at 2.08% drift

The column reached its maximum lateral load resistance of 123-kips as it was cycled to 3.30% drift in the South direction. At this drift level, the gap between the grout pad and the column flange increased to approximately 10-mm as each side was loaded into tension. In addition, the opening at the base of the grout pad on the South side of the specimen increased to approximately 5-mm under tensile loading. Additional hairline cracks developed radially on the top surface of the cap beam, as well as vertically down the East and West faces of the cap beam. Some of the existing cracks on the top surface of the cap beam widened to approximately 1-mm. Figure 5.20 shows the grout pad

openings and increased radial crack widths on the South side of the specimen at 3.43% drift in the North direction.

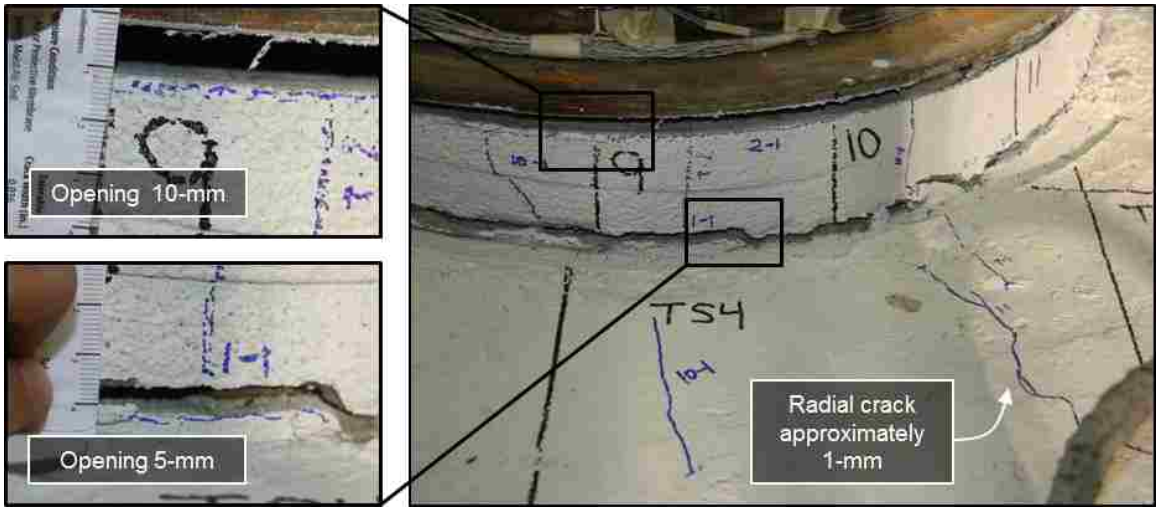

Figure 5.20: WRC South grout pad cracking at 3.43% drift North

After the cycle was complete and the column returned to zero drift, the widths of the residual soffit openings were measured. As shown in Figures 5.21a and 5.21b, both the North and South sides of the specimen had a residual soffit-flange opening of 2-mm. Similarly, the opening between the soffit and cap beam on the South side of the specimen had a residual width of approximately 1-mm, also shown in Figure 5.21b.

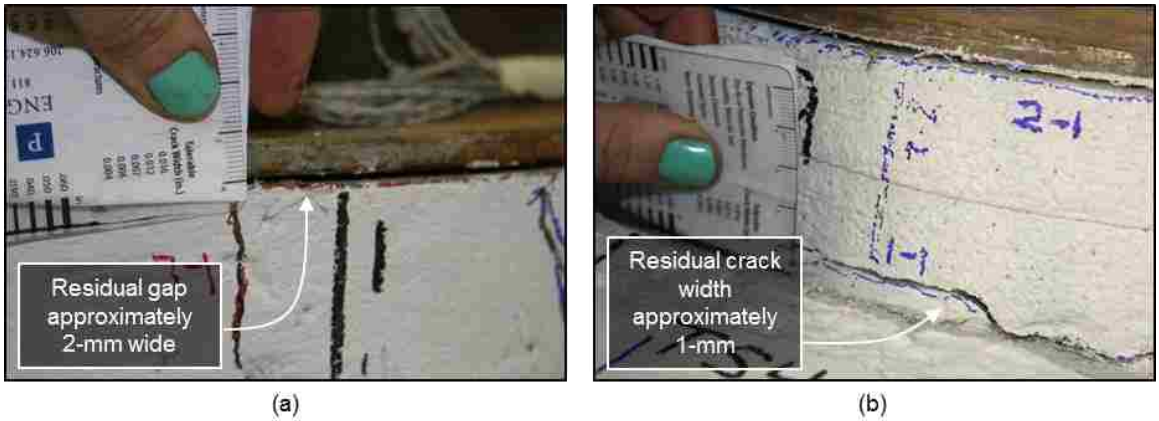

Figure 5.21: WRC Residual soffit openings after 10th load set (a) North side of column, and (b) south side of column

After the cycle was completed, it was also observed that the grout pad had deformed laterally from underneath the column flange. As shown in Figure 5.22, the width of the grout extending beyond the edge of the flange approximately 4-mm.

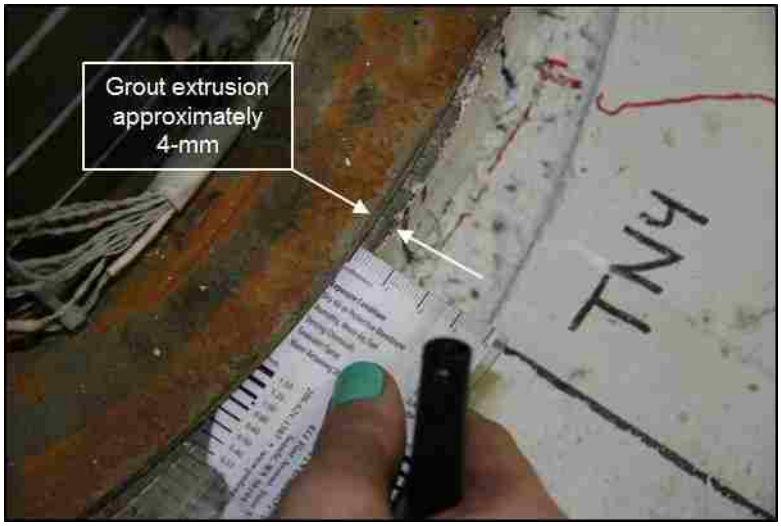

Figure 5.22: WRC residual grout extrusion after 10th load set

During the 11th cycle level, new hairline cracks developed radially from the column towards the rebar lifting loops located in the four corners of the cap beam, shown in Figures 5.23a and 5.23b.

(a) (b)

Figure 5.23: WRC cap beam cracking during the 11th cycle level (a) North side of specimen, (b) South side of specimen

During the 13th cycle level, a crack propagated radially from the column down the South face of the cap beam, as shown in Figure 5.24. At this point in testing, this was the only crack visible on the South face of the cap beam, and no cracks were visible on the North face.

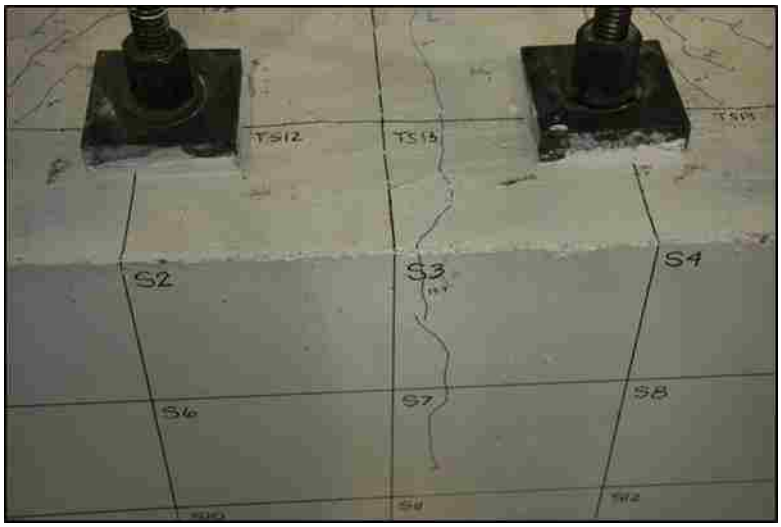

Figure 5.24: WRC cracking on South face of cap beam at 7.04% drift

During the same cycle level, several existing radial cracks in the cap beam increased in width to approximately 2-mm. The cracks that experienced this increase in width were primarily those strutting towards the rebar lifting loops, as shown in Figure 5.25.

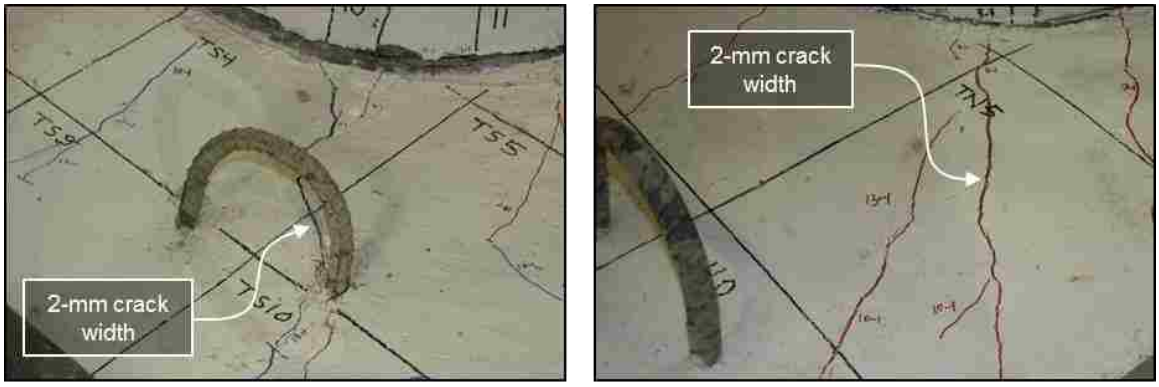

(a) (b)

Figure 5.25: WRC cap beam cracking on (a) South side of specimen, and (b) North side of specimen

During this cycle level, the widths of the radial cracks in the soffit increased to approximately 5-mm. The gap between the soffit and flange opened to 30-mm as the column approached peak drift. No reinforcing bars were visible at this point. Figure 5.26 shows the North side of the soffit while the column was subject to 7.08% drift in the South direction.

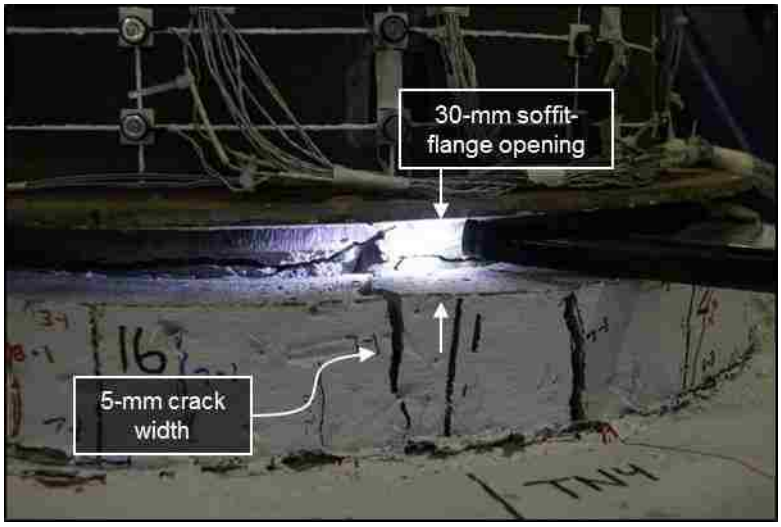

Figure 5.26: WRC North soffit cracking at 7.08% drift South

During the 14th cycle level, the gap between the soffit and the flange on the North side of the specimen increased to approximately 35-mm as the column was cycled to 8.43% drift in the South direction. At this point, the Northern-most reinforcing bar became visible between the soffit-flange opening, as shown in Figure 5.27.

Figure 5.27: WRC exposed reinforcing bar at 8.43% drift South

As the column was cycled to 8.33% drift in the North direction, the soffit-flange and soffit-cap beam openings on the South side of the specimen reached approximately 25-mm and 20-mm at peak loading, respectively, as shown in Figure 5.28. No reinforcing bars were currently visible on the South side of the specimen.

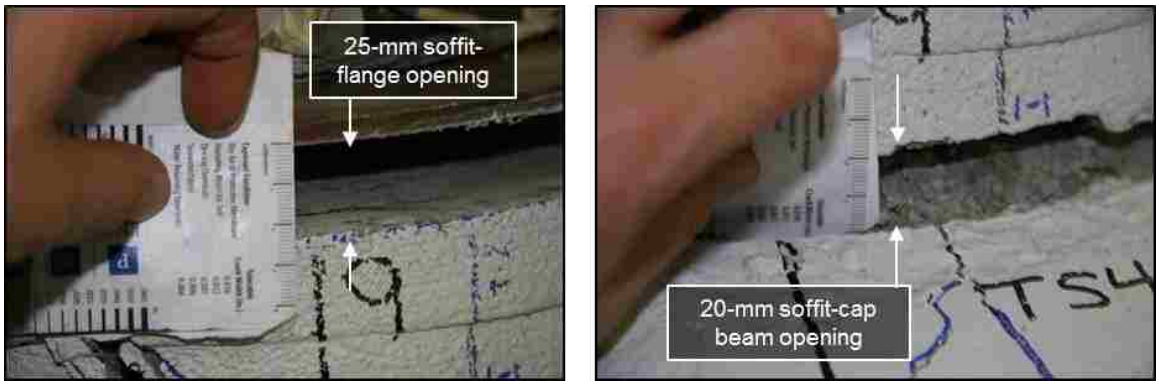

Figure 5.28: WRC South soffit openings at 8.33% drift North

At this point in the cycle, concrete uplift was observed at the South end of the cap beam. The uplift was approximately 5-mm in height, and it strutted between the corners of the two bearing plates where the Williams Rods anchored down the South end of the cap

beam, as shown in Figure 5.29. The lateral load resistance remained relatively stable throughout this cycle.

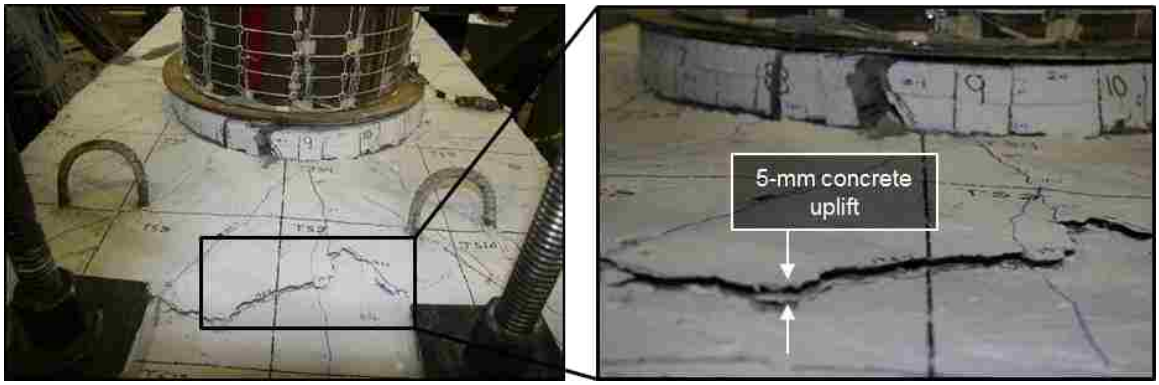

Figure 5.29: WRC South cap beam concrete uplift at 8.33% drift North

5.4.4 Specimen Failure (8.0% + Drift)

During the first cycle of the 16th cycle level, slight concrete uplift was noticed at the North end of the cap beam. Similar to the uplift that occurred in the previous cycle, this uplift also strutted between the two Williams Rods that anchored down the end of the cap beam. The uplift was approximately 2-mm in height, as shown in Figure 5.30a. In addition to this uplift, a significant increase in crack width was observed as the North end of the specimen was subject to tensile loading. Figure 5.30b shows a crack propagating from the Northern-most point on the column that increased to 3-mm in width during this cycle. At this point, the lateral load resistance of the column dropped to 90.87-kips; a 26% decrease from the column's maximum resistance.

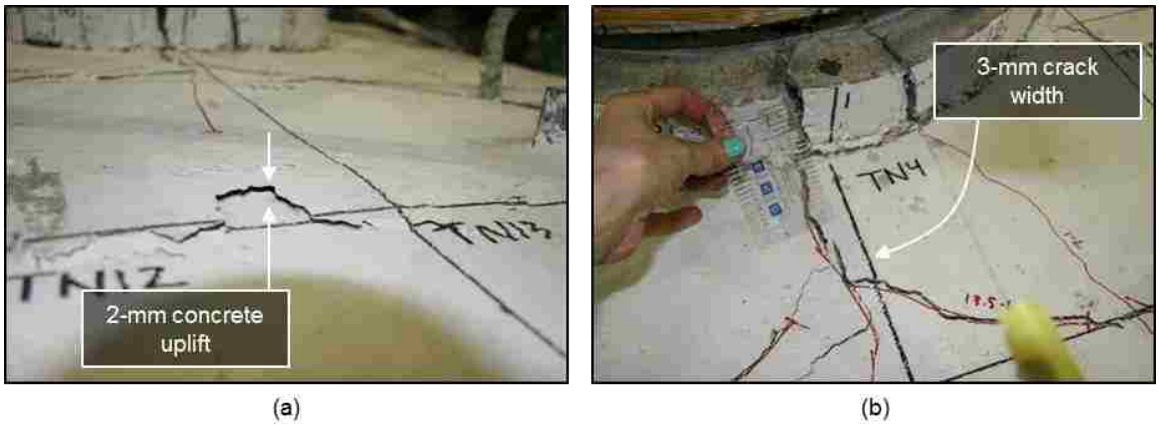

Figure 5.30: WRC North cap beam damage at 9.71% drift South (Cycle 1)

As the South end of the specimen was cycled into tensile loading, the gap between the flange and the soffit exposed the Southern-most reinforcing bar. In addition, the existing uplift at the South end of the cap beam increased from 5-mm to approximately 10-mm in height, as shown in Figure 5.31.

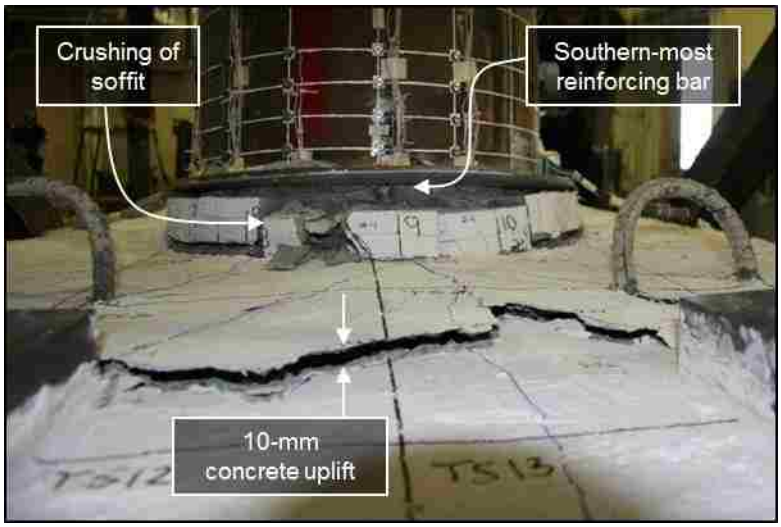

Figure 5.31: WRC South cap beam damage at 9.46% drift North

During the second cycle of the same drift set, the existing uplift at the North end of the specimen increased from 2-mm to approximately 5-mm in height, and propagated to the other side of the William Rod anchors. Figure 5.32 shows the propagation of uplift on the

outside of the NE Williams Rod, as well as the existing 5-mm uplift strutting between the two Williams Rods. The existing uplift at the South end of the cap beam increased to just over 10-mm as it was subjected to its second tension loading cycle during this drift set.

Figure 5.32: WRC North cap beam uplift at 9.71% drift South (Cycle 2)

During the 18th cycle level, there was a significant increase in cap beam damage. Figure 5.33 shows the damage on the North side of the specimen as it was subject to 11.47% drift in the South direction. As shown in Figure 5.33, the existing uplift strutting between the two North Williams Rod anchors increased from 5-mm to just over 10-mm. The existing cracks that propagated through the NE and NW rebar lifting loops increased in width to nearly 10-mm towards the edge of the cap beam. At this point, the lateral load resistance of the column had dropped to 80.1-kips; a 35% decrease compared to the column's maximum lateral load.

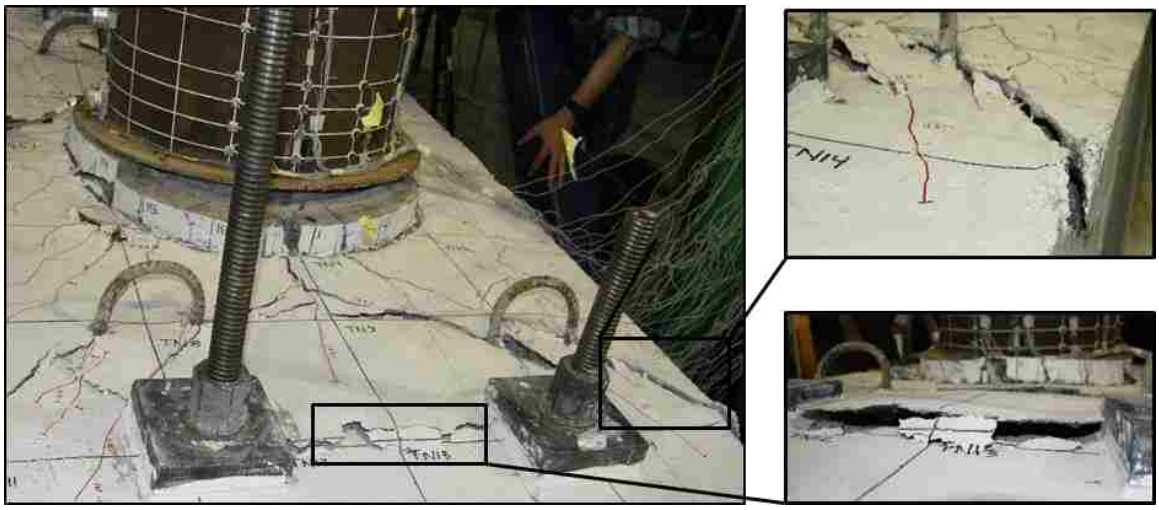

Figure 5.33: WRC North cap beam damage at 11.47% drift South

On the opposite side of the specimen, there was an increase in soffit crushing. Figure 5.34 shows the South side of the soffit as it was subject to compression at 11.47% drift.

Figure 5.34: WRC South soffit damage at 11.47% drift South

As the specimen cycled to 11.01% drift in the North direction, similar damage was observed to the South end of the specimen. The existing cracks strutting to the South rebar lifting loops increased in width to approximately 10-mm, similar to those on the North side of the specimen. The existing uplift strutting between the two South Williams

Rods remained at just over 10-mm in height. This uplift and cap beam cracking through the rebar lifting loops is shown in Figures 5.35a and 5.35b, respectively.

Figure 5.35: WRC South cap beam (a) uplift and (b) cracking at 11.01% drift North

After the previous drift set, the specimen was subject to one final cycle prior to termination. The specimen was cycled to 12.96% drift in the South direction, and 12.35% drift in the North direction. Due to a significant reducing in lateral load resistance, the test was terminated after this cycle. Figures 5.36a and 5.36b show the cap beam damage on the North and South sides of the specimen after the final cycle.

Figure 5.36: WRC (a) North, and (b) South cap beam damage after test termination

As shown in Figures 5.36a and 5.36b, failure of the specimen consisted of significant grout crushing, concrete cracking and uplift, with no reinforcing bar fracture.

5.5 SPECIMEN WRCUB

Specimen WRCUB consisted of a 20-in. diameter CFT column connected to a precast RC cap beam via 8 No. 9 longitudinal headed reinforcing bars that were partially debonded from the surrounding concrete. The reinforcing bars were welded to the inside of the column, and extended 14-in. ($12d_b$) into the cap beam. The purpose of testing this specimen was to compare its behavior to Specimen WRC, which had fully bonded reinforcing bars. Figure 5.37 shows the WRCUB connection detail.

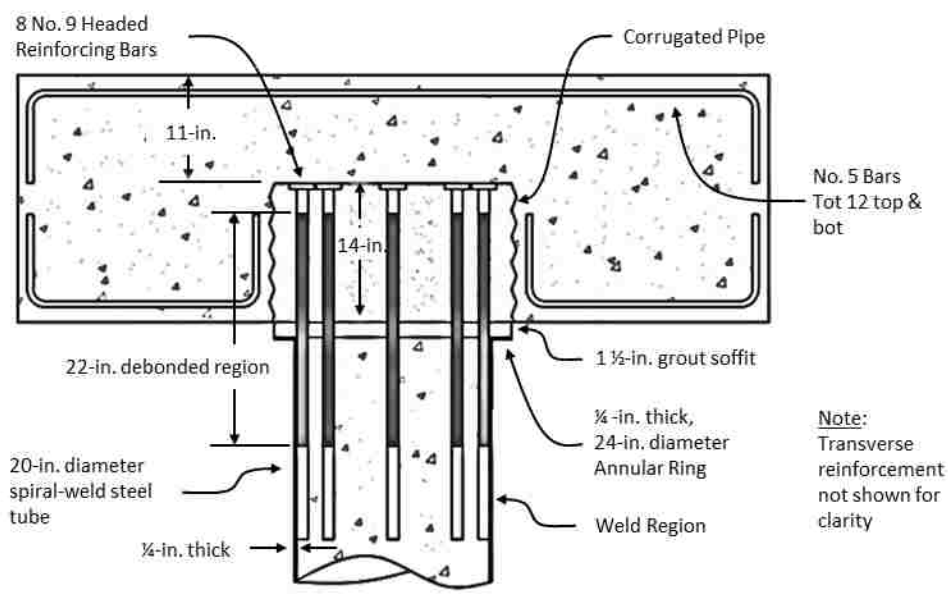

Figure 5.37: WRCUB Connection Detail

Specimen WRCUB was subjected to a constant axial load of 350-kips, as well as a cyclic, displacement-controlled lateral load following the load protocol outlined in Table 5.2. The actual drift history achieved during testing is summarized in Table 5.8.

The behavior of the specimen consisted of yielding of the reinforcing bars, followed by crushing of the grouted soffit region. Failure of the specimen consisted of fracture of two reinforcing bars at the North side of the column, with concrete uplift at the South end of the cap beam. The moment-drift response of the specimen, with noted damage states, is shown in Figure 5.38. The dashed line represents the plastic moment capacity of the CFT, calculated using the PSDM method with specified design strengths.

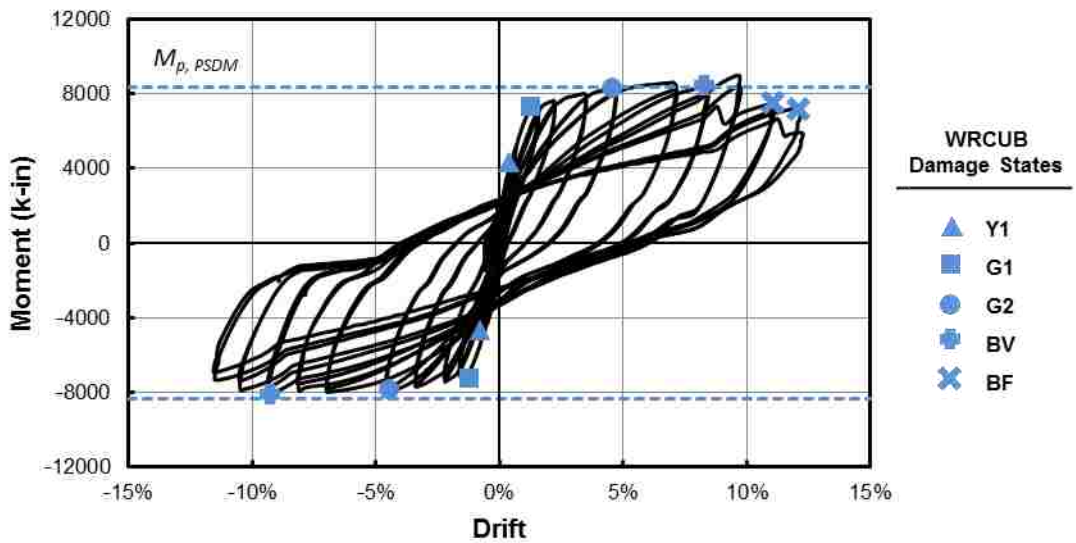

Figure 5.38: WRCUB Moment-drift response

5.5.1 WRCUB Performance State Summary

Table 5.8 summarizes the progression of damage that was observed to the column and cap beam during testing, as well as the magnitude of repair that would be required at each damage state. As shown in the table, failure of the specimen consisted of bar fracture at 11.07% drift, with uplift in the South side of the cap beam. The proceeding section provides a detailed description of the damage progression, and will refer to the damage state progression table.

Table 5.8: WRCUB Damage State Progression Table

Set No.	Target Drift (%)	Actual Drift (%)	Column	Cap Beam		Lateral Load (kips)
				North	South	
1	0.10	0.07				16.9
	-0.10	-0.09				-16.6
2	0.21	0.13				31.7
	-0.21	-0.16				-32.1
3	0.42	0.31	**Y1**			48.1
	-0.42	-0.34				-48.0
4	0.63	0.48				59.0
	-0.63	-0.52				-57.9
5	0.83	0.65				68.0
	-0.83	-0.69				-66.8
7	1.88	1.58	**G1**	**C1**		92.7
	-1.88	-1.63			**C1**	-88.6
8	2.50	2.24				96.7
	-2.50	-2.24				-93.7
10	3.75	3.51				97.0
	-3.75	-3.42				-92.8
11	5.00	4.72	**G2**			96.3
	-5.00	-4.62				-91.7
13	7.50	7.17	**BV (PVC)**			93.4
	-7.50	-7.00				-83.3
14	8.75	8.46	**BV**			84.1
	-8.75	-8.19			**C2**	-76.6
16	10.00	9.76				85.0
	-10.00	-9.39				-74.0
18	11.25	11.07	**BF**	**C2**		64.8
	-11.25	-10.53			**U1**	-66.4
20	12.50	12.27				51.6
	-12.50	-11.58			**U2**	-55.4

Repair States

	No Repair Required
	Repair
	Full Replacement

5.5.2 Low Drift Cycles (0.0% - 2.0% Drift)

There was no cracking observed in the cap beam or grout region until the second set of loading. At .16% drift to the North, a circumferential hairline crack formed at the soffit-cap beam interface on the South side of specimen. A similar circumferential crack initiated on the North side of the soffit as the specimen was subjected to 1.58% drift in South direction. At this drift level, radial hairline cracking was observed in the grouted soffit region, as well as in the cap beam. The cap beam cracks initiated radially from the grout region, and propagated vertically and diagonally down the East and West sides of the cap beam. As the column cycled back and forth, an opening formed between the soffit and the annular ring on the side of the specimen subjected to tensile loading. During this cycle level, this gap opened to approximately 5 mm, as shown in Figure 5.39.

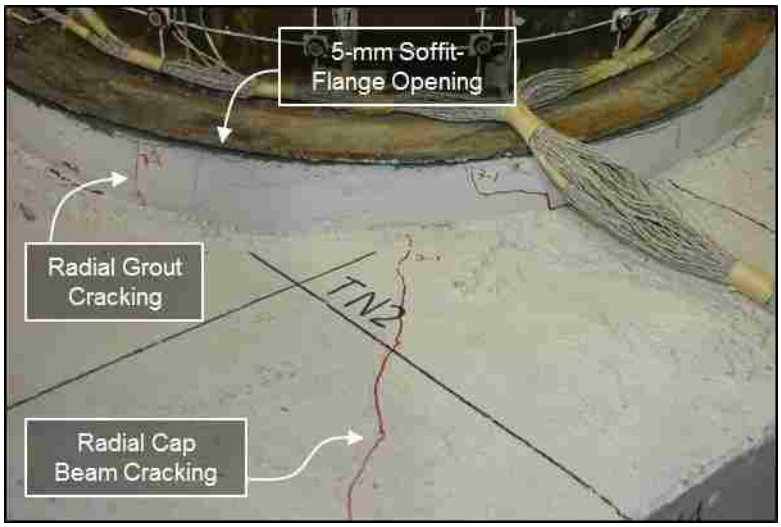

Figure 5.39: WRCUB North cap beam damage at 1.58% drift South

5.5.3 Moderate to High Drift Cycles (2.0% - 11.0% Drift)

As drift levels increased, new radial cracks continued to develop throughout the grout pad and the cap beam. While the majority of them remained hairline in width for several

proceeding cycles, a few of the cracks increased slightly in width during the 8th drift set. At 2.24% drift to the South, the cracks propagating in the NE and NW directions increased to approximately 0.5-mm in width, as shown in Figure 5.40b. At this point, the opening between the soffit and the flange on the North side of the specimen reached approximately 10-mm as it was subjected to peak tensile loading, as shown in Figure 5.40a.

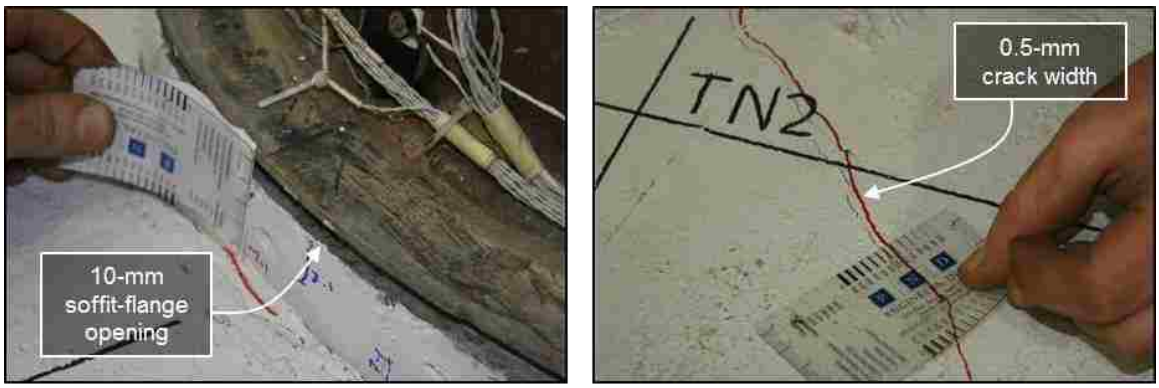

(a) (b)

Figure 5.40: WRCUB North (a) soffit-flange opening, and (b) cap beam crack widths at 2.24% drift South

During the 10th cycle level, the maximum lateral load resistance of the specimen was reached. The maximum load was 97.03-kips, and it occurred as the column was pushed to 3.51% drift in the South direction. At this drift, the opening between the soffit and steel flange on the North side of the specimen reached approximately 13-mm in height, as shown in Figure 5.41. During this drift set, new hairline cracks initiated along the top surface and East and West faces of the cap beam, and the radial cracks in the soffit region increased to approximately 1-mm in width.

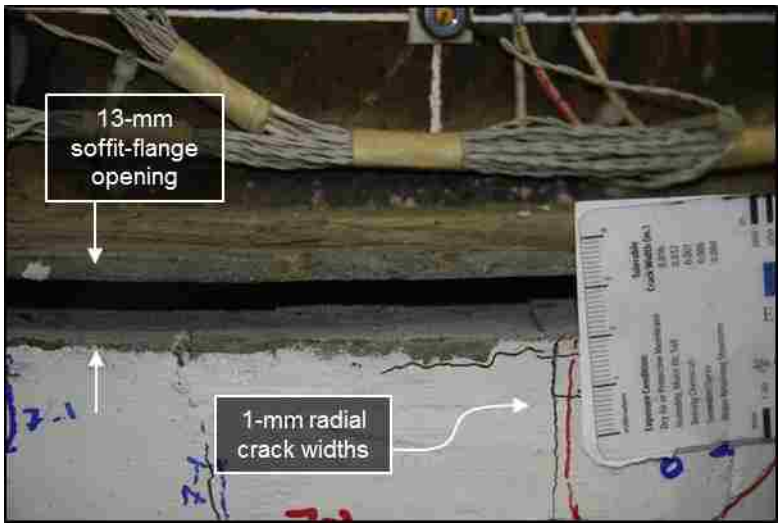

Figure 5.41: WRCUB North soffit-flange opening at 3.51% drift South

In the following cycle level, the column was cycled to 4.72% drift in the South direction, and 4.62% drift in the North direction. At this point, the opening between the grout and the soffit increased to approximately 18-mm at peak loading, as shown in Figure 5.42a. On the opposite side of the specimen, crushing of the grout pad was observed, as shown in Figure 5.42b. There was no new cracking observed in the cap beam during this cycle level.

Figure 5.42: WRCUB (a) soffit-flange opening, and (b) grout crushing at 4.72% drift South

During the 13th cycle level, the opening between the soffit and the annular ring reached approximately 30-mm at peak tensile loading, exposing the PVC pipes that encased the three Northern-most longitudinal reinforcing bars. Figure 5.43 shows the exposed PVC pipes on the North side of the specimen as it was subjected to 7.17% drift to the South.

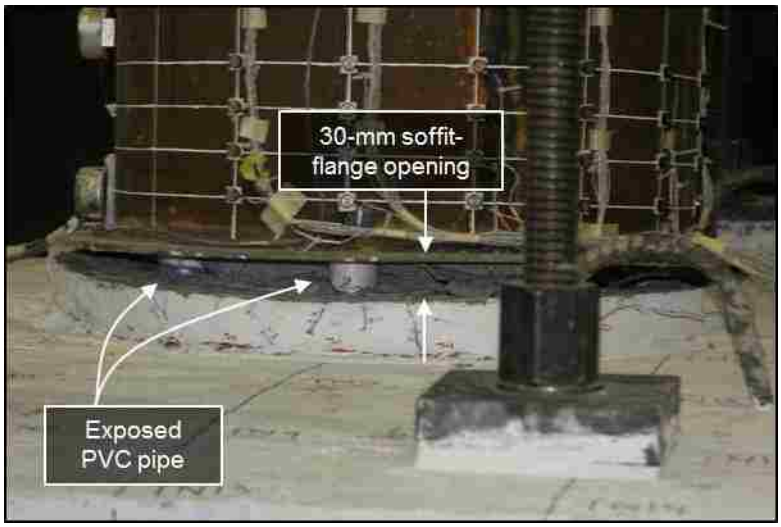

Figure 5.43: WRC North soffit opening at 7.17% drift South

After the cycle was complete and the column returned to zero drift, the widths of the residual soffit-flange openings and lateral grout extrusions were measured. As shown in Figure 5.44a, the grout extended approximately 16-mm from underneath the edge of the annular ring. The residual gap between the flange and the soffit was approximately 11-mm, as shown in Figure 5.44b.

(a) (b)

Figure 5.44: WRCUB (a) grout extrusion, and (b) residual soffit-flange opening after 13th cycle level

During the 14th cycle level, new hairline cracks initiated radially form the column, as well as down the East and West faces of the cap beam. Additionally, an increase in cap beam crack width was observed as the South side of the specimen was subject to tensile loading, specifically in the regions where cracks strutted from the column towards the two Southern rebar lifting loops. Figure 5.45a shows a crack of approximately 2-mm in width strutting towards the SE rebar lifting loop as the column was subjected to 8.19% drift in the North direction. At this same drift, the Southern-most reinforcing bar became exposed from within the PVC, as shown in Figure 5.45b.

(a) (b)

Figure 5.45: WRCUB South (a) cap beam cracking, and (b) exposed reinforcing bar at 8.19% drift North

As the North side of the specimen was subjected to tensile loading during the 16th load set, the opening between the soffit and the annular ring increased to approximately 45-mm. the PVC encasing the reinforcing bars had split open, such that the three Northern-most reinforcing bars were now visible, as shown in Figure 5.46. At this point, the lateral load resistance reached at peak drift had decreased by approximately 20% compared to the maximum load reached at 3.51% drift.

Figure 5.46: WRCUB North exposed reinforcing bars at 9.76% drift South

5.5.4 Specimen Failure (11.0%+ Drift)

As the column was first displaced to 11.07% drift in the South direction, reinforcing bar fracture was heard. The opening between the soffit and the annular ring on the North side of the specimen was approximately 55-mm in height, but the location of the reinforcing bar fracture could not yet be seen. At this point in testing, the lateral load resistance of the specimen was 64.8-kips; a 33% decrease from its maximum resistance. Figure 5.47a shows the soffit-flange opening on the North side of the specimen at the time of bar fracture. As the column was sequentially cycled to 10.53% drift in North direction, initial

uplift was observed at the South end of the cap beam. The uplift was approximately 2-mm in height, and it strutted between the South Williams Rods and lifting loops, as shown in Figure 5.47b.

(a) (b)

Figure 5.47: WRCUB (a) Soffit-flange opening at first bar fracture, and (b) South concrete uplift at 10.53% drift North

During the following load set, the location of the existing bar fracture became visible as the North side of the column was cycled into tensile loading. As anticipated, the fracture occurred on the Northern-most reinforcing bar within the soffit region, shown in Figure 5.48a. As the column approached peak drift, fracture of a second reinforcing bar was heard at the North end of the column. The location of the second fracture was not visible. At this point, the lateral load resistance of the specimen was 51.6-kips; a 46% decrease from the maximum lateral load of 97-kips. Figure 5.48b shows the limited damage state of the North side of the cap beam at this drift level.

(a) (b)

Figure 5.48: WRCUB (a) North bar fracture, and (b) North cap beam damage at 12.27% drift South

As the South side of the specimen was cycled into tensile loading, significant crack widening was observed in the cracks strutting from the grout pad to the Southern reinforcing lifting loops, shown in Figure 5.49. An increase in concrete uplift height was also observed near the Southwest Williams anchor rod. No uplift was observed in the North side of the cap beam.

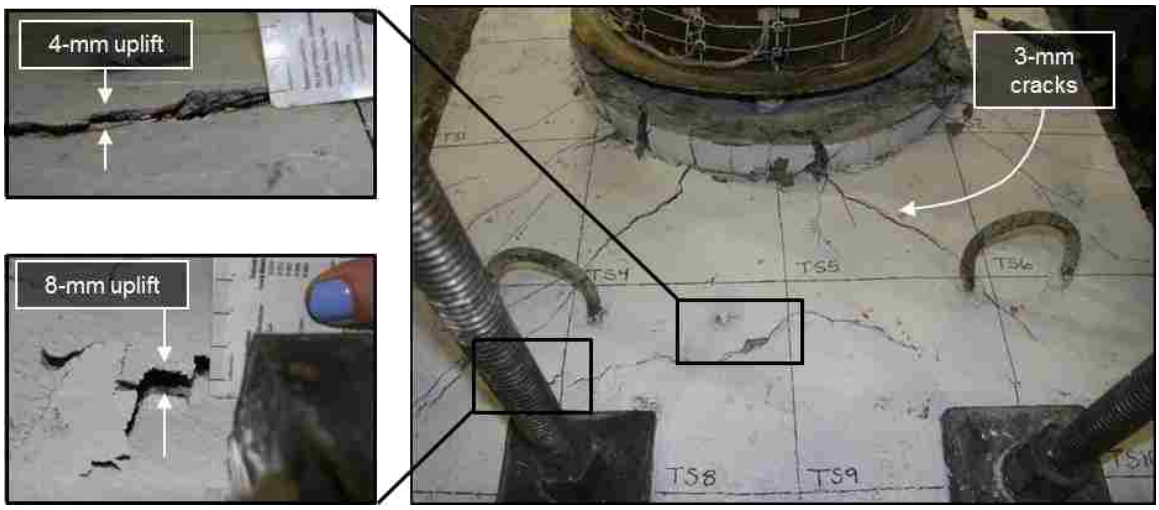

Figure 5.49: WRCUB South cap beam damage at 11.58% drift North

5.6 SPECIMEN RC

Specimen RC consisted of a typical RC connection, in which 8 No. 9 longitudinal reinforcing bars with transverse reinforcing extended from the CFT column into the cap beam. A 1-in. cover was provided between the longitudinal reinforcing bars and the inside of the steel tube. Figure 5.50 shows the RC connection detail. The purpose of testing this specimen was to compare its behavior to the WRC specimens, as this connection detail is standard practice in the state of Alaska.

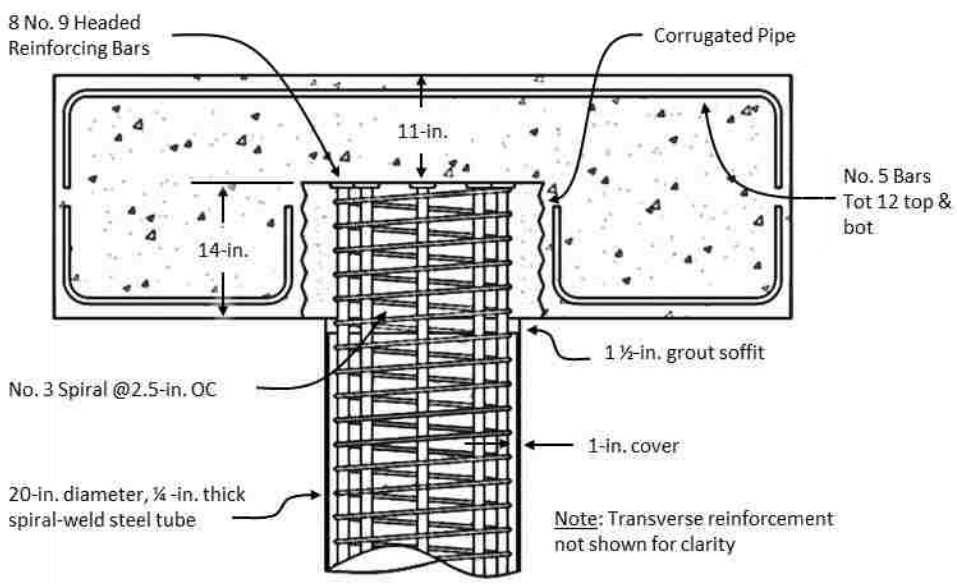

Figure 5.50: RC Connection Detail

Specimen RC was subjected to a constant axial load of 350-kips, as well as a cyclic, displacement-controlled lateral load following the load protocol outlined in Table 5.2. The actual drift history achieved during testing is summarized in Table 5.9.

The behavior of the specimen consisted of yielding of the reinforcing bars, followed by crushing of the grouted soffit region. Failure of the specimen consisted of fracture of six reinforcing bars, with slight concrete uplift at the North and South ends of the cap beam. The moment-drift response of the specimen, with noted damage states, is shown in Figure 5.51. The dashed line represents the plastic moment capacity of the CFT, calculated using the PSDM method with specified design strengths.

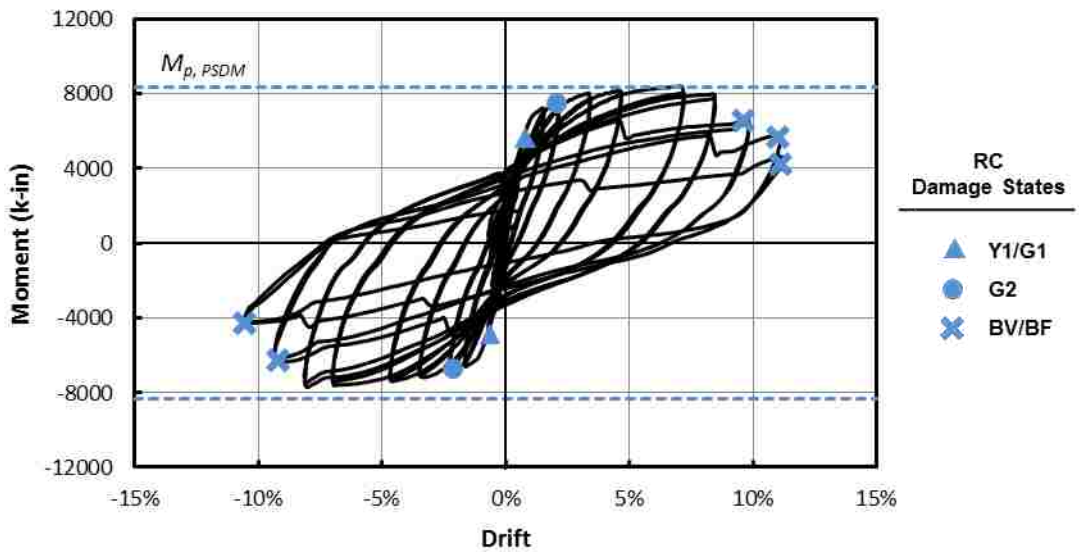

Figure 5.51: RC Moment-Drift Behavior

5.6.1 RC Performance State Summary

Table 5.9 summarizes the damage that was observed to the column and cap beam during testing, as well as the magnitude of repair required at each damage state. As shown in the table, failure of the specimen consisted of bar fracture at 9.83% drift, with slight concrete uplift observed on the North and South sides of the cap beam at 8.46% and 4.70% drift, respectively. The proceeding section provides a detailed description of the damage progression, and will refer to the damage state progression table.

Table 5.9: RC Damage State Progression Table

Set No.	Target Drift (%)	Actual Drift (%)	Column	Cap Beam		Lateral Load (kips)
				North	South	
1	0.10	0.04				23.1
	-0.10	-0.08				-12.7
2	0.21	0.12				35.5
	-0.21	-0.16				-25.9
3	0.42	0.28	**Y1, G1**			50.7
	-0.42	-0.33				-40.3
4	0.63	0.44				60.4
	-0.63	-0.51				-51.0
5	0.83	0.62				69.8
	-0.83	-0.70				-61.1
7	1.88	1.54		**C1**		94.3
	-1.88	-1.67			**C1**	-85.0
8	2.50	2.14	**G2**			96.1
	-2.50	-2.27				-86.4
10	3.75	3.42				97.5
	-3.75	-3.50				-86.2
11	5.00	4.67				94.7
	-5.00	-4.70			**U1**	-83.8
13	7.50	7.20				91.0
	-7.50	-7.02				-80.3
14	8.75	8.46		**U1**		80.4
	-8.75	-8.15	**BV (Trans.)**			-74.3
16	10.00	9.83	**BV / BF**			72.0
	-10.00	-9.40				-55.7
18	11.25	11.19				37.7
	-11.25	-10.57				-21.2

Repair States

	No Repair Required
	Repair
	Full Replacement

5.6.2 Low Drift Cycles (0.0% - 2.0% Drift)

There was no observed damage to the specimen during the first two cycle levels. At .28% drift, slight cracking and flaking was observed in the grouted soffit region. The pieces of grout that spalled off were approximately 1/16 – 1/8-in. thick, as shown in Figure 5.52a. At .44% drift, circumferential cracks formed on the North and South sides of the specimen, along the soffit-steel tube and soffit-cap beam interfaces, as shown in Figure 5.52b.

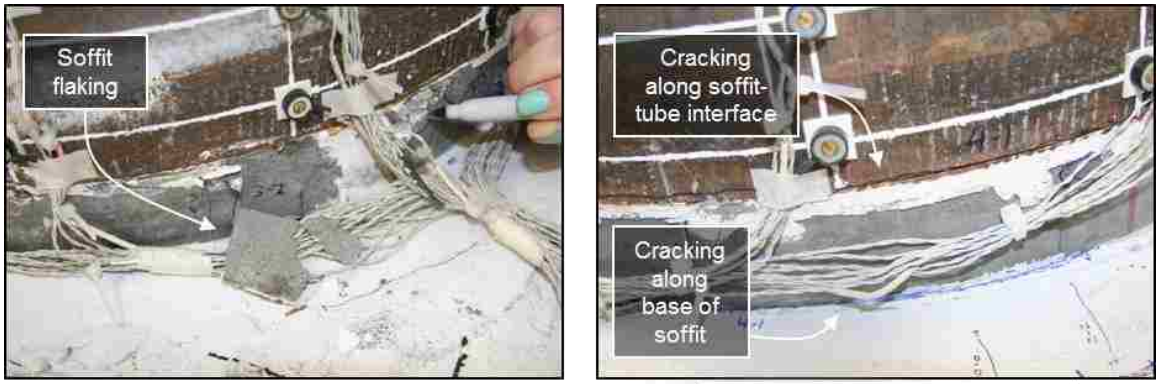

(a) (b)

Figure 5.52: WRC (a) Soffit spalling at .28% drift, and (b) Soffit cracking at .44% drift

As the drift levels increased, the widths of the circumferential cracks along the top and bottom of the soffit gradually increased on the side of the specimen subject to tensile loading. During the 7th cycle level, these circumferential cracks along the soffit-steel tube and soffit-cap beam interfaces opened to approximately 1.5-mm and 1-mm, respectively.

During the same cycle level, circumferential hairline cracks began to initiate at the location where the corrugated pipe separates the grout from the concrete cap beam, as shown in Figure 5.53. Additionally, hairline cracks began to initiate radially from the column, continuing vertically down the East and West faces of the cap beam. Figure 5.53

shows radial cracking on the South side of the cap beam as the column was loaded to 1.67% drift in the North direction.

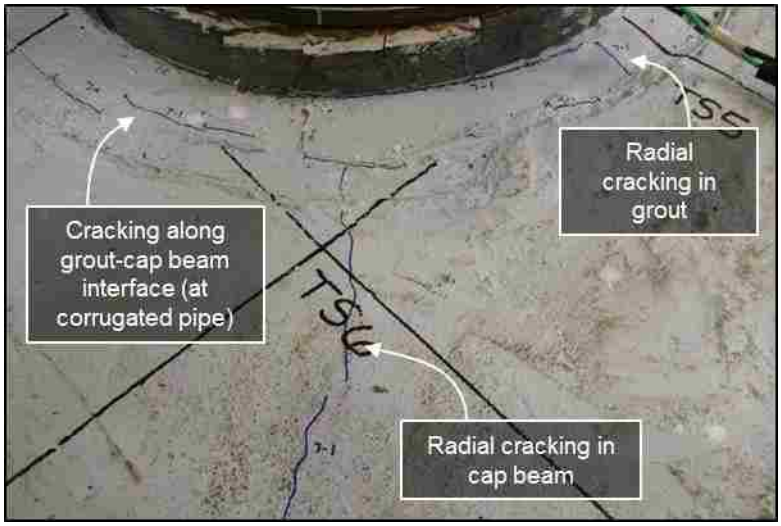

Figure 5.53: WRC South cap beam cracking at 1.67% drift North

5.6.3 Moderate to High Drift Cycles (2.0% - 9.0% Drift)

During the 8th cycle level, crushing of the grouted soffit was observed as each side was subjected to compressive loading. Figures 5.54a and 5.54b show the crushing on the North and South sides of the soffit, respectively. During this cycle level, hairline cracks continued to develop radially in the grouted region, as well as along the top surface and East and West faces of the cap beam. These cracks remained hairline in width for several proceeding cycles.

Figure 5.54: WRC Soffit crushing (a) North side of specimen, (b) South side of specimen

The column reached its maximum lateral load resistance during the 10th cycle level. The peak load was 97.54-kips, and it occurred as the column was first cycled to 3.42% drift in the South direction.

By the 11th cycle level, the openings between the soffit and the column had increased to approximately 10-mm while subject to tensile loading. Figure 5.55 shows the soffit-column opening on the North side of the specimen as it is subject to 4.67% drift in the South direction.

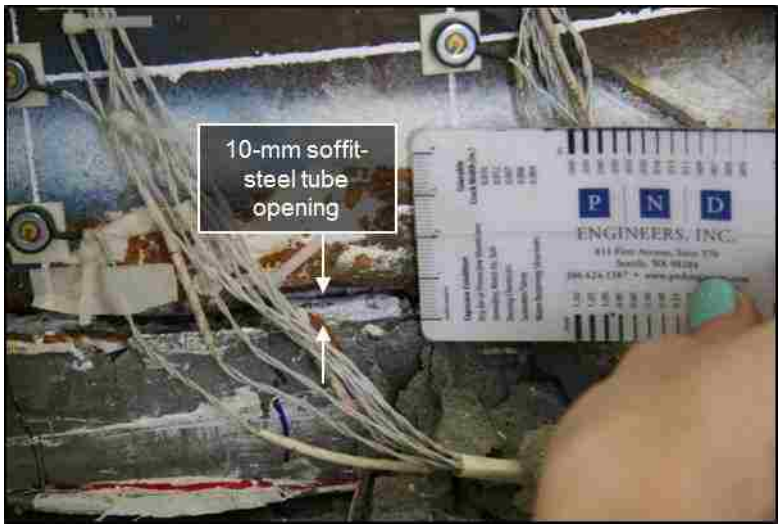

Figure 5.55: WRC North soffit-tube opening at 4.67% drift South

During this cycle level, slight surface uplift of the grouted region was observed between the soffit and the cap beam on the South side of the specimen, as shown in Figure 5.56a. Additionally, slight concrete uplift was also observed in the South side of the cap beam, just outside of the grouted region. The uplift was approximately 1-mm in height and 5-in. in length, as shown in Figure 5.56b.

Figure 5.56: WRC initial uplift in (a) South grout region, and (b) South cap beam

During the 13th cycle level, slight crack widening was observed in cracks propagating radially in the NE, NW, SE, & SW directions. The widths of these cracks ranged between .8-mm and 1-mm, as shown in Figure 5.57a**.** Additional uplift was observed in the South grouted region, towards the grout-concrete interface, as shown in Figure 5.57b. During the second cycle of this cycle level, the lateral load resistance of the column had dropped to 82.8-kips; a 15% decrease from the maximum lateral load.

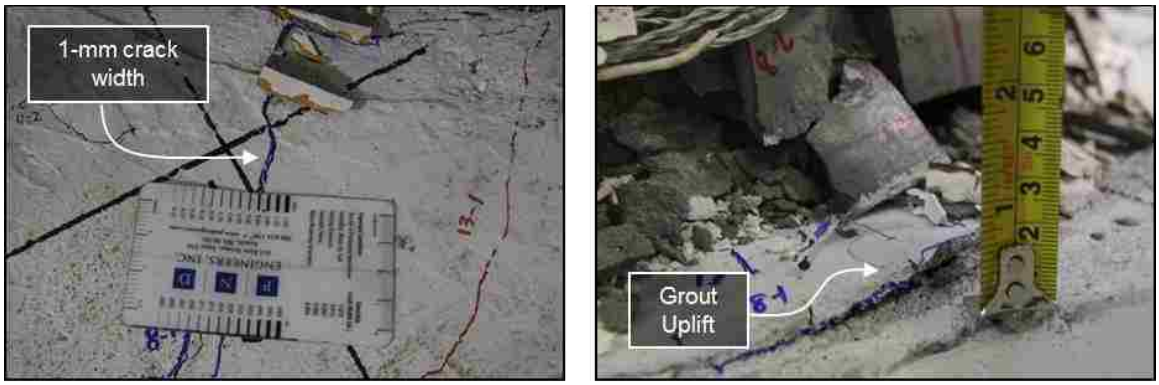

(a) (b)

Figure 5.57: RC (a) Cap beam crack widening, and (b) South grout uplift at 7.02% drift North

During the 14th cycle level, the column was cycled to 8.46% drift in the South direction, followed by 8.15% drift in the North direction. As the column approached peak drift in the North direction, the transverse spiral reinforcing on the South side of the column became exposed through the soffit-steel tube opening. As shown in Figure 5.58a, the spiral began to bend around the longitudinal reinforcing bars, such that it formed an octagonal shape. On the opposite side of the specimen, slight concrete uplift was observed in the cap beam just outside of the grouted region, as shown in Figure 5.58b.

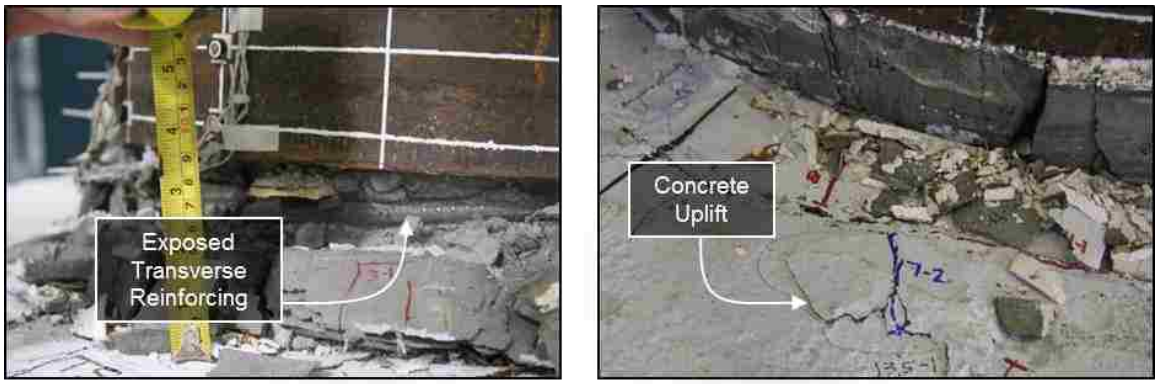

(a) (b)

Figure 5.58: WRC (a) South transverse reinforcing, and (b) North concrete uplift at 8.15% drift

5.6.4 Specimen Failure (9.0%+ Drift)

During the 16th cycle level, the opening between the soffit and steel tube increased such that the transverse reinforcing on the North side of the specimen became exposed as it was subjected to tensile loading. At peak drift, fracture of the Northern-most reinforcing bar was heard, but the location of the fracture was not yet visible. At this point, the lateral load resistance of the column had dropped to 54.5-kips; a 44% decrease compared to its maximum lateral load.

As the South side of the specimen was cycled to tensile loading, subsequent fracture occurred in the Southern-most reinforcing bar. Figure 5.59a shows the reinforcing bar fracture as the column is loaded to 9.40% drift in the North direction. At this point, the existing concrete uplift at the South side of the cap beam propagated to approximately 8-in. in length, as shown in Figure 5.59b.

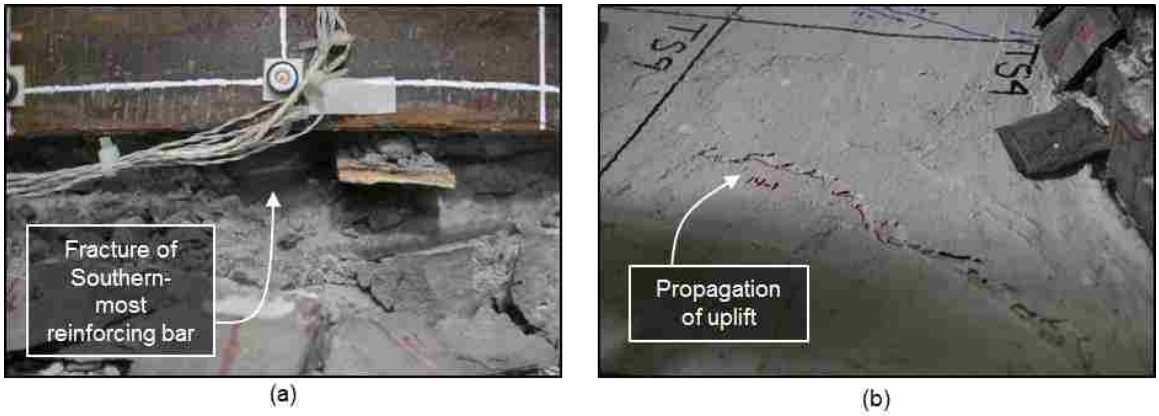

Figure 5.59: WRC South (a) reinforcing bar fracture, and (b) Cap beam concrete uplift at 9.40% drift North

In the cycle level, the NE, NW, SE and SW reinforcing bars fractured as they were each respectively subjected to tensile loading. As the reinforcing bars fractured, the lateral load resistance of the column continued to drop dramatically. Figure 5.60 shows the North &

South sides of the specimen at the final drift state after the reinforcing bars fractured. No additional damage to the cap beam was observed at this drift state.

(a) (b)

Figure 5.60: WRC Reinforcing bar fractures (a) North, and (b) South

After the last cycle was complete, the spalled grout pieces were removed from the specimen for closer inspection of the reinforcing bars. Figures 5.61a and 5.61b show the North and South sides of the specimen after the grout had been removed.

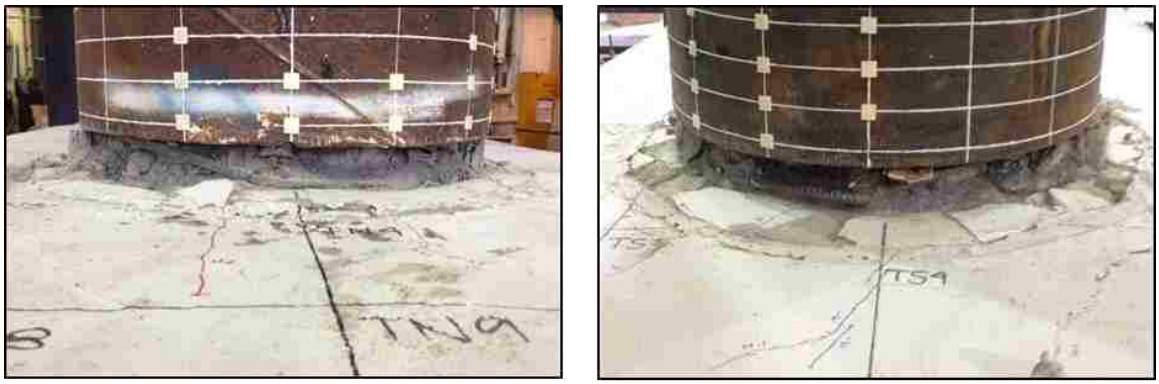

(a) (b)

Figure 5.61: WRC(a) North and (b) South side of specimen after removal of spalled grout

5.7 SPECIMEN EMB96

Specimen EMB96 consisted of a 24-in. diameter straight-seam CFT embedded 20.75-in. (.9D) into a precast reinforced concrete cap beam, as shown in Figure 5.62. The thickness of the steel tube was ¼-in, resulting in a diameter-to-thickness (D/t) ratio of 96. The purpose of testing this specimen was to evaluate the performance of the connection and cap beam using a straight-seam tube, as opposed to the spiral-welded tube used in Specimen EMB80.

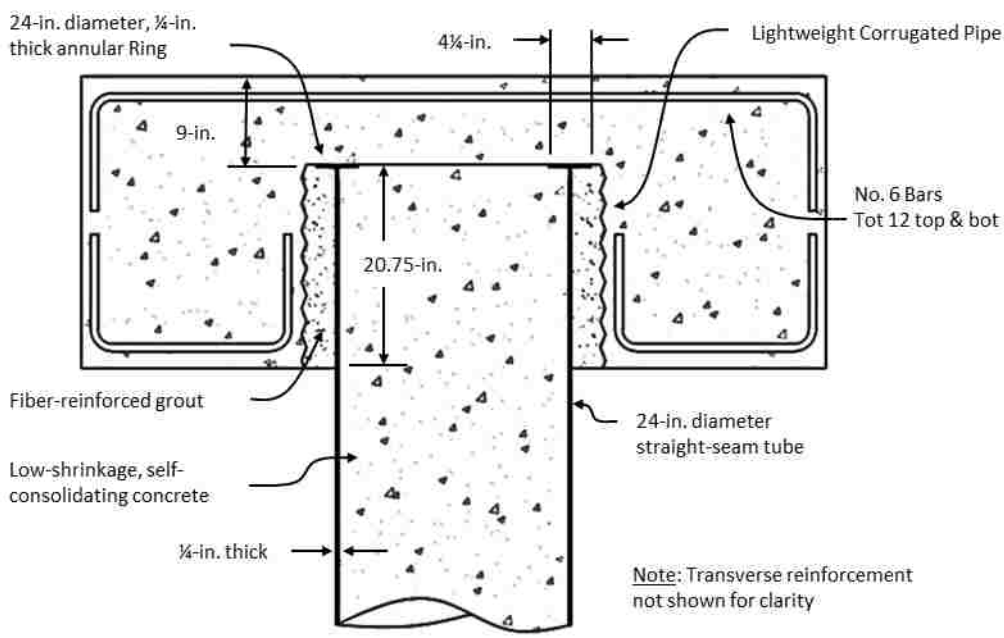

Figure 5.62: EMB96 Connection Detail

Specimen EMB96 was subjected to a constant axial load equal to 5% of its gross compressive capacity, as well as a cyclic, displacement-controlled lateral load following the load protocol outlined in Table 5.2. The actual drift history achieved during testing is summarized in Table 5.10.

The general behavior of the specimen consisted of yielding of the steel tube, followed by local buckling at the base of the column. Failure consisted of subsequent ductile tearing at the apex of the buckled region on South side of the tube, and at the base of the buckled region on the North side of the tube. The moment-drift response of the specimen, with noted damage states, is shown in Figure 5.63. The dashed line represents the plastic moment capacity of the CFT, calculated using the PSDM method with specified design strengths.

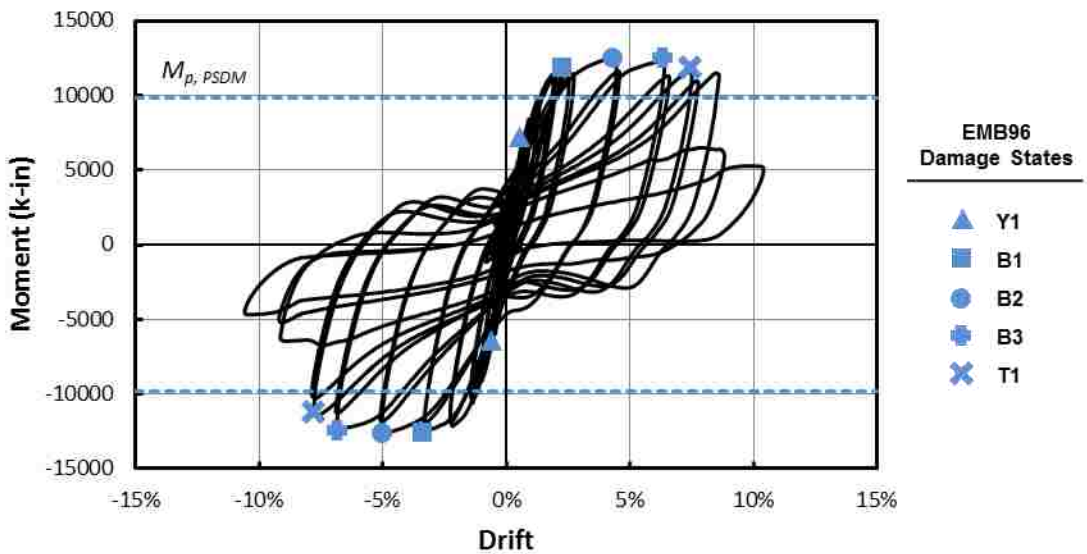

Figure 5.63: EMB96 Moment-Drift Response

5.7.1 EMB96 Performance State Summary

Table 5.10 summarizes the damage that was observed to the column and cap beam during testing, as well as the magnitude of repair required at each damage state. As shown in the table, failure of the specimen consisted of ductile tearing of the steel tube at 7.50% drift, with minimal damage to the cap beam. The proceeding section provides a detailed description of the damage progression, and will refer to the damage state progression table.

Table 5.10: EMB96 Damage State Progression Table

Set No.	Target Drift (%)	Actual Drift (%)	Column Damage	Cap Beam Damage		Lateral Load (kips)
				North	South	
1	0.12	0.07				24.0
	-0.12	-0.08				-21.6
2	0.24	0.13				38.2
	-0.24	-0.14				-39.8
3	0.49	0.31				55.9
	-0.49	-0.32				-60.4
4	0.73	0.49				76.2
	-0.73	-0.47				-81.1
5	0.97	0.65	**Y1**			88.2
	-0.97	-0.65				-95.6
7	1.46	0.94				114.3
	-1.46	-1.02				-123.8
8	1.94	1.29				132.5
	-1.94	-1.44				-143.0
10	2.92	2.01				155.0
	-2.92	-2.28				-161.9
11	3.89	2.55	**B1**			155.9
	-3.89	-3.36				-163.6
13	5.83	4.46	**B2**		**C1**	161.4
	-5.83	-5.07				-160.7
14	7.78	6.39	**B3**			152.4
	-7.78	-6.86				-151.3
16	8.75	7.50	**T1**			139.6
	-8.75	-7.81				-136.9
18	9.72	8.60				135.1
	-9.72	-9.15				-71.9
20	11.18	10.40				45.0
	-11.18	-10.60				-35.8

Repair States

	No Repair Required
	Repair
	Full Replacement

5.7.2 Low Drift Cycles (0.0% - 2.0% Drift)

There was no visible damage to the cap beam or column during the first two cycle levels. During the third cycle level, two hairline cracks formed in grout region, propagating radially in the NE and SW direction. Figure 5.64b shows the radial crack on the South side of the specimen. At 0.5% drift, circumferential hairline cracks initiated along the column-grout interface on both the North and South sides of the specimen, as each side was respectively subjected to tensile loading. Figures 5.64a and 5.64b show the circumferential grout pad cracks on the North and South side of the specimen, respectively.

Figure 5.64: EMB96 (a) North and (b) South grout pad cracking at 0.5% drift

During the 5th load set, strain gauges located 3-in. above the surface of the cap beam measured yielding of the steel tube at .57% drift in the South direction. During the 7th load set, a circumferential hairline crack formed along the grout-cap beam interface as the South side of the specimen was loaded into tension. At the same drift, the opening between the column and grout interface increased to approximately 1.5-mm while loaded in tension. Figure 5.65 shows the cracking along the column-grout and grout-cap beam

interfaces on the South side of the specimen as it is subjected to 1.02% drift in the North direction.

Figure 5.65: EMB96 South grout pad cracking at 1.02% drift North

During the subsequent load set, similar circumferential cracks formed along the grout-cap beam interface on the North side of the specimen as it was displaced to 1.29% drift in the South direction. These cracks were hairline in width, and approximately 1-in. in length. During this load set, the crack between the column and the grout region increased to approximately 2-mm in width as each side of the specimen was subjected to tensile loading.

5.7.3 Moderate to High Drift Cycles (2.0% - 7.0% Drift)

There was no new damage observed during the 10th load set. As the column approached 2.3% drift in the South direction, three of the threaded rods that attached the actuator to the column fractured, and the test was paused such that the rods could be replaced. The lateral load was 158.2-kips at the time of fracture. After the rods were replaced, the

column returned to its original location at zero displacement, and the target load protocol was continued from the beginning of the drift set.

During the subsequent cycle of the 11th load set (post-rod replacement), the onset of local buckling of the steel tube was observed as both the North and South sides of the column were respectively subjected to compressive loading. The apex of the local buckling was approximately 2.5-in. from the surface of the cap beam. Figures 5.66a and 5.66b show the buckling of the steel tube on the South and North sides of the column as they are respectively subjected to 2.55% drift South and 3.36% drift North. During this load set, the column was subjected to its maximum lateral load resistance of 163.6-kips in the North direction.

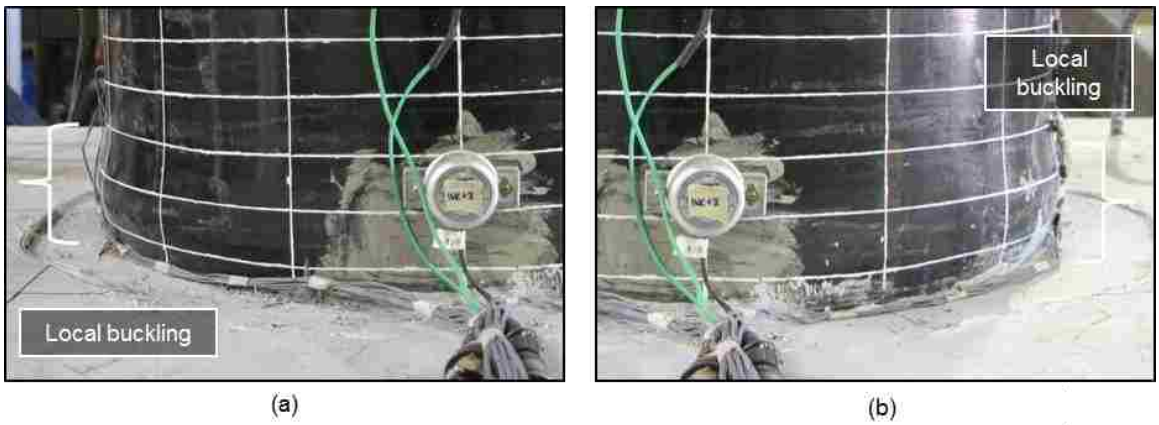

Figure 5.66: EMB96 Onset of local buckling on (a) South and (b) North side of the column

As the column was displaced to 4.46% drift in the North direction, a crack formed in the surface of the cap beam, propagating radially from the column in the SE direction. The crack was hairline in width, and approximately 2-in. long, as shown in Figure 5.67a. During the same load set, the magnitude of the out-of-plane displacement of the buckled region increased to approximately 0.50-in., and the distance to the apex of the buckled region shifted such that it was approximately 2-in. from the top surface of the cap beam.

Figure 5.67b shows the residual local buckling on the North side of the specimen after the column had returned to zero displacement.

Figure 5.67: EMB96 (a) South cap beam cracking and (b) North column buckling after 13th load set

During the 14th load set, there was no new damage observed to the cap beam or grout region. The magnitude of the residual out-of-plane displacement of the buckled region increased to approximately 1-in., and the height of the apex remained at approximately 2-in. from the surface of the cap beam. Figure 5.68 shows the buckled region on the South side of the column at zero displacement after the 14th load set.

Figure 5.72: EMB96 South local buckling after 14th load set

5.7.4 Specimen Failure (7.0%+ Drift)

During the second cycle of the 16th drift set, tearing was observed on the South side of the column. The tear initiated circumferentially along the apex of the buckled region, and it was approximately 1-in. in length, as shown in Figure 5.69. At this point, the lateral load resistance was 129.6-kips in the South direction, and 120.5-kips in the North direction.

Figure 5.69: EMB96 Initiation of South tube tearing

As the column was first displaced to 8.60% drift in the South direction, tearing initiated on the North side of the column, at the base of the buckled region. The original tear at the South side of the specimen propagated circumferentially to approximately 4-in. in length. Figures 5.70a and 5.70b show the tearing on the North and South sides of the specimen, respectively, while the column is at its peak drift in the South direction.

Figure 5.70: EMB96 (a) North and (b) South tube tearing at 8.60% drift South

As the column was subsequently displaced to 9.15% drift in the North direction, the tear along the base of the buckled region on the North side of the specimen became invisible. The tear along the South side of the specimen propagated to approximately 16-in. length, as shown in Figure 5.71.

Figure 5.71: EMB96 South tear propagation at 9.15% drift North

At this point, the lateral load resistance had dropped to 71.91-kips in the North direction, and no new cracks were observed in the cap beam concrete or grouted region.

Figure 5.72 shows the propagation of tearing on the North side of the specimen as the column was subjected to its second cycle at 8.60% drift in the South direction. During this cycle, the lateral load resistance dropped to 46-kips and 67.5-kips in the North and South directions, respectively.

Figure 5.72: EMB96 North tear propagation during second cycle at 8.60% drift South

The specimen was subjected to one final load set, in which the column was displaced to 10.4% drift in the South direction, and 10.6% drift in the North direction. During this load set, the lateral load resistance dropped 35.8-kips and 45-kips in the North and South directions, respectively. No new cracking was observed in the cap beam concrete or grout region. Figure 5.73 shows the final state of the specimen after the termination of testing.

Figure 5.73: EMB96 Specimen damage at termination of test

CHAPTER 6

DATA INTERPRETATION AND ANALYSIS

This chapter presents the measured responses of the specimens as obtained through laboratory testing. The data collected from strain gauges, potentiometers, inclinometers, and the NDI Optotrak motion capture system is used to produce strain and curvature profiles, rotation profiles, and hysteretic responses to better understand the specimens' behavior on the component and global level.

6.1 FORCE-DRIFT RESPONSE

The hysteretic force-drift response of each specimen is presented in Figures 6.1 – 6.5. The maximum lateral load resisted by each specimen is summarized in Table 6.1, along with the corresponding drift ratio at each peak load. As shown in Table 6.1, the maximum lateral load resisted by each specimen occurred at approximately 3.0% drift. It should be noted that the forces tabulated in Table 6.1 and displayed in Figures 6.1 – 6.5 are measured directly from the MTS load cell, and do not take into account the additional contribution from P-Delta effects.

Table 6.1: Specimen Peak Lateral Loads

Specimen Designation		Peak Lateral Load (kips)	Drift at Peak Load
I	EMB80	137	3.1%
II	WRC	123	3.0%
III	WRCUB	97	3.3%
IV	RC	98	3.2%
V	EMB96	164	-3.3%[1]

[1] Sign indicates direction of loading

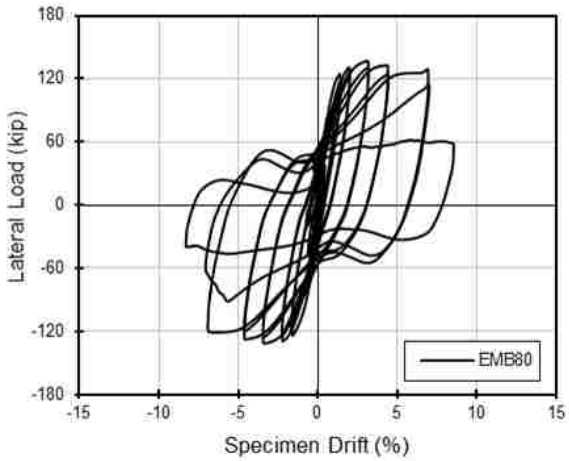

Figure 6.1: EMB80 Force-Drift Response

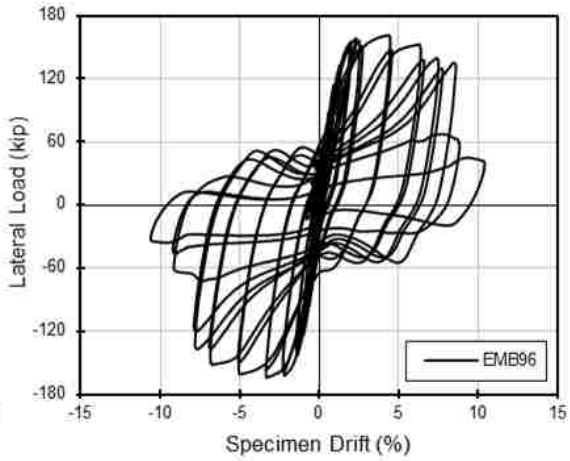

Figure 6.2: EMB96 Force-Drift Response

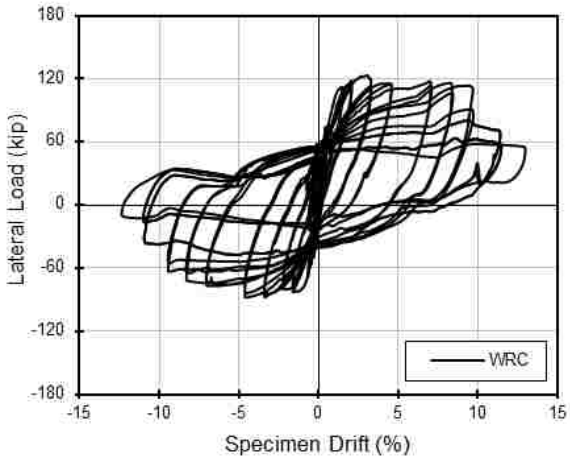

Figure 6.3: WRC Force-Drift Response

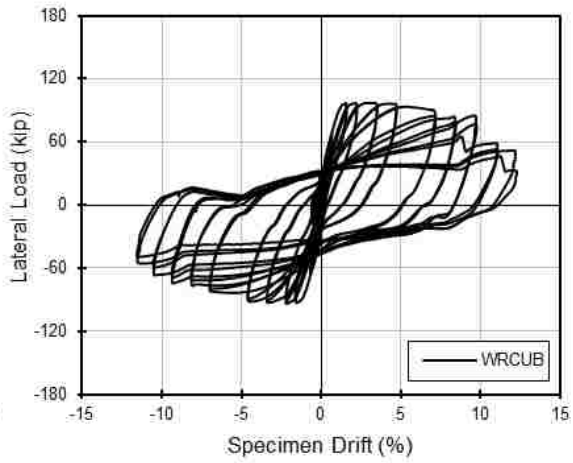

Figure 6.4: WRCUB Force-Drift Response

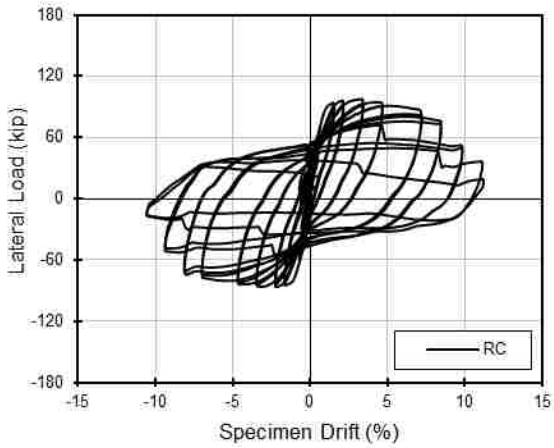

Figure 6.5: RC Force-Drift Response

6.2 MOMENT-DRIFT RESPONSE

Figures 6.6 through 6.10 present the hysteretic moment-drift responses of the five CFT column-to-cap beam specimens. The moments are calculated using Equation 5.1, which takes into account the additional moment contribution from P-Delta effects.

Table 6.2 summarizes the peak moment experienced by each specimen, as well as the corresponding drift ratios where the maximum moments occurred. For each specimen, the peak moment occurred several cycles after the peak lateral load was applied. This shift in maximum load can be attributed to the P-Delta moment contribution which becomes significant at large rotations.

Table 6.2: Specimen Peak Moments

Specimen Designation		Peak Moment (kip-in)	Drift at Peak Moment	Plastic Moment, M_p (kip-in)	Peak Moment/M_p
I	EMB80	11334	6.9%	8340	1.36
II	WRC	11004	9.5%	8340	1.32
III	WRCUB	8956	9.6%	8340	1.07
IV	RC	8374	7.1%	8340	1.00
V	EMB96	12555	4.4%	9800	1.28

Table 6.2 also presents the peak moment of each specimen normalized by the plastic moment capacity of the CFT section. The plastic moment capacity was calculated using the PSDM outlined in Section 2.1.5 with design material strengths. The plastic moment capacities are represented by red dashed lines in Figures 6.6 through 6.10.

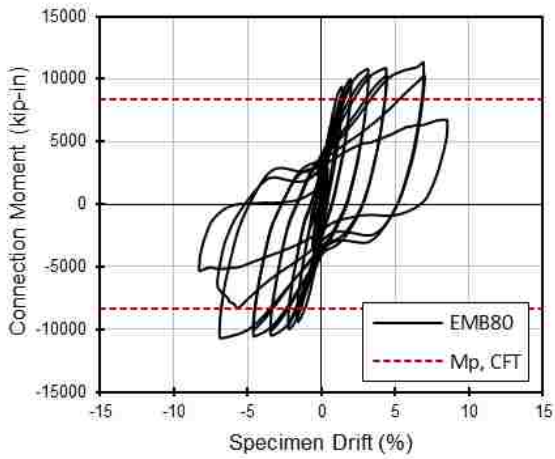

Figure 6.6: EMB80 Moment-Drift Response

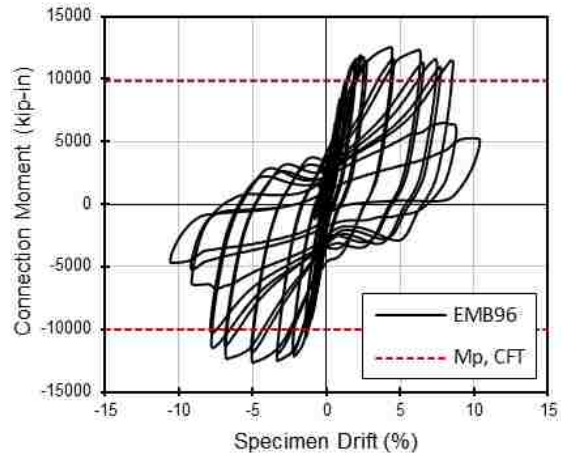

Figure 6.7: EMB96 Moment-Drift Response

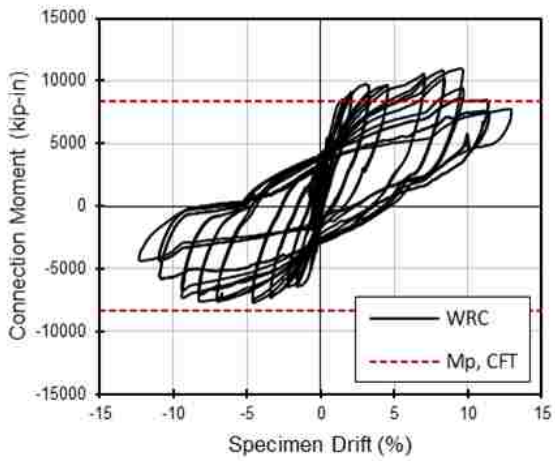

Figure 6.8: WRC Moment-Drift Response

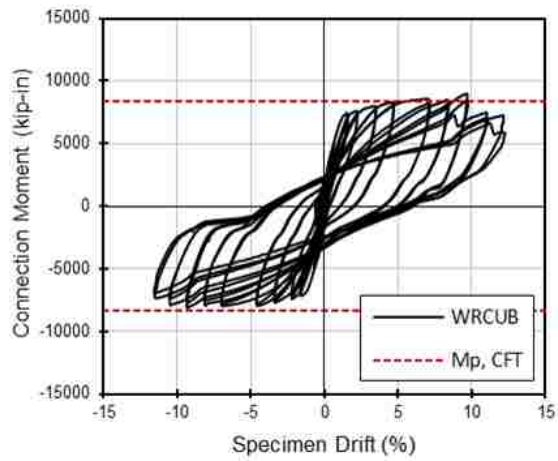

Figure 6.9: WRCUB Moment-Drift Response

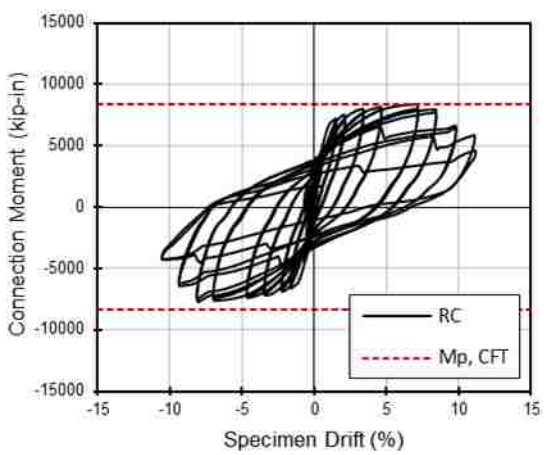

Figure 6.10: RC Moment-Drift Response

Figure 6.11 presents the envelopes of the five moment-drift hysteresis plots. The envelopes were created using the moment and drift values that corresponded to the maximum moment of the first cycle in each drift set. For comparison, the moments of each specimen have been normalized by their respective CFT plastic moment capacities as calculated by the PSDM method and tabulated in Table 6.2.

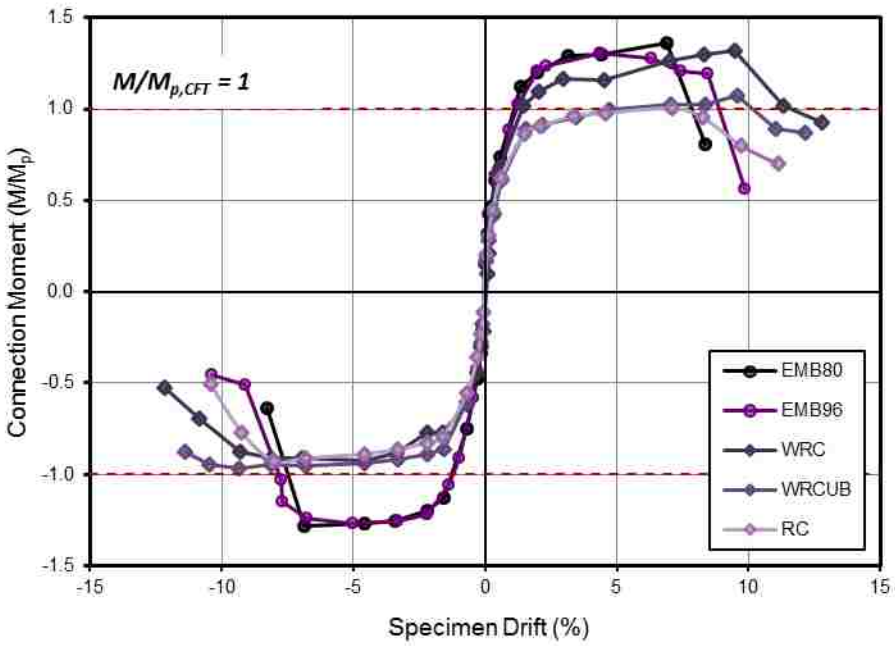

Figure 6.11: Normalized moment-drift envelope comparison of all specimens

As shown in Figure 6.11, each specimen developed the full plastic moment capacity of the CFT column when loaded in the South direction (first direction of loading). When loaded in the North direction, however, only the two embedded specimens developed the full plastic moment capacity of the CFT.

6.3 LONGITUDINAL STRAIN PROFILES

This section present the longitudinal strain profiles at four increasing drift levels for each specimen. Section 6.3.1 presents the longitudinal strain profiles for the two embedded specimens, followed by the strain profiles of the three RC specimens in Section 6.3.2.

For the two embedded specimens, the strain profiles were created using strain gauge data from the Northern & Southern-most faces of the column. For the three RC specimens, the strain profiles were created using strain gauge data from the Northern & Southern-most longitudinal reinforcing bars.

It should be noted that there was a problem with the data acquisition system while testing Specimen WRC, so manual corrections were made at data point 837. The raw strain gauge data is presented in Appendix A.

6.3.1 Longitudinal Tube Strains

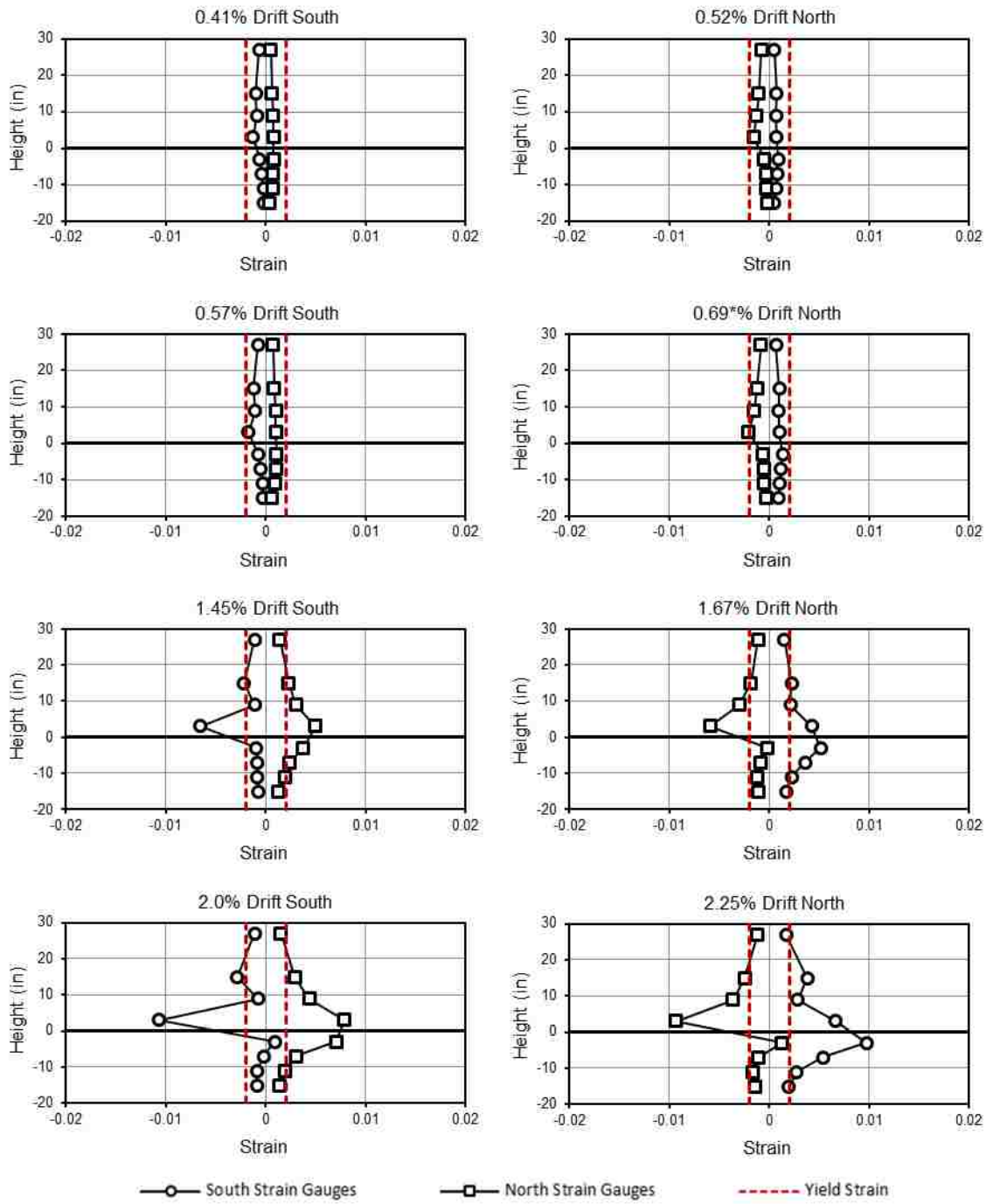

Figure 6.12: EMB80 Longitudinal strain profiles of steel tube

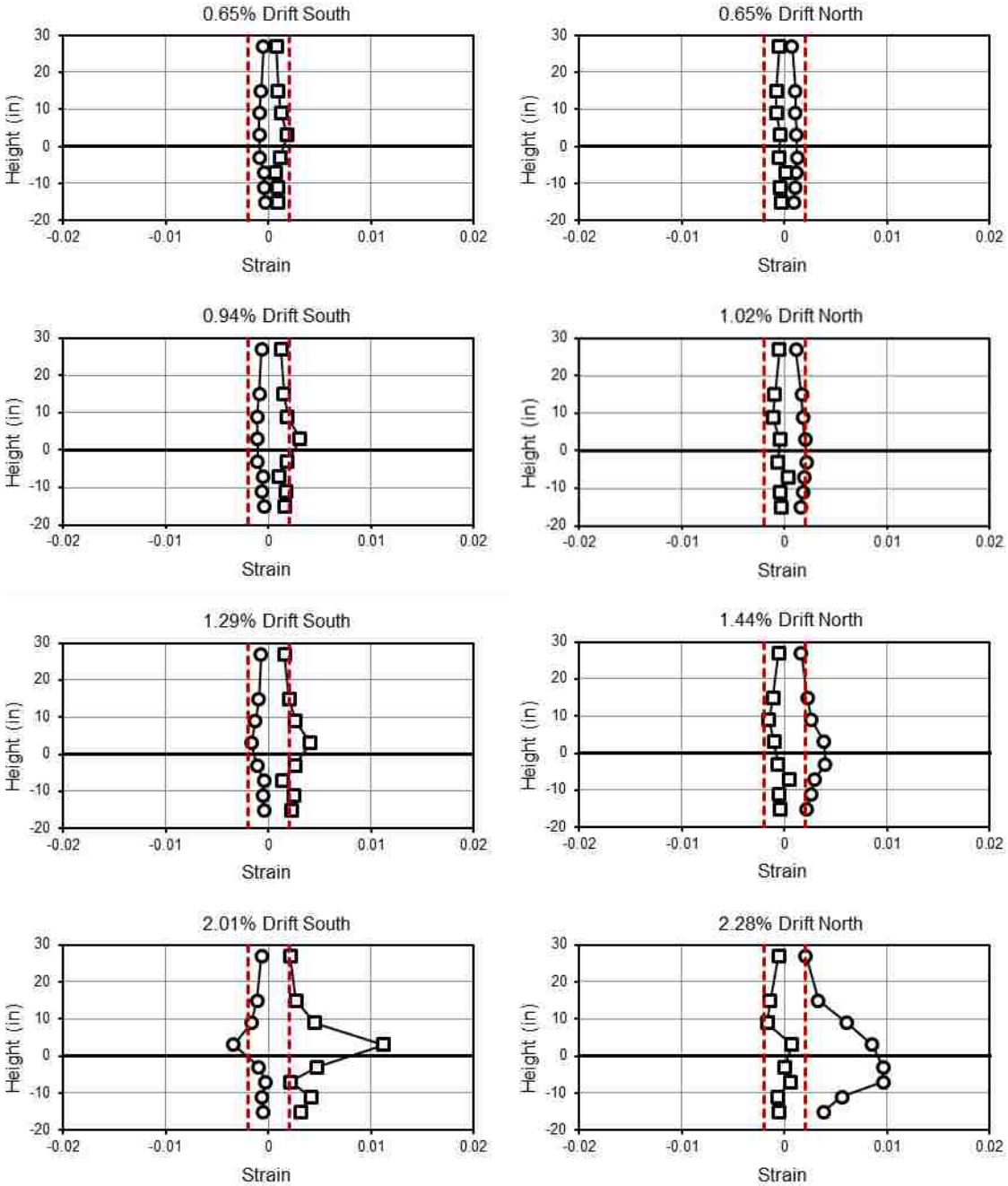

Figure 6.13: Longitudinal strain profiles of steel tube

6.3.2 Longitudinal Reinforcing Bar Strains

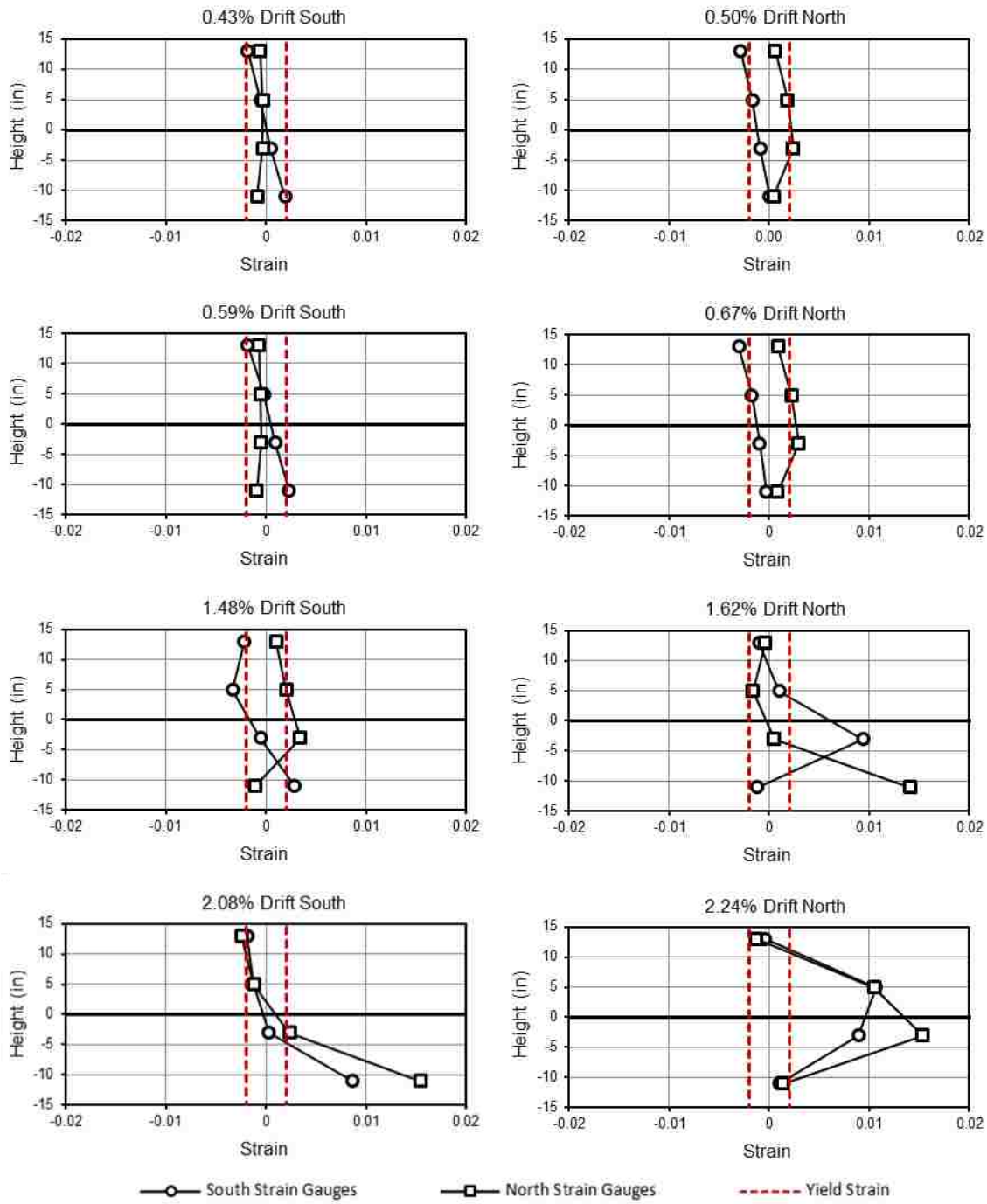

Figure 6.14: WRC Longitudinal strain profiles of North & South reinforcing bars

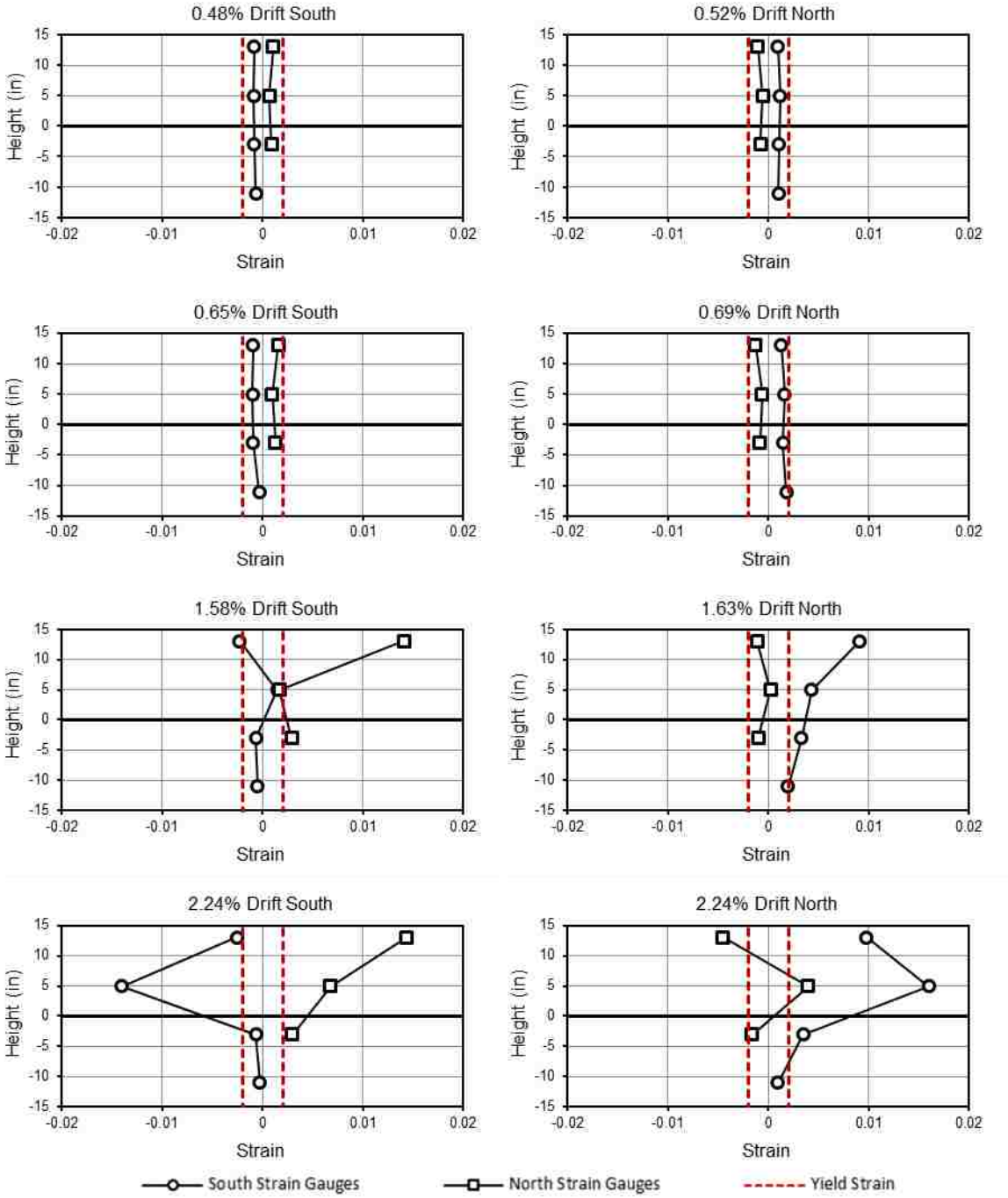

Figure 6.15: WRCUB Longitudinal Strain Profiles of North & South reinforcing bars

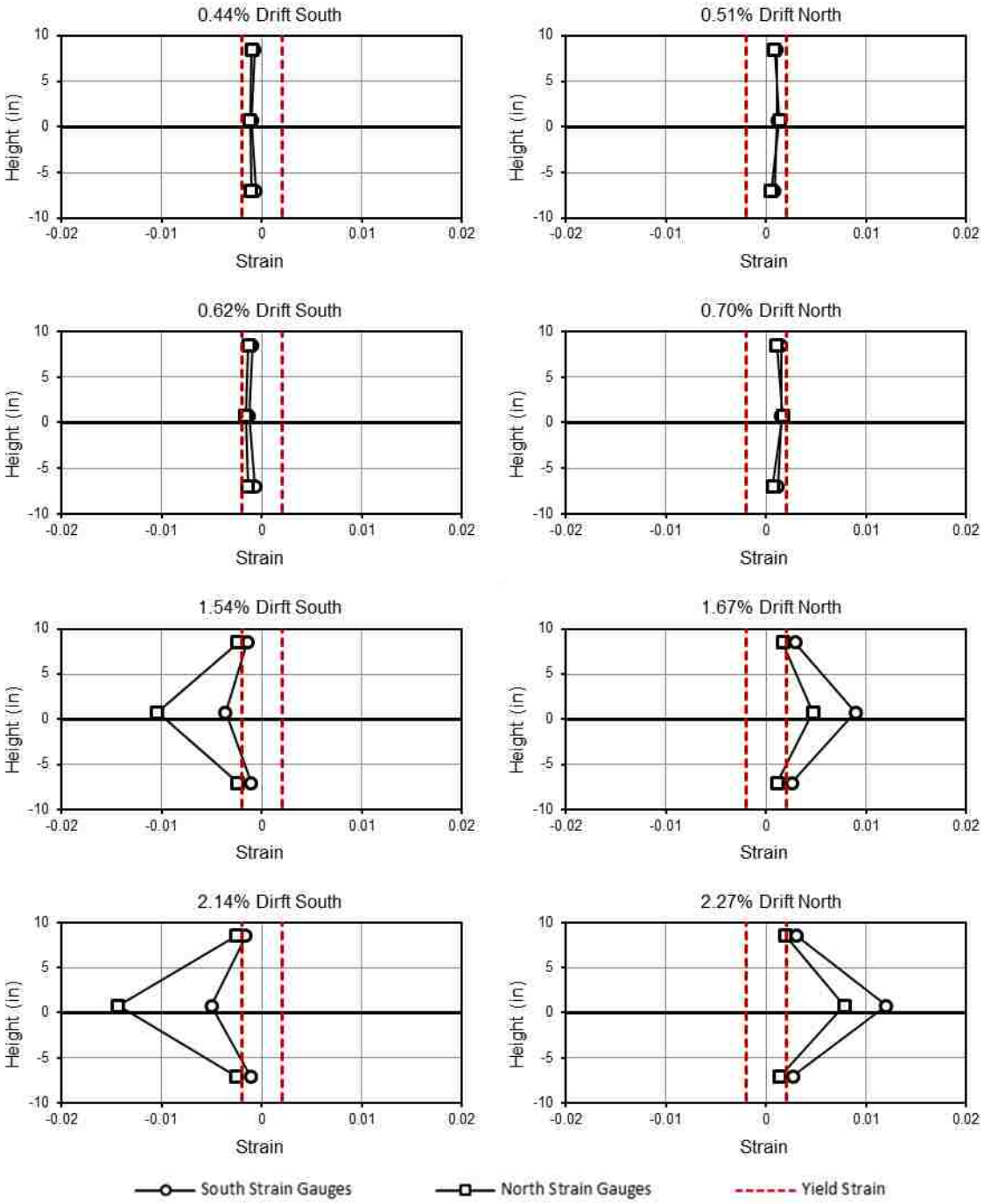

Figure 6.16: RC Longitudinal strain profiles of North & South reinforcing bars

6.4 CURVATURE PROFILES

This section presents the column curvature profiles for each specimen at four increasing drift levels. The curvatures were calculated by taking the difference in strains on the North and South sides of the column, and dividing by the distance between the two gauges, as shown by Equation 6.1.

$$\phi_{strain\ gauge} = \frac{\varepsilon_N - \varepsilon_S}{D_{column}} \tag{6.1}$$

This method of calculating curvature assumes plane sections remain plane, as shown in Figure 6.17.

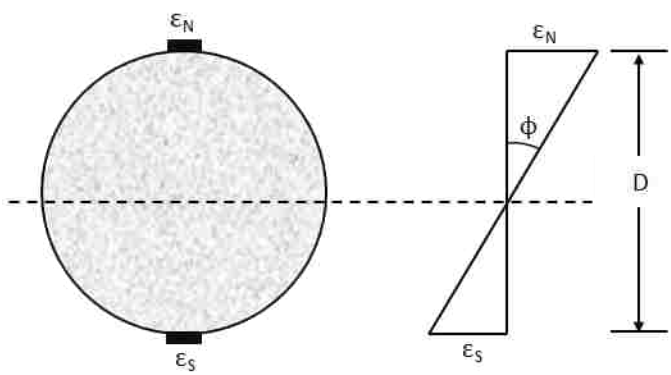

Figure 6.17: Curvature calculation from strain gauges

The resulting curvature profiles of the five specimens are presented in Figures 6.18 – 6.22.

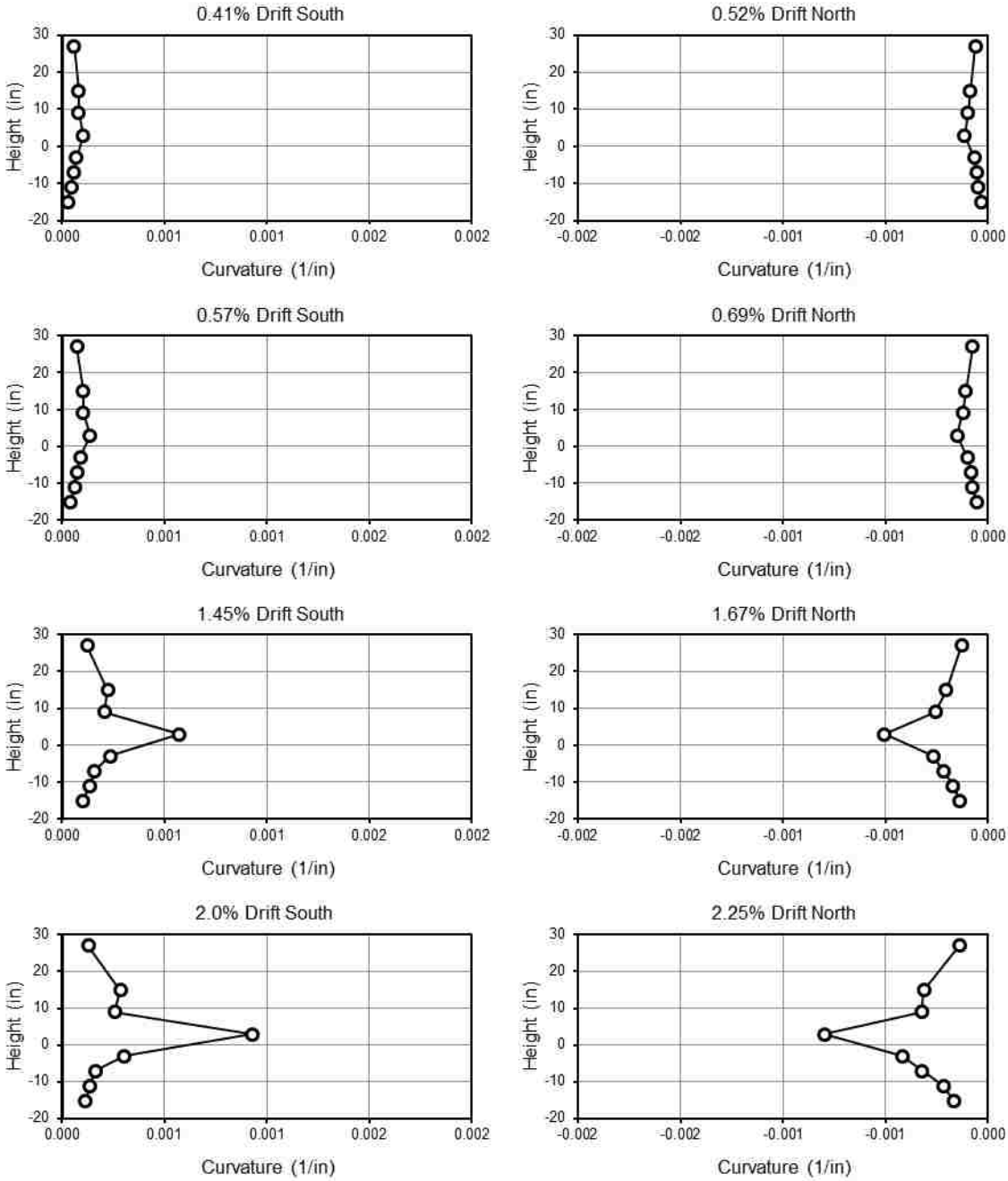

Figure 6.18: EMB80 Curvature profiles

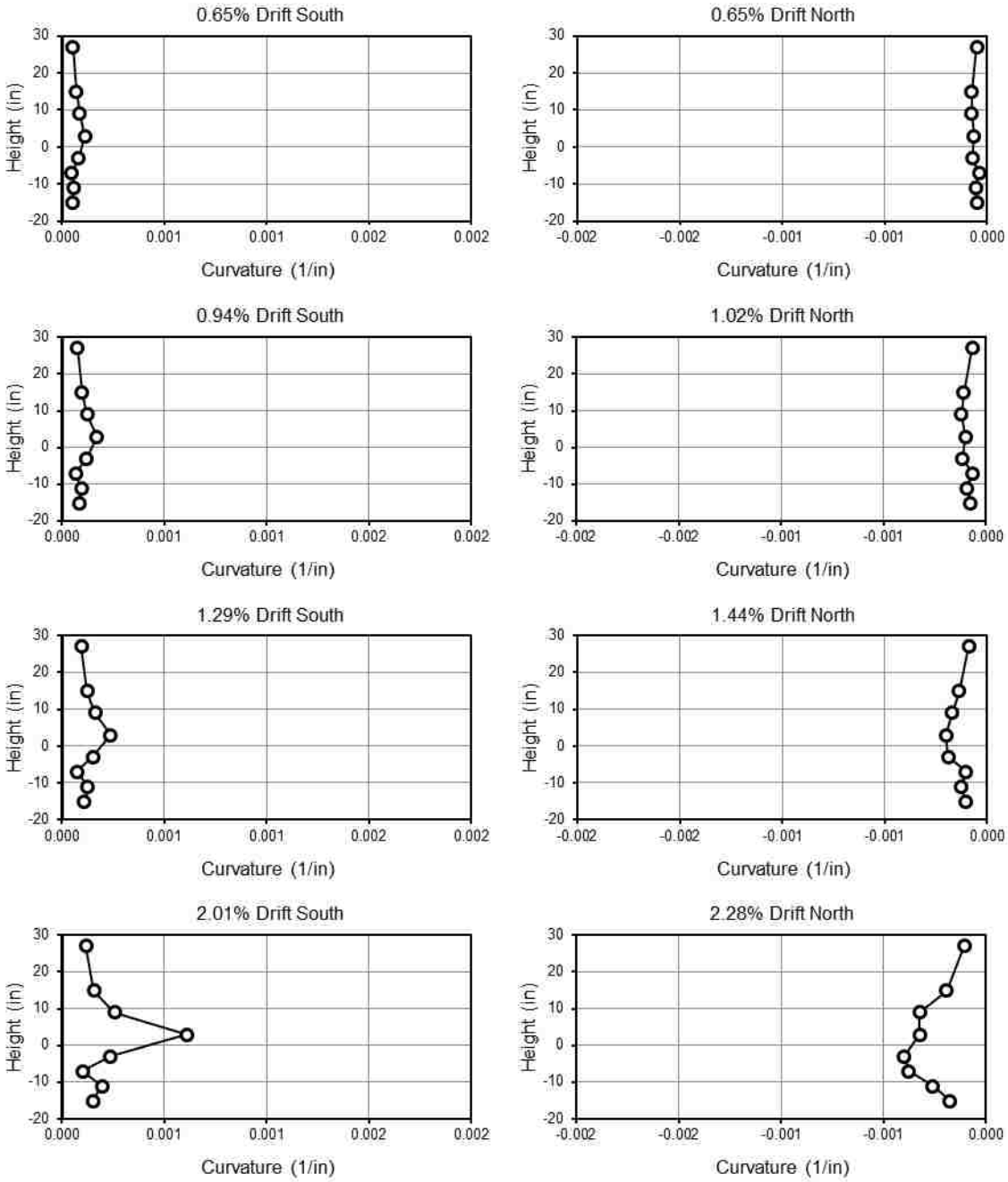

Figure 6.19: EMB90 Curvature Profiles

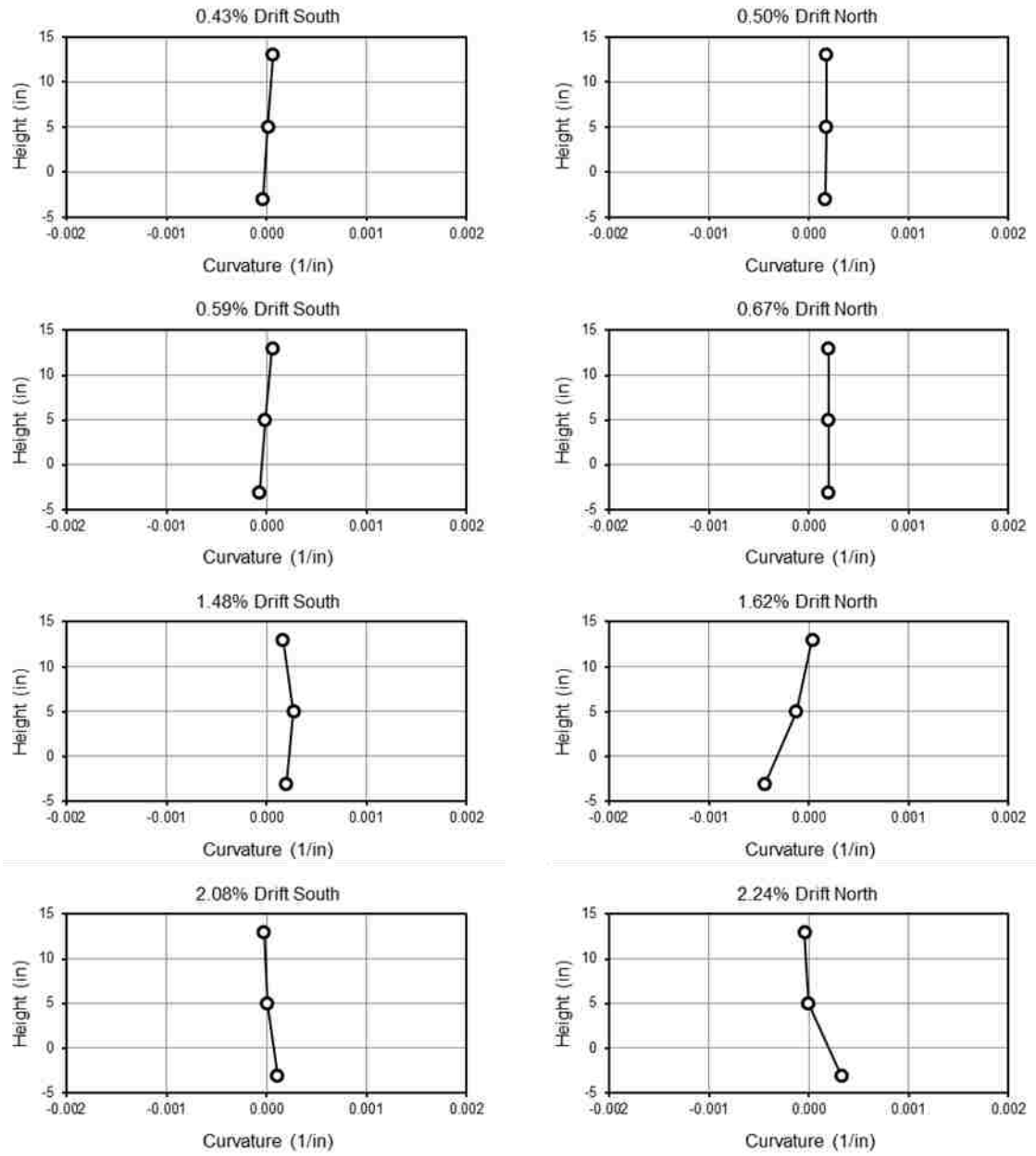

Figure 6.20: WRC Curvature profiles

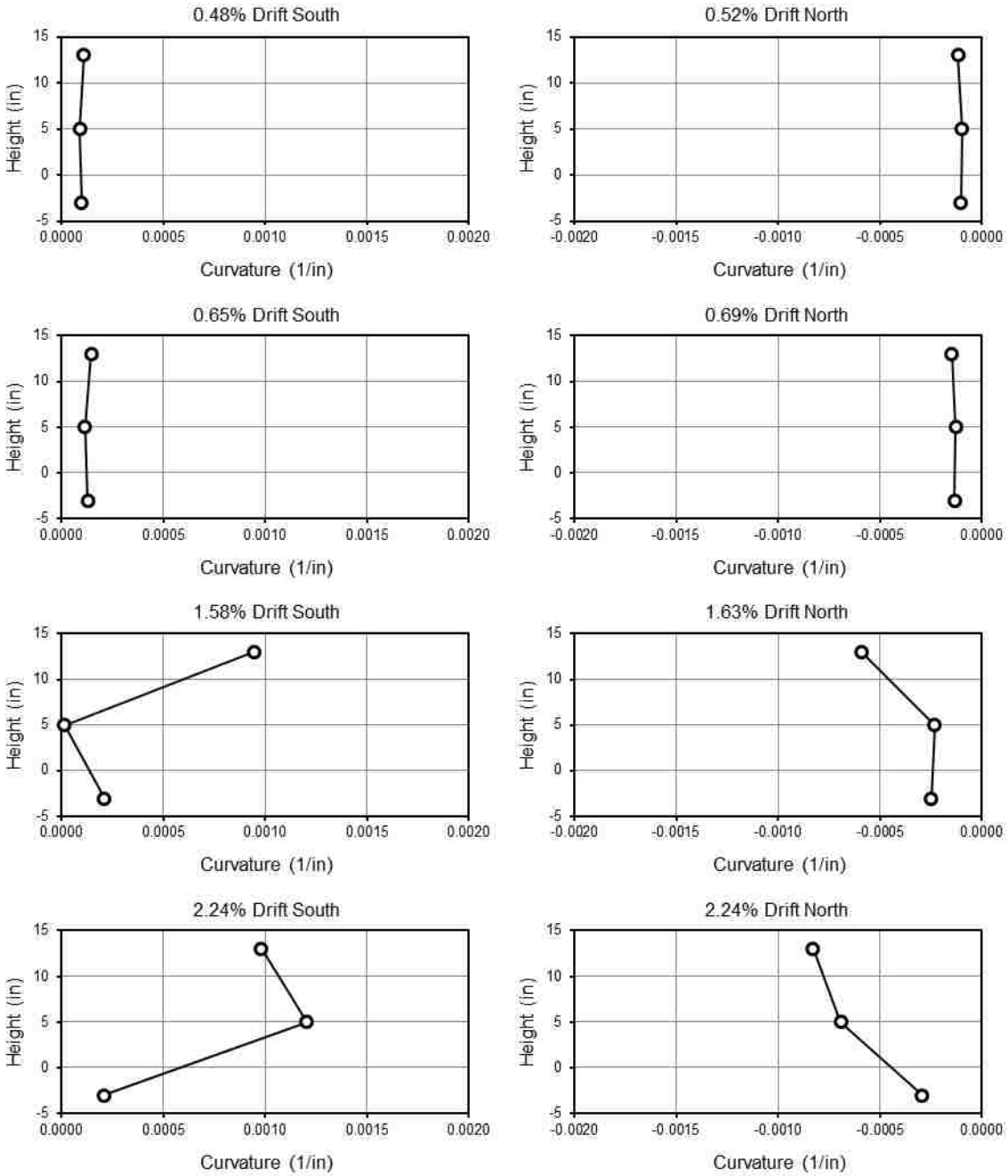

Figure 6.21: WRCUB Curvature profiles

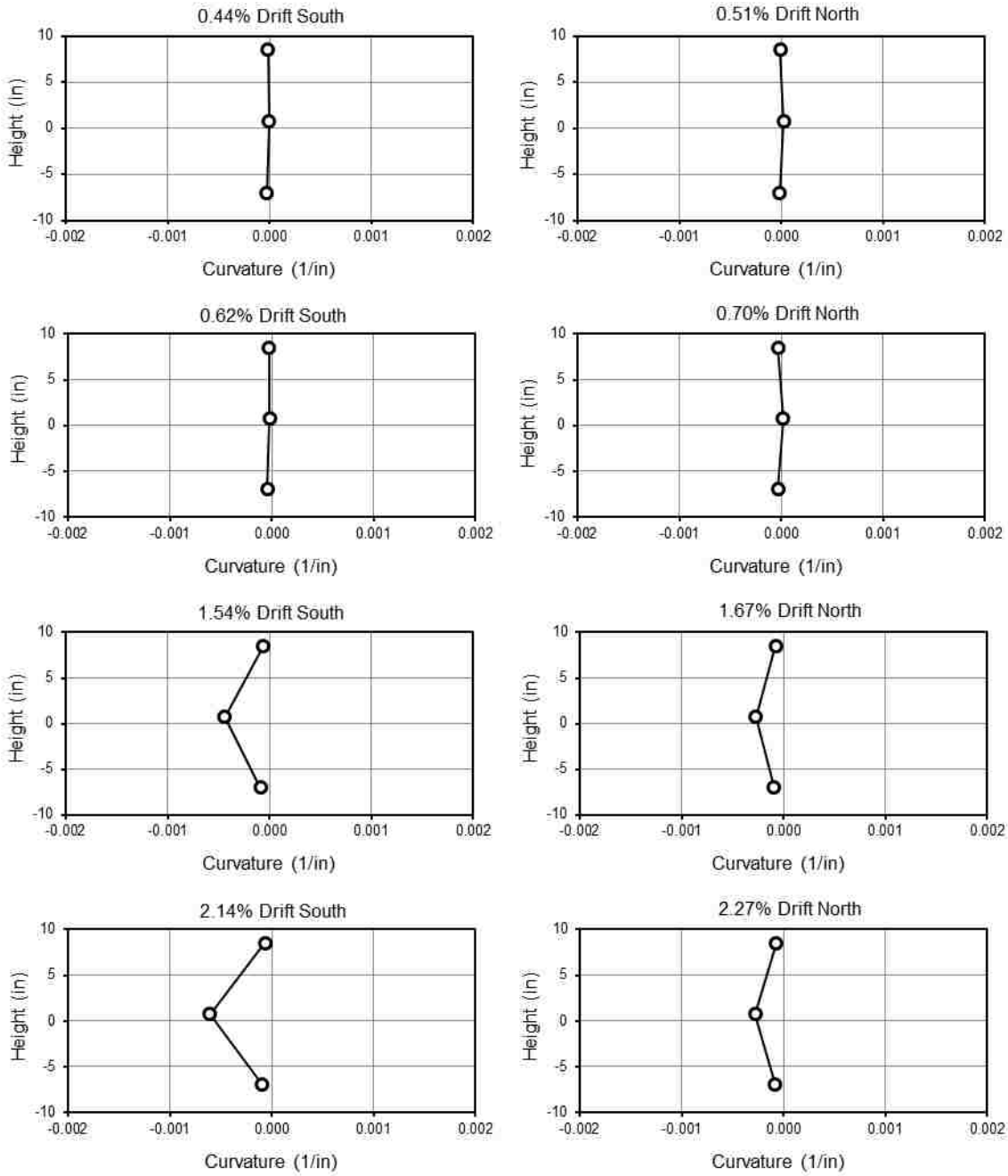

Figure 6.22: RC Curvature profiles

6.5 COLUMN ROTATION PROFILES

Figures 6.23 through 6.27 show the rotation profiles for each specimen at four increasing drift levels. The rotations were measured directly by inclinometers located on the East side of the column at 3-in., 9-in., and 15-in. above the surface of the cap beam.

Figures 6.23 and 6.24 present the rotation profiles of the two specimens with embedded connections. While the rotation profiles appear nearly linear at low drift levels, they begin to gradually curve along the height of the column as drift levels increase; indicating that more deformation is occurring in the connection and at the base of the column.

Figures 6.25 through 6.27 present the rotation profiles of the three specimens with RC connections. These rotation profiles appear to have constant rotation along the height of the column, suggesting the CFT acted as a rigid body, with the majority of the deformations occurring in the reinforcing bars.

6.5.1 Embedded CFT Specimen Rotation Profiles

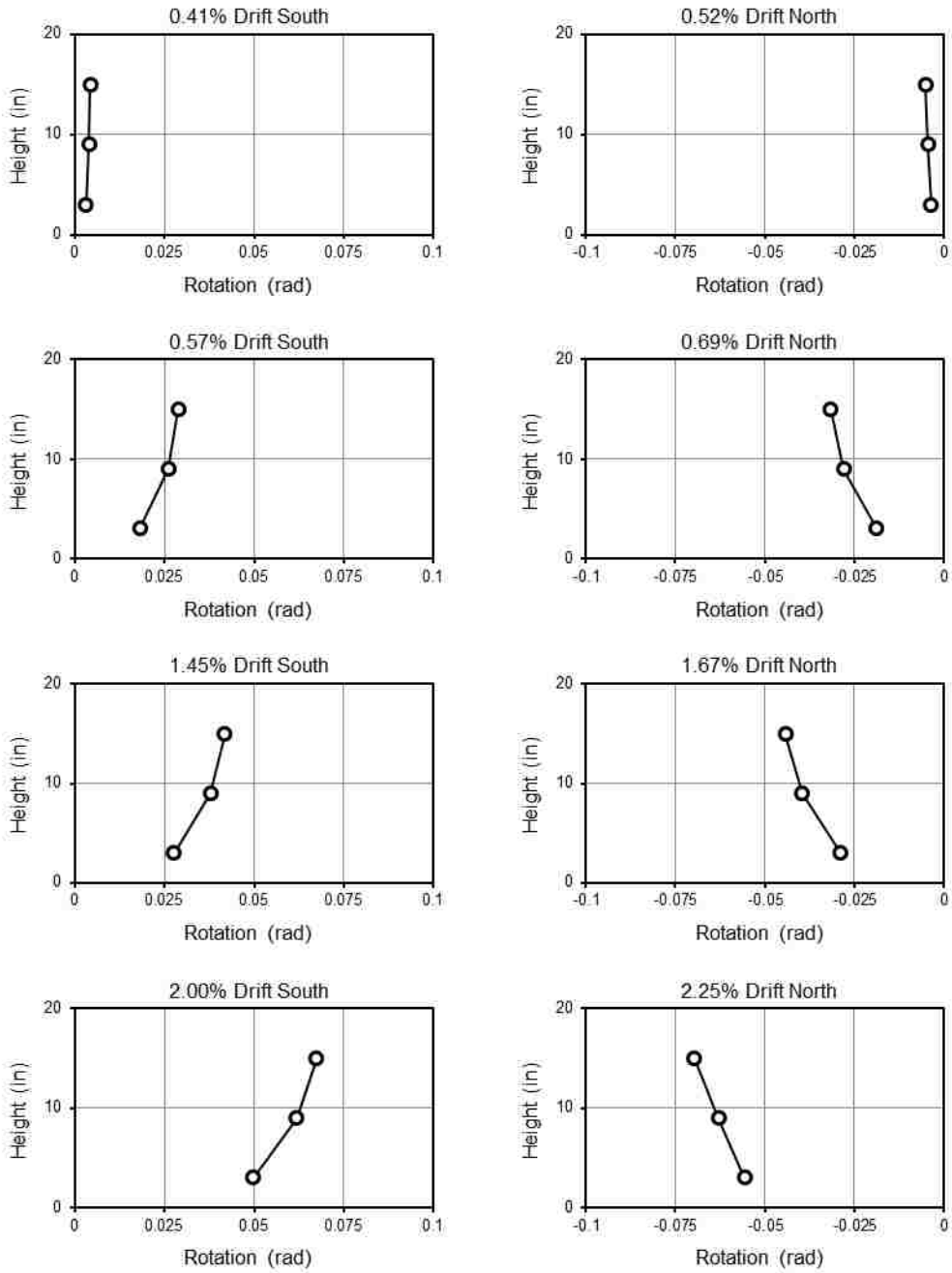

Figure 6.23: EMB80 Rotation profiles

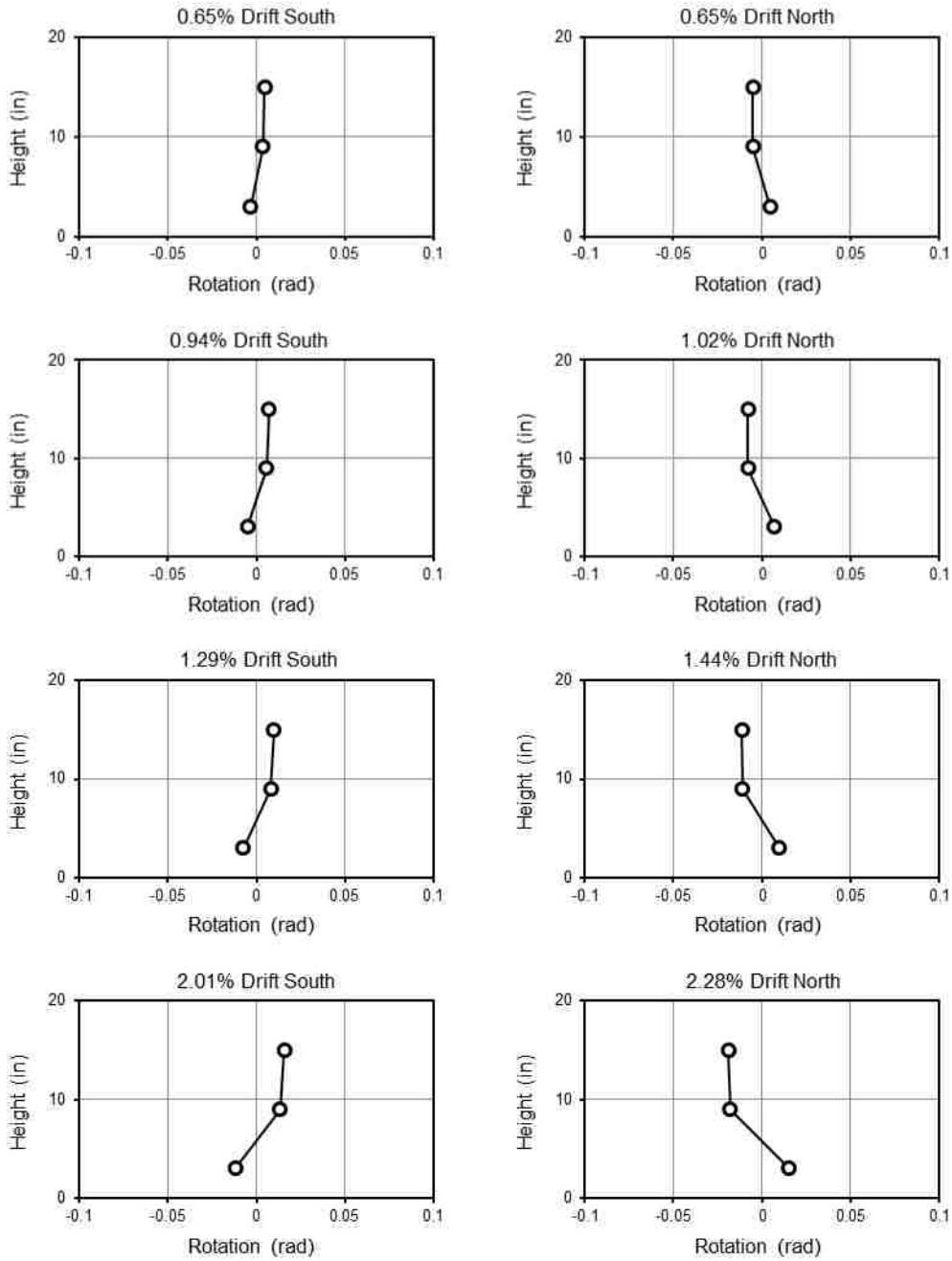

Figure 6.24: EMB96 Rotation profiles

6.5.2 RC Connection Rotation Profiles

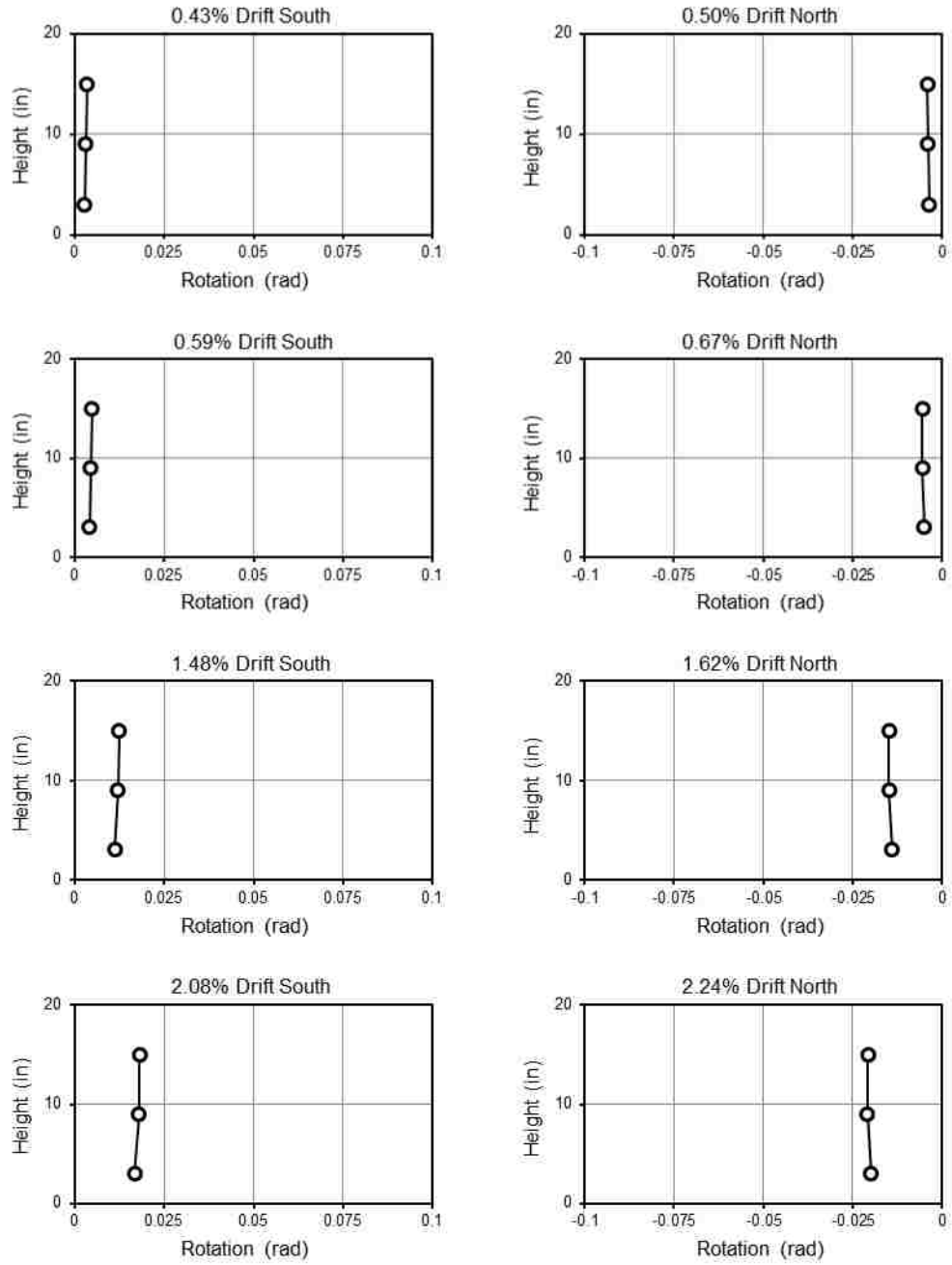

Figure 6.25: WRC Rotation profiles

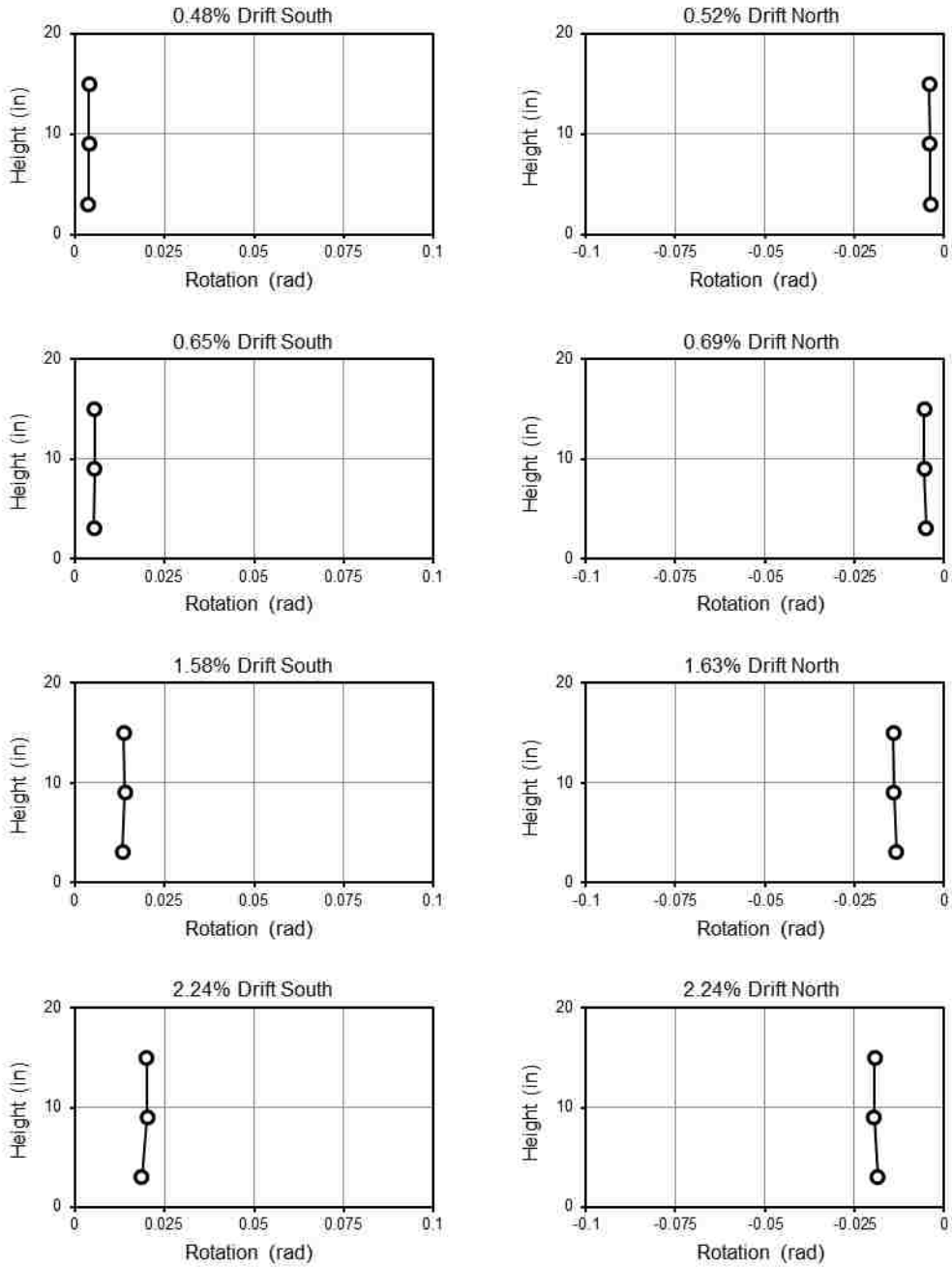

Figure 6.26: WRCUB Rotation profiles

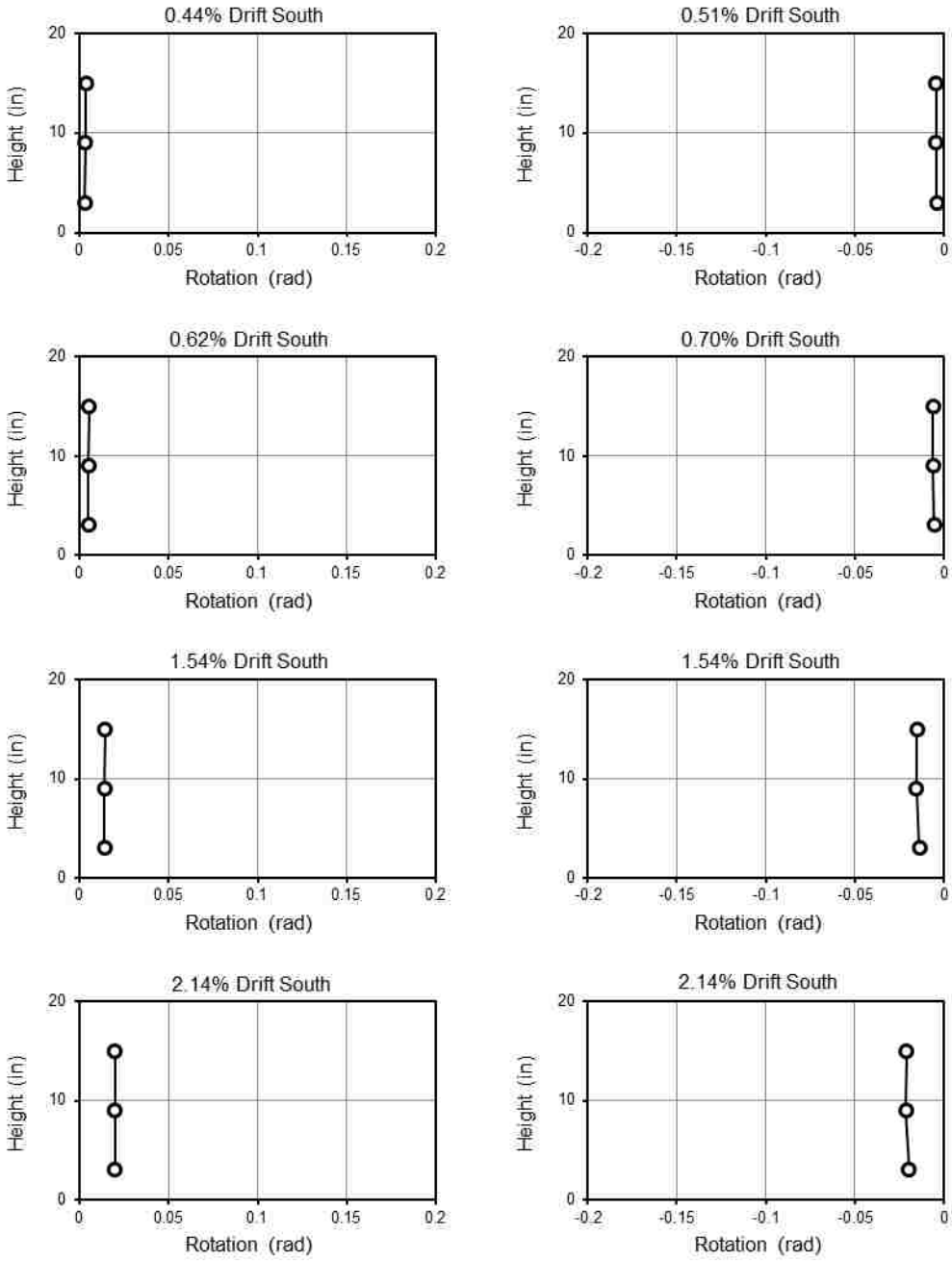

Figure 6.27: RC Rotation profiles

6.6 MOMENT-ROTATION

Figures 6.28 through 6.32 show the moment-rotation responses for each specimen. The rotations are measured directly by inclinometers located 9-in. above the surface of the cap beam.

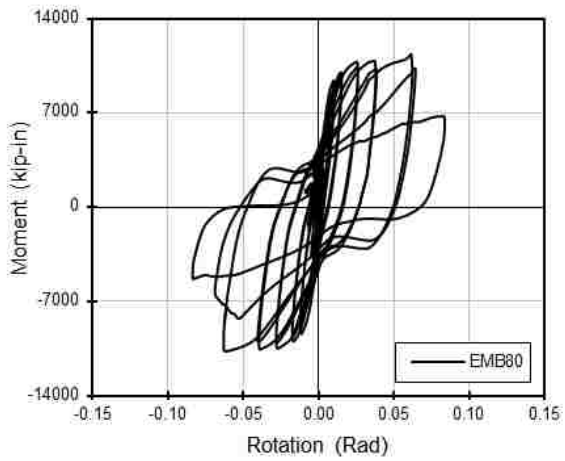

Figure 6.28: EMB80 Moment-rotation response

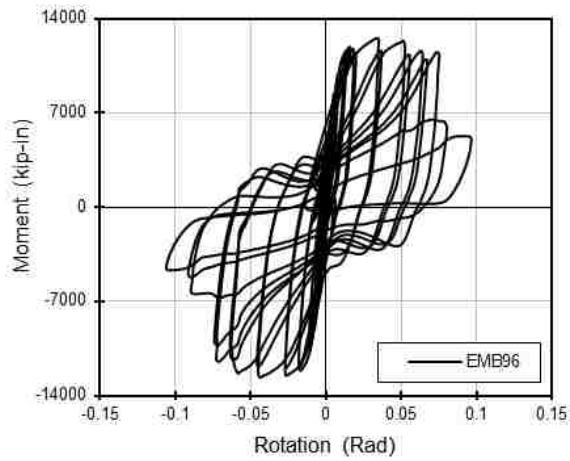

Figure 6.29: EMB96 Moment-rotation response

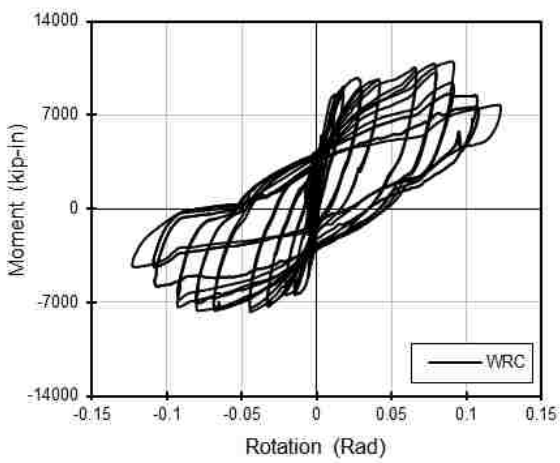

Figure 6.30: WRC Moment-rotation response

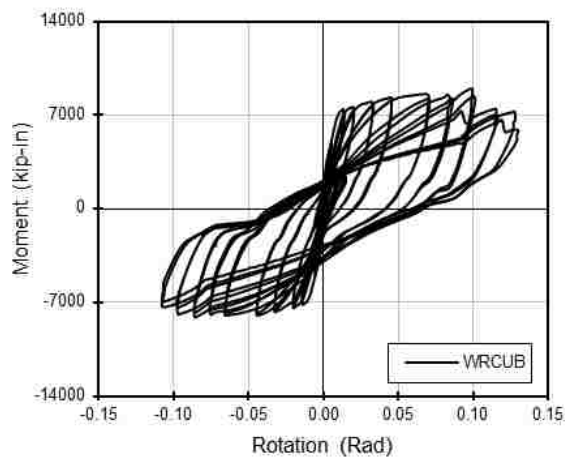

Figure 6.31: WRCUB Moment-rotation response

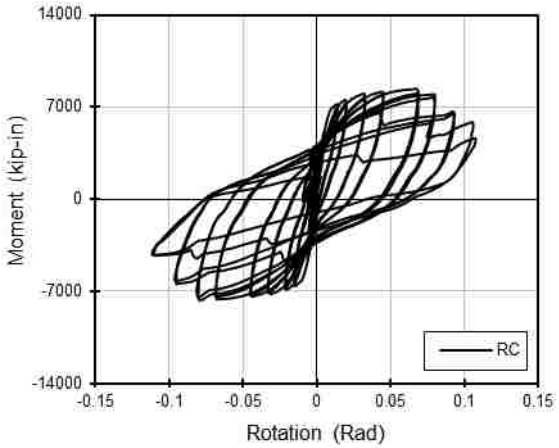

Figure 6.32: RC Moment-rotation response

6.7 COLUMN DISPLACEMENT PROFILES

Figures 6.33 through 6.37 present the displaced column profiles for each specimen at their respective damage state drift levels. The displacements are measured directly from string potentiometers located on the North side of the specimen at heights of 6-in, 12-in, 18-in, and 72-in. above the surface of the cap beam.

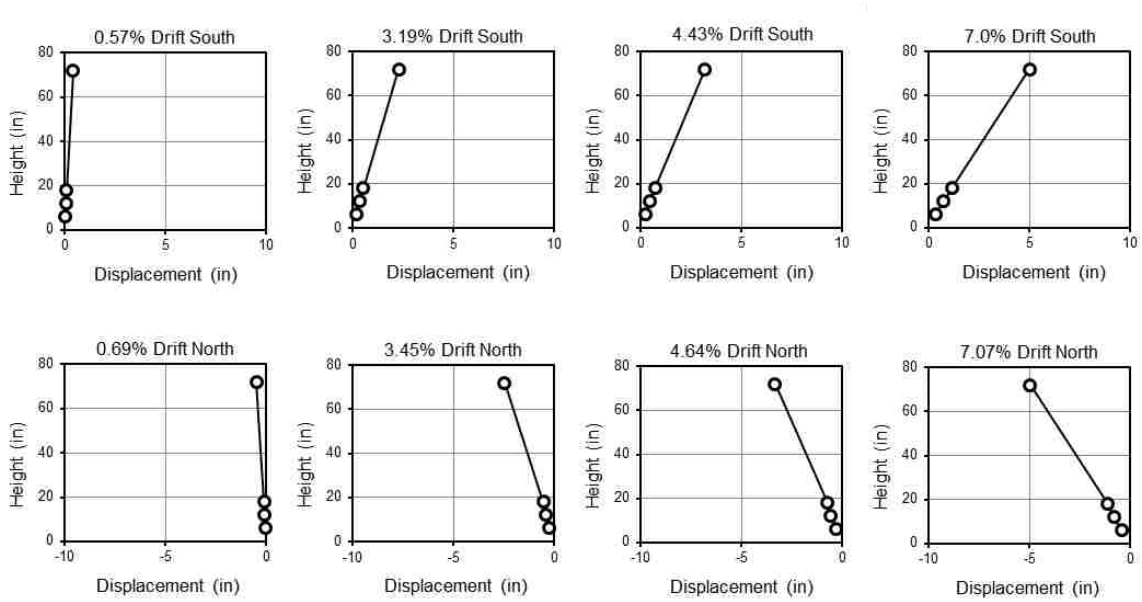

Figure 6.33: EMB80 Column displacement profile measured from string potentiometers

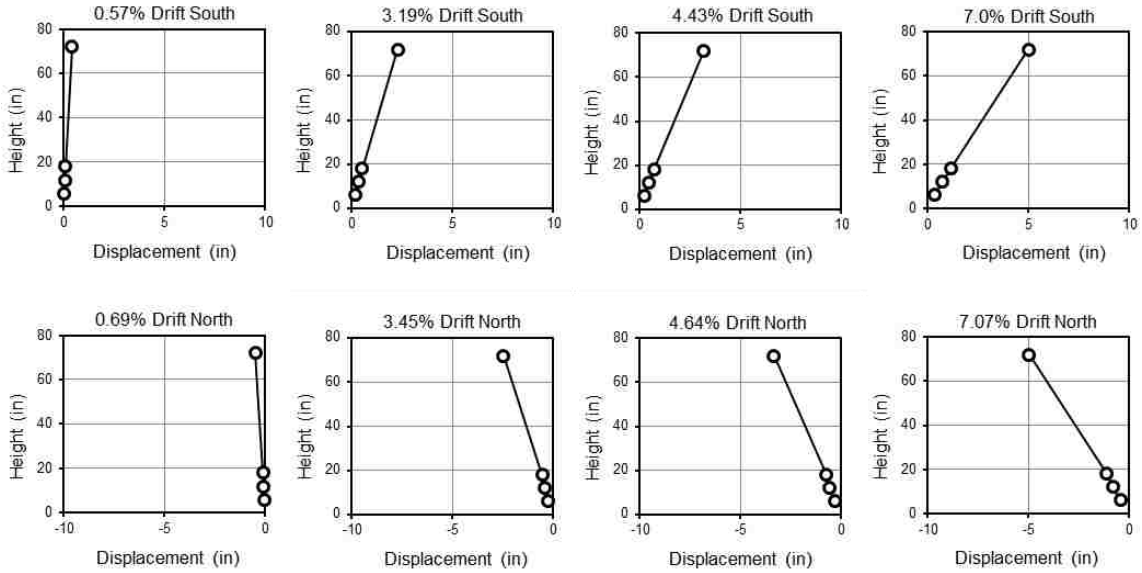

Figure 6.34: EMB96 Column displacement profile measured from string potentiometers

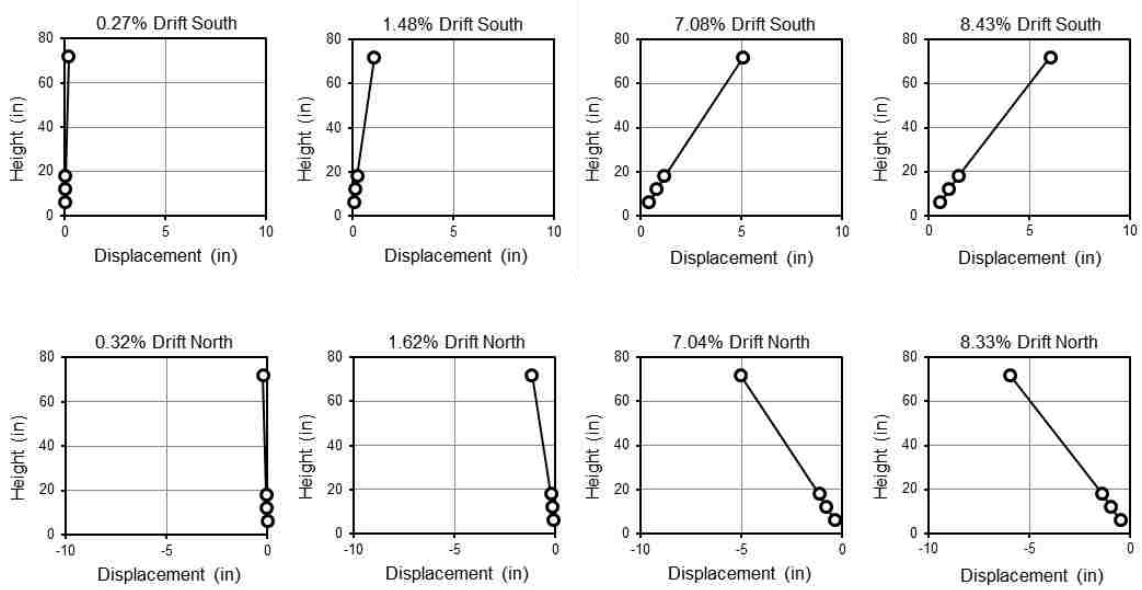

Figure 6.35: WRC Column displacement profile measured from string potentiometers

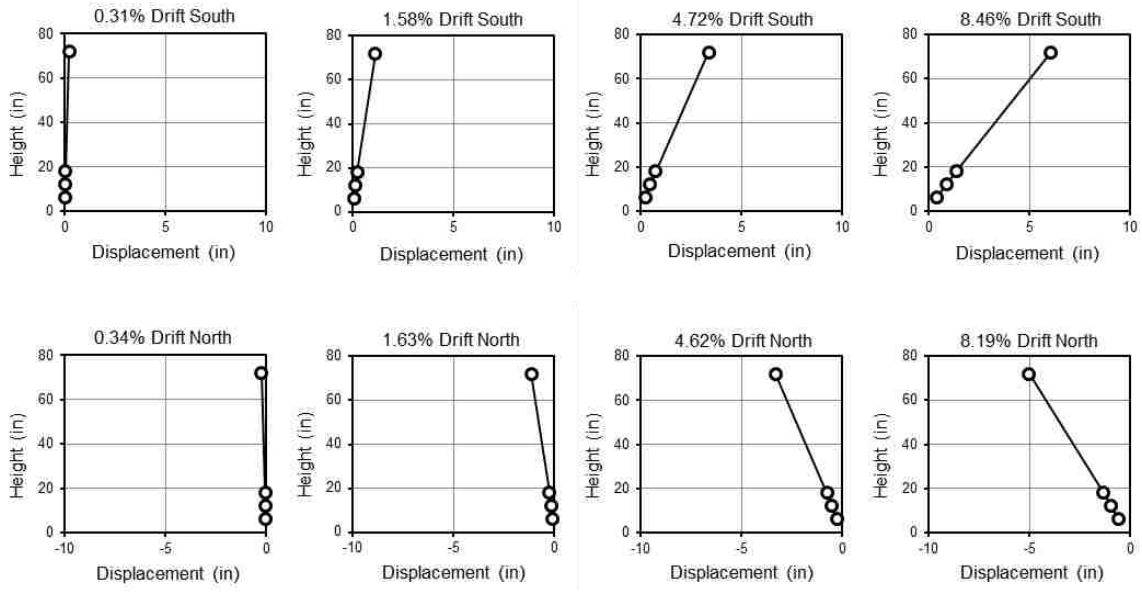

Figure 6.36: WRCUB Column displacement profile measured from string potentiometers

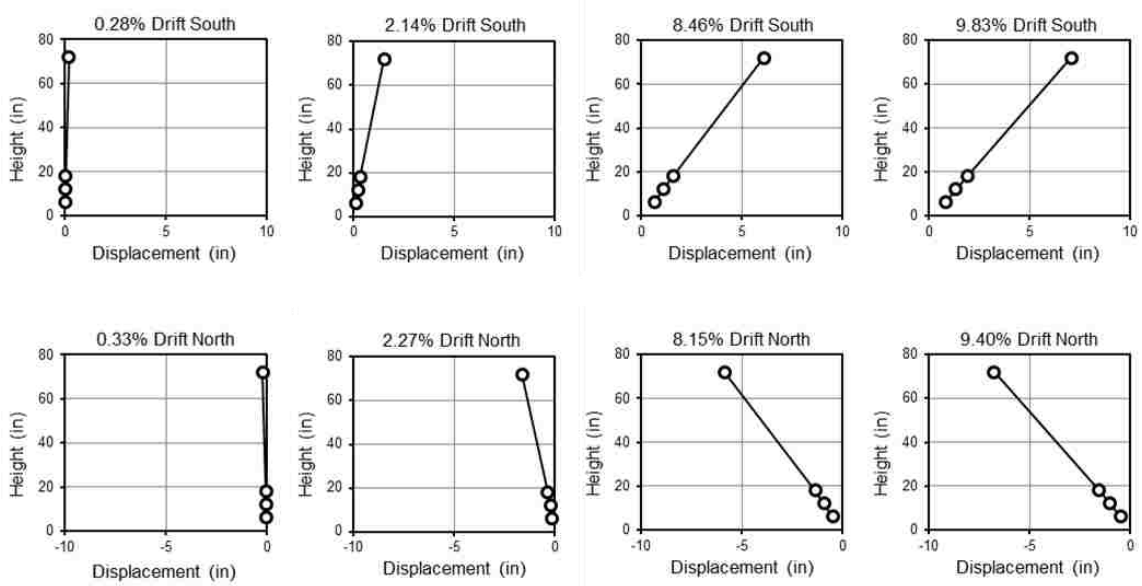

Figure 6.37: RC Column displacement profile measured from string potentiometers

6.8 CONNECTION ROTATION AND COLUMN ROTATION

This section separates the overall specimen rotation into two components: rotation attributed to the connection region, and rotation attributed to the column. Connection rotation is defined as the rotation occurring below the lowest inclinometer, located 3-in. above the surface of the cap beam. The remaining rotation is assumed to result from deformations occurring within the column above the lowest inclinometer. Sections 6.8.1 through 6.8.3 present the breakdown of column rotation contributions for the embedded specimens, welded RC specimens, and RC specimen, respectively.

6.8.1 Embedded Specimen Rotation Contributions

Figures 6.38 and 6.39 present the breakdown of column rotation for Specimens EMB80 and EMB96, respectively. For both specimens, it should be noted that the lowest inclinometer was located within the buckled region, and consequently fell off during high drift levels. For this reason, the rotation contribution plots for the two embedded specimens only include data up to the point of the inclinometer falling off. Additionally, the data for Specimen EMB96 has been corrected to account for a .02° offset.

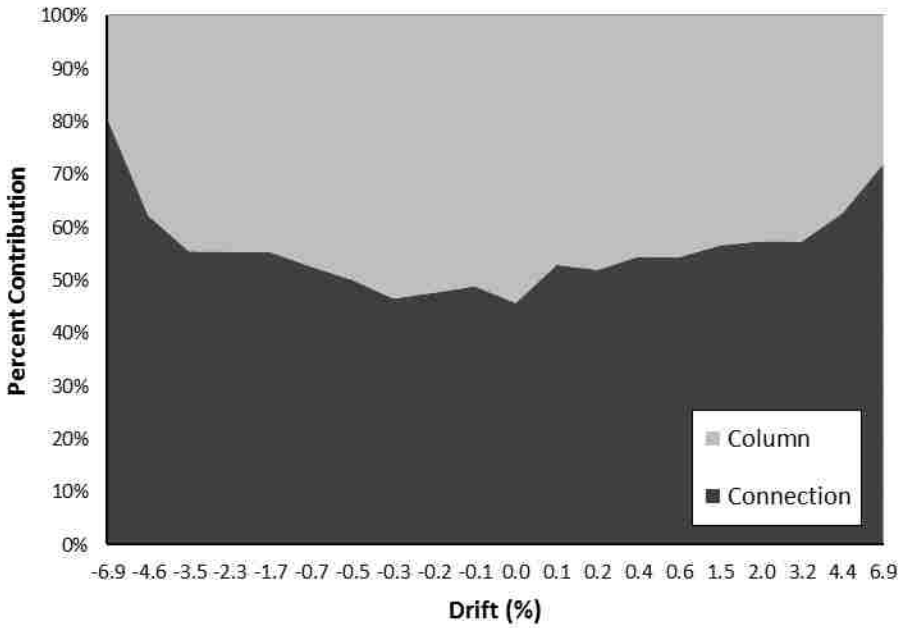

Figure 6.38: EMB80 Rotation Contributions from column & connection

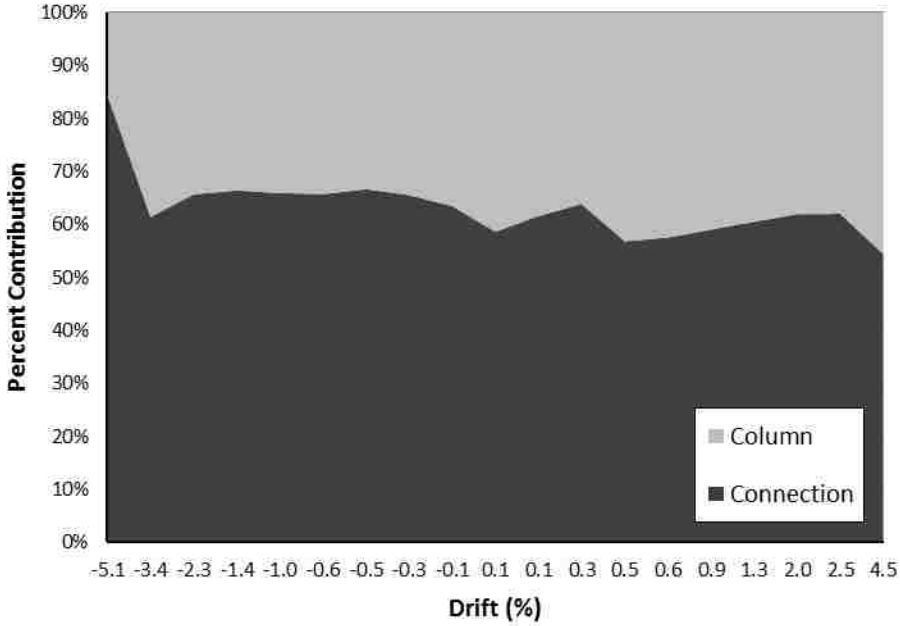

Figure 6.39: EMB96 Rotation Contributions from column & connection

6.8.2 WRC Specimen Rotation Contributions

Figures 6.40 and 6.41 present the breakdown of column rotation contribution for Specimens WRC and WRCUB, respectively.

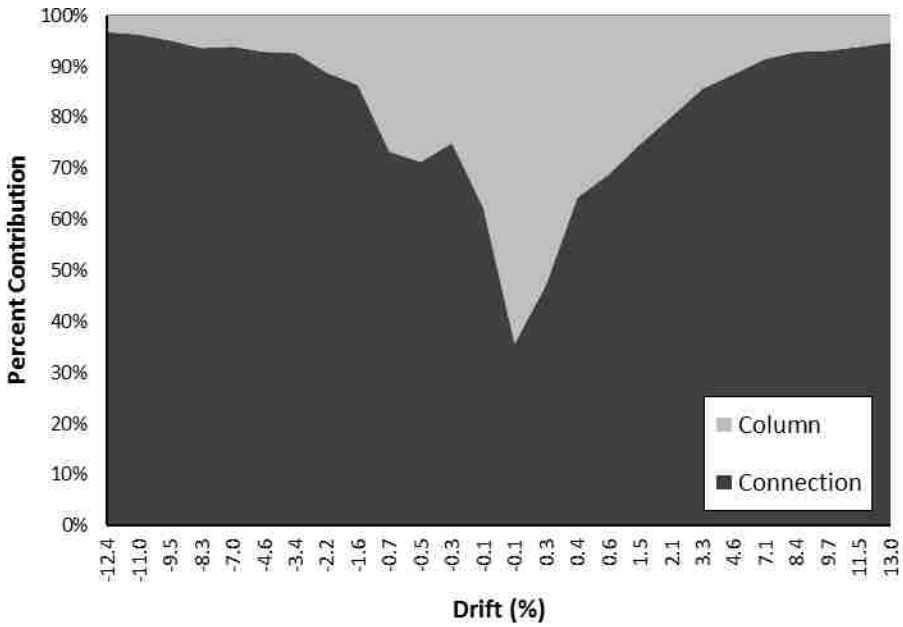

Figure 6.40: WRC Rotation Contributions from column & connection

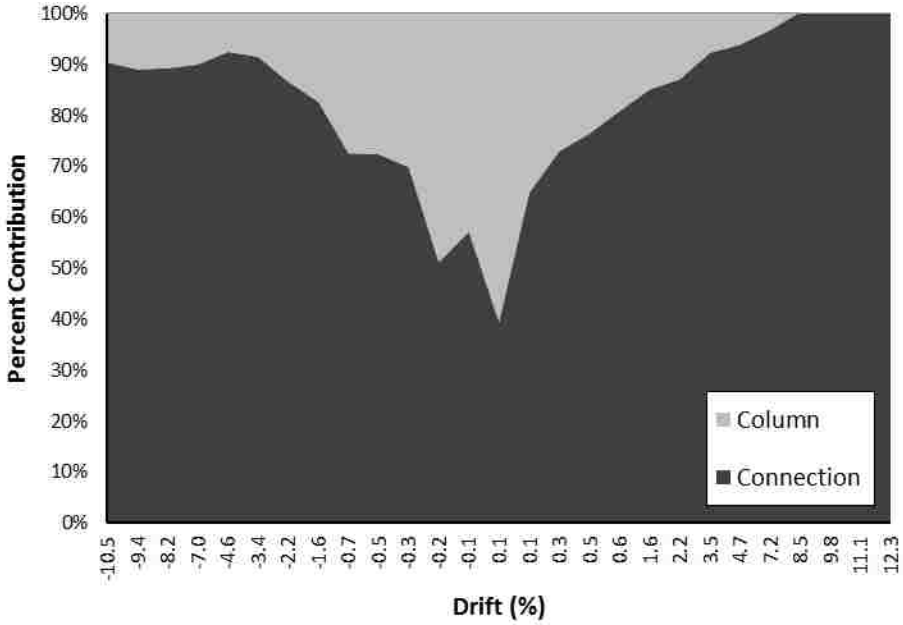

Figure 6.41: WRCUB Rotation Contributions from column & connection

6.8.3 RC Specimen Rotation Contributions

Figure 6.42 presents the breakdown of column rotation contribution for Specimen RC. It should be noted that data is only presented for drifts through 4.7%, as the inclinometer slipped after this drift set.

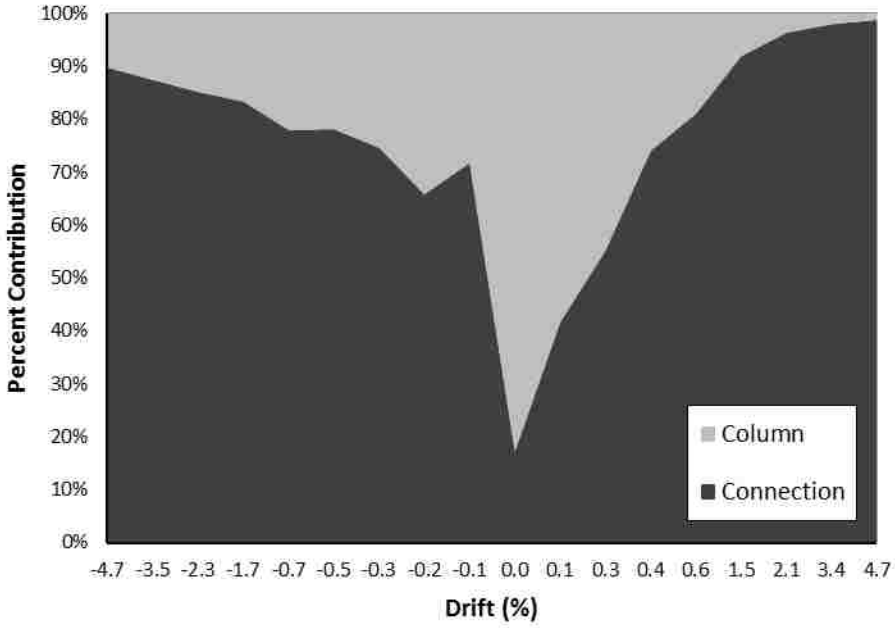

Figure 6.38: RC Rotation Contributions from column & connection

6.9 COLUMN BUCKLED SHAPE PROFILE

Sections 6.9.1 and 6.9.2 display the buckled profile progression of Specimens EMB80 and EMB96, respectively. The buckled profile was created using Optotrak data from the Northern & Southern-most faces of the specimens.

6.9.1 Buckled Profile of Specimen EMB80

Figures 6.43 and 6.44 show the progression of the buckled region of Specimen EMB80 using the Optotrak data. While visual buckling was first observed at 3.19% drift in the South direction and 3.45% drift in the North direction, Figure 6.44 shows initial buckling occurring at 1.48% drift and 1.62% drift in the South and North directions, respectively. Due to a corrupt file, Optotrak data is only available for Specimen EMB80 through drift set 7.

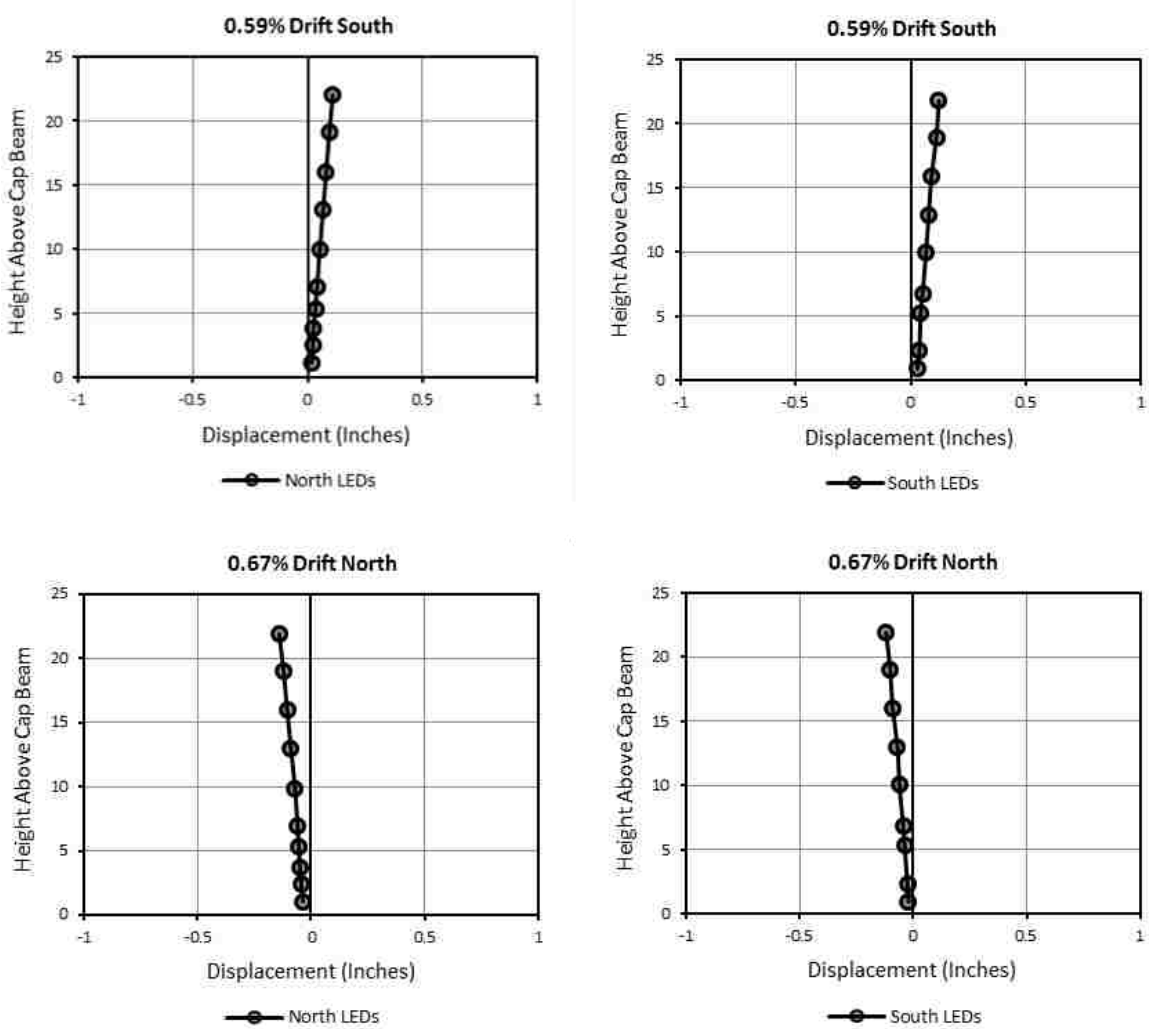

Figure 6.39: EMB80 Buckled Profile – Drift Set 5

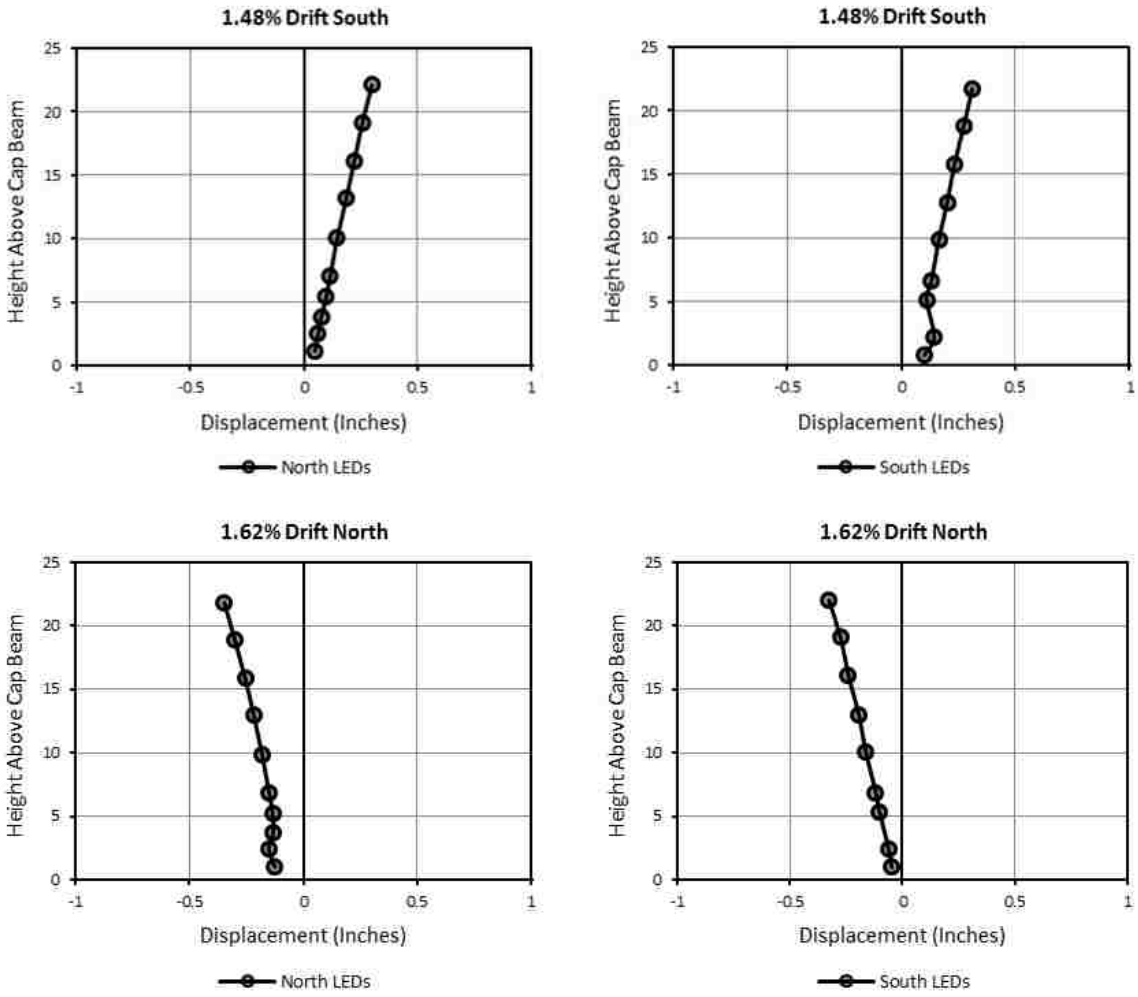

Figure 6.40: EMB80 Buckled Profile – Drift Set 7

6.9.2 Buckled Profile of Specimen EMB96

Figures 6.45 through 6.49 show the progression of the buckled region of Specimen EMB96 using the Optotrak data. While visual buckling was first observed at 2.55% drift in the South direction and 3.36% drift in the North direction, Figure 6.46 shows initial buckling occurring at 2.01% drift and 2.29% drift in the South and North directions, respectively.

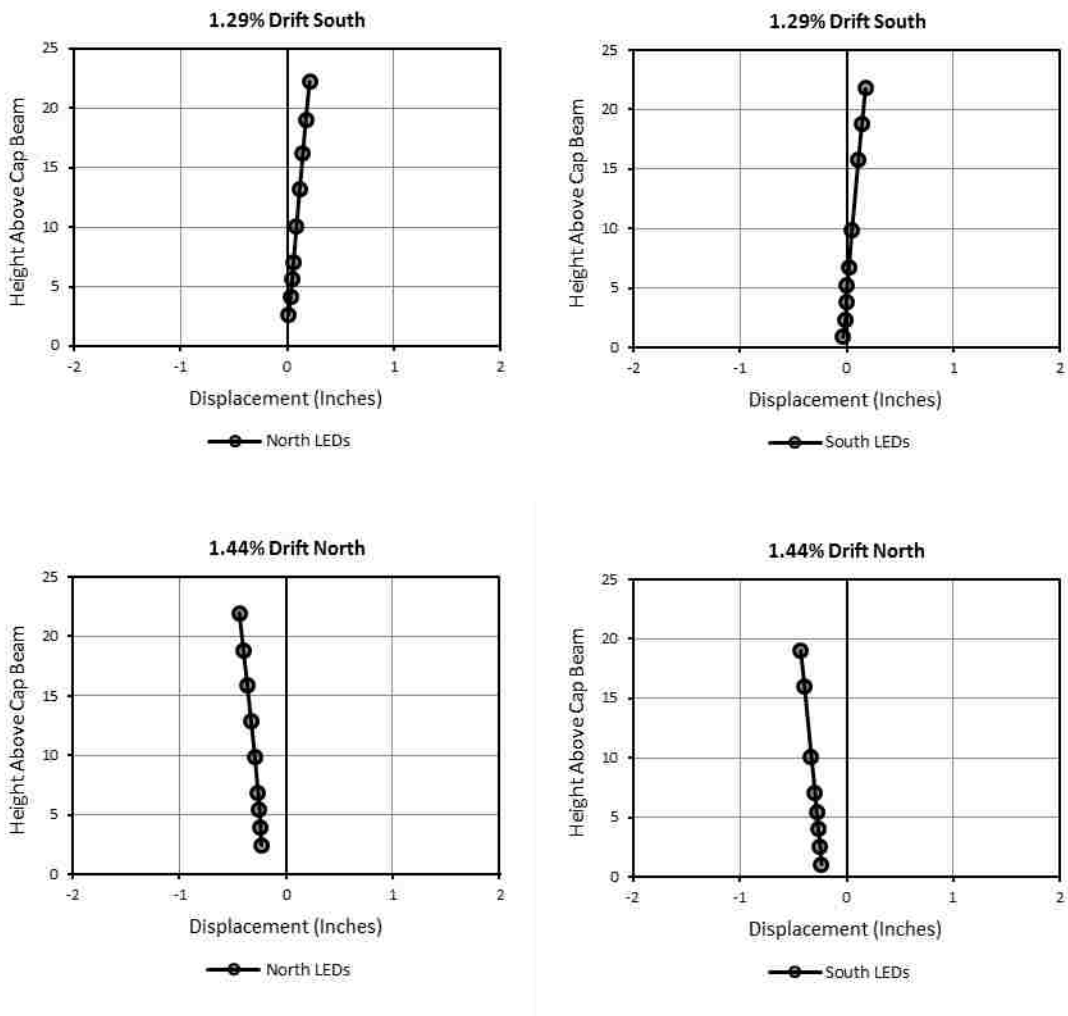

Figure 6.45: EMB96 Buckled Profile – Drift Set 8

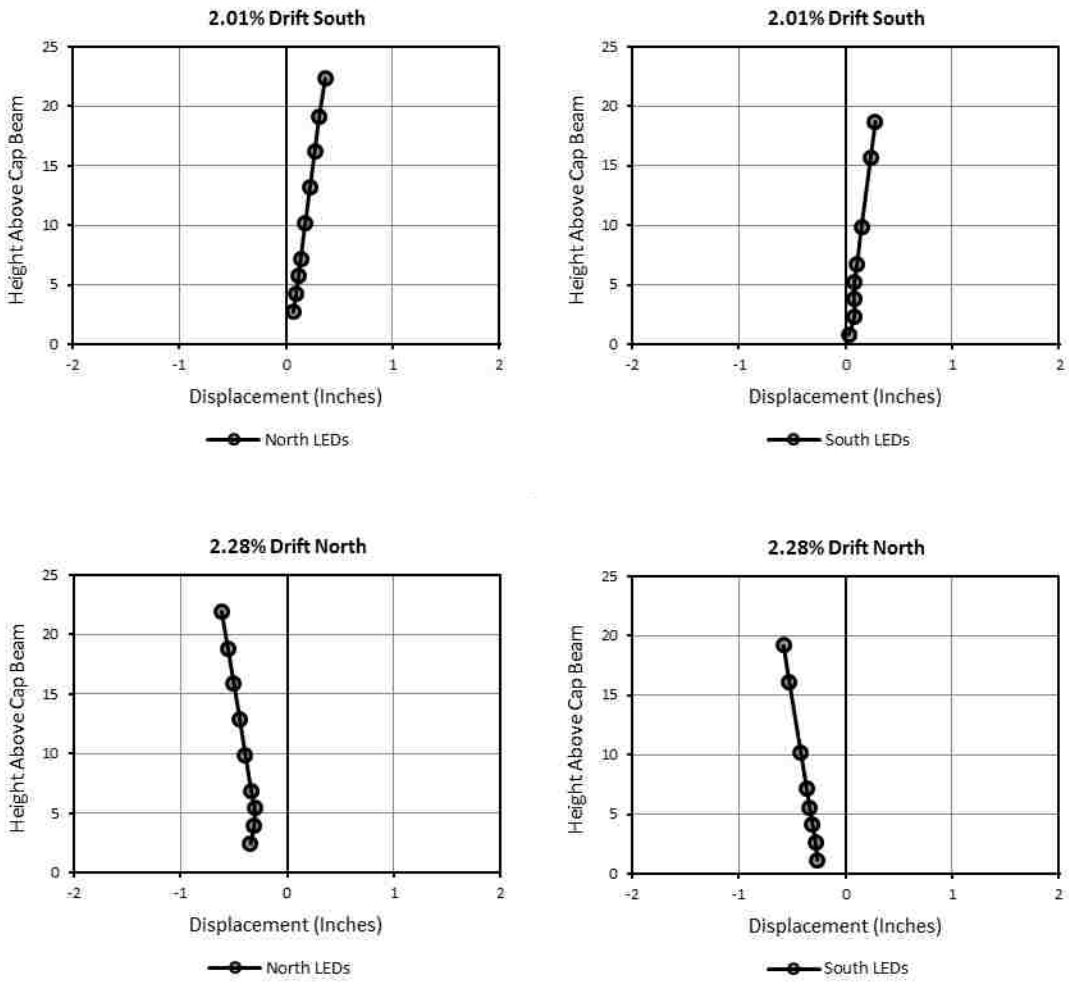

Figure 6.41: EMB96 Buckled Profile – Drift Set 10

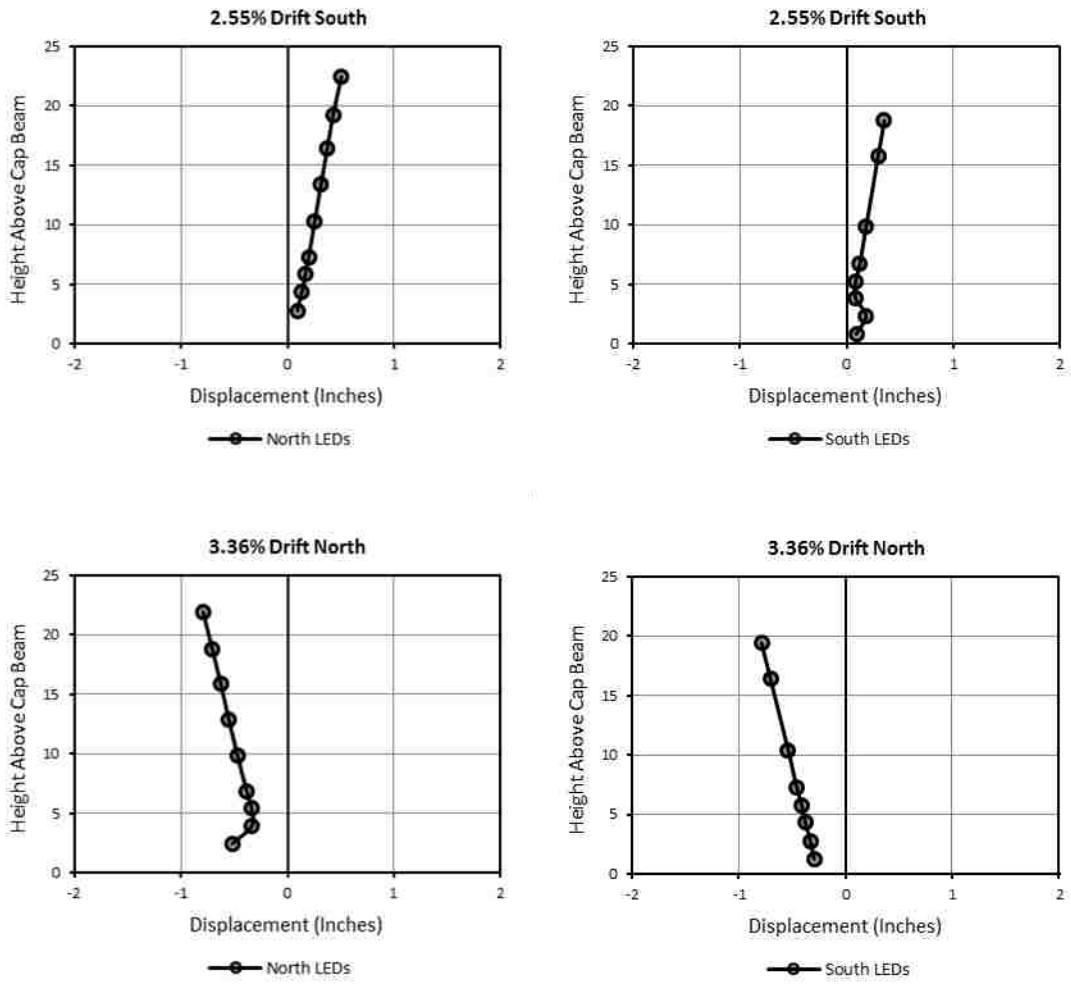

Figure 6.42: EMB96 Buckled Profile – Drift Set 11

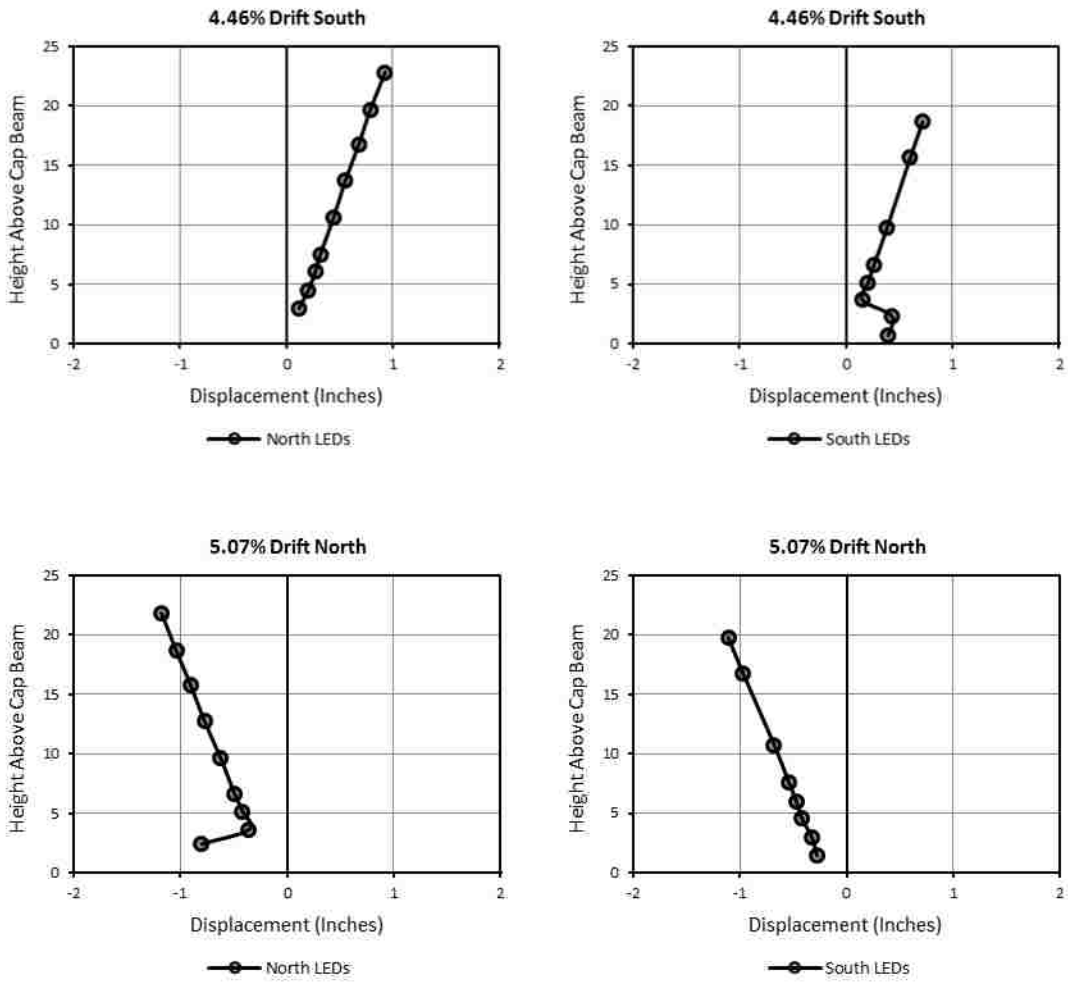

Figure 6.43: EMB96 Buckled Profile – Drift Set 13

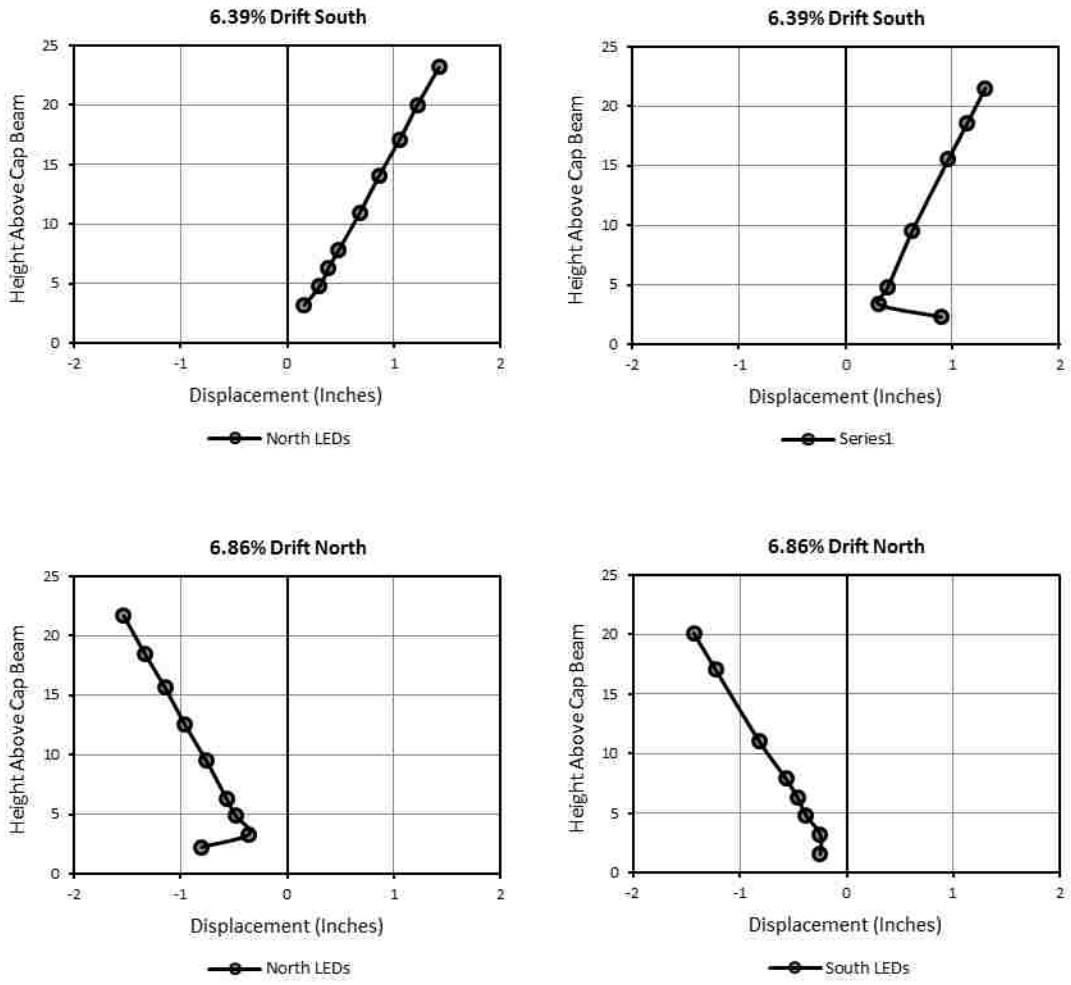

Figure 6.44: EMB96 Buckled Profile – Drift Set 14

6.10 FRAGILITY CURVES

The data from this research program has been combined with that from previous CFT column-to-footing connection tests conducted at the University of Washington to produce fragility functions capable of predicting the probability of damage state occurrences as a function of column drift. For comparison purposes, the data has been divided into two categories dependent on the type of steel tube used; spiral-weld or straight-seam. Tables 6.3 and 6.4 present the data used to create the fragility functions for the spiral-welded and straight-seam specimens, respectively.

Although a total of 19 CFT column-to-footing tests have been conducted at the University of Washington, the specimens that tested punching shear or exhibited pull-out failure modes have been omitted from the creation of these fragility curves. Figures 6.50 and 6.51 show the fragility curves resulting from the data presented in Tables 6.3 and 6.4 for spiral-weld and straight-seam specimens, respectively.

Table 6.3: Data used to produce fragility curves of spiral-welded specimens based on specimen drift

GSR	Specimen Designation	Test Parameters	Damage State Drift Ratios		
			Steel Yielding	Local Buckling	Tube Tearing
Kingsley	III	Embedment depth	0.6%	N.M.	N.M
Williams	5	Flexible underlay	1.0%	4.1%	7.1%
Williams	6	Flexible underlay	1.2%	3.2%	8.6%
Lee	3-50	Grouted, spiral weld	0.8%	1.4%	7.4%
Lee	4-50	Monolithic, spiral weld	0.8%	2.2%	7.4%
Lee	5-50	grouted, spiral weld	0.8%	3.2%	7.4%
Lee	6-50	grouted, spiral weld	0.8%	3.2%	7.5%
Berg	EMB80	Reduced annular ring, & cap beam width	0.6%	3.2%	7.0%

Table 6.4: Data used to produce fragility curves of straight-seam specimens based on specimen drift

GSR	Specimen Designation	Test Parameters	Damage State Drift Ratios		
			Steel Yielding	Local Buckling	Tube Tearing
Lee	1-50	Monolithic, straight weld	0.9%	3.2%	11.3%
Lee	2-50	grouted, straight weld	0.9%	2.2%	10.4%
Berg	EMB96	straight seam	0.7%	2.6%	7.5%

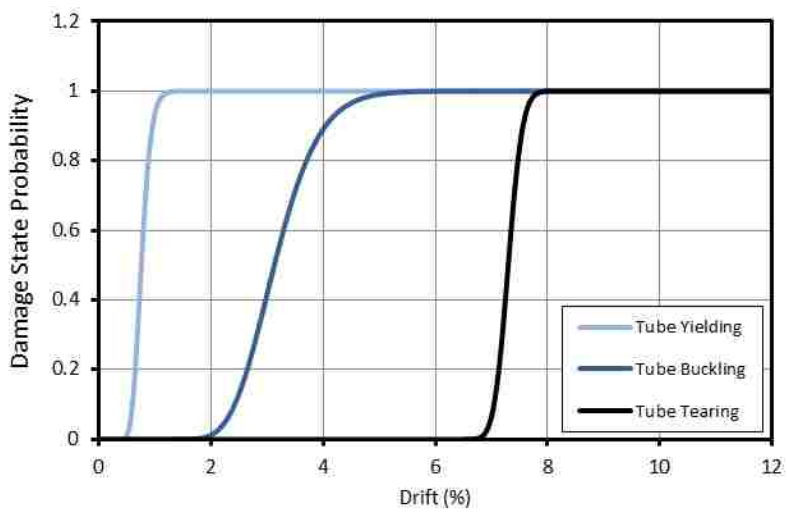

Figure 6.50: Fragility curves for tube yielding, buckling, and tearing of spiral-welded CFT specimens

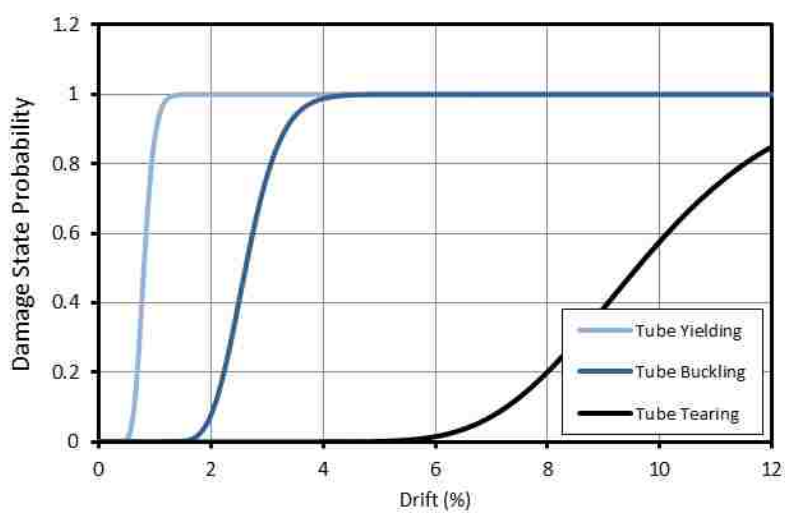

Figure 6.51: Fragility curves for tube yielding, buckling, and tearing of straight-seam CFT specimens

6.11 ASSESSMENT OF PERFORMANCE

This section evaluates the performance of the five specimens by comparing their observed behaviors and measured responses. Tables 6.5 through 6.9 summarize the response of the specimens at their respective damage states.

Table 6.5: Specimen EMB80 Response at Damage States

	Damage State		Drift Level	Lateral Load (kips)	M (k-in)	M/M_p
Column	Y1	Yielding	0.6%	83	5983	0.72
	B1	Initial Buckling	3.2%	137	10326	1.24
	B2	Buckling > 2t	4.4%	133	10405	1.25
	B3	Buckling > 4t	7.0%	129	10919	1.31
	T1	Tube Tearing	7.0%	129	10919	1.31
Cap Beam	C1	Initial Cracking	1.5%	125	8718	1.05
	C2	Cracking > 2mm	X	X	X	X
	U1	Initial Uplift	X	X	X	X
	U2	Uplift > 5mm	X	X	X	X
	U3	Uplift > 10mm	X	X	X	X

Table 6.6: Specimen EMB96 Response at Damage States

	Damage State		Drift Level	Lateral Load (kips)	M (k-in)	M/M_p
Column	Y1	Yielding	0.7%	88	6150	0.63
	B1	Initial Buckling	2.6%	156	11498	1.17
	B2	Buckling > 2t	4.5%	161	12382	1.26
	B3	Buckling > 4t	6.4%	152	11834	1.21
	T1	Tube Tearing	7.5%	140	11268	1.15
Cap Beam	C1	Initial Cracking	4.5%	161	12382	1.26
	C2	Cracking > 2mm	X	X	X	X
	U1	Initial Uplift	X	X	X	X
	U2	Uplift > 5mm	X	X	X	X
	U3	Uplift > 10mm	X	X	X	X

Table 6.7: Specimen WRC Response at Damage States

	Damage State		Drift Level	Lateral Load (kips)	M (k-in)	M/M_p
Column	Y1	Yielding	0.3%	45	3308	0.40
	G1	Grout Cracking	1.5%	112	8175	0.98
	G2	Grout Crushing	7.1%	117	9736	1.17
	BV	Bars Visible	8.4%	116	10065	1.21
	BV	Bar Fracture	X	X	X	X
Cap Beam	C1	Initial Cracking	1.5%	112	8175	0.98
	C2	Cracking > 2mm	7.10%	117	9736	1.17
	U1	Initial Uplift	7.10%	117	9736	1.17
	U2	Uplift > 5mm	-8.30%[1]	-74	-6930	0.83
	U3	Uplift > 10mm	-9.50%	-63	-6197	0.74

[1] Sign indicates direction of loading

Table 6.8: Specimen WRCUB Response at Damage States

	Damage State		Drift Level	Lateral Load (kips)	M (k-in)	M/M_p
Column	Y1	Yielding	0.3%	48	3563	0.43
	G1	Grout Cracking	1.6%	93	6964	0.84
	G2	Grout Crushing	4.7%	96	7757	0.93
	BV	Bars Visible	8.5%	84	8184	0.98
	BV	Bar Fracture	11.1%	65	6680	0.80
Cap Beam	C1	Initial Cracking	1.6%	93	6964	0.84
	C2	Cracking > 2mm	-8.2%	-77	-7482	0.90
	U1	Initial Uplift	-10.5%	-66	-6920	0.83
	U2	Uplift > 5mm	-11.6%	-55	-6900	0.83
	U3	Uplift > 10mm	X	X	X	X

Table 6.9: Specimen RC Response at Damage States

	Damage State		Drift Level	Lateral Load (kips)	M (k-in)	M/M_p
Column	Y1	Yielding	0.3%	51	3648	0.44
	G1	Grout Cracking	0.3%	51	3648	0.44
	G2	Grout Crushing	2.1%	96	7156	0.86
	BV	Bars Visible	9.8%	72	6416	0.77
	BV	Bar Fracture	9.8%	72	6416	0.77
Cap Beam	C1	Initial Cracking	1.5%	94	6868	0.82
	C2	Cracking > 2mm	X	X	X	X
	U1	Initial Uplift	-4.7%	-84	-7132	0.86
	U2	Uplift > 5mm	X	X	X	X
	U3	Uplift > 10mm	X	X	X	X

6.11.1 Comparison of EMB80 with Previous Work

In order to evaluate the performance of Specimen EMB80, the results of Specimen 3-50 tested by Jason Lee (2011) are summarized in this section to provide a basis for comparison.

Overview of Specimen 3-50

Specimen 3-50 consisted of a 20-in. diameter spiral-welded CFT column embedded 15.5-in. (0.775) into a precast reinforced concrete footing. The specimen was constructed using the isolated construction method, in which the embedded end of the CFT column was placed inside a void in the precast footing, which was subsequently filled with high-strength, fiber-reinforced grout. The annular ring welded to the embedded end of the steel tube was 0.25-in. thick, with respective inner and outer diameters of 16-in. and 28-in. The footing stood 24-in. deep, 76-in. long, and 68-in. wide.

The specimen was subjected to a constant axial load equivalent to 10% of its gross axial capacity, as well as a cyclic, displacement-controlled lateral load. The specimen was subjected to 28 complete cycles following ATC-24 loading protocol.

The overall behavior of the specimen consisted of yielding of the steel tube, followed by local buckling near the base of the column. Failure of the specimen consisted of ductile tearing at the apex of the buckled region at 7.40% drift. Figure 6.52 shows the hysteretic moment-drift behavior of Specimen 3-50 with highlighted damage states.

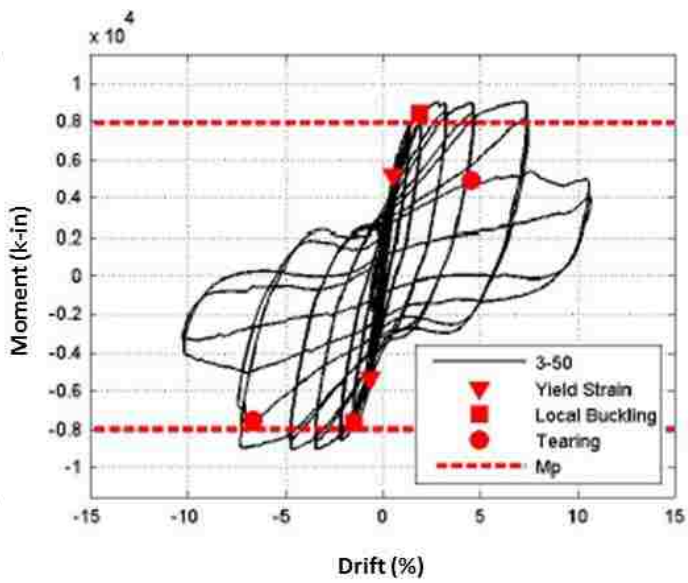

Figure 6.52: Moment-drift behavior of Specimen 3-50 (Adapted from Lee, 2011)

Table 6.10 summarizes the response of Specimen 3-50 at its damage states of tube yielding, buckling, and tearing, as well as cap beam cracking and pullout.

Table 6.10: Specimen 3-50 Response at Damage States

	Damage State	Drift Level	Lateral Load (kips)	M (k-in)	M/M_p
Column	Yielding	0.8%	N.M	6309	0.79
	Local Buckling	1.4%	N.M	7499	1.04
	Initial Tearing	7.4%	N.M	8241	0.94
Cap Beam	Radial Cracking	0.6%	N.M	5200	0.65
	Connecting Cracks	X	X	X	X
	Cone Pullout	X	X	X	X

6.11.2 Comparison of Specimens EMB80 and 3-50

A comparison of tables 6.5 and 6.10 show similar progressions of damage for Specimens EMB80 and 3-50. The overall behavior of both specimens consisted of yielding between 0.6% and 0.8% drift, followed by local buckling and initial tearing at 7.0% drift and 7.4% for Specimens EMB80 and 3-50, respectively.

While neither specimen experienced any pullout, the primary difference in behavior between the two specimens was that Specimen EMB80 experienced an increase in the magnitude of cap beam cracking compared to Specimen 3-50. However, the cracks were all hairline in width.

While Specimen EMB80 experienced an increase in concrete damage, a comparison of strengths show that the reduced cap beam width and reduced annular ring diameter of Specimen EMB80 did not affect its overall capacity, as it was still able to exceed the full plastic moment capacity of the CFT.

6.11.3 Comparison of Specimens EMB80 and EMB96

Results from Tables 6.5 and 6.6 show the following trends:

- Both specimens reached the column damage states of initial yielding, buckling, and tube tearing at comparable drifts (within 0.6% drift of one another), despite EMB96 having a larger D/t ratio.
- Specimen EMB96 experienced initial cap beam cracking several cycles later than EMB80 (4.5% drift compared to 1.5% drift).

6.11.4 Comparison of Specimens WRC AND WRCUB

Results from Tables 6.7 and 6.8 show the following trends:

- Both welded RC specimens had a pull-out failure mode. Specimen WRC experienced uplift exceeding 10mm with no reinforcing bar fracture, while Specimen WRCUB experienced uplift exceeding 5mm with reinforcing bar fracture at 11.1% drift.
- Specimen WRCUB experienced less cap beam damage compared to Specimen WRC. While both specimens experienced initial cap beam cracking at similar drifts (1.5% drift compared to 1.6% drift), Specimen WRC reached damage states C2, U1, and U2 at earlier drift levels compared to WRC. In addition, Specimen WRC experienced uplift exceeding 10mm, whereas Specimen WRCUB did not.

6.11.5 Comparison of Specimens RC and WRC

A comparison of Specimen RC with Specimens WRC/WRCUB shows the following trends:

- Specimen RC experienced initial cap beam cracking at the same drift as Specimen WRC.
- Specimen RC experienced initial uplift earlier than both WRC and WRCUB (4.7% drift vs. 8.3% & 10.6%, respectively). Despite this, Specimen RC experienced less overall uplift compared to WRC and WRCUB.
- Specimen RC experienced less cracking than both WRC and WRCUB.

6.12 DESIGN RECOMMENDATIONS

Results from numerical analyses and experimental investigations were used to develop the following design recommendations for CFT column-to-cap beam connections:

Diameter of Annular Ring

In order to provide adequate anchorage and transfer stresses to the surrounding concrete and reinforcement, it is recommended that the outer diameter of the annular ring be dimensioned as:

$$D_0 = D + 16t \tag{6.2}$$

where D_0 is the outer diameter of the annular ring, D is the diameter of the column, and t is the thickness of the steel tube. The measured response of Specimen EMB80 shows that the diameter of the annular ring can be reduced according to Eq. 6.4 without influencing the capacity of the embedded connection.

Width of Cap Beam

Results from Specimen EMB80 also show that the width of the cap beam, b_{cap}, can be reduced to twice the diameter of the column without influencing the capacity of the embedded CFT connection.

$$b_{cap} = 2D \tag{6.3}$$

Length of Weld In WRC Connections

The welds of the welded RC connections should be designed to develop the full capacity of the reinforcing bar.

CHAPTER 7
CONCLUSIONS

An experimental research program was undertaken at The University of Washington to investigate the behavior of CFT column-to-cap beam connections. This chapter summarizes the research which was conducted, presents the results and conclusions, and provides recommendations for future research.

7.1 SUMMARY OF RESEARCH

Five scaled CFT bridge piers were experimentally tested under combined axial-flexure loading to investigate the performance of different CFT column-to-cap beam connection types. Three categories of connections were evaluated; 1) an embedded connection in which the steel tube is embedded in the cap beam concrete, 2) a welded reinforced concrete connection in which headed reinforcing bars are welded to the inside of the steel tube and extend into the cap beam, and 3) a reinforced concrete connection in which a traditional reinforced concrete cage is placed within the CFT column and extends into the cap beam. Two embedded connection tests were conducted to evaluate the influence of steel tube fabrication methods; one with a straight seam welded tube, and one with spiral welded tube. In addition, two welded reinforced concrete connection test were conducted to evaluate the influence of debonded reinforcing bars. Each specimen was subjected to a constant axial load, as well as a cyclic, displacement-controlled lateral loading protocol. The behavior of each specimen was observed, measured, and compared to evaluate the influence of the different connection parameters.

7.2 RESEARCH RESULTS AND CONCLUSIONS

The following conclusions were drawn based on the interpretation of experimental observations and measured responses:

Influence of Reduced Cap Beam Width and Annular Ring Diameter:

- The width of the cap beam can be reduced to 2D without influencing the capacity of the embedded CFT connections. Specimens with a reduced cap beam width of 2D experience an increase in cap beam damage.
- The diameter of the annular ring can be reduced to D + 16t without influencing the capacity of the embedded connection.

Influence of Steel Fabrication Type:

- Steel tubes fabricated with a straight seam weld provide an increase in drift ductility. Specimen EMB96 reached its final damage state of steel tube tearing at a greater drift than Specimen EMB80, despite its larger D/t ratio.

Influence of Debonded Reinforcing Bars:

- Specimens with debonded Welded RC connections experience reduced cap beam damage compared to those with bonded RC connections. The failure mode of Specimen WRCUB was reinforcing bar fracture, compared to pullout of Specimen WRC.

Influence of Transverse Reinforcement

- The specimen with transverse reinforcement experienced a decrease in cap beam damage compared to those without. This decrease in damage can be attributed to the confining effect of the transverse reinforcement in the void and soffit region.

7.3 RECOMMENDATIONS FOR FUTURE RESEARCH

The objective of this research program was to develop connection details capable of sustaining cyclic loading while mitigating damage in the superstructure components. While the embedded specimens achieved the design objectives, additional research is required to further develop the welded RC connection details to achieve design objectives. Based on the improved response of the RC connection detail, it is recommended to incorporate transverse reinforcement in the embedded region of the WRC connection.

BIBLIOGRPAHY

AASHTO (2011). AASHTO LRFD Bridge Design Specification. American Association of State Highway and Transportation Official, Washington, DC.

ACI (2011). Building Code Requirements for Structural Concrete. American Concrete Institute, Farmington Hills, MI.

AISC (2011). *Steel Construction Manual*. American Institute of Steel Construction, Chicago, IL, 14 edition.

ATC-24 (1992). *Guidelines for Testing Steel Components*. Applied Technology Council, Redwood City, CA.

Caltrans (2010). *Caltrans Seismic Design Criteria*. California Department of Transportation, Sacramento, CA.

Kawaguchi, J. and Morino, S. (2006). Experimental study on strength and stiffness of bare type cft column base with central reinforcing bars. *Composite Construction in Steel and Concrete V*.

Kingsley, A. (2005). Experimental and analytical investigation of embedded column base connections for concrete filled high strength steel tubes. Master's thesis, University of Washington.

Lee, J. (2011). Experimental investigation of embedded connections for concrete-filled steel tube columns subjected to combined axial-flexural loading. Master's thesis, University of Washington.

Lehman and Roeder (2012) Initial Investigation of Reinforced Concrete Filled Tubes for use in Bridge Foundations

Marson, J. and Bruneau, M. (2004). Cyclic testing of concrete-filled circular steel bridge piers having encased fixed-base detail. *ASCE Journal of Bridge Engineering*, 9(1):14–23.

Montejo, L., Gonzalez-Roman, L. A., and Kowalsky, M. (2013). Seismic performance evaluation of reinforced concrete-filled steel tube pile/column bridge bents. *Journal of Earthquake Engineering*, 16(3):401–424.

O'Neill, K. (2011). Experimental Investigation of Circular Concrete Filled Steel Tube Geometry on Seismic Performance. Master's thesis, University of Washington.

Stephens, M. (2014). Performance Based Design Expressions for CFT Bridges. Proposal, University of Washington.

Williams, T. (2006). Experimental investigation of high strength concrete filled steel tubes in embedded column base foundation connections. Master's thesis, University of Washington.

APPENDIX A

RAW STRAIN GAUGE DATA

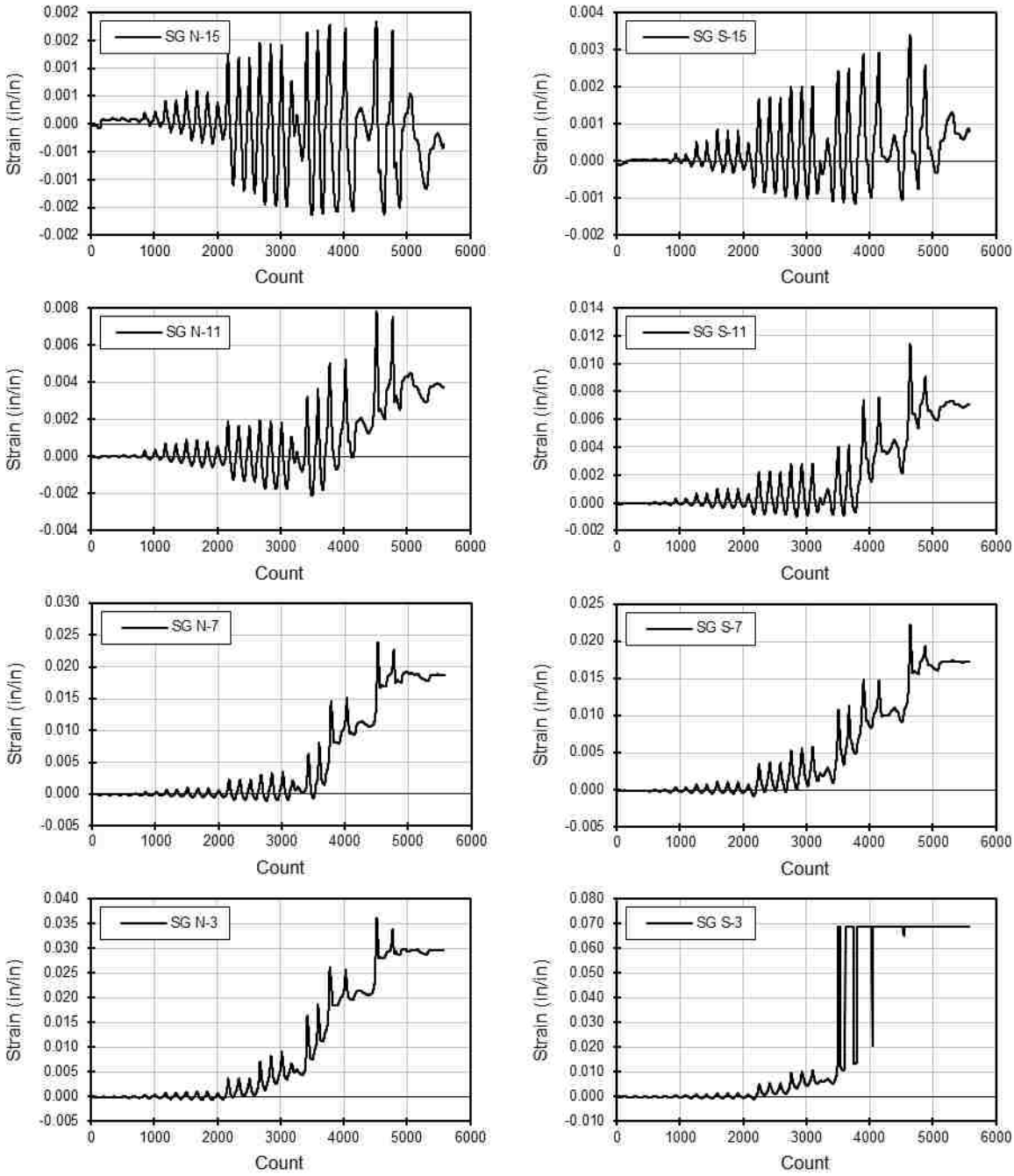

Figure A.1: EMB80 Raw tube strain gauge data 1

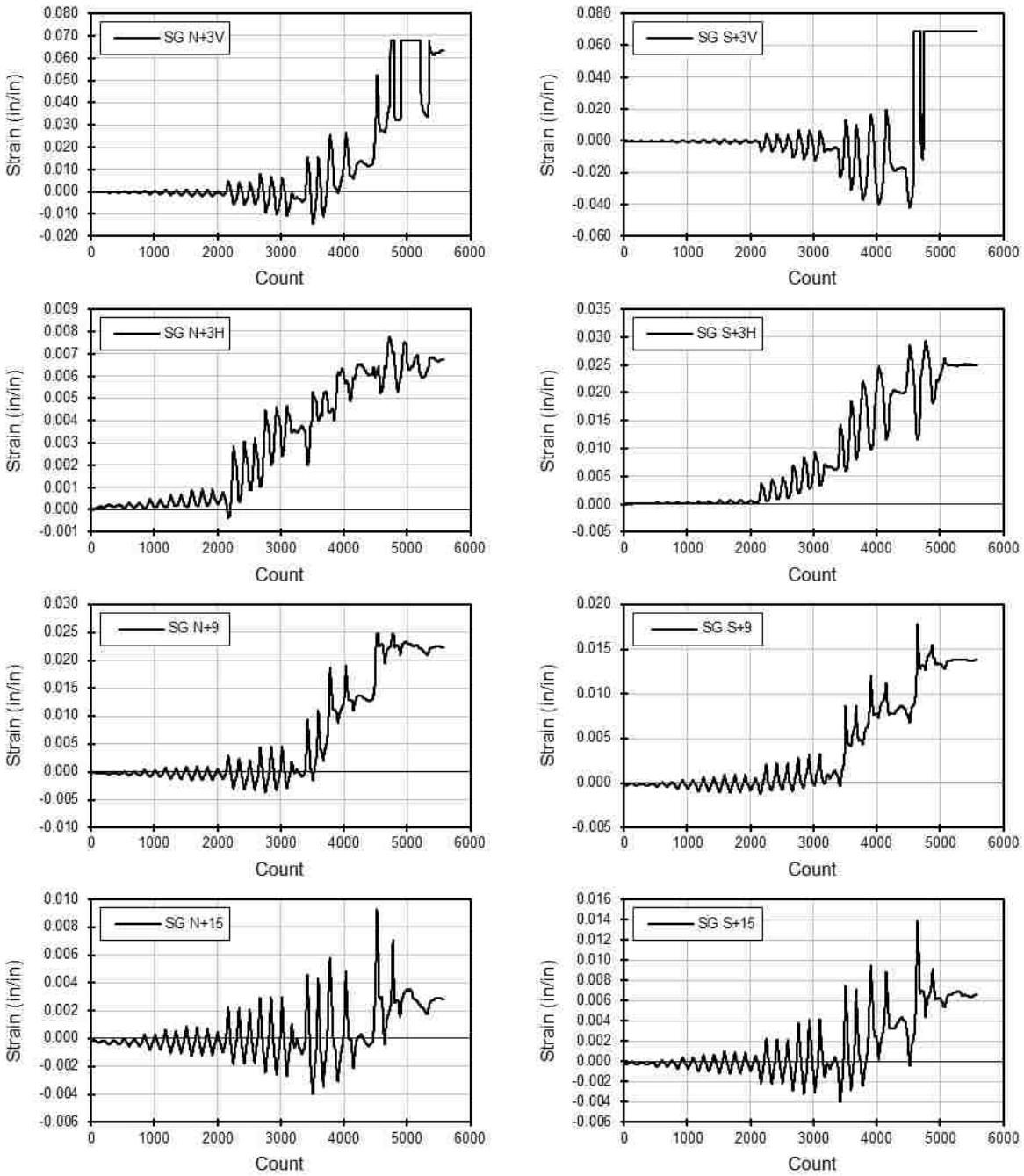

Figure A.2: EMB80 Raw tube strain gauge data 2

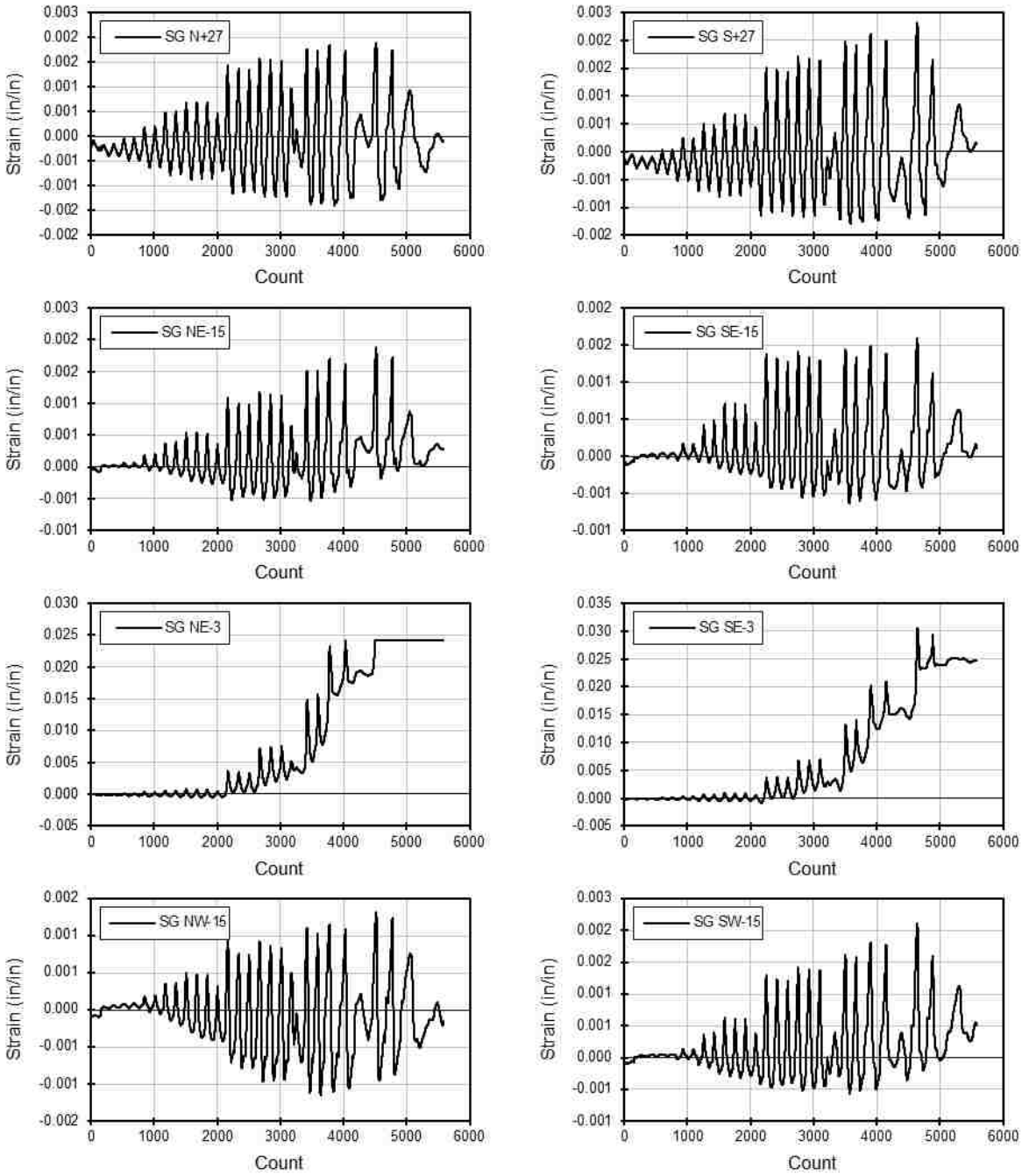

Figure A.3: EMB80 Raw tube strain gauge data 3

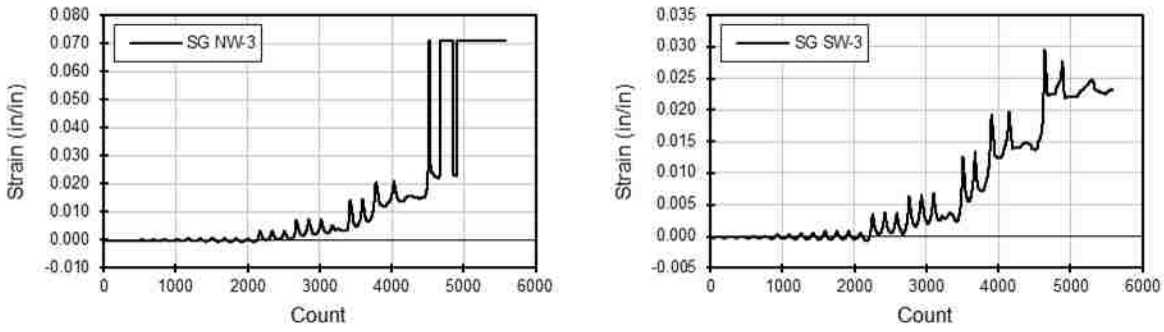

Figure A.4: EMB80 Raw tube strain gauge data 4

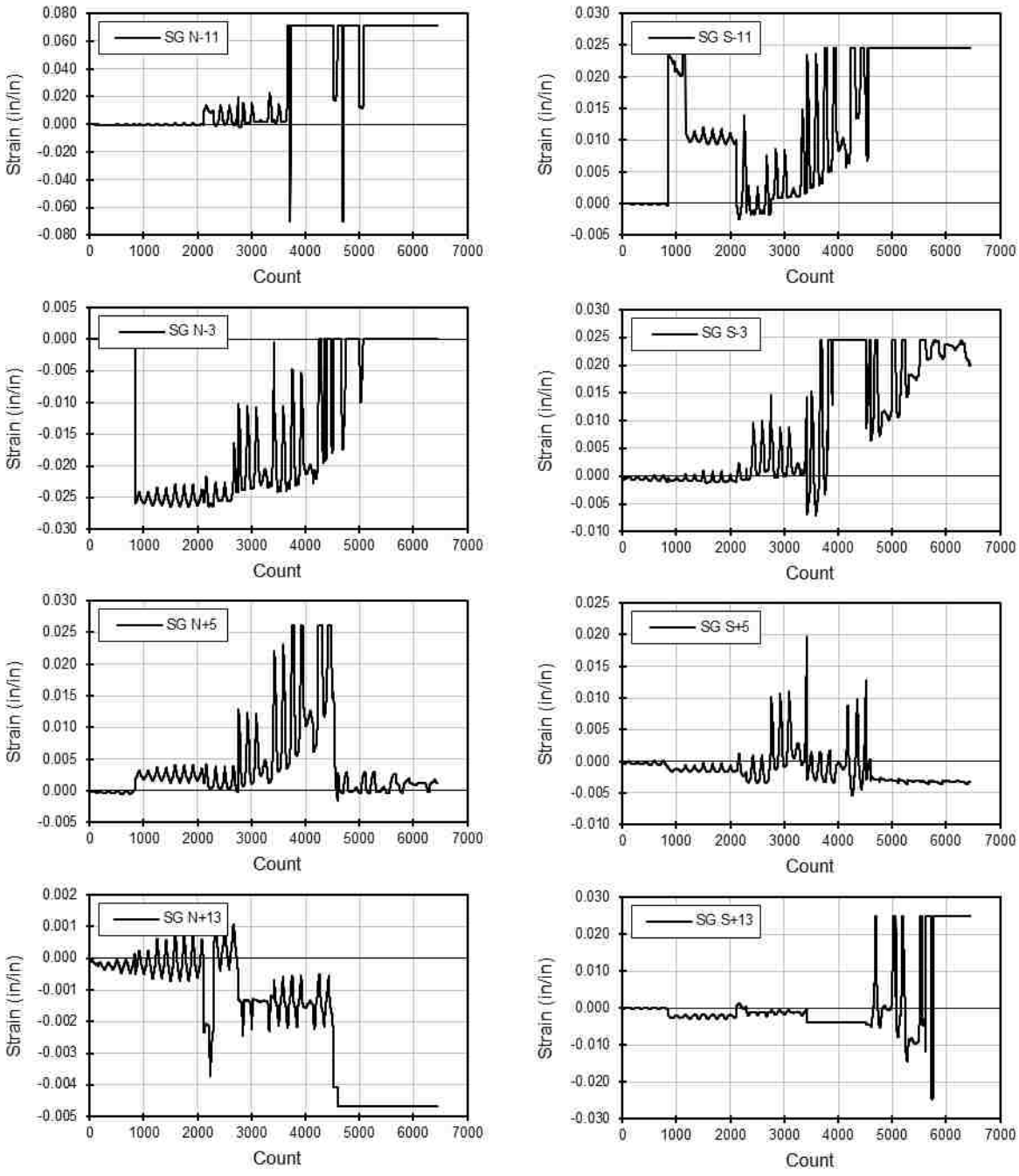

Figure A.5: WRC Raw longitudinal reinforcing bar strain gauge data 1

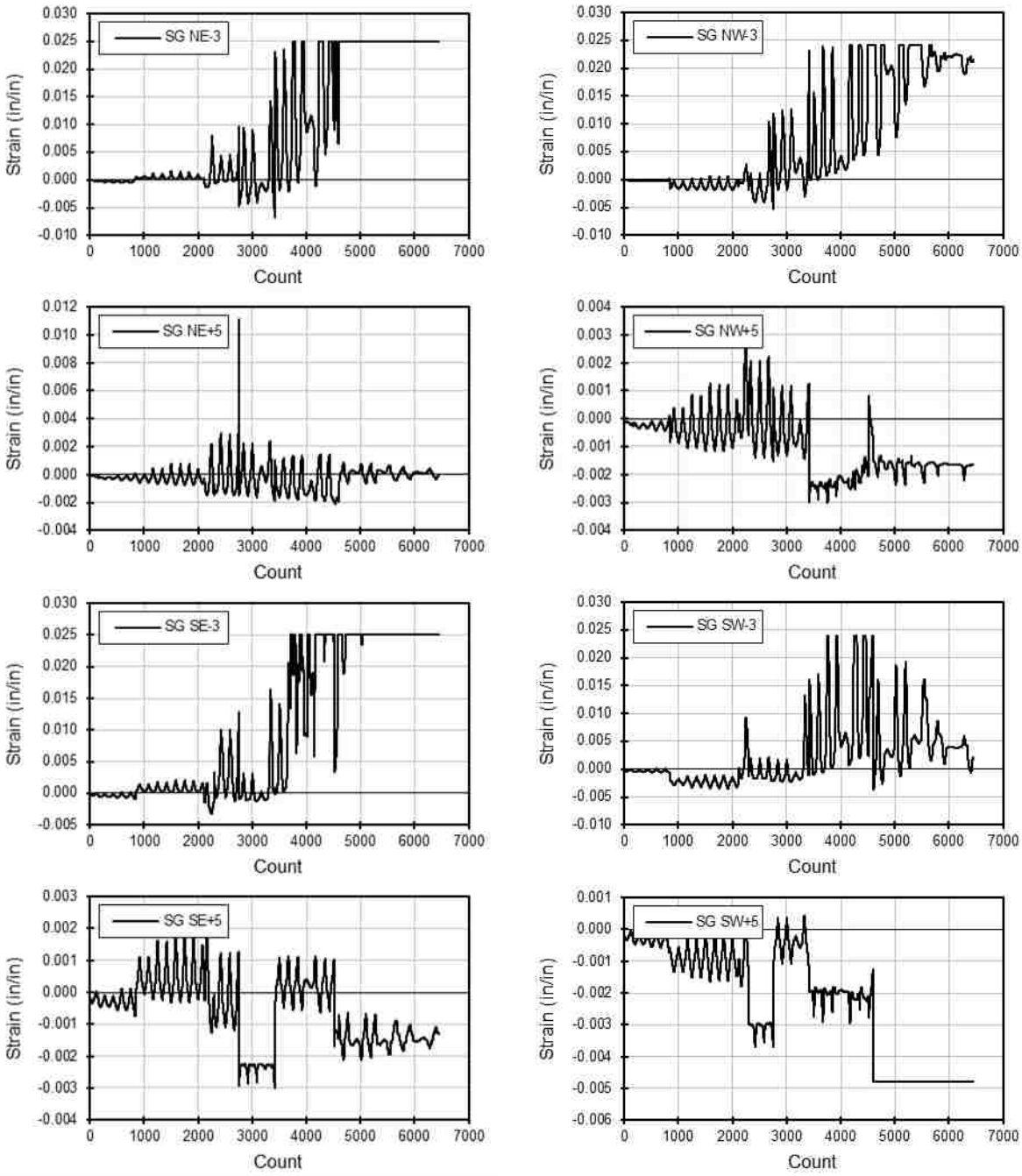

Figure A.6: WRC Raw longitudinal reinforcing bar strain gauge data 2

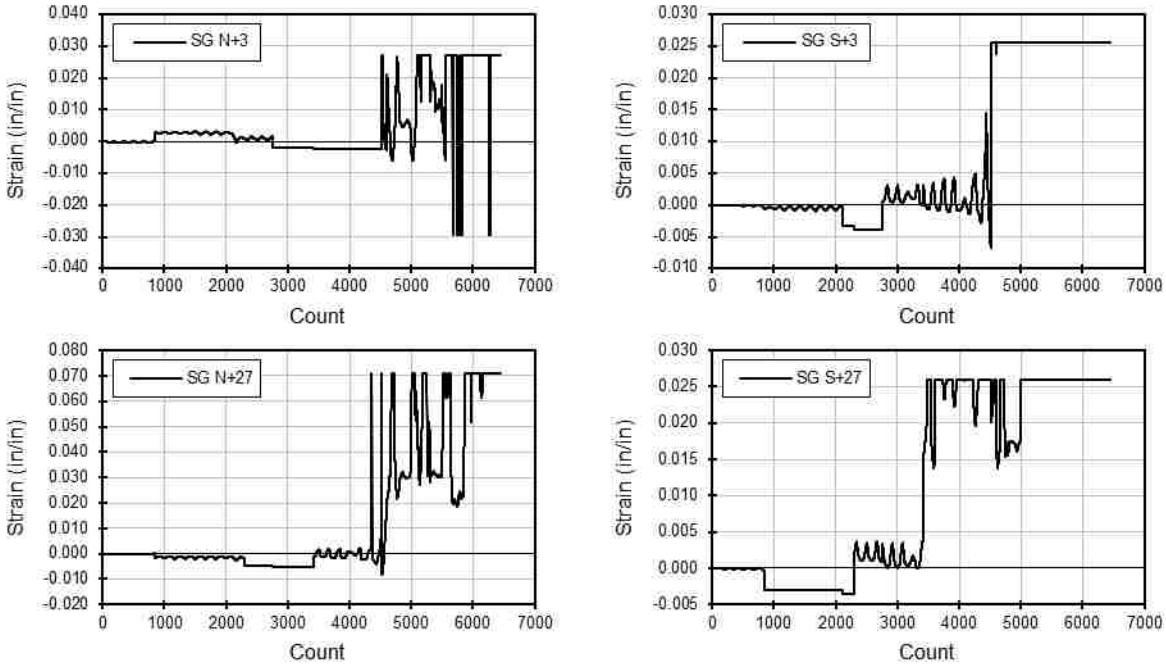

Figure A.7: WRC Raw longitudinal tube strain gauge data

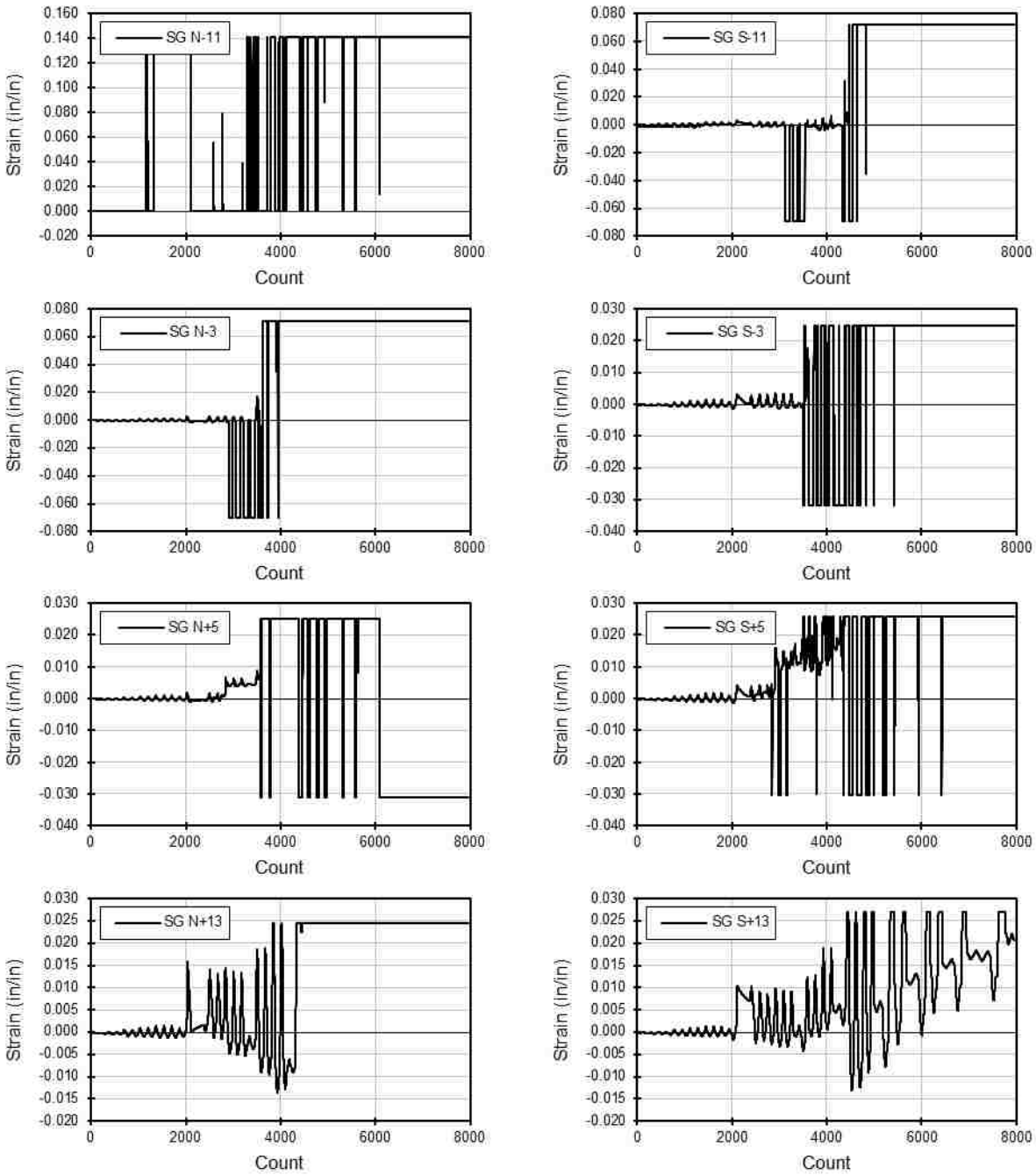

Figure A.8: WRCUB Raw longitudinal reinforcing bar strain gauge data 1

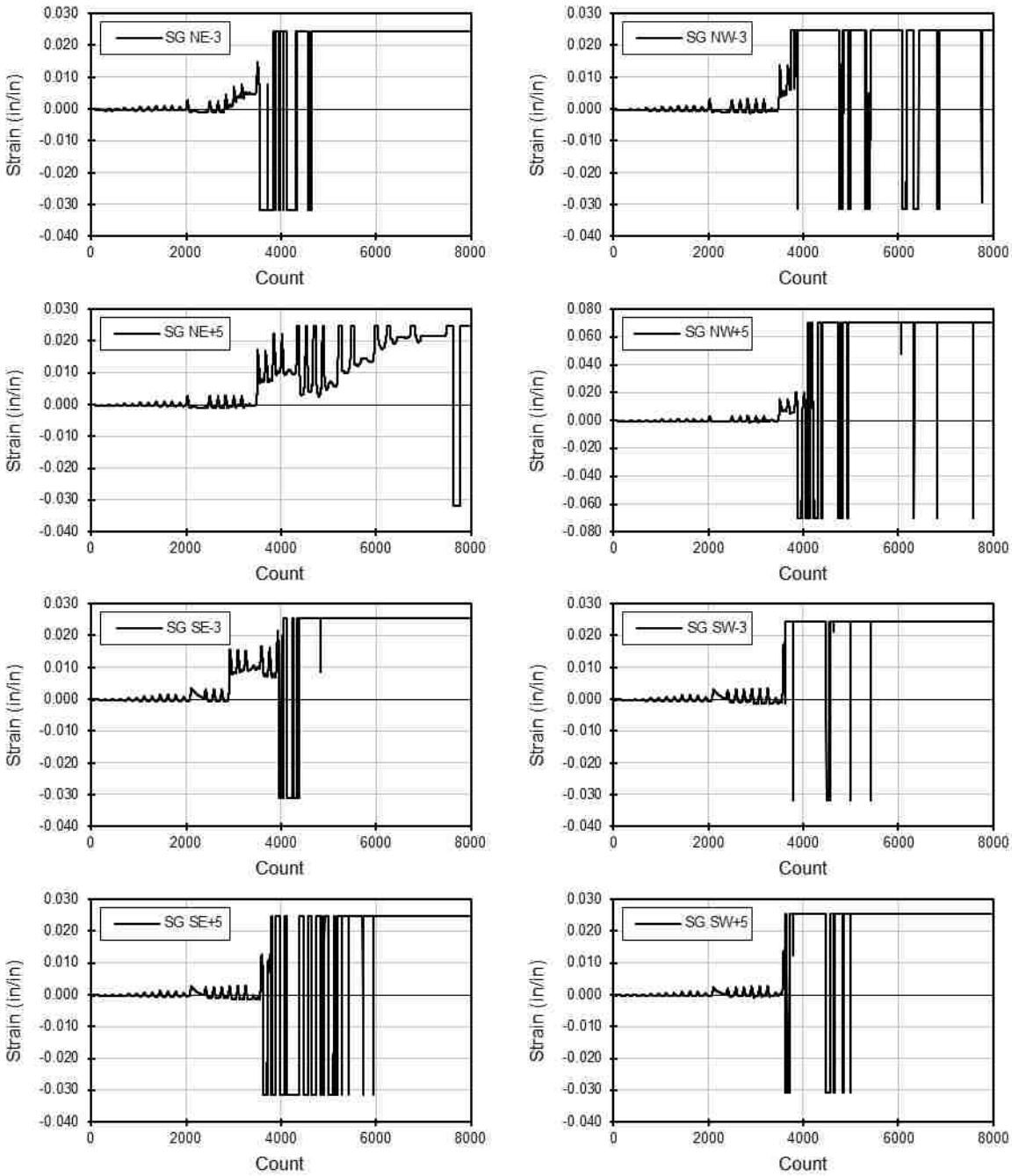

Figure A.9: WRCUB Raw longitudinal reinforcing bar strain gauge data 2

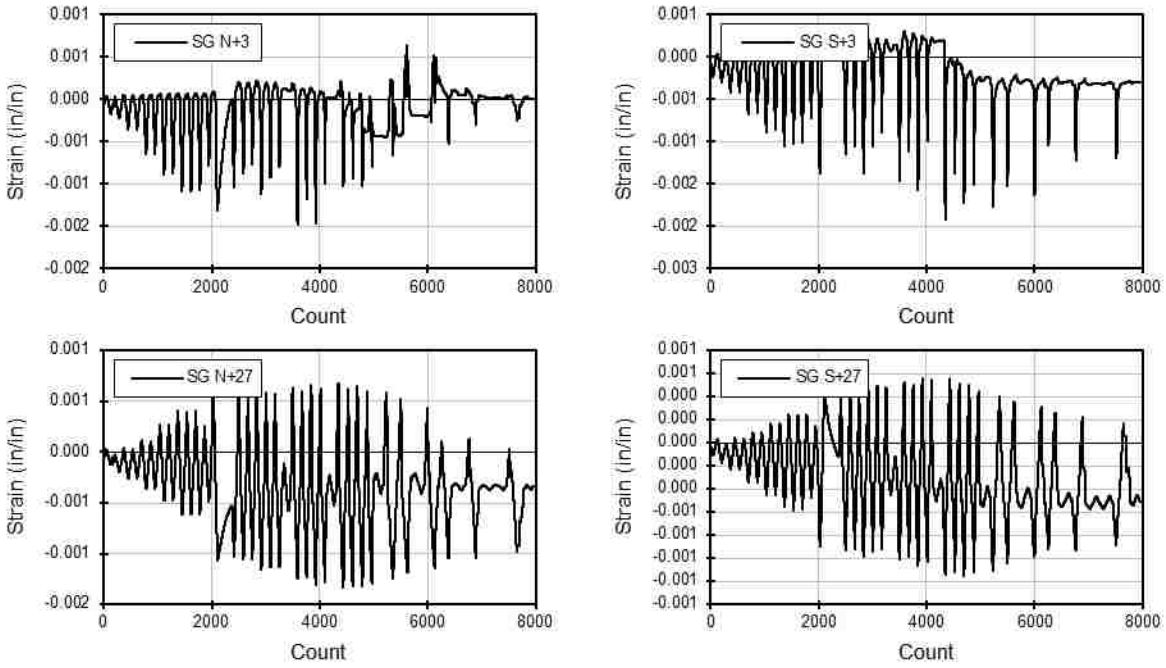

Figure A.10: WRCUB Raw longitudinal tube strain gauge data

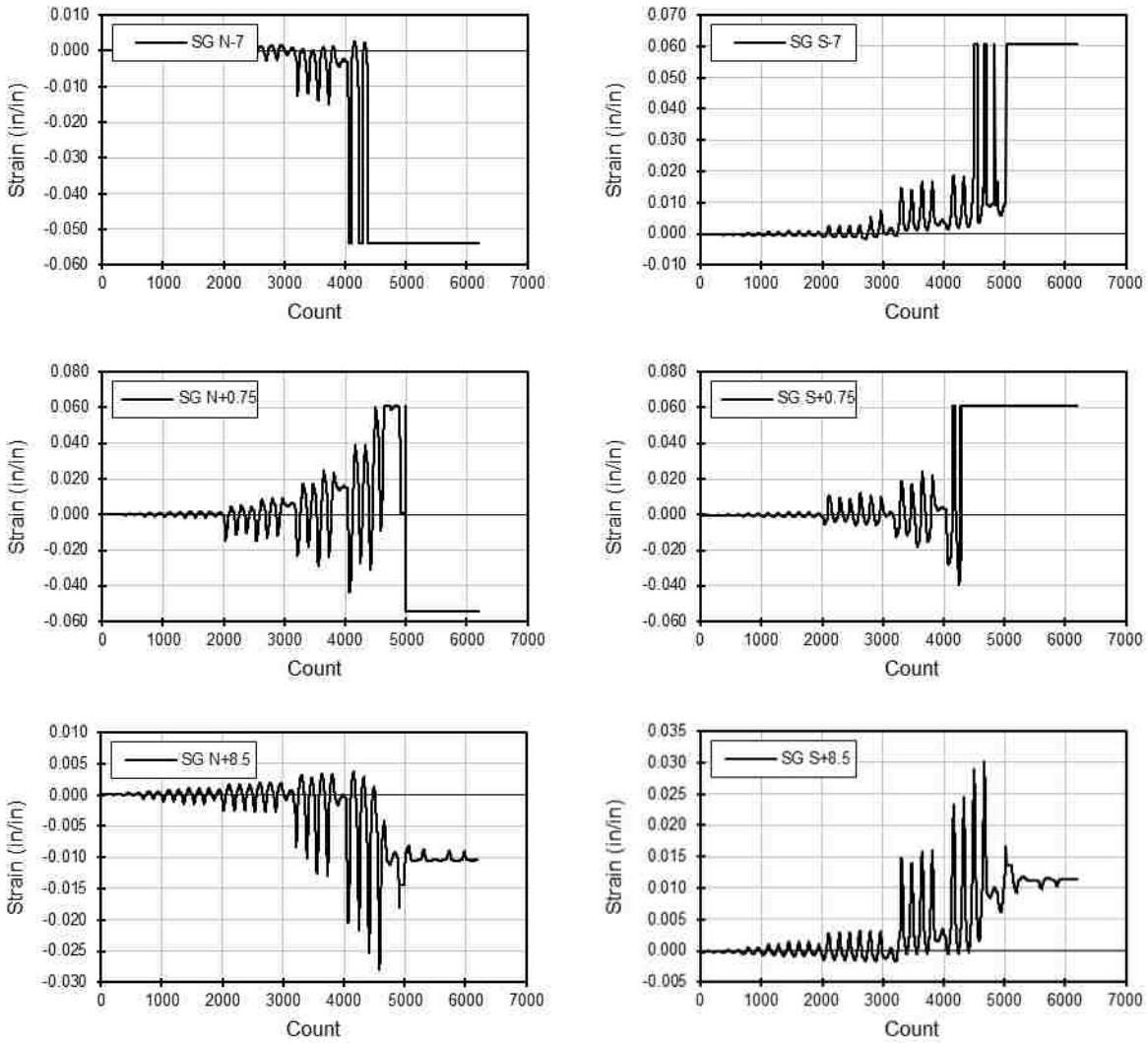

Figure A.11: RC Raw longitudinal reinforcing bar strain gauge data 1

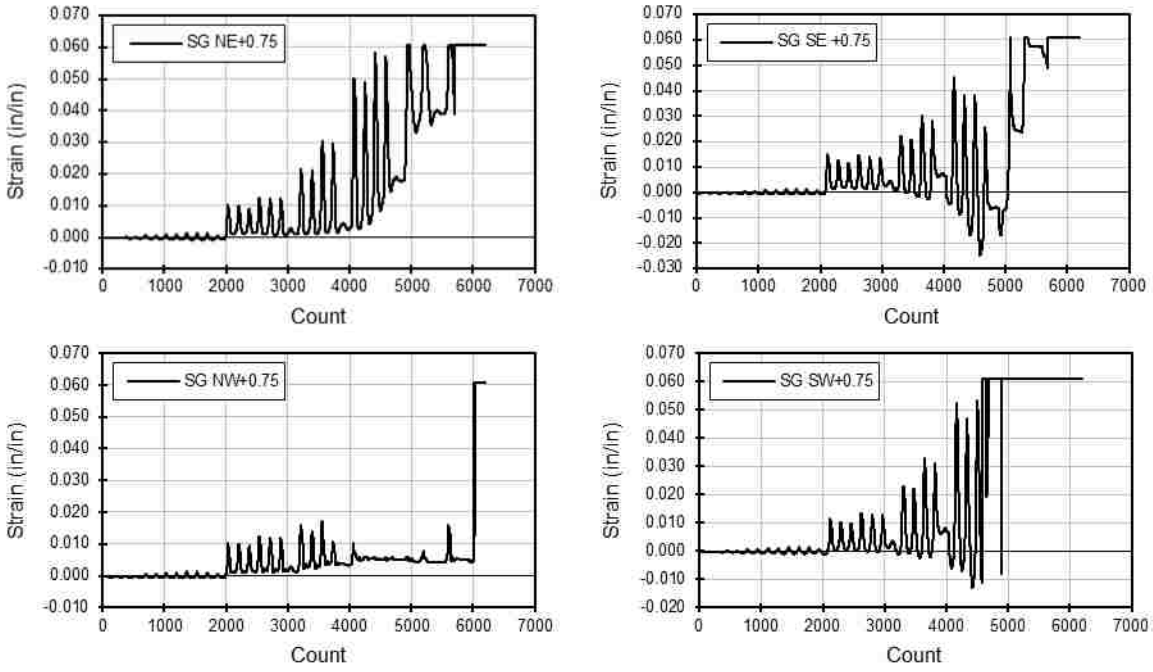

Figure A.12: RC Raw longitudinal reinforcing bar strain gauge data 2

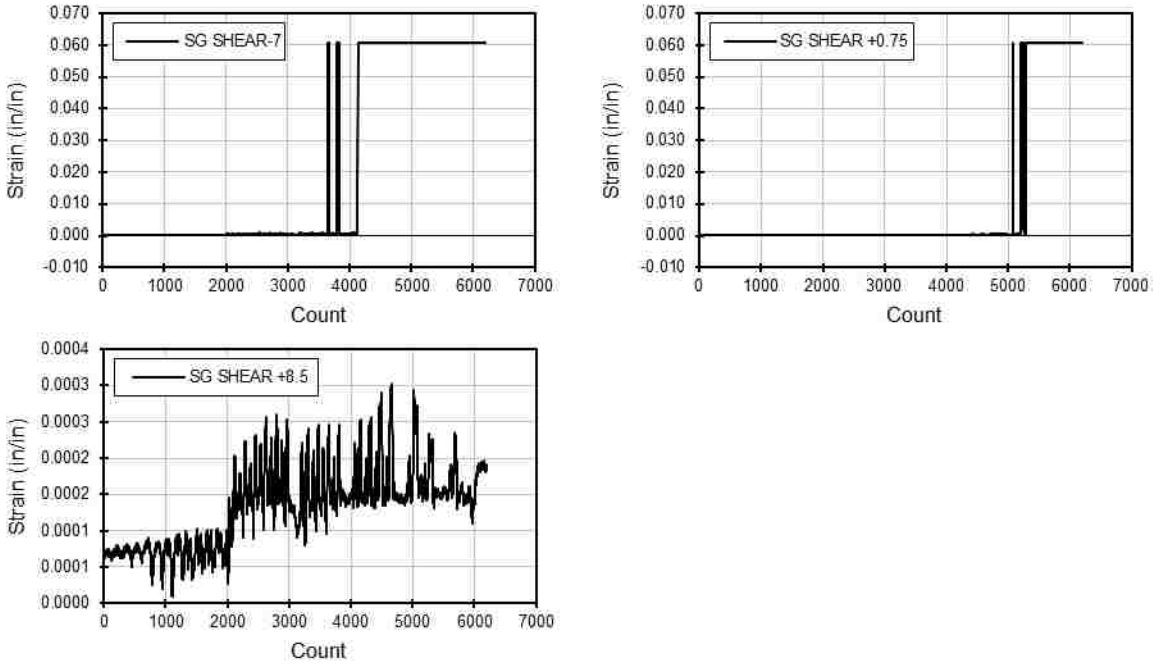

Figure A.13: RC Raw transverse reinforcing bar strain gauge data